Functionalised Microbubbles for Dual-Modality Imaging

Bethany Ivy Harriss

June 2017

Imperial College London

Department of Chemistry

Thesis submitted in partial fulfilment of the requirements for the degree of Doctor of Philosophy in Chemistry

Acknowledgements

Firstly, I would like to thank my supervisor Prof. Nicholas Long, who welcomed me into his research group over 3 years ago. The encouragement and advice that you have provided has allowed me to work on an amazingly diverse project and has motivated me even in difficult times.

I would also like to thank the staff at Imperial College London. In particular, thank you to Lisa Haigh for training me on so many pieces of mass spectrometry equipment and for fixing all of the problems that I encountered. Also, thank you to Peter Haycock who was always willing to have a chat whilst explaining NMR experiments to me. Sorry for making you run so many hated DOSY experiments! Finally, thanks to Paul, Steve and Jamie for making a trip to stores much more entertaining (and much longer) than expected.

I also need to thank all of the people that I have worked with during my projects. Firstly, to Marta Braga, Laurence Carroll and Javier Hernández-Gil for putting up with microbubbles with me. To Raquel Fraccari for making AFM enjoyable, Shengtao Lin for teaching me about nanodroplets and Jie Pan (Shirley) for looking after me in Hong Kong. Finally, to Sophie Morse, who has worked really hard to try to get results in our project before I finished.

A massive thank you needs to go to all of the Long Group for being so much fun and having plenty of tea breaks. I feel really privileged to have worked with so many friends, a few of which I would like to thank personally. Firstly, to Juan for taking me under your wing when I first started, patiently helping me and even taking me to my first conference. To Dave and James who helped me settle into the group by encouraging regular early pub trips. To Stu for always making everyone smile when you (occasionally) turn up in the office. To Adam for putting up with so many women with a smile and Tamara for all of the distracting and bizarre conversations we have had. To Lucy, Emma, Charlie C and Samantha for being such a supportive group of friends, for looking after me when I needed you and for being part of so many unforgettable memories. May we continue to make more! Finally, a special thank you to Stu and Lucy for managing to live and work with me and for being with me every step of the way.

I would also like to thank my friends and family who have shown me so much love and support. Most importantly, to my parents who have helped me in everything I do. These final months would have been much more difficult without your patience and support; thank you

for always being there for me. Also, to Jess for always being available with wine when I need to escape, I have really enjoyed living in the same town as you again.

Last but not least, to my boyfriend Dom. You have made me laugh, encouraged me when things got tough and provided me with an unlimited number of hugs. I have particularly enjoyed your distractions while writing up my thesis. Going through our PhD's together has been amazing and this experience would not have been the same without you by my side.

Thank you to all of you so much, you are all an inspiration and I couldn't have done it without you.

Declarations

I hereby declare that the work described in this thesis is entirely my own and was completed at Imperial College London between October 2013 and March 2017. When others have contributed, they have been clearly acknowledged within the text.

Copyright Declaration

The copyright of this thesis rests with the author and is made available under a Creative Commons Attribution Non-Commercial No Derivatives licence. Researchers are free to copy, distribute or transmit the thesis on the condition that they attribute it, that they do not use it for commercial purposes and that they do not alter, transform or build upon it. For any reuse or redistribution, researchers must make clear to others the licence terms of this work.

Abstract

Medical imaging is ubiquitous in disease diagnosis and monitoring, with many different methods available. The aim of dual-modal contrast agents is to synergistically combine two of these into one probe in order to enhance the information obtained. Early and accurate detection of diseases is crucial in improving patient prognosis and survival rates. For this reason, this thesis aims to develop cancer-specific contrast agents which combine multiple imaging modalities into one probe.

Ultrasound is a commonly used imaging modality as it is cheap, easy to use, portable and provides real-time images. It is frequently used to assess the abdominal organs and monitor foetus development, however cancerous tissues can be difficult to observe under normal conditions. Microbubbles are clinically used ultrasound contrast agents that can improve the visualisation of tumours. These are composed of a gas core stabilised by a surface coating such as a phospholipid and are the ideal platform for further functionalisation.

During this project, phospholipids have been functionalised with the cancer-targeting peptide RGD and fully characterised using NMR, MALDI-TOF and UPC^2-ES+. These were then formed into microbubbles and their selective binding proved through *in vivo* work.

Phospholipids were then functionalised with moieties to allow for coordination to ^{68}Ga, a PET isotope. Initial experiments involved the radiolabelling of a small molecule followed by functionalisation of the microbubble surface. Unfortunately this did not yield radiolabelled microbubbles, therefore latter experiments focussed on direct radiolabelling of a phospholipid and subsequent formation into microbubbles. This route resulted in radiolabelled microbubbles, with further development underway to improve this reaction.

Phospholipid functionalisation with pH sensitive and pH insensitive fluorophores was also performed, their fluorescence properties assessed and incorporation of modified phospholipids into microbubbles proved by microscope visualisation under laser irradiation. These were then formed into nanodroplets, with the goal of using the optical absorbers to induce selective vaporisation into microbubbles. Further work will assess the vaporisation properties of these nanodroplets.

Finally, small molecule fluorescence-MRI and fluorescence-PET probes were developed for use with microbubbles to mediate delivery across the blood-brain-barrier. Preliminary results indicate successful, selective delivery using this technique, with further testing underway.

Publications

Gallium and Functionalized-Porphyrins Combine to Form Potential Lysosome-Specific Multimodal Bioprobes, Jie Pan, Bethany I. Harriss, Chi-Fai Chan, Lijun Jiang, Tik-Hung Tsoi, Nicholas J. Long, Wing-Tak Wong, Wai-Kwok Wong, Ka-Leung Wong, *Inorganic Chemistry*, 2016, **55**, 14, 6839-6841.

Gadolinium and Platinum in Tandem: Real-time Multi-Modal Monitoring of Drug Delivery by MRI and Fluorescence Imaging, Hongguang Li, Bethany I. Harriss, Alkystis Phinikaridou, Sara Lacerda, Gregory Ramniceanu, Bich-Thuy Doan, Ka-Lok Ho, Chi-Fai Chan, Wai-Sum Lo, René M. Botnar, Rongfeng Lan, Cyrille Richard, Ga-Lai Law, Nicholas J. Long and Ka-Leung Wong, *Nanotheranostics*, 2017, **1**, 2, 186-195.

Probing T_1-T_2 Interactions and their Imaging Implications Through a Thermally Responsive Nanoprobe, Juan Gallo, Bethany I. Harriss, Javier Hernández-Gil, Manuel Bañobre-López, Nicholas J. Long, *Nanoscale*, In Press.

Optically and Acoustically Triggerable Sub-Micron Phase-Change Contrast Agents for Enhanced Photoacoustic and Ultrasound Imaging, Shengtao Lin, Anant Shah, Javier Hernández-Gil, Antonio Stanziola, Bethany I. Harriss, Terry O. Matsunaga, Nicholas Long, Jeffrey Bamber, Meng-Xing Tang, *Photoacoustics*, 2017, **6**, 26-36.

Table of Contents

Acknowledgements 2
Declarations 4
Abstract 5
Publications 6
Table of Contents 7
Abbreviations 14
Final Novel Compounds in the Thesis 17

1. Introduction 19

1.1 Imaging Modalities 20

1.2 Ultrasound Imaging 22
1.2.1 Microbubbles 23
1.2.2 Nanodroplets 28
1.2.3 Sonoporation 29

1.3 PET 29
1.3.1 [^{18}F]Fluro-2-deoxy-D-glucose (^{18}F-FDG) 31
1.3.2 ^{68}Ga Contrast Agents 32

1.4 Optical Imaging 34
1.4.1 Fluorescent Probes 36
1.4.2 Lanthanides 36

1.5 MRI 37
1.5.1 T_1 Contrast Agents 38

1.6 Targeted Imaging Probes 41
1.6.1 Cancer Properties 41
1.6.2 Cancer Targeting 42
1.6.2.1 Clinical Studies - TOC, TATE and PSMA Targeting Peptides 43
1.6.2.2 RGD Targeting Peptide 43

1.7Aims and Objectives 44

1.8 References 45

2. Cancer Targeted Microbubbles 51

2.1 Introduction 52

2.1.1 Aims 54

2.2 Direct Targeting of Microbubbles 55

2.2.1 Synthesis and Characterisation of an RGD Phospholipid 55

2.2.2 Microbubble Formation and Characterisation 62

2.2.2.1 Acoustic Characterisation 62

2.2.3 *In Vitro* Characterisation 63

2.2.4 *In Vivo* Experiments 66

2.3 Pre-Targeting of Microbubbles 67

2.3.1 Synthesis and Characterisation 67

2.4 Conclusions 70

2.5 References 70

3. PET Labelling of Microbubbles 73

3.1 Introduction 74

3.1.1 PET-Labelled Microbubbles 74

3.1.2 ^{68}Ga Microbubble Radiolabelling Methods 76

3.2.3 Aims 78

3.2 Radiolabelling of Microbubbles Using the TCO-Tetrazine Reaction 78

3.2.1 Characterisation of TCO-Containing Microbubbles 78

3.2.1.1 *In Vitro* Characterisation 79

3.2.2 Synthesis and Characterisation of Tetrazine-Containing Ga Chelators 80

3.2.2.1 DO3A-Tetrazine 80

3.2.2.2 DOTAGA-Tetrazine 82

3.2.3 TCO-Tetrazine Reactivity 83

3.2.4 Radiolabelling 88

3.2.4.1 DOTAGA-Tetrazine 88

3.2.4.2 DO3A-Tetrazine 91

3.2.4.3 Reaction with Microbubbles 93

3.3 Direct Radiolabelling of Microbubbles 94

3.3.1 Synthesis and Characterisation of Chelating Phospholipids 95
3.3.1.1 DSPE-PEG_{2000}-DOTA 95
3.3.1.2 DSPE-PEG_{2000}-NOTA 95
3.3.2 Radiolabelling 96
3.3.2.1 DSPE-PEG_{2000}-DOTA 96
3.3.2.2 DSPE-PEG_{2000}-NOTA 100
3.3.3 Acoustic Characterisation 103
3.4 Conclusions 103
3.5 References 104

4. Fluorescent Microbubbles and Nanodroplets 106

4.1 Introduction 107
4.1.1 Fluorescent Phospholipid Structures 107
4.1.2 Nanodroplets 109
4.1.3 Fluorophore Selection 110
4.1.4 Aims 112
4.2 Synthesis and Characterisation of Fluorescent Phospholipids 112
4.2.1 ROX Phospholipid 113
4.2.1.1 Synthesis 113
4.2.1.2 pH Titration 113
4.2.2 pH Sensitive Rhodamine Phospholipid 115
4.2.2.1 Synthesis 115
4.2.2.2 pH Titration 116
4.2.3 pH Insensitive Rhodamine Phospholipid 119
4.2.3.1 Synthesis 119
4.2.3.2 pH Titration 120
4.3 Microbubble Formation and Characterisation 121
4.3.1 N-Rh-PE Phospholipid 121
4.3.2 ROX Phospholipid 123
4.3.3 pH Sensitive and pH Insensitive Rhodamine Phospholipids 124
4.3.4 Acoustic Characterisation 127
4.4 Nanodroplet Formation and Characterisation 128

4.4.1 Microscope Images 128
4.4.2 DLS Measurement 130
4.5 Nanodroplet Vaporisation 131
4.6 Conclusions 133
4.7 References 134

5. Ultrasound Mediated Delivery of Contrast Agents 137

5.1 Introduction 138
5.1.1 Modalities for Brain Imaging 140
5.1.2 Aims 141
5.2 Dual-Modal MRI-Fluorescence Probe 142
5.2.1 Synthesis 143
5.2.2 Characterisation 143
5.2.2.1 Fluorescence Measurements 143
5.2.2.2 T_1 Relaxation Studies – Determination of Relaxivity (r_1) 143
5.2.2.3 Luminescence Studies – Determination of Hydration Number (q) 145
5.2.2.4 NMRD Profile – Aggregate Analysis 147
5.2.3 *In Vivo* Studies 149
5.3 Dual-Modal PET-Fluorescence pH Sensitive Probe 151
5.3.1 Synthesis and Characterisation 151
5.3.2 Radiolabelling 151
5.3.3 *In Vivo* Studies 152
5.4 Conclusions 153
5.5 References 154

6. Conclusions and Future Work 157

6.1 Targeting 158
6.2 Dual-Modal PET-Ultrasound 160
6.3 Dual-Modal Fluorescence-Ultrasound 162
6.4 Sonoporation 164
6.5 References 165

7. Experimental 167

7.1 General 168

7.2 Equipment and Instrumentation 168

7.2.1 NMR 168

7.2.2 Mass Spectrometry 168

7.2.3 UV-Vis. Measurements 169

7.2.4 LCMS 169

7.2.5 T_1 Measurements at 400 MHz 169

7.2.6 Relaxometer 169

7.2.7 Photophysical Measurements 170

7.2.8 Acoustic Characterisation 170

7.2.9 Additional 170

7.3 Microbubble Formation and Analysis 171

7.3.1 General Procedure 171

7.3.2 Formulations 171

7.4 Nanodroplet Formation and Analysis 174

7.4.1 General Procedure 174

7.4.2 Formulations 175

7.4.3 Laser Irradiation 176

7.5 Synthesis of Compounds in Chapter 2 176

7.5.1 DSPE-PEG_{2000}-maleimide – 2.1a 176

7.5.2 DSPE-PEG_{2000}-cRGDfK – 2.1 177

7.5.3 Tert-butyl (4-(aminomethyl)benzocarbamate) – 2.2a 178

7.4.4 Tert-butyl 4-(6-methyl-1,2,4,5-tetrazin-3-yl)benzylcarbamate – 2.2b 178

7.5.5 4-(6-Methyl-1,2,4,5-tetrazin-3-yl)benzylamine (Tetrazine) – 2.2 179

7.5.6 Tetrazine-maleimide – 2.3a 179

7.5.7 RGD-tetrazine – 2.3 180

7.5.8 DSPE-PEG_{2000}-TCO – 2.4 180

7.6 Synthesis of Compounds in Chapter 3 181

7.6.1 Tetrazine-Cl – 3.1a 181

7.6.2 ^{t}Bu-DO3A-COOEt – 3.1c 181

7.6.3 DO3A-COOH – 3.1d 182

7.6.4 ^{t}Bu-DO3A-tetrazine – 3.1e 182
7.6.5 DO3A-tetrazine – 3.1 183
7.6.6 ^{t}Bu-DOTAGA-tetrazine – 3.3e 184
7.6.7 DOTAGA-tetrazine – 3.3 184
7.6.8 TCO-PEG$_4$ Reaction with 3.1 and 3.3 185
7.6.9 2.4 and 3.1 Reaction 185
7.6.10 2.4 and 3.3 Reaction 185
7.6.11 DSPE-PEG$_{2000}$-DOTA – 3.5 186
7.6.12 DSPE-PEG$_{2000}$-NOTA – 3.6 186

7.7 Synthesis of Compounds in Chapter 4 187
7.7.1 DSPE-PEG$_{2000}$-ROX – 4.1 187
7.7.2 Rh-COOH – 4.2b 187
7.7.3 DSPE-PEG$_{2000}$-Rh – 4.2 188
7.7.4 Rh+-COOH – 4.3c 188
7.7.5 DSPE-PEG$_{2000}$-Rh+ – 4.3 189

7.8 Synthesis of Compounds in Chapter 5 190
7.8.1 Rh+-Cl – 5.1a 190
7.8.2 ^{t}Bu-DO3A-Rh+ – 5.1b 190
7.8.3 DO3A-Rh+ – 5.1 191
7.8.4 Gd-DO3A-Rh+ – 5.1-Gd 192
7.8.5 Tb-DO3A-Rh+ – 5.1-Tb 192
7.8.6 Yb-DO3A-Rh+ – 5.1-Yb 192

7.9 Radiochemistry 193
7.9.1 Eckert & Ziegler IGG100 ^{68}Ge/^{68}Ga Generator 193
7.9.1.1 HCl Elution 193
7.9.1.2 NaCl Elution 193
7.9.2 iThemba 740 MBq ^{68}Ge/^{68}Ga Generator 194
7.9.2 1 HCl Elution 194
7.9.2.2 NaCl Elution 194
7.9.3 DO3A-tetrazine – 3.1 194
7.9.3.1 Reaction with TCO-Microbubbles 194
7.9.3.2 Reaction with DSPE-PEG$_{2000}$-TCO 2.4 194
7.9.4 DOTAGA-tetrazine – 3.3 195

7.9.4.1 Reaction with TCO-Microbubbles....195
7.9.4.2 Reaction with DSPE-PEG_{2000}-TCO 2.4....195
7.9.5 DSPE-DOTA – 3.5....195
7.9.6 DSPE-NOTA – 3.6....196
7.9.7 DO3A-Rh – 5.2....196
7.10 *In Vitro* Studies....197
7.10.1 Washing Studies....197
7.10.2 Blocking Experiments....197
7.11 *In Vivo* Studies....197
7.11.1 Ultrasound Imaging....197
7.11.2 Ultrasound Delivery....198
7.12 References....199
Appendix....200

Abbreviations

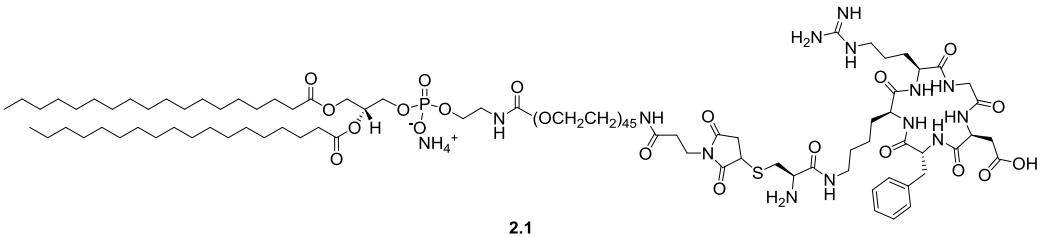
2D	two-dimensional
3D	three-dimensional
ANS	1-anilino-8-napthalene sulfonate
BBB	blood-brain barrier
Boc	*tert*-butyloxycarbonyl
BODIPY	boron-dipyrromethene
cRGDfK	cyclic peptide sequence Arg-Gly-Asp-(D)Phe-Lys
C_{18}-Rh	octadecylrhodamine B
calcd.	calculated
$CDCl_3$	deuterated chloroform
CD_3OD	deuterated methanol
cmc	critical micelle concentration
CT	computed tomography
Cy	cyanine
DHB	dihydroxybenzoic acid
DLS	dynamic light scattering
DO3A	1,4,7-tris(carboxymethyl)-1,4,7,10-tetraazacyclododecane
DOSY	diffusion-ordered NMR spectroscopy
DOTA	1,4,7,10-tetraazacyclododecane-1,4,7,10-tetraacetic acid
DOTAGA	2-(4,7,10-tris(carboxymethyl)-1,4,7,10-tetraazacyclododecan-1-yl)pentanedioic acid
DOX	doxorubicin
DPH	diphenylhexatriene
DPPC	1,2-dipalmitoyl-*sn*-glycero-3-phosphocholine
DSPE	1,2-distearoyl-*sn*-glycero-3-phosphoethanolamine]
DTPA	diethylenetriaminepentaacetic acid
EDC	1-ethyl-3-(3-dimethylaminopropyl)carbodiimide
EPR	enhanced permeation and retention
ES+	positive electrospray ionisation
ET	energy transfer
FRET	Förster resonance energy transfer
FUS	Focussed ultrasound

HBTU	2-(1H-benzotriazol-1-yl)-1,1,3,3-tetramethyluronium hexafluorophosphate
HOMO	highewst occupied molecular orbital
HPLC	high-performance liquid chromatography
HSA	human serum albumin
I	nuclear spin
ICG	indocyanine green
ISC	intersystem crossing
λ_{em}	emission wavelength
λ_{ex}	excitation wavelength
λ_{max}	maximum wavelength
LCMS	liquid chromatography-mass spectrometry
Ln	lanthanide
LUMO	lowest unoccupied molecular orbital
MALDI	matrix-assisted laser desorption ionisation
MB	microbubble
MRI	magnetic resonance imaging
MS	mass spectrometry
m/z	mass to charge ratio
NBD	4-nitrobenzo-2-oxa-1,3-diazole
NBD-PC	4-nitrobenzo-2-oxa-1,3-diazole phosphatidylcholine
ND	nanodroplet
n.d.c	non-decay-corrected
NIR	near infrared
NMR	nuclear magnetic resonance
NMRD	nuclear magnetic relaxation dispersion
NOTA	2,2',2''-(1,4,7-triazacyclononane-1,4,7-triyl)triacetic acid
N-Rh-PE	sulforhodamine B phosphatidylethanolamine
PBS	phosphate-buffered saline
PEG_x	poly(ethylene glycol) x units
PeT	photoinduced electron transfer
PET	positron emission tomography
ppm	parts per million

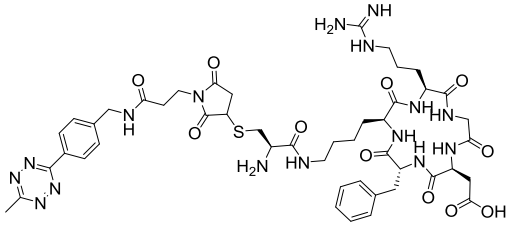
q	hydration number
R_1	rate of relaxation
r_1	relaxivity
RCY	radiochemical yield
RGD	peptide sequence Arg-Gly-Asp
Rh	rhodamine
ROI	region of interest
ROX	5(6)-carboxy-X-rhodamine
RT	room temperature
S_0	singlet ground state
S_1	singlet excited state
SEC	size exclusion chromatography
SPECT	single photon emission computed tomography
τ_m	water residence lifetime
τ_R	rotational correlation time
T_1	triplet excited state
T_1	longitudinal relaxation time
T_2	transverse relaxation time
TCO	*trans*-cyclooctene
TFA	trifluoroacetic acid
TMR	tetramethyl-rhodamine
ToF	time-of-flight
UPC^2	ultra-performance convergence chromatography
US	ultrasound
UV-vis.	Ultra violet-visible
v/v	volume/ volume
ω	Larmor frequency

Final Novel Compounds in the Thesis

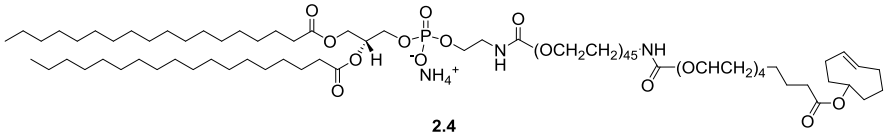
Chapter 2



2.1

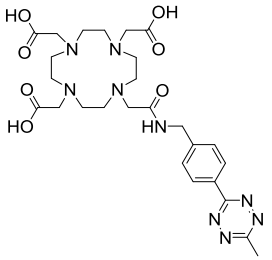


2.3

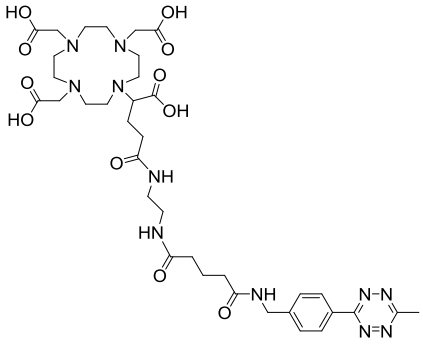


2.4

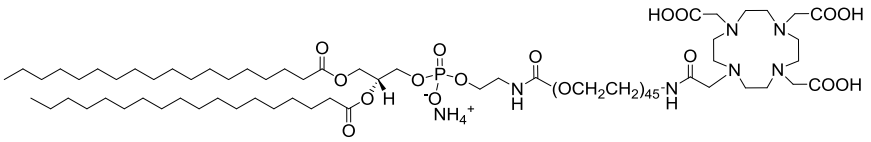
Chapter 3



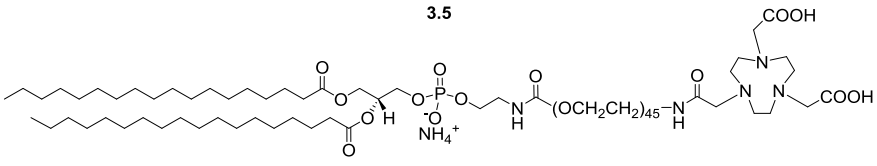
3.1



3.3

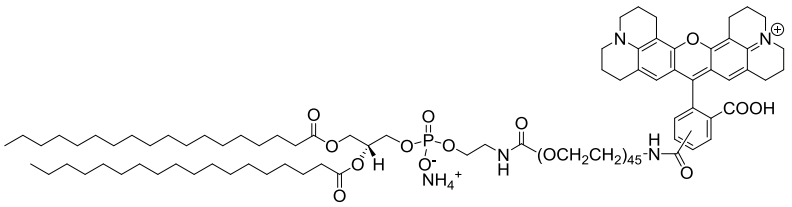


3.5

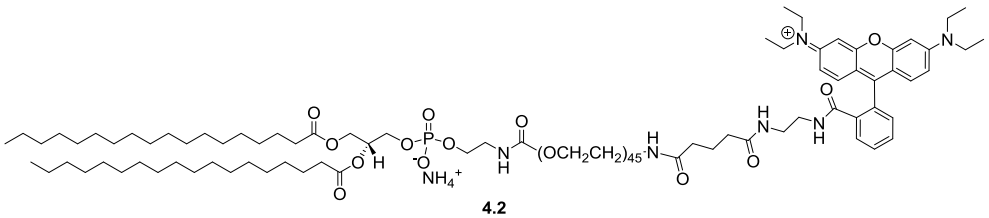


3.6

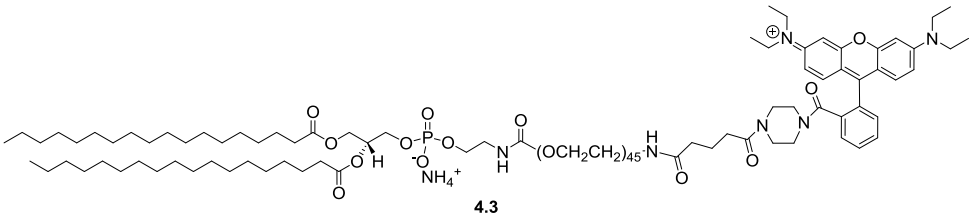
Chapter 4



4.1

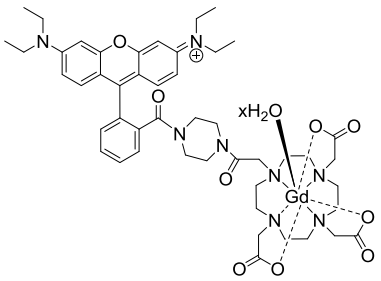


4.2

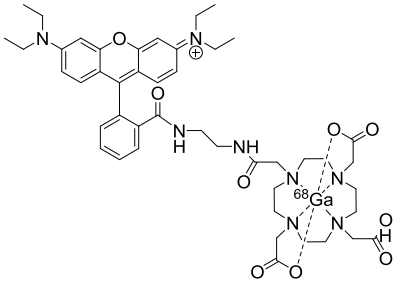


4.3

Chapter 5



5.1-Gd



5.2-Ga

Chapter 1

Introduction

This chapter aims to provide a general overview of medical imaging. This preferentially focuses on ultrasound imaging and ultrasound contrast agents, i.e. microbubbles. Alternative imaging modalities, contrast agents and targeting methodologies that are relevant to this thesis are also discussed. At the beginning of subsequent chapters, a more focussed introduction is provided in the relevant areas. Chapter 2 focuses upon cancer targeting of microbubbles; Chapter 3 discusses dual-modal PET-ultrasound probes; Chapter 4 explores fluorescent microbubbles and nanodroplets and, finally, Chapter 5 moves into ultrasound-mediated delivery of contrast agents and the synthesis of small molecule dual-modal fluorescence-MRI or fluorescence-PET probes.

1.1 Imaging Modalities

The goal of imaging is to non-invasively detect changes or processes in intact subjects without perturbing the living system.[1] This does not require the removal of tissue for *ex vivo* analysis which results in unavoidable changes in physiological conditions making them non-representative of the situation *in vivo*.[2]

Medical imaging has existed for many years, with the first X-ray having famously been collected by Wilhelm Röntgen in 1895.[3] This was the first of a range of imaging modalities developed until the late 1970's that could be used to visualise morphological changes as a result of disease.[1, 4] This is commonly referred to as structural or anatomic imaging. Improvements in these techniques resulted in higher spatial resolutions becoming accessible. This, in combination with the introduction of contrast agents, allowed for imaging at the mesoscale and therefore information about physiological parameters in live subjects could be acquired; this is termed functional imaging.[5] Molecular imaging began to emerge over 30 years ago in order to visualise biological processes at the cellular and molecular level by imaging specific molecules and pathways.[2, 5, 6]

There are multiple modalities available for imaging, as demonstrated in **Table 1.1**. These include ultrasound (US), magnetic resonance imaging (MRI), optical imaging, X-rays, computed tomography (CT), single-photon emission computed tomography (SPECT) and positron emission tomography (PET). As all imaging modalities operate using different methodologies and equipment, they are suited to different applications. These differences are discussed in **Table 1.1** and highlight that no imaging modality is universally applicable. The mechanisms underlying these modalities are discussed in more detail below.

Table 1.1: Details of the different imaging modalities.[1, 5]

Modality	Radiation	Resolution[a]	Depth	Amount	Scan Time	Sensitivity
Ultrasound	Sound waves	50-500 μm	mm-cm	μg-mg	Sec	High
MRI	Radiowaves	4-100 μm	No limit	μg-mg	Min- hours	Low
Optical	Visible-NIR	15-1000 nm	< 1 cm	μg-mg	Sec	High
X-ray	X-rays	12-50 μm	No limit	None	Min	Low
CT		50-200 μm				
SPECT	γ-rays[b]	1-2 mm	No limit	ng	Min	High
PET	γ-rays[c]	1-2 mm	No limit	ng	Min	High

[a]Limit for high-resolution, small animal systems. [b]High energy. [c]Low energy.

A contrast agent can be used in combination with these imaging modalities either to provide a signal for detection, to add additional information to an existing anatomical image or to improve the quality of the image.[1] In nuclear imaging, the molecule producing the signal is referred to as a tracer. These can all be referred to as imaging probes.

The inherent advantages and disadvantages of each of these imaging techniques brought about the advent of dual-modal imaging. This is the synergistic combination of two imaging techniques, made possible by the development of dual-modal contrast agents. These combinations can reduce the required scan time, improve data analysis and enhance the information obtained. This led to the development of the first fused PET/CT instrument in 1998,[7] which combines functional/ molecular PET imaging with morphological CT information. Since this, standalone PET has become virtually redundant, with all new machines bought as part of multimodality systems.[8] Following this success, PET/MRI instruments have been developed[8, 9] which improve upon PET/CT as CT exposes patients to high levels of radiation, limiting the number of scans that can be performed within a given time frame.[2] The combination of other imaging modalities such as MRI/optical have been the focus of research, however these have not been transferred into the clinic.[8]

Ultrasound imaging is one of the most frequently used methods of biomedical imaging, second only to X-ray imaging;[10] however, it remains understudied for molecular imaging in comparison to other modalities.[2] This has many advantages over other modalities as it is cheap (a factor of at least ten times cheaper than MRI, PET and X-ray imaging), portable and

provides real-time information,[11] with depth penetration and spatial resolution that can be adjusted depending upon the application.[2] Ultrasound contrast agents are also unique, in the form of stabilised gas bubbles in the micrometre range, termed microbubbles (MBs). The high surface area of these microbubbles provides the ideal platform for functionalisation with additional imaging modalities, targeting agents or drugs for therapy.

This thesis will explore the potential applications for functionalisation and use of these microbubbles. The fundamental principles behind all of the imaging modalities used as part of this work are discussed below. Due to the wide range of techniques used, only those aspects directly relevant to this thesis will be mentioned, however the imaging field extends far beyond those probes and methodologies discussed.

1.2 Ultrasound Imaging

Ultrasound waves are longitudinal sound waves that oscillate at a frequency higher than human hearing can detect, typically between 1-20 MHz for clinical scanners.[2] As a result, they cannot diffract around objects as typical sound waves can but are reflected by these boundaries.[1] It is this reflection that is used in ultrasound imaging.

The propagation of a sound wave through a medium is determined by the acoustic impedance of the material (Z), calculated as shown in **Equation 1.1**:

$$Z = \rho c = \sqrt{K\rho} \qquad \textbf{Equation 1.1}$$

Where ρ = density, c = the speed of sound in a material and K = the bulk modulus which is the reciprocal of compressibility. When a sound wave encounters a material with different acoustic impedance, it is scattered; this backscatter can be detected, creating ultrasound contrast. The velocity of sound in different biological substances varies due to changes in density and/ or compressibility, as shown in **Figure 1.2**. The velocity in most soft tissues is close to that of water (1498 ms^{-1}), with any differences caused by variations in compressibility alone.[10] These differences mean that the interfaces between different biological tissues can be detected, creating an anatomic image.

The ultrasound frequency, peak-rarefactional pressure (PRP, also peak-negative pressure, PNP), pulse length and pulse repetition frequency are all important in determining the effectiveness and safety of an imaging experiment.[12] For example, the use of higher frequencies results in higher resolution images at the expense of depth penetration as shorter

wavelengths are more likely to interact with matter, reducing their travelling distance. Attenuation of ultrasound waves is predominantly caused by the absorption of sound waves by tissue; this can result in localised heating if the ultrasound pulses are not well designed.[2]

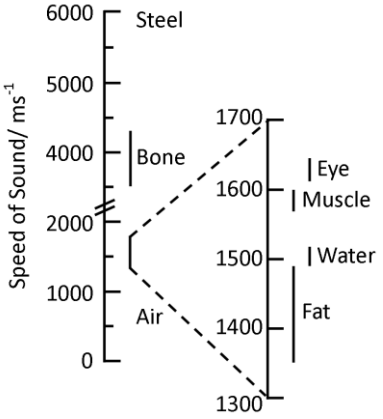


Figure 1.2: The velocity of sound in a variety of biological and non-biological substances. Figure recreated from reference.[10]

During ultrasound imaging, a transducer emits short pulses of ultrasound into the tissue and detects the echoes that are reflected back. The time interval between pulse and detection of the echo can be used to calculate the depth of the interface and thus begin to build a picture.[13] Millions of these pulses are transmitted and received every second, creating an image.[1] Currently, ultrasound cannot be used for whole-body imaging.[14]

1.2.1 Microbubbles

Ultrasound imaging alone is limited to morphological data collection, with no method to enable molecular imaging. Additionally, blood vessels and some diseases such as cancer cannot be detected effectively with ultrasound alone.[15] The addition of a targeted contrast agent can facilitate development into functional and molecular imaging and improve visualisation of certain conditions.[2]

As mentioned above, microbubbles can be used as contrast agents in ultrasound imaging and produce superior results to any alternatives that have been developed.[16] These contain gas, which has a significantly different acoustic impedance than tissue (see **Figure 1.2**), resulting in efficient ultrasound scattering. In addition, at specific frequencies (dictated by bubble type and size) microbubbles can oscillate due to the compressibility of the core gas; this is known as cavitation. When microbubble contraction and expansion is uniform (known as stable cavitation) this oscillation transmits harmonic signals of the original frequency back to the detector, allowing for suppression of background tissue scattering and improvement of the

contrast-to-noise ratio. If the incorrect ultrasound parameters are used, such as high PRP, expansion can be unstable and results in microbubble collapse (termed inertial cavitation). This is depicted in **Figure 1.3**. Different pulse sequences can also be used to eliminate background signals which similarly rely upon the non-linear acoustic response of microbubbles.[13, 17]

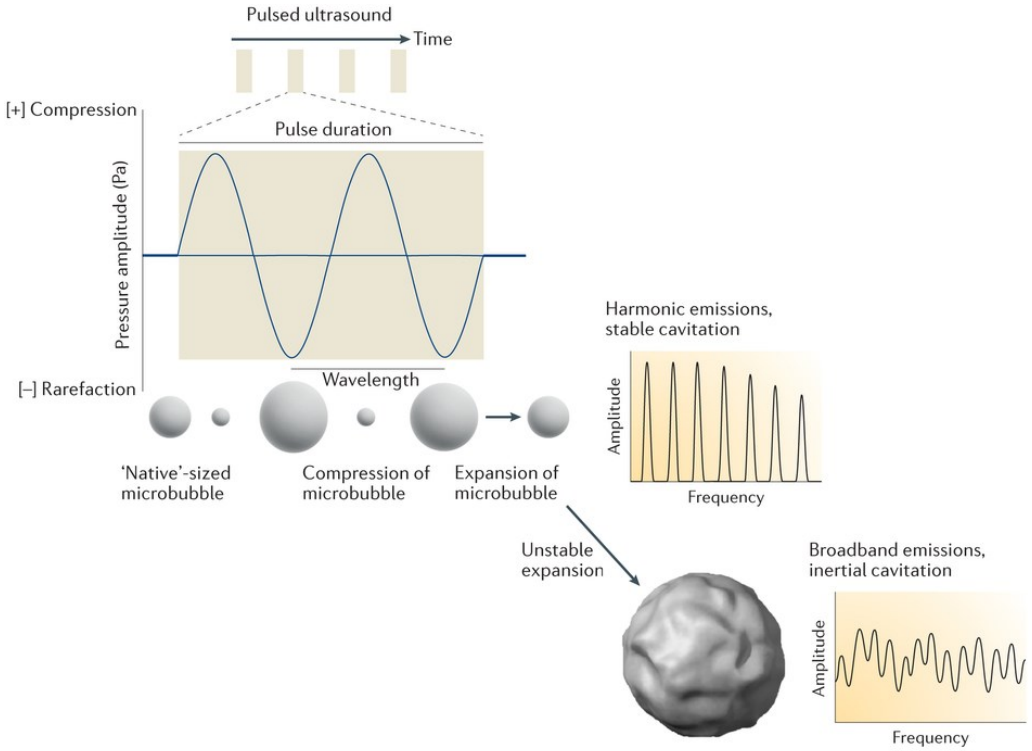


Figure 1.3: Schematic representation of microbubble cavitation in the presence of an ultrasound wave. This demonstrates microbubble size change during compression and rarefaction and the difference between stable and unstable cavitation. Reproduced with permission.[17]

Microbubbles are composed of an inert gas core which should have low solubility in the blood. Examples include perfluorocarbons (PFCs) or sulphur hexafluoride, although air is still used in some instances. These are coated in a stabilising biocompatible layer such as a lipid membrane, a polymer coating or a denatured protein such as serum albumin.[13, 16] This is depicted schematically in **Figure 1.4**. The development of microbubbles can be classed in generations, with first generation microbubbles containing air with no surface stabilisation, second generation microbubbles comprising a surface coating and third generation formulations using alternative filling gasses.[18]

First generation microbubbles had very short *in vivo* lifetimes, with an air bubble of 2.5 μm having a calculated lifetime in the bloodstream of ~ 0.175 s.[19] These could only be used to enhance the right side of the circulation as they could not survive passage though the lungs.[18]

The use of a filling gas with low solubility in blood can help to increase the microbubble lifetime,[13, 20] with an analogous uncoated perfluorobutane droplet of 2.5 μm having a calculated lifetime of ~ 1 minute.[21]

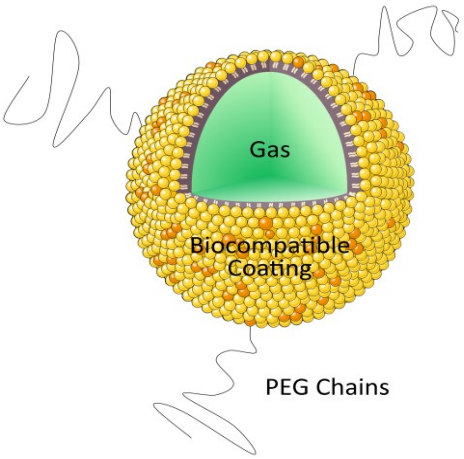


Figure 1.4: Schematic representation of a microbubble.

The incorporation of a shell can also significantly improve this stability and has a large impact on the acoustic properties of the microbubble. Phospholipid microbubbles have much thinner shells than polymer or protein analogues (3 nm thick as opposed to 50-500 nm), resulting in easy compressibility and thus better ultrasound contrast.[22] In addition, albumin shells are much more rigid and are therefore less stable to ultrasound; they can also cause immunogenicity issues as they are animal-derived. In comparison, phospholipid shells are biocompatible, easy to manufacture and allow for a mixture of components to be used, facilitating controlled functionalisation of the surface. However, phospholipid coatings allow for lower surface loading than other shell types.[21] In a general calculation for a 4 μm microbubble, the typical surface area is 50 μm^2 with a gas volume of ~ 34 μm^3, comprising 10^8 lipid molecules (PC has a headgroup area of approximately 50 $Å^2$ [23, 24]) which have a mass of < 1 pg.[25]

In order to stop microbubbles aggregating or coalescing, poly(ethylene glycol) (PEG) polymer units are often attached to the surface as these prevent close approach of the microbubbles. This also helps prevent their recognition by the immune system and thus increase their lifetime *in vivo*.[26] These PEG brushes are typically 2000 or 5000 Da as shorter chains are unable to stabilise the microbubble, with a maximum of 10 mol% loading.[21]

Most microbubble formulations comprise three different types of lipid: a matrix lipid, an emulsifying lipid and a functionalised lipid. The matrix lipid is the main component and

provides stabilisation. It is typically below its main transition temperature, such as DPPC at 41 ^{o}C.[27] The emulsifying lipid contains the PEG chain, whilst the functionalised lipid contains any additional features to be incorporated into the microbubble; on a targeting lipid, a polymer spacer is generally necessary to ensure that this extends past the PEG brush.[21]

Even including these features, microbubbles have very short lifetimes *in vivo*, measured in minutes (Optison ~5 min).[28] This can be advantageous as it means that after a typical human microbubble dose (~ 5 x 10^9 MBs/ 30 kg),[29] repeat ultrasound experiments can be performed approximately every 30 minutes as ~ 95 % of microbubbles are cleared after this time in many formulations.[30] It does however mean that they are not well suited for longer-term imaging.

Many microbubble formulations are commercially available and clinically used. The compositions of these microbubbles vary which impacts upon their safety and their acoustic properties.[18, 31] **Table 1.2** provides an overview of currently available products. The approval of these differs across the world, with Europe having approved the widest variety of microbubble contrast agents for a range of applications.[32] None of these clinically approved contrast agents are targeted.

Table 1.2: Summary of commercially available, clinically licensed microbubbles.[18, 32]

Year	Name	Gas	Coating	Manufacturer
		First Generation		
1982	Echovist	Air	None	Schering AG
		Second Generation		
1985	Levonist	Air	Palmitic acid	Schering
1994	Albunex*	Air	Sonicated albumin	Mallinckrodt
		Third Generation		
1997	Optison	Perfluoropropane	Sonicated albumin	GE Healthcare
2001	SonoVue	Sulphur hexafluoride	Phospholipid	Bracco Imaging S.p.A
2001	Definity	Perfluoropropane	Phospholipid	Bristol-Myers-Squibb
2007	Sonazoid	Perfluorobutane	Phospholipid	GE Healthcare

*No longer commercially available.

Microbubbles typically have diameters in the range 1-10 μm,[32] with each formulation having a specific size distribution (as demonstrated in **Figure 1.5**). Microbubble size greatly effects the acoustic enhancement, with intensity increasing with the sixth power of the radius. However, microbubbles larger than 10 μm are filtered through the lung capillary bed, reducing their circulation times.[28, 33] Most studies have found that microbubbles of several microns in diameter produce good contrast at clinically relevant frequencies,[34] with SonoVue microbubbles below 2 μm not contributing appreciably to the echogenicity.[35] This ideal size results in microbubbles being of similar size to red blood cells (~7.8 μm).[20, 32] Studies have shown that microbubbles flow at approximately the same velocity as red blood cells with blood flow being unaffected by their injection, indicating that they are safe *in vivo*.[28, 36] Upon retrospective studies, microbubbles have displayed an exceptional safety profile in patients, with very few serious adverse side effects.[37]

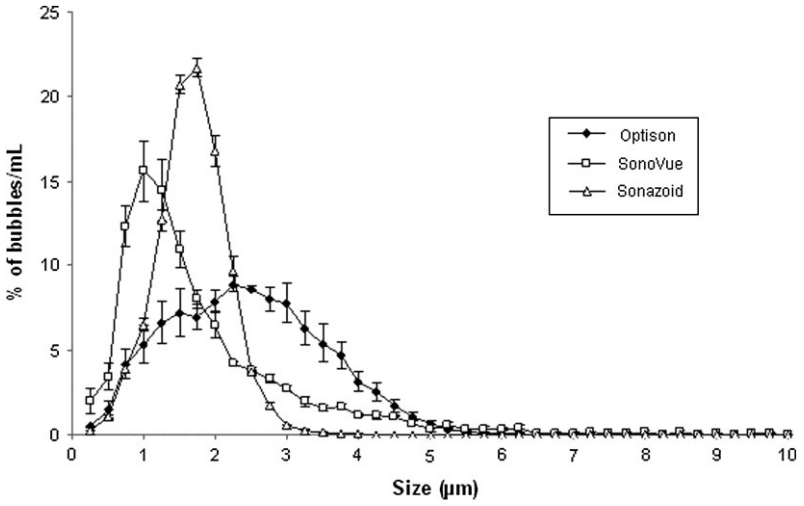


Figure 1.5: Size distribution of commercially available microbubbles Optison, SonoVue and Sonazoid displayed as a percentage of microbubbles per volume. Bin size of 0.25 μm. Reproduced with permission.[38]

Due to the large size of the microbubbles, they do not pass through the vascular endothelium and hence serve as purely intravascular contrast agents. This is both an advantage as it means that blood flow can be selectively probed, allowing for identification of atherosclerotic plaques and tumours, whilst being a disadvantage as abnormalities away from blood flow cannot be imaged.[32]

In addition to pure imaging, microbubbles can be used for drug delivery. There are two general methods: drug molecules can be attached to the shell of the microbubble or encapsulated inside them. The latter method has been used in gene therapy to deliver genetic

material to a specific site. When at the targeted location, the microbubble can be destroyed by high frequency ultrasound to release its payload.[39]

1.2.2 Nanodroplets

Nanodroplets are condensed microbubbles containing a liquid state perfluorocarbon core and are metastable under physiological conditions, limiting spontaneous vaporisation into microbubbles and extending their lifetime *in vivo*.[40] These nanodroplets can be vaporised into microbubbles using either acoustic[41, 42] or optical[43, 44] activation, resulting in ultrasound detection only in desired regions. The former may require high acoustic frequencies and pressures and cannot reach gaseous areas such as the lungs,[43, 44] hence the development of the latter technique.

Sizes vary dependent upon composition, but are typically in the low 100's of nanometres.[41] Upon vaporisation, these droplets can expand to 3-10 times their original size (a droplet of 200 nm forming a microbubble of around 1 μm under ideal gas conditions),[41, 45] providing significant ultrasound enhancement. This is shown schematically in **Figure 1.6**. The amount of energy required to vaporise a nanodroplet decreases with increasing size, with calculations indicating that perfluorobutane nanodroplets should remain stable in the 200-600 nm range at body temperature.[45] In addition, the lower boiling the filling gas, the less energy that is required to trigger vaporisation.[45, 46]

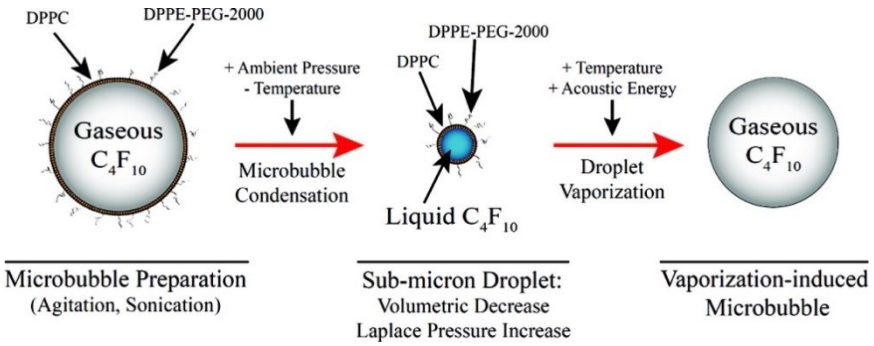


Figure 1.6: Schematic representation of nanodroplet formation and vaporisation showing the key features of these particles and the processes which form them. Reproduced with permission.[47]

In order to facilitate laser-induced vaporisation, a photoabsorber must be incorporated into the nanodroplet. This has been performed using silica coated lead sulphide nanoparticles (1064 nm),[44] gold nanoparticles (535 nm),[48] gold nanorods (absorption at 1064 nm),[43] encapsulated metal complexes (Epolight 3072, dithiolene nickel, 1054 nm),[49, 50] organic dyes (indocyanine green, ICG, 780 nm)[51] and recently covalently attached dyes (Cy 7.5, 788

nm).[52] The laser fluence required to vaporise these nanodroplets varies depending upon composition,[53] however it is known that pulsed lasers are necessary.[54]

1.2.3 Sonoporation

Microbubbles can be used in the reversible opening (sonoporation) of cell membranes and the blood-brain barrier (BBB).[55] At low frequencies, this effect is caused by linear oscillations of the bubbles, which are controlled by the ultrasound pulses used. BBB disruption has been shown to last about 4 hours after sonication and allows for transport of drugs up to 40 kDa[56] with no apparent tissue damage or toxicity. At high ultrasound frequencies, unstable cavitation and microbubble destruction can produce the same effect; however, this can damage the cell wall.[57]

Sonoporation has been applied on a small scale in a clinical setting, using the combination of microbubbles and ultrasound during chemotherapy to aid in drug delivery to pancreatic tumours. This was effective in increasing the average patient life span and reducing the tumour size.[58]

1.3 PET

PET and SPECT are related as both are nuclear imaging modalities that require the use of radioactive tracers; however, PET is more sensitive, easier to quantify, requires shorter imaging protocols and provides improved image quality than SPECT.[59, 60] As only PET was used in this thesis, SPECT will not be discussed.

PET uses unstable neutron deficient nuclei which decay via positron (β^+) emission, as demonstrated in **Equation 1.2**, resulting in formation of an element of atomic number (Z) one less than the parent isotope (e.g. ^{11}C decays to ^{11}B).[61, 62] This is accompanied by the formation of a neutrino (υ).

$$ {}^{A}_{Z}X \rightarrow {}^{A}_{Z-1}Y + \upsilon + \beta^+ \qquad \textbf{Equation 1.2} $$

This positron is not detected directly, but travels around 0.5-2 cm through tissue before colliding with an electron. Upon collision, this positron and electron annihilate, producing two gamma ray (γ) photons of 511 keV which are emitted at approximately 180^o to each other. The concurrent detection of these quanta by a ring of detectors and time-of-flight analysis can be used to determine the origin of the γ-rays and thus the location of the probe.

Millions of these annihilation events are required to construct a PET image.[13, 62] This process is illustrated in **Figure 1.7**.

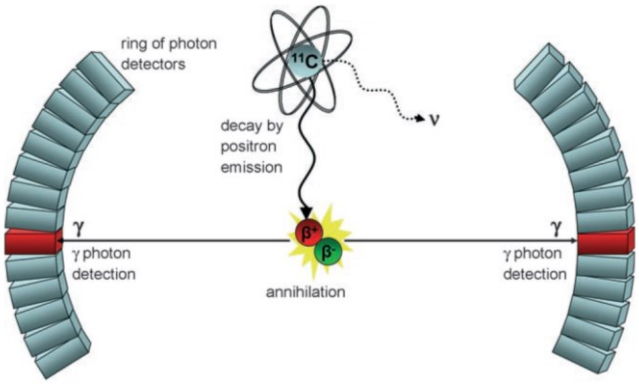


Figure 1.7: Diagram illustrating the PET imaging process showing positron (β^+) emission, annihilation of the positron with an electron (β^-) and detection of the two resulting γ photons by a ring of detectors. Reproduced with permission.[62]

The distance travelled by a positron before annihilation depends upon the radionuclide as each produces positrons with a characteristic kinetic energy (see **Table 1.3**). Lower energy positrons travel shorter distances through tissue, producing higher resolution images; for example, a positron emitted by ^{18}F travels on average 0.6 mm whereas one produced by ^{68}Ga travels 2.9 mm.[63] Due to this distance between positron emission and annihilation, PET is inherently a low resolution technique.[62] In addition, it cannot be performed without a tracer; therefore, no anatomical information can be obtained. It is for this reason that PET/CT combinations have been so successful as it allows for the co-registration of functional PET with morphological CT images.[62]

PET is a very sensitive technique and therefore only small amounts of tracer are required.[62] This low concentration means that the development process can be accelerated as toxicology issues are likely to be less significant. This is particularly evident in microdosing studies, termed Phase 0 clinical trials, which allow for earlier human testing at concentrations low enough that they will not induce pharmacological effects.[64]

Numerous nuclei can be used for PET, with some of these listed in **Table 1.3**. Ideal isotopes have a half-life long enough to allow for their incorporation into the tracer and their injection into the patient, but a half-life short enough to allow for acceptable imaging times. ^{18}F is currently the most widely used radionuclide, however ^{11}C, ^{15}O and ^{13}N are also popular as they are found in biomolecules and can therefore be incorporated without interfering with the molecular structure or biological activity.[13, 62]

Table 1.3: Properties of common PET radioisotopes, separated according to production method.[13, 65, 66]

Radionuclide	Half-life	Max. β^+ Energy/ MeV	Production
^{11}C	20.4 min	0.96	Cyclotron
^{13}N	9.9 min	1.20	Cyclotron
^{15}O	2.8 min	1.74	Cyclotron
^{18}F	109.8 min	0.63	Cyclotron
^{64}Cu	12.7 h	0.65	Cyclotron
^{89}Zr	78.5 d	0.90	Cyclotron
^{52m}Mn	21.1 min	2.63	Generator
^{68}Ga	68.0 min	1.83	Generator

More recently, interest has grown in radionuclides obtainable from a generator due to their wider availability than those produced by a cyclotron. This follows from the success in SPECT imaging of ^{99m}Tc, which can be produced from a generator and formulated using facile, low cost kits. This has dominated the area for many years. Such an isotope that can be used in PET, with a suitable half-life for conventional imaging, is ^{68}Ga.[67]

1.3.1 [^{18}F]Fluoro-2-deoxy-D-glucose (^{18}F-FDG)

^{18}F-FDG, shown in **Figure 1.8**, is the most commonly used clinically approved PET tracer and is the reason for the availability and use of PET equipment today.[67] ^{18}F-FDG is taken up by the cells using the glucose transporter, however the presence of fluorine at the 2' position inhibits metabolic degradation until it decays.[1] As such, accumulation of ^{18}F-FDG is an indicator of glucose uptake. This means that those regions with high glucose uptake, such as the brain, heart and tumorous regions, display high signals. However, as all cells in the body metabolise glucose, there is an inherent background signal.[13]



Figure 1.8: Structures of a) α-glucose and b) ^{18}F-FDG.

1.3.2 ^{68}Ga Tracers

In 2014, the first ^{68}Ge/^{68}Ga generator was granted marketing authorisation for clinical use and as a result many centres, particularly in Europe, are now using ^{68}Ga clinically.[67] This predominantly makes use of somatostatin receptor-targeting probes such as DOTATATE and DOTATOC. These chelate ^{68}Ga using 1,4,7,10-tetraazacyclododecane-1,4,7,10-tetraacetic acid (DOTA) in combination with cancer targeting peptides 'TATE' or 'TOC' (*vida infra*).[68, 69] Recently, HBED-PMSA has also been used clinically for prostate cancer imaging (*vida infra*).[70, 71]

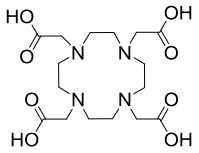
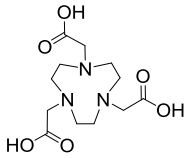
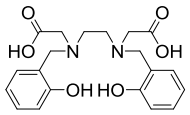
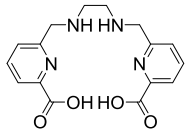
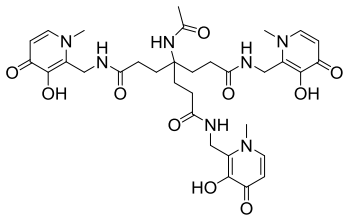
Gallium is a metal, therefore its incorporation into a desired molecule requires chelation of its ionic form as opposed to covalent bond formation (as used in ^{18}F, ^{15}O, ^{13}N and ^{11}C radiochemistry). It is a hard, acidic metal, preferring hard O and N donor atoms, with a small ionic radius of 47-62 pm (dependent on coordination number). The predominant oxidation state is +3, with the radiometal typically formed as $^{68}GaCl_3$.[72] It has a high affinity for hydroxide ions, forming insoluble $Ga(OH)_3$ at pH 3-7 and the gallate anion $Ga(OH)_4^-$ at higher pH. In order to prevent the formation of these species, weakly coordinating ligands such as acetate are used in most radiolabelling procedures.[73] In most instances, ^{68}Ga complexes are hexacoordinate, adopting pseudo-octahedral geometries. These features dictate the nature of chelators that can be designed, examples of which are shown in **Table 1.4**.[72]

DOTA has become the standard chelator for use with ^{68}Ga due to its commercial availability; however, its coordination requires the use of elevated temperatures under mildly acidic conditions which are not ideal for use with sensitive components.[65] This labelling can also require up to 30 min reaction times, resulting in significant decay. The smaller chelator 1,4,7-triazacyclononane-1,4,7-triacetic acid (NOTA) exhibits preferable radiolabelling conditions, with labelling at 25 ^{o}C performed within 10 minutes. In addition, NOTA forms more stable complexes with ^{68}Ga.[74]

In general, these macrocyclic systems exhibit high kinetic inertness at the expense of poor chelation properties, therefore further development has studied the use of acyclic chelators. These show more favourable complex formation kinetics under mild conditions at the expense of stability, with examples including *N,N'*-bis(2-hydroxybenzyl)- ethylenediamine-*N,N'*-diaceticacid (HBED) and 1,2-[[6-(carboxy)-pyridin-2-yl]-methylamino]ethane (H_2dedpa). More recently, the development of the CP256 (also abbreviated to THP and HP) tris(hydroxypyridinone) chelator has dramatically improved the properties of these ligands. It

has been found that this coordinates to ^{68}Ga effectively at 25 ^{o}C within 5 minutes.[75] The chelation properties of this molecule are so superior that it can sequester free gallium *in vivo*.[65, 67] As a result, it is being studied for kit formation.[76, 77] The structures and chelation properties of these ligands are summarised in **Table 1.4**.

Table 1.4: Details for ^{68}Ga complexation with various ligands.[61, 65]

Chelator	Temperature/ ^{o}C	Time/ min	pH	logK_{ML}[a]
 DOTA	37-90	10-30	4.0-5.5	26.1
 NOTA	25	10-60	3.5-5.5	31.0
 HBED	25	10-20	4-4.5	38.5
 H_2dedpa	25	5-10	4.5	28.1
 CP256	25	5	6.5	No transchelation to transferrin within 4 hours[75]

[a]Thermodynamic stability/ formation constant $K_{ML} = [ML]/[M][L]$, M = ^{68}Ga, L = chelator, ML = complex.

1.4 Optical Imaging

Fluorescence is the result of a molecule absorbing a photon of the correct energy to excite an electron from the highest occupied molecular orbital (HOMO, also known as the electronic ground state S_0) to the lowest unoccupied molecular orbital (LUMO, also known as the excited electronic state S_1). Upon relaxation back to the electronic ground state, this energy can be released as a photon. The emitted photon will have lower energy than that absorbed as any vibrational excitation in the excited electronic state will be lost via radiationless pathways. This difference between absorption and emission wavelengths is called the Stokes shift. For this transition to be allowed, the change in spin of the electron should be zero ($\Delta S = 0$); therefore phosphorescence, which involves a change in spin, is less probable and has a low intensity. Phosphorescence occurs from the triplet excited state (T_1), which can be populated from the S_1 state by a process called intersystem crossing (ISC).[13, 78] This is shown diagrammatically in **Figure 1.9**.

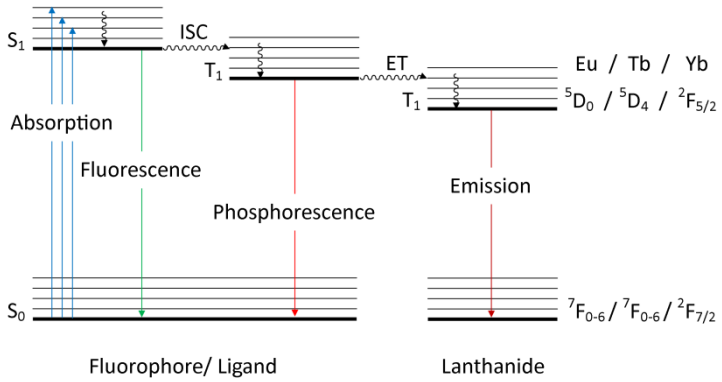


Figure 1.9: Jablonski diagram showing the relative energy levels of different ground and excited states. Fluorescence and phosphorescence from a fluorophore is shown in addition to the sensitisation process for the excitation of relevant lanthanides. Lanthanide emissive states taken from reference.[79]

The main disadvantage of optical imaging is the shallow depth penetration, which is dependent on the wavelength of light used, as shown in **Figure 1.10**. This is caused by the absorption, reflection, refraction and scattering of incident light by tissues.[80] As a result, the more tissue that the photons must pass through before detection (i.e. the deeper the fluorophore), the broader and less defined the signal detected at the surface.[13]

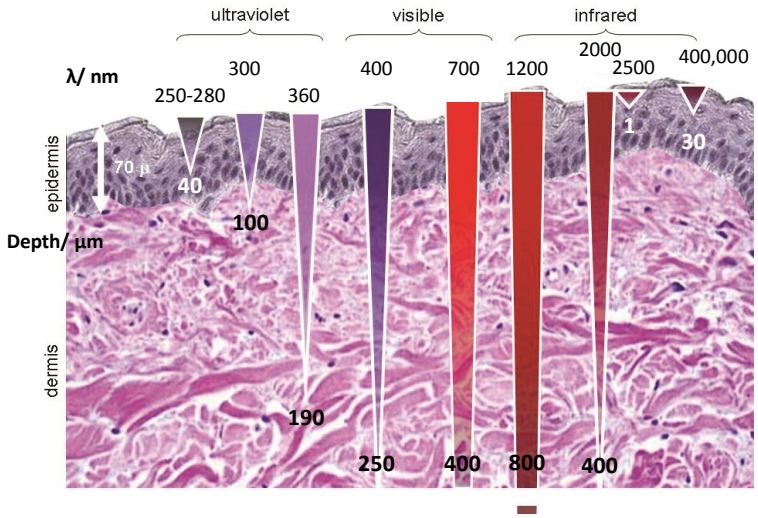


Figure 1.10: Light penetration through skin at different wavelengths. Depth penetration shown indicates attenuation down to 1 % of the original intensity. Reproduced with permission[81] and modified prior to use.

Most organic molecules absorb at wavelengths shorter than 250 nm (UV); however, as can be seen in **Figure 1.10**, the depth penetration of this wavelength is poor in biological systems. This is due to high tissue absorption. The region between 650 and 900 nm is termed the near infrared (NIR) window as there is low absorption by tissue (namely haemoglobin) and water, as displayed in **Figure 1.11**. This results in increased light penetration *in vivo*, making these wavelengths well suited for both excitation and emission.[13, 80]

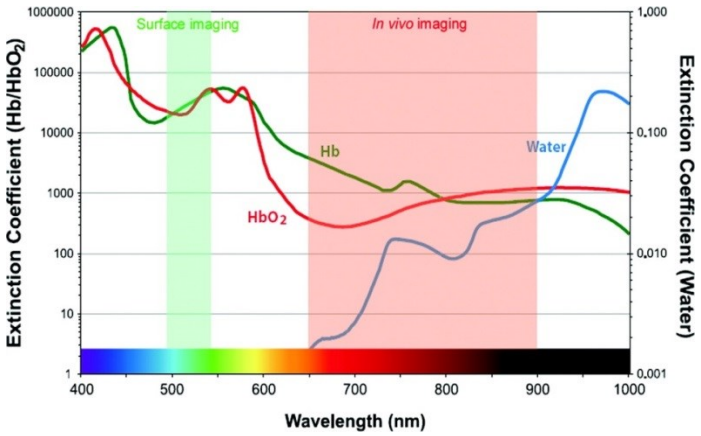


Figure 1.11: Extinction coeffienients at different wavelengths for haemoglobin and water. Hb = deoxyhaemoglobin, HbO_2 = haemoglobin. Reproduced with permission.[82]

Fluorescence imaging has many advantages. It is a very sensitive imaging method, it does not require the use of ionising radiation and high spatial resolutions of around 1 μm can be obtained, a length scale comparable to many intracellular structures. Finally, it can produce

environment-sensitive real-time information and can therefore be used to track rapid events and to guide therapy or surgery.[83]

1.4.1 Fluorescent Probes

There are a number of fluorescently tagged biological molecules such as proteins and antibodies that can be purchased for *in vitro* and *in vivo* staining. The most well-known of these is green fluorescent protein which can be used to monitor gene expression among other applications.[13]

The synthesis of small fluorescent molecules with tuneable wavelengths and high quantum yields has also been extensively researched, with numerous families of dyes having been developed. These include boron dipyrromethene (BODIPY), fluorescein, rhodamine (Rh) and cyanine (Cy) dyes, as depicted in **Figure 1.12**. These probes are typically small organic molecules with extended conjugated systems. Longer conjugated systems result in a red shift in absorption/ emission due to a smaller HOMO-LUMO transition. Although desirable, an increase in chain length can increase the lipophilicity of the molecule, making it less soluble in biological media and increasing the possibility of aggregate formation.[84, 85]

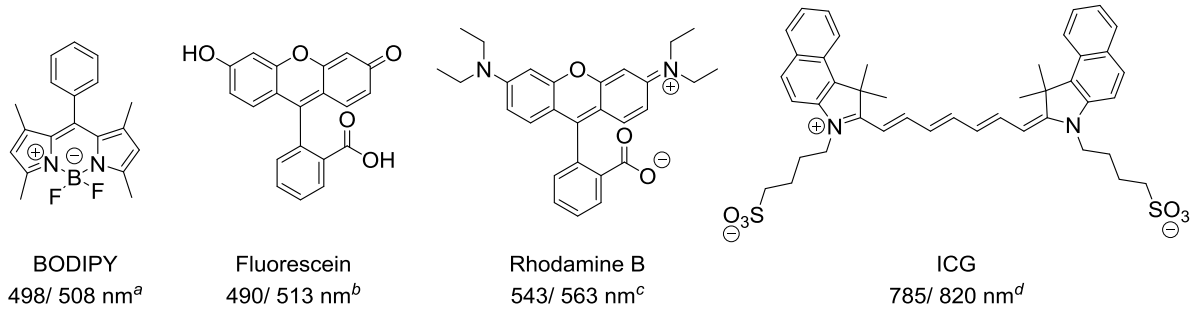


Figure 1.12: Structures, names and excitation/ emission wavelengths of common small-molecule dyes. [a]MeOH. [b]1% NaCl pH 7.5. [c]EtOH. [d]H_2O.[86-89]

1.4.2 Lanthanides

There are a number of lanthanides with energy gaps suitable for luminescence. The most important for imaging purposes are Eu^{3+} and Tb^{3+}, with Yb^{3+} being used due to its emission in the NIR. The energy levels of these emissive states are shown in **Figure 1.13**. Luminescence from these metals originates from Laporte forbidden f-f transitions; this causes their lifetimes to be long when compared to organic fluorophores (μs-ms compared to ns)[90] and results in direct excitation being very inefficient.

In order to populate these excited states, a sensitising chromophore can be used which absorbs light and subsequently transfers it to the lanthanide, as demonstrated in **Figure 1.9**. Due to the longer-lived nature of the triplet state, this typically sensitises the lanthanide to a greater extent; as such this must be at higher energy than the lanthanide accepting level. This energy difference should be > 1500 cm^{-1} to prevent thermally activated transfer from the lanthanide back to the sensitiser.[91]

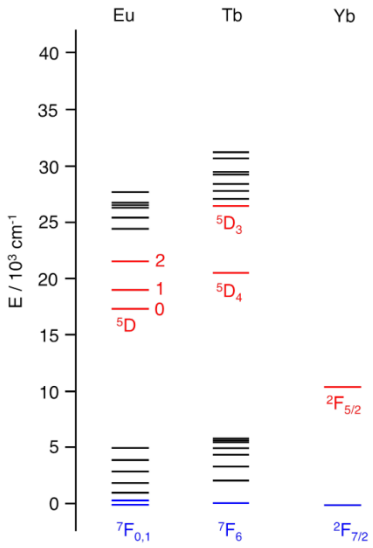


Figure 1.13: Partial energy levels of lanthanide aqua ions that can be used in luminescence imaging. Ground levels are shown in blue and the excited levels in red. Reproduced with permission[92] and modified prior to use.

1.5 MRI

MRI relies upon nuclear spin ($I \neq 0$) and is based upon the principles of NMR. ^{1}H ($I = ½$) is present in water, which is abundant in human and animal bodies and is the nucleus of choice for imaging.[1] In the presence of a magnetic field (B_0), these spins align themselves with the applied field and the spin states split into a higher energy and a lower energy state. The distribution between these states at equilibrium will be determined by the Boltzmann distribution and will result in an overall magnetisation vector.[13]

When an external radiofrequency pulse is applied at the Larmor frequency (ω), some of the spins are excited into the higher energy state. When the pulse ends these relax back to equilibrium by either longitudinal (T_1) or transverse (T_2) relaxation pathways (in addition to emitting energy at their ω).[13, 93] In this thesis, only T_1 will be discussed.

In order to obtain 3D images, a magnetic field gradient is applied to spatially encode ω, which is dependent upon B_0 according to **Equation 1.3**:[13]

$$\gamma B_0 = \omega \qquad \textbf{Equation 1.3}$$

Where γ = the gyromagnetic ratio of the nucleus in question; for ^{1}H γ = 42.58 MHz/Tesla.[93, 94] This produces a (free induction decay, FID) signal composed of multiple frequencies which can be processed by a Fourier transformation to obtain the magnitude at each value; this is proportional to the hydrogen density at that location.[1] The inherent differences in water content between parts of the body (e.g. organs) means that MRI can often differentiate between these without the need for additional contrast enhancement.

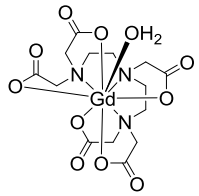
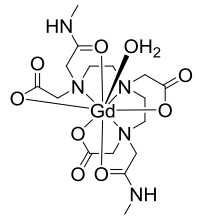
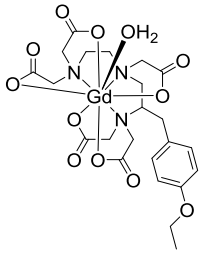
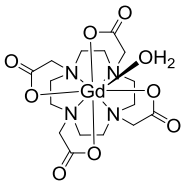
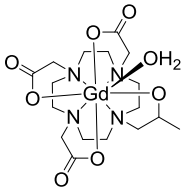
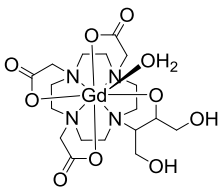
1.5.1 T_1 Contrast Agents

In some instances, the difference in proton concentration is not significant enough to produce good MRI contrast. This concentration is not easy to modify, however the intensity of the MRI signal is not solely dependent upon this. T_1 dictates the speed with which magnetisation reaches equilibrium along the longitudinal axis (i.e. along B_0); the faster this occurs, the more intense the signal.[1] This also varies between tissue types, for example the T_1 of human breast tissue = 0.367 s whilst that of a breast tumour = 1.080 s,[95] however this is not always sufficient.

T_1 relaxation of the nuclear spins is caused by magnetic fields present in the sample that oscillate at the correct frequency (ω) to flip the ^{1}H spins. In aqueous environments this is caused by the molecular motion of other water molecules.[13] Unpaired electrons have a much stronger magnetic moment than these molecules and can therefore induce strong magnetic fields and much faster relaxation.[1, 96] Contrast agents therefore incorporate those elements with many unpaired electrons, such as Mn^{3+}, Fe^{3+} and Gd^{3+} with 4, 5 and 7 unpaired electrons respectively. Due to its isotropic electron distribution (symmetric ^{8}S ground state) and large magnetic moment (Gd^{3+} = 7.9 BM), Gd^{3+} is the most frequently used of these.[97]

In order for gadolinium to effectively increase T_1 contrast, it must bind to water molecules *in vivo*.[97] Free Gd^{3+} is highly toxic as it has a high affinity for Ca^{2+} sites in biological molecules owing to its similar ionic radius.[98] The safe use of this ion therefore requires its stable chelation in a molecule[99] which also allows for the coordination of at least one water molecule.

Table 1.5: Clinically used gadolinium MRI contrast and their properties.[96, 99, 100]

Name	Abbreviation	r_1/ mM^{-1} s^{-1}	$logK_{ML}$[a]	Manufacturer
 Magnevist	Gd-DTPA	4.3	22.2	Bayer AG
 Omniscan	Gd-DTPA-BMA	4.6	16.8	GE Healthcare
 MultiHance	Gd-BOPTA	6.7	18.4	Bracco Imaging S.p.A
 Dotarem	Gd-DOTA	4.2	25.3	Guerbet
 ProHance	Gd-HP-DO3A	4.4	23.8	Bracco Imaging S.p.A
 Gadovist	Gd-BT-DO3A	5.3	20.8	Bayer AG

[a]Thermodynamic stability/ formation constant K_{ML} = [ML]/[M][L], M = Gd, L = chelator, ML = complex.

Two families of ligands have been developed, those based upon acyclic triamines such as DTPA and macrocycles based upon cyclen such as DOTA. These are all octadentate ligands with one water molecule bound, forming a nine coordinate Gd^{3+} complex. Numerous variations of these have been developed and clinically approved; these are shown in **Table 1.5**.

Although all of the contrast agent shown in **Table 1.5** are clinically approved, studies have found that linear chelators form less stable complexes for use *in vivo*, with Omniscan depositing 2-4 times more gadolinium in bone than ProHance.[101] In addition, it has recently been found that patients who have undergone numerous MRI scans exhibit gadolinium deposits in the brain.[102] Insufficient evidence as to the cause of these deposits makes it difficult to determine the clinical significance. A literature review has recently been published describing the studies performed and their limitations.[100]

There are many parameters that must be considered when developing MRI contrast agents. The relaxivity (r_1) is the rate of relaxation (R_1) per unit concentration of contrast agent (c), as shown in **Equation 1.4**:[13]

$$\frac{1}{T_1} = R_1 = r_1 \times \mathrm{c} \qquad \textbf{Equation 1.4}$$

Strong magnetic fields of 1.5 or 3 Tesla are commonly used clinically as this can increase the sensitivity of MRI.[103] This reduces the effect of these contrast agents as the relaxivity is inversely proportional to the square of the Larmor Frequency, as shown in **Equation 1.5**:[13]

$$\omega \propto \sqrt{\frac{1}{r_1}} \qquad \textbf{Equation 1.5}$$

When combined with the fact that only gadolinium complexes coordinated to one water molecule are currently stable enough for *in vivo* use, this results in comparatively large concentrations of contrast agent being used for MRI imaging (0.1 mmol/ kg).[1] This makes the design of the molecule of even greater importance as an increase in relaxivity will result in reduced concentration and potentially fewer side effects.

There are multiple factors that can be used to improve the relaxivity of a compound. The first of these is the hydration number, q. The more water molecules bound to the gadolinium centre, the greater r_1. This comes at the expense of complex stability; for this reason all of the contrast agents shown in **Table 1.5** have $q = 1$.

Similarly, the water molecules bound to the gadolinium centre should exchange with bulk water in order to increase r_1. The residence lifetime of the water molecule at the gadolinium centre (τ_m) should be long enough to promote relaxation whilst short enough that many water molecules can be affected. This can be decreased by modifying the residual charge on the metal centre to make it more negative[97] or by increasing the steric crowding around the water coordination site.[104]

Finally, the rotational correlation time (τ_R) is a measure of how fast the complex is rotating, with larger molecules displaying longer times and increased relaxivities. For this reason, chelates have been attached to a number of large groups in the attempt to improve the effect; these include proteins[105] and polymers.[106]

1.6 Targeted Imaging Probes

The targeting of contrast agents to a specific disease has numerous uses as it reduces the background signal caused by unspecific uptake, which can be a particular issue for tracers such as ^{18}F-FDG. It also minimises the dose required to achieve the same concentration at the desired location, reducing potential side effects; this is of particular importance in MRI where high concentrations are typically used.

There are numerous diseases that can be targeted, with atherosclerosis[107] and cancer being heavily studied areas. This thesis will focus upon cancer targeting; however, those probes developed in this thesis have the potential for use with other diseases.

1.6.1 Cancer Properties

Current imaging methods such as CT, ultrasound and MRI are limited in their ability to visualise small tumours. These must typically grow to a size of 1 cm, have a mass of over one gram and contain approximately 10^8 cells for detection by these methods. This means that two thirds of the natural progression of cancer has already occurred, resulting in little time before this reaches an irreversible stage.[108] This clearly demonstrates the need for improved probes for the visualisation of cancer, for which many methods have been developed.

^{18}F-FDG is currently used to visualise cancer and relies upon the inherent requirement of growing tissues for glucose. The rapid growth rate of tumours in comparison to other regions in the body means that this probe accumulates in these areas.[109]

Six hallmarks of cancer have been proposed, which include the up- or down-regulation of biological processes in order to allow for proliferation.[110] For example, angiogenesis is a critical process in the formation of new blood vessels from pre-existing ones. This is induced once tumours reach a certain size in order to deliver oxygen and nutrients to the rapidly replicating cells. This leads to the upregulations of proteins such as vascular endothelial growth factor (VEGF) and involves a variety of cell adhesion molecules such as $\alpha_v\beta_3$ integrin.[111] These biomarkers can be targeted by contrast agents and used as indicators of cancerous regions.

This rapid growth of vasculature also modifies the anatomy of tumour vessels, making them irregular in shape, dilated and leaky and causes fenestrations in endothelial cells. This makes it easier for small molecules and particles to extravasate from the blood pool.[112] This is termed the enhanced permeability and retention (EPR) effect and has been shown to accumulate particles up to 780 nm.[113]

It has also been shown that cancer cells have a more acidic extracellular environment than normal healthy cells. Intracellular pH's remain near neutral to slightly alkaline (6.9-7.4) in both tissue types, while extracellular pH's in cancerous cells are 5.6-7.6 compared to 7.2-7.6 in normal tissues.[114] This is due to increased aerobic glycolysis, which preferentially produces lactic acid from glucose,[115] and inefficient removal of acidic respiration by-products by poorly vascularised tumours.[114] This pH difference can be used to sense tumorous regions.

1.6.2 Cancer Targeting

Antibodies are widely used to target a desired biological process due to their specificity.[116] There are, however, a few drawbacks. Firstly, they are expensive, precluding their use in basic studies. They are also large, therefore their properties may alter those of the probe.[117] In addition, they can cause immune responses unless they are human derived or humanised and therefore their safety is questionable.[118]

For this reason targeting peptides are often used, which are safer, less expensive and small enough so as not to significantly alter the properties of the probe. Small molecules can also target probes to desired sites, however this is often less effective than peptide targeting.[119]

1.6.2.1 Clinical Studies - TOC, TATE and PSMA Targeting Peptides

TOC, TATE and PSMA are all targeting ligands that have been used in humans to diagnose neuroendocrine tumours (former two) and prostate cancer (latter). These have been used with ^{68}Ga to allow for targeted PET imaging.[69, 70, 120]

TOC and TATE are peptide ligands for somatostatin receptors which are overexpressed in neuroendocrine tumours. These are used in combination with DOTA to chelate ^{68}Ga. Prostate-specific membrane antigen (PSMA) is overexpressed in prostate cancer and is targeted by a PSMA ligand (also named PSMA). The most widely used ligand in Europe is PSMA HBED-CC, which uses HBED to chelate ^{68}Ga.[121] The structures of these are shown in **Figure 1.14**. In order to increase use and availability, ^{68}Ga-THP-TATE has been developed which displays the same labelling as ^{68}Ga-DOTATATE and can be developed into a kit.[76]

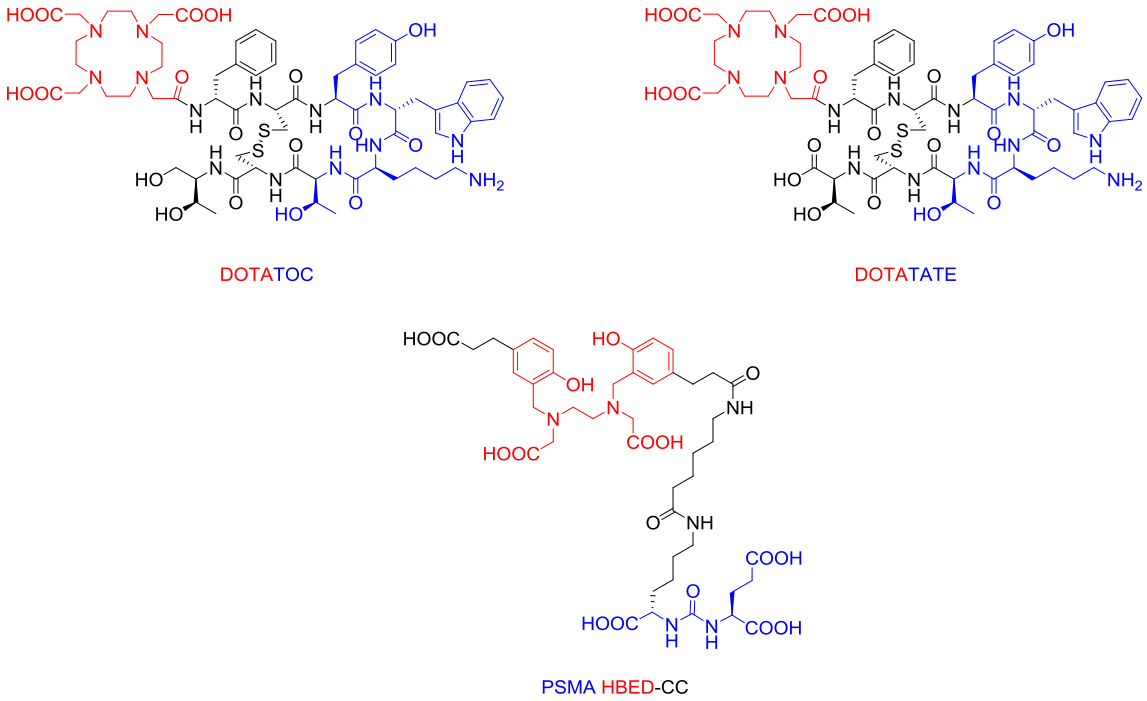


Figure 1.14: Structures of targeted probes used in human studies; DOTATOC, DOTATATE[68] and PSMA HBED-CC.[122] Chelating groups are highlighted in red, whilst targeting moieties are in blue.

1.6.2.2 RGD Targeting Peptide

The integrin $\alpha_v\beta_3$ is a receptor for the peptide sequence Arg-Gly-Asp (RGD),[123] therefore the use of this peptide to target cancer is well documented. It was found that cyclisation of this peptide resulted in a more active and selective antagonist and that the addition of a lysine residue into this sequence did not affect its activity or selectivity (cRGDfK).[124, 125] This peptide is shown in **Figure 1.15**. The amine side chain on this lysine residue allows for

attachment of additional molecules for PET,[126] SPECT,[127] MRI,[128] optical[129] and ultrasound[130] imaging and can allow for drug delivery.[131] Numerous reviews have been written of the area.[111, 123, 132]

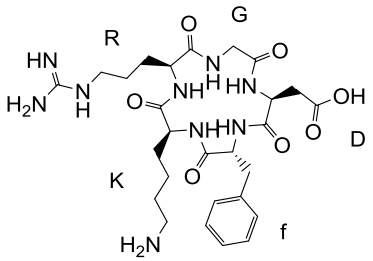


Figure 1.15: Structure of cRGDfK with amino acid residues labelled with the single letter code.

Derivatives of this peptide have been used to target many of the ^{68}Ga ligands discussed in **Table 1.4** such as DOTA,[133] NOTA,[134] H_2dedpa[135] and CP256.[136] It has also been used in MRI to target Gd-DOTA[128] and Gd-DTPA[137] and in optical imaging to target Cy5.5.[129] In many instances, multiple RGD targeting groups were attached to the probe, which showed improved accumulation in tumours when compared to mono-targeted analogues.[138, 139]

1.7 Aims and Objectives

The aim of this project was to synthesise dual-modal, cancer-targeted contrast agents based upon microbubbles. These microbubbles used a phospholipid surface coating owing to the advantages of these over proteins or polymers (*vide supra*). Therefore, this project initially required methods of phospholipid manipulation, purification and characterisation to be determined.

Work primarily focused on the synthesis of phospholipids that incorporated a targeting moiety, a PET tracer or a fluorophore and their incorporation into microbubbles, as discussed in Chapters 2-4 respectively. These can be used in combination to form targeted, multi-modal probes as required. This flexibility in formulation allows for application of these microbubbles in numerous circumstances as they can be adapted to the situation.

This work was then expanded into microbubble-mediated contrast agent delivery across the BBB, which required the synthesis of small-molecule dual-modal probes with characteristics suitable for this type of delivery. These are discussed in Chapter 5.

This aim of this introduction was to provide a general overview of various imaging modalities, how they work and examples relevant to this research. Subsequent chapters

explore the literature in more focused areas: Chapter 2 discusses cancer targeting of microbubbles, Chapter 3 gives examples of PET-ultrasound probes, Chapter 4 focuses upon fluorescent microbubbles and nanodroplets and Chapter 5 provides more detail on microbubble-mediated BBB opening and relevant dual-modal probes.

1.8 References

1. G.-L. Law and W.-T. Wong, in *The Chemistry of Molecular Imaging*, eds. N. J. Long and W.-T. Wong, John Wiley & Sons, Hoboken, 2014, pp. 1-24.
2. M. L. James and S. S. Gambhir, *Physiol. Rev.*, 2012, **92**, 897-965.
3. W. Röntgen, in *Aus den Sitzungsberichten der Würzburger Physik.-medic. Gesellschaft Würzburg*, 1985, pp. 137–147.
4. M. F. Kircher and J. K. Willmann, *Radiology*, 2012, **264**, 349-368.
5. M. Rudin and R. Weissleder, *Nat. Rev. Drug Discov.*, 2003, **2**, 123-131.
6. N. J. Long and W.-T. Wong, in *The Chemistry of Molecular Imaging*, eds. N. J. Long and W.-T. Wong, John Wiley & Sons, Hoboken, 2014, pp. i-xii.
7. D. W. Townsend, T. Beyer and T. M. Blodgett, *Semin. Nucl. Med.*, **33**, 193-204.
8. S. R. Cherry, *Semin. Nucl. Med.*, 2009, **39**, 348-353.
9. A. Louie, *Chem. Rev.*, 2010, **110**, 3146-3195.
10. C. Guy and S. ffytche, *An Introduction to the Principles of Medical Imaging*, Imperial College Press, London, 2005.
11. Q. Wen, S. Wan, Z. Liu, S. Xu, H. Wang and B. Yang, *J. Nanosci. Nanotechnol*, 2014, **14**, 190-209.
12. J. J. Choi, K. Selert, F. Vlachos, A. Wong and E. E. Konofagou, *Proc. Natl. Acad. Sci.*, 2011, **108**, 16539-16544.
13. M. Rudin, *Molecular Imaging Basic Principles and Applications in Biomedical Research*, Imperial College Press London, 2005.
14. S. Kunjachan, J. Ehling, G. Storm, F. Kiessling and T. Lammers, *Chem. Rev.*, 2015, **115**, 10907-10937.
15. C. Guo, Y. Jin and Z. Dai, *Bioconjugate Chem.*, 2014, **25**, 840-854.
16. N. Deshpande, A. Needles and J. K. Willmann, *Clin. Radiol.*, 2010, **65**, 567-581.
17. G. Leinenga, C. Langton, R. Nisbet and J. Gotz, *Nat. Rev. Neurol.*, 2016, **12**, 161-174.
18. M. Blomley, M. Claudon and D. Cosgrove, *Ultrasound Med. Biol.*, 2007, **33**, 180-186.
19. E. G. Schutt, D. H. Klein, R. M. Mattrey and J. G. Riess, *Angew. Chem. Int. Ed.*, 2003, **42**, 3218-3235.
20. E. Quaia, *Eur. Radiol.*, 2007, **17**, 1995-2008.
21. M. A. Borden, S. Qin and K. W. Ferrara, in *Molecular Imaging: Principles and Practice*, eds. R. Weissleder, B. D. Ross, A. Rehemtulla and S. A. Gambhir, PMPH-USA, Shelton, 2010, pp. 427-446.
22. F. Kiessling, S. Fokong, J. Bzyl, W. Lederle, M. Palmowski and T. Lammers, *Adv. Drug Del. Rev.*, 2014, **72**, 15-27.
23. H. Hauser, I. Pascher, R. H. Pearson and S. Sundell, *Biochim. Biophys. Acta, Rev. Biomembr.*, 1981, **650**, 21-51.

24. R. B. Gennis, in *Biomembranes: Molecular Structure and Function*, ed. R. B. Gennis, Springer, New York, 1989, pp. 36-84.
25. A. L. Klibanov, P. T. Rasche, M. S. Hughes, J. K. Wojdyla, K. P. Galen, J. H. Wible and G. H. Brandenburger, *Invest. Radiol.*, 2004, **39**, 187-195.
26. D. Marshall, R. B. Pedley, J. A. Boden, R. Boden, R. G. Melton and R. H. Begent, *Br. J. Cancer*, 1996, **73**, 565-572.
27. J. R. Silvius, in *Lipid-Protein Interactions*, eds. P. C. Jost and O. H. Griffith, John Wiley & Sons Inc., New York, 1982, pp. 239–281.
28. K. K. Wong, I. Huang, Y. R. Kim, H. Tang, E. S. Yang, K. K. Kwong and E. X. Wu, *Magn. Reson. Med.*, 2004, **52**, 445-452.
29. M. S. Tartis, D. E. Kruse, H. Zheng, H. Zhang, A. Kheirolomoom, J. Marik and K. W. Ferrara, *J. Control. Release*, 2008, **131**, 160-166.
30. J. K. Willmann, Z. Cheng, C. Davis, A. M. Lutz, M. L. Schipper, C. H. Nielsen and S. S. Gambhir, *Radiology*, 2008, **249**, 212-219.
31. A. M. Chow and E. X. Wu, in *The Chemistry of Molecular Imaging*, eds. N. J. Long and W.-T. Wong, John Wiley & Sons, Hoboken, 2014, pp. 321-334.
32. A. W. Appis, M. J. Tracy and S. B. Feinstein, *Echo Research and Practice*, 2015, **2**, R55-R62.
33. R. L. Conhai and L. A. Rodenkirch, *Microcirculation*, 1997, **4**, 51-59.
34. M. J. Benchimol, M. J. Hsu, C. E. Schutt, D. J. Hall, R. F. Mattrey and S. C. Esener, *Soft Matter*, 2013, **9**, 2384-2388.
35. J.-M. Gorce, M. Arditi and M. Schneider, *Invest. Radiol.*, 2000, **35**, 611-671.
36. D. M. Skyba, G. Camarano, N. C. Goodman, R. J. Price, T. C. Skalak and S. Kaul, *J. Am. Coll. Cardiol.*, 1996, **28**, 1292-1300.
37. F. Piscaglia and L. Bolondi, *Ultrasound Med. Biol.*, 2006, **32**, 1369-1375.
38. J. Alter, C. A. Sennoga, D. M. Lopes, R. J. Eckersley and D. J. Wells, *Ultrasound Med. Biol.*, 2009, **35**, 976-984.
39. M. J. K. Blomley, J. C. Cooke, E. C. Unger, M. J. Monaghan and D. O. Cosgrove, *BMJ*, 2001, **322**, 1222-1225.
40. P. A. Mountford and M. A. Borden, *Adv. Colloid Interface Sci.*, 2016, **237**, 15-27.
41. P. S. S. T. O. Matsunaga, S Luois,J. E. Streeter, L. B. Mullin, B. Banerjee, P. A. Dayton, *Theranostics*, 2012, **12**, 1185-1198.
42. O. D. Kripfgans, J. B. Fowlkes, D. L. Miller, O. P. Eldevik and P. L. Carson, *Ultrasound Med. Biol.*, 2000, **26**, 1177-1189.
43. K. Wilson, K. Homan and S. Emelianov, *Nat. Commun.*, 2012, **3**, 618.
44. E. Strohm, M. Rui, I. Gorelikov, N. Matsuura and M. Kolios, *Biomed. Opt. Express*, 2011, **2**, 1432-1442.
45. P. S. Sheeran, V. P. Wong, S. Luois, R. J. McFarland, W. D. Ross, S. Feingold, T. O. Matsunaga and P. A. Dayton, *Ultrasound Med. Biol.*, 2011, **37**, 1518-1530.
46. P. S. Sheeran, S. H. Luois, L. B. Mullin, T. O. Matsunaga and P. A. Dayton, *Biomaterials*, 2012, **33**, 3262-3269.

47. P. S. Sheeran, S. Luois, P. A. Dayton and T. O. Matsunaga, *Langmuir*, 2011, **27**, 10412-10420.
48. J. D. Dove, P. A. Mountford, T. W. Murray and M. A. Borden, *Biomed. Opt. Express*, 2014, **5**, 4417-4427.
49. A. S. Hannah, G. P. Luke and S. Y. Emelianov, *Theranostics*, 2016, **6**, 1866-1876.
50. G. P. Luke, A. S. Hannah and S. Y. Emelianov, *Nano Lett.*, 2016, **16**, 2556-2559.
51. A. Hannah, G. Luke, K. Wilson, K. Homan and S. Emelianov, *ACS Nano*, 2014, **8**, 250-259.
52. S. Lin, A. Shah, J. Hernández-Gil, A. Stanziola, B. I. Harriss, T. O. Matsunaga, N. Long, J. Bamber and M.-X. Tang, *Photoacoustics*, 2017, **6**, 26-36.
53. Y. Ma, S. Tong, G. Bao, C. Gao and Z. Dai, *Biomaterials*, 2013, **34**, 7706-7714.
54. A. S. Hannah, Thesis, Optically-Triggered Nanodroplets for Enhanced Ultrasound and Photoacoustic Imaging, The University of Texas at Austin, May 2015.
55. N. Sheikov, N. McDannold, N. Vykhodtseva, F. Jolesz and K. Hynynen, *Ultrasound Med. Biol.*, 2004, **30**, 979-989.
56. N. Sheikov, N. McDannold, S. Sharma and K. Hynynen, *Ultrasound Med. Biol.*, 2008, **34**, 1093-1104.
57. P. Prentice, A. Cuschieri, K. Dholakia, M. Prausnitz and P. Campbell, *Nat Phys*, 2005, **1**, 107-110.
58. S. Kotopoulis, G. Dimcevski, O. H. Gilja, D. Hoem and M. Postema, *Med. Phys.*, 2013, **40**, 0729021-0729029.
59. T. M. Bateman, *J. Nucl. Cardiol.*, 2012, **19**, 3-11.
60. J. R. Dilworth and S. I. Pascu, in *The Chemistry of Molecular Imaging*, eds. N. Long and W.-T. Wong, John Wiley & Sons, Hoboken, 2014, pp. 137-164.
61. T. W. Price, J. Greenman and G. J. Stasiuk, *Dalton Trans.*, 2016, **45**, 15702-15724.
62. P. W. Miller, N. J. Long, R. Vilar and A. D. Gee, *Angew. Chem. Int. Ed.*, 2008, **47**, 8998-9033.
63. M. Partridge, A. Spinelli, W. Ryder and C. Hindorf, *Nucl. Instrum. Methods Phys. Res., Sect. A*, 2006, **568**, 933-936.
64. J. C. Hung, *Theranostics*, 2013, **3**, 885-893.
65. E. W. Price and C. Orvig, *Chem. Soc. Rev.*, 2014, **43**, 260-290.
66. R. W. Atcher, A. M. Friedman, J. R. Huizenga, G. V. Rayudu, E. A. Silverstein and D. A. Turner, *J. Nucl. Med*, 1980, **21**, 565-569.
67. P. J. Blower, *Dalton Trans.*, 2015, **44**, 4819-4844.
68. S. R. Banerjee and M. G. Pomper, *Appl. Radiat. Isot.*, 2013, **76**, 2-13.
69. R. P. Baum and H. R. Kulkarni, *Theranostics*, 2012, **2**, 437-447.
70. A. Afshar-Oromieh, C. M. Zechmann, A. Malcher, M. Eder, M. Eisenhut and H. G. Linhart, *Eur. J. Nucl. Med. Mol. Imaging*, 2014, **41**, 11-20.
71. W. P. Fendler, D. F. Schmidt, V. Wenter, K. M. Thierfelder, C. Zach, C. Stief, P. Bartenstein, T. Kirchner, F. J. Gildehaus, C. Gratzke and C. Faber, *J. Nucl. Med.*, 2016, **57**, 1720-1725.
72. T. J. Wadas, E. H. Wong, G. R. Weisman and C. J. Anderson, *Chem. Rev.*, 2010, **110**, 2858-2902.
73. B. P. Burke, G. S. Clemente and S. J. Archibald, *J. Labelled Compd. Radiopharm.*, 2014, **57**, 239-243.
74. I. Velikyan, H. Maecke and B. Langstrom, *Bioconjugate Chem.*, 2008, **19**, 569-573.
75. D. J. Berry, Y. Ma, J. R. Ballinger, R. Tavare, A. Koers, K. Sunassee, T. Zhou, S. Nawaz, G. E. D. Mullen, R. C. Hider and P. J. Blower, *Chem. Commun.*, 2011, **47**, 7068-7070.

76. M. T. Ma, C. Cullinane, K. Waldeck, P. Roselt, R. J. Hicks and P. J. Blower, *EJNMMI Research*, 2015, **5**, 1-11.
77. J. D. Young, V. Abbate, C. Imberti, L. K. Meszaros, M. T. Ma, S. Y. A. Terry, R. C. Hider, G. E. Mullen and P. J. Blower, *J. Nucl. Med.*, 2017, In Press.
78. J. W. Lichtman and J.-A. Conchello, *Nat Meth*, 2005, **2**, 910-919.
79. J.-C. G. Bünzli and S. V. Eliseeva, in *Lanthanide Luminescence: Photophysical, Analytical and Biological Aspects*, eds. P. Hänninen and H. Härmä, Springer, Berlin, 2011, pp. 1-45.
80. V. J. Pansare, S. Hejazi, W. J. Faenza and R. K. Prud'homme, *Chem. Mater.*, 2012, **24**, 812-827.
81. E. Commission, *Health Effects of Artificial Light*, Scientific Committee on Emerging and Newly Identified Health Risks, March 2012.
82. H. Kobayashi, M. Ogawa, R. Alford, P. L. Choyke and Y. Urano, *Chem. Rev.*, 2010, **110**, 2620-2640.
83. E. Baggaley, J. A. Weinstein and J. A. G. Williams, *Coord. Chem. Rev.*, 2012, **256**, 1762-1785.
84. S. Kim, M. Fujitsuka, N. Tohnai, T. Tachikawa, I. Hisaki, M. Miyata and T. Majima, *Chem. Commun.*, 2015, **51**, 11580-11583.
85. B. Z. Packard, A. Komoriya, D. D. Toptygin and L. Brand, *J. Phys. Chem. B*, 1997, **101**, 5070-5074.
86. A. Loudet and K. Burgess, *Chem. Rev.*, 2007, **107**, 4891-4932.
87. M. J. Doughty, *Ophthalmic Physiol. Opt.*, 2010, **30**, 167-174.
88. M. Beija, C. A. M. Afonso and J. M. G. Martinho, *Chem. Soc. Rev.*, 2009, **38**, 2410-2433.
89. T. Desmettre, J. M. Devoisselle and S. Mordon, *Surv. Ophthalmol.*, 2000, **45**, 15-27.
90. A. Beeby, I. M. Clarkson, R. S. Dickins, S. Faulkner, D. Parker, L. Royle, A. S. de Sousa, J. A. Gareth Williams and M. Woods, *J. Chem. Soc. Perk. Trans. 2*, 1999, 493-504.
91. D. Parker, *Coord. Chem. Rev.*, 2000, **205**, 109-130.
92. J.-C. G. Bunzli and C. Piguet, *Chem. Soc. Rev.*, 2005, **34**, 1048-1077.
93. D. B. Plewes and W. Kucharczyk, *J. Magn. Reson. Imaging*, 2012, **35**, 1038-1054.
94. M. H. Levitt, *Spin Dynamics: Basics of Nuclear Magnetic Resonance*, Wiley & Sons, New York, 2001.
95. R. Damadian, K. Zaner, D. Hor and T. DiMaio, *Proc. Natl. Acad. Sci.*, 1974, **71**, 1471-1473.
96. P. Hermann, J. Kotek, V. Kubicek and I. Lukes, *Dalton Trans.*, 2008, **23**, 3027-3047.
97. S. Faulkner and O. A. Blackburn, in *The Chemistry of Molecular Imaging*, eds. N. J. Long and W.-T. Wong, John Wiley & Sons, Hoboken, 2014, pp. 179-197.
98. S. P. Fricker, *Chem. Soc. Rev.*, 2006, **35**, 524-533.
99. J. Ramalho, R. C. Semelka, M. Ramalho, R. H. Nunes, M. AlObaidy and M. Castillo, *Am. J. Neuroradiol.*, 2015, **37**, 1192-1198.
100. N. K. Pinter, J. P. Klein and L. L. Mechtler, *Continuum (Minneap Minn)*, 2016, **22**, 1678-1684.
101. G. W. White, W. A. Gibby and M. F. Tweedle, *Invest. Radiol.*, 2006, **41**, 272-278.
102. T. Kanda, K. Ishii, H. Kawaguchi, K. Kitajima and D. Takenaka, *Radiology*, 2013, **270**, 834-841.
103. R. S. Butler, C. Chen, R. Vashi, R. J. Hooley and L. E. Philpotts, *World J. Radiol.*, 2013, **5**, 285-294.
104. S. Laus, R. Ruloff, É. Tóth and A. E. Merbach, *Chem. Eur. J.*, 2003, **9**, 3555-3566.
105. E. Boros and P. Caravan, *J. Med. Chem.*, 2013, **56**, 1782-1786.
106. D. A. Fulton, E. M. Elemento, S. Aime, L. Chaabane, M. Botta and D. Parker, *Chem. Commun.*, 2006, **10**, 1064-1066.

107. R. K. Kanwar, R. Chaudhary, T. Tsuzuki and J. R. Kanwar, *Nanomedicine*, 2012, **7**, 899-916.
108. L. V. Wang, *Dis. Markers*, 2004, **19**, 123-138.
109. A. K. Demetriades, A. C. Almeida, R. S. Bhangoo and S. F. Barrington, *The Surgeon*, 2014, **12**, 148-157.
110. D. Hanahan and Robert A. Weinberg, *Cell*, 2011, **144**, 646-674.
111. F. Danhier, A. L. Breton and V. Préat, *Mol. Pharm.*, 2012, **9**, 2961-2973.
112. S. S. Kelkar and T. M. Reineke, *Bioconjugate Chem.*, 2011, **22**, 1879-1903.
113. S. K. Hobbs, W. L. Monsky, F. Yuan, W. G. Roberts, L. Griffith, V. P. Torchilin and R. K. Jain, *Proc. Natl. Acad. Sci.*, 1998, **95**, 4607-4612.
114. J. R. Griffiths, *Br. J. Cancer*, 1991, **64**, 425-427.
115. R. A. Gatenby and R. J. Gillies, *Nat. Rev. Cancer*, 2004, **4**, 891-899.
116. A. M. Scott, J. D. Wolchok and L. J. Old, *Nat. Rev. Cancer*, 2012, **12**, 278-287.
117. C. A. Janeway, P. Travers, M. Walport and M. J. Shlomchik, *Immunobiology 5: The Immune System in Health and Disease*, Garland Publishing, New York, 2001.
118. A. M. Scott, J. P. Allison and J. D. Wolchok, *Cancer Immun.*, 2012, **12**, 14.
119. W.-b. Zhang, J.-M. Navenot, B. Haribabu, H. Tamamura, K. Hiramatu, A. Omagari, G. Pei, J. P. Manfredi, N. Fujii, J. R. Broach and S. C. Peiper, *J. Biol. Chem.*, 2002, **277**, 24515-24521.
120. J. Yang, Y. Kan, B. H. Ge, L. Yuan, C. Li and W. Zhao, *Acta Radiol.*, 2014, **55**, 389-398.
121. I. Rauscher, T. Maurer, W. P. Fendler, W. H. Sommer, M. Schwaiger and M. Eiber, *Cancer Imaging*, 2016, **16**, 14.
122. S. Lütje, S. Heskamp, A. S. Cornelissen, T. D. Poeppel, S. A. M. W. v. d. Broek, S. Rosenbaum-Krumme, A. Bockisch, M. Gotthardt, M. Rijpkema and O. C. Boerman, *Theranostics*, 2015, **5**, 1388-1401.
123. S. Liu, *Bioconjugate Chem.*, 2009, **20**, 2199-2213.
124. M. Gurrath, G. MÜLler, H. Kessler, M. Aumailley and R. Timpl, *Eur. J. Biochem.*, 1992, **210**, 911-921.
125. R. Haubner, R. Gratias, B. Diefenbach, S. L. Goodman, A. Jonczyk and H. Kessler, *J. Am. Chem. Soc.*, 1996, **118**, 7461-7472.
126. J. Haukkala, I. Laitinen, P. Luoto, P. Iveson, I. Wilson, H. Karlsen, A. Cuthbertson, J. Laine, P. Leppänen, S. Ylä-Herttula, J. Knuuti and A. Roivainen, *Eur. J. Nucl. Med. Mol. Imaging*, 2009, **36**, 2058-2067.
127. M. Yoshimoto, T. Hayakawa, M. Mutoh, T. Imai, K. Tsuda, S. Kimura, I. O. Umeda, H. Fujii and K. Wakabayashi, *J. Nucl. Med.*, 2012, **53**, 765-771.
128. J.-A. Park, J.-J. Lee, J.-C. Jung, D.-Y. Yu, C. Oh, S. Ha, T.-J. Kim and Y. Chang, *ChemBioChem*, 2008, **9**, 2811-2813.
129. X. Chen, P. S. Conti and R. A. Moats, *Cancer Res.*, 2004, **64**, 8009-8014.
130. C. R. Anderson, X. Hu, J. Tlaxca, A.-E. Decleves, R. Houghtaling, K. Sharma, M. Lawrence, K. Ferrara and J. J. Rychak, *Invest. Radiol.*, 2011, **46**, 215-224.
131. N. Nasongkla, X. Shuai, H. Ai, B. D. Weinberg, J. Pink, D. A. Boothman and J. Gao, *Angew. Chem. Int. Ed.*, 2004, **43**, 6323-6327.

132. W. Cai and X. Chen, *J. Nucl. Med.*, 2008, **49**, 113S-128S.

133. E. Blom, I. Velikyan, S. Estrada, H. Hall, T. Muhammad, C. Ding, M. Nair and B. Långström, *Int. J. Clin. Exp. Med.*, 2012, **5**, 165-172.

134. C. L. Ferreira, D. T. T. Yapp, D. Mandel, R. K. Gill, E. Boros, M. Q. Wong, P. Jurek and G. E. Kiefer, *Bioconjugate Chem.*, 2012, **23**, 2239-2246.

135. E. Boros, C. L. Ferreira, D. T. T. Yapp, R. K. Gill, E. W. Price and M. J. Adam, *Nucl. Med. Biol.*, 2012, **39**, 785-794.

136. M. T. Ma, C. Cullinane, C. Imberti, J. Baguña Torres, S. Y. A. Terry, P. Roselt, R. J. Hicks and P. J. Blower, *Bioconjugate Chem.*, 2016, **27**, 309-318.

137. C. Burtea, S. Laurent, O. Murariu, D. Rattat, G. Toubeau, A. Verbruggen, D. Vansthertem, L. Vander Elst and R. N. Muller, *Cardiovasc. Res.*, 2008, **78**, 148-157.

138. C. Imberti, S. Y. A. Terry, C. Cullinane, F. Clarke, G. H. Cornish, N. K. Ramakrishnan, P. Roselt, A. P. Cope, R. J. Hicks, P. J. Blower and M. T. Ma, *Bioconjugate Chem.*, 2017, **28**, 481-495.

139. Z. Cheng, J. Levi, Z. Xiong, O. Gheysens, S. Keren, X. Chen and S. S. Gambhir, *Bioconjugate Chem.*, 2006, **17**, 662-669.

Chapter 2

Cancer Targeted Microbubbles

People that have contributed to this chapter:

Marta Braga

Javier Hernández-Gil

Shengtao Lin

2.1 Introduction

The use of targeted contrast agents greatly improves the quality of data obtained during cancer imaging. This is particularly relevant to microbubble contrast agents as lipid shells were recently found to interfere with immune responses and have potential toxic effects on the kidney and liver.[1, 2] This makes selective delivery to tumours desirable as it will reduce the required concentration of contrast agent.[3]

There are many different methods that can be used to target cancer, as discussed in Chapter 1, from passive targeting using the EPR effect to the attachment of various small molecules, peptides and antibodies to the contrast agent. The EPR effect has been shown to accumulate particles up to 780 nm,[4] with particles required to have a circulation lifetime of over 6 hours in order to show significant accumulation.[5] Due to the short lifetime of microbubbles *in vivo* (Optison ~5 min)[6] and their average size of 3 μm, this method is ill-suited to the targeting of microbubbles. Due to their large size, expense and safety concerns, antibodies may not be ideal for microbubble work.[7, 8] The targeting offered by small molecules is often less effective than peptides[9] and therefore may not be sufficient to target large structures such as microbubbles. This rationale led to the use of peptides to target microbubbles in this work.

There are a wide variety of peptides that can be used to target a range of cancer biomarkers, as discussed in Chapter 1. The transmembrane receptor $\alpha_v\beta_3$ integrin is significantly upregulated in cancerous blood vessels (in particular during angiogenesis),[10, 11] making it an ideal target for microbubbles which are trapped in the intravascular space. This integrin is a receptor for the peptide sequence Arg-Gly-Asp (RGD),[12] with the cyclic peptide cRGDfK (**Figure 2.1**) having been used extensively to target contrast agents to cancer (see Chapter 1).

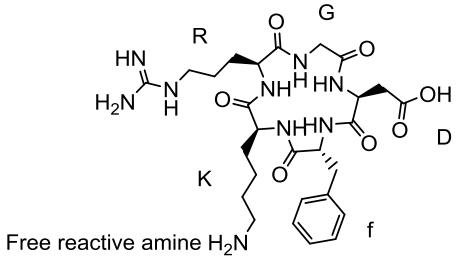


Figure 2.1: Structure of cRGDfK with amino acid residues labelled with the single letter code. Contrast agents can be conjugated to the free amine on the lysine side chain.

The use of RGD to target polymer[13] and phospholipid micelles[14] or liposomes,[15] phospholipid microbubbles[16-19] and phospholipid nanodroplets[20] is well documented. In addition, RGD has

been used to target commercial ultrasound contrast agents, with Visistar Integrin (VS-101) produced by Targeson (San Diego, USA). An example of tumour targeting with RGD-modified microbubbles is shown in **Figure 2.2**, with a 33-fold increase in intensity over non-targeted microbubbles in the tumour.

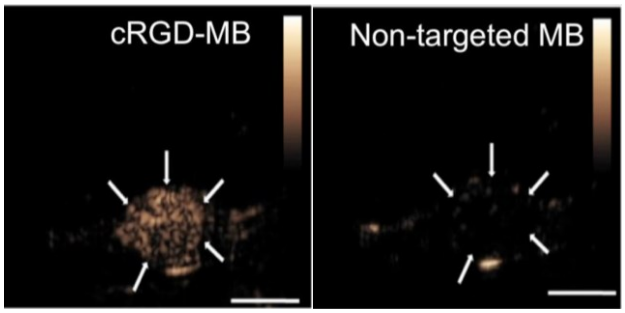


Figure 2.2: Accumulation of microbubbles within a tumour (arrows) measured by ultrasound. Normalised ultrasound intensities of RGD-targeted (left) and non-targeted (right) microbubbles 7 minutes post injection show a clear increase in accumulation when microbubbles are targeted. Scale bars represent 5mm. Reproduced with permission.[17]

An interesting report on RGD-targeted microbubbles buried the targeting ligand beneath long PEG brushes on the microbubble surface. The goal of this study was to improve the circulation persistence time by preventing recognition of the microbubbles by the immune system; this approach improved the lifetime by threefold. Only upon activation of the microbubble through the application of ultrasound was tumour binding visualised. This technique also allows for secondary targeting of the microbubbles as ultrasound pulses were only applied to the tumorous region.[18]

The ability to synthesise bespoke targeted microbubbles has been made easier by the availability of preformed streptavidin-coated microbubbles (MicroMarker Target-Ready Contrast Agents) by VisualSonics (Toronto, Canada). These microbubbles have been used in a recent pre-targeting study using the bio-orthogonal reaction between *trans*-cyclooctene (TCO) and tetrazine. Briefly, streptavidin-coated microbubbles were reacted with a tetrazine-biotin molecule and TCO was conjugated to a cancer-targeting antibody (antiVEGFR2). This allowed for pre-targeting to be performed through incubation of the antibody for 30 min *in vitro* and 24 h *in vivo* followed by administration of the microbubbles.[21] This is shown schematically in **Figure 2.3**.

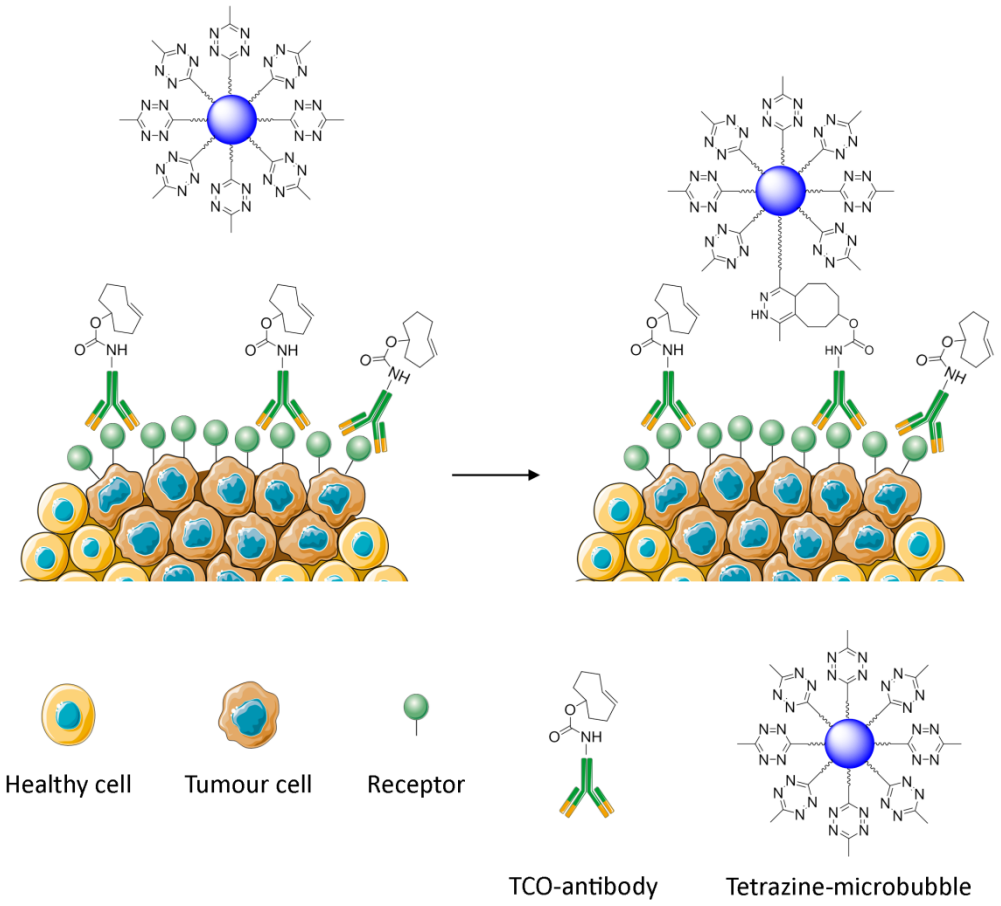


Figure 2.3: The use of the reaction between tetrazine and TCO in microbubble pre-targeting. An antibody conjugated to TCO was incubated with cells, following which tetrazine-decorated microbubbles were injected, resulting in enhanced ultrasound signal at the tumorous site.

2.1.1 Aims

The focus of this project is to synthesise and fully characterise a cancer-targeting phospholipid, to incorporate it into microbubbles and to prove selective binding of these contrast agents. In literature, this has been achieved by modification of the phospholipid followed by microbubble formation[16] and by post-modification of preformed microbubbles.[17-19] The latter method is problematic as the exact number of RGD molecules per microbubble is unknown and the constituents are not characterised. Even when the former methodology is used, characterisation is poor due to the small quantities synthesised, relying only on MALDI-ToF mass spectrometry. ^{1}H NMR has been used on polymer species, however these systems are much simpler than those based upon phospholipids and no other studies were performed.[14] Better characterisation of phospholipid modifications will allow for confirmation that mass spectrometry provides reliable information for subsequent chapters.

When considering the amount of literature present on RGD-targeting, it seems logical to develop dual-modal contrast agents using this peptide before expanding into alternative and potentially more problematic cancer targets. Targeting of these microbubbles to the less-studied CXCR4 receptor has subsequently been undertaken as part of this project; however, this was performed by another collaborating student and therefore will not be discussed in this thesis.

This approach could then be extended into pre-targeting of these microbubbles using the peptide RGD as opposed to the antibody used in the example above.[21] An advantage of these peptide pre-targeted microbubbles will be the omission of streptavidin-biotin chemistry as this can cause an immune response and allergic reactions in some patients.[22] Accelerated clearance from the circulation[23] and the possibility of binding to physiologically available biotin within the body[8] also limits the utility of streptavidin-containing contrast agents. This means that streptavidin- or avidin-containing microbubbles are unlikely to be clinically translatable,[24] making the contrast agents developed in this thesis more viable for future development.

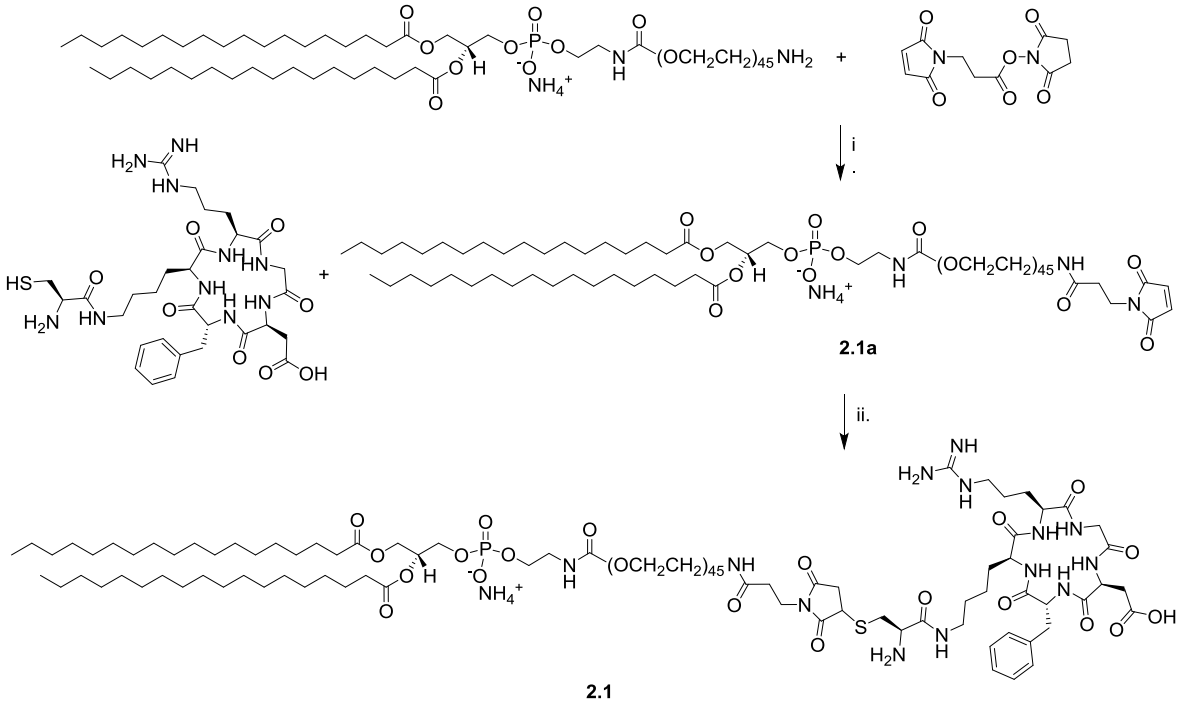
2.2 Direct Targeting of Microbubbles

Initial work focused on attaching the targeting peptide to the phospholipid, following which it could be incorporated into microbubbles.

2.2.1 Synthesis and Characterisation of an RGD Phospholipid

Many biomolecule modifications use the reaction between thiols and maleimides as it is reliable and selective, making it ideal for conjugation of expensive materials. In addition, it is easy to incorporate a thiol into a peptide through the addition of a cysteine residue. Thiol modification of targeting groups, followed by reaction with maleimide-functionalised phospholipids or polymers has been used to conjugate RGD to liposomes[15] and microbubbles.[16, 14]

The synthetic scheme devised for the preparation of **2.1** (DSPE-PEG_{2000}-cRGDfK) is shown in **Scheme 2.1**. This requires modification of the phospholipid with a maleimide functionality, followed by reaction with the thiol-containing peptide cRGDfK-C. Reactions proceeded in acceptable yields of 92 % and 60 % over subsequent steps.



Scheme 2.1: Scheme for the synthesis of DSPE-PEG_{2000}-cRGDfK **2.1**. i. NEt_3, $CHCl_3$, 24 h, RT, 92 % yield; ii. cRGDfK-C, PBS pH 7.27, N_2, 48 h, RT, 60 % yield.

This reaction was followed my multiple techniques in order to fully characterise these phospholipids. This characterisation was more extensive than that performed for any phospholipids discussed in later chapters as the reliability of different characterisation methods was being determined.

Firstly, both lipids **2.1a** and **2.1** were characterised by MALDI mass spectrometry. The masses observed in these spectra are a distribution due to the PEG polymer chain as not all polymer chains are exactly 45 units long. These peaks are separated by an m/z of 44 (corresponding to the mass of one ethylene glycol unit). This makes it difficult to obtain an exact mass value; however, what can be seen is a shift in the mass distribution which is appropriate for addition of the maleimidopropinoic acid and the cRGDfK peptide. This is shown in **Figure 2.4** and correlates well to the type of spectra observed in literature for an analogous compound.[16]

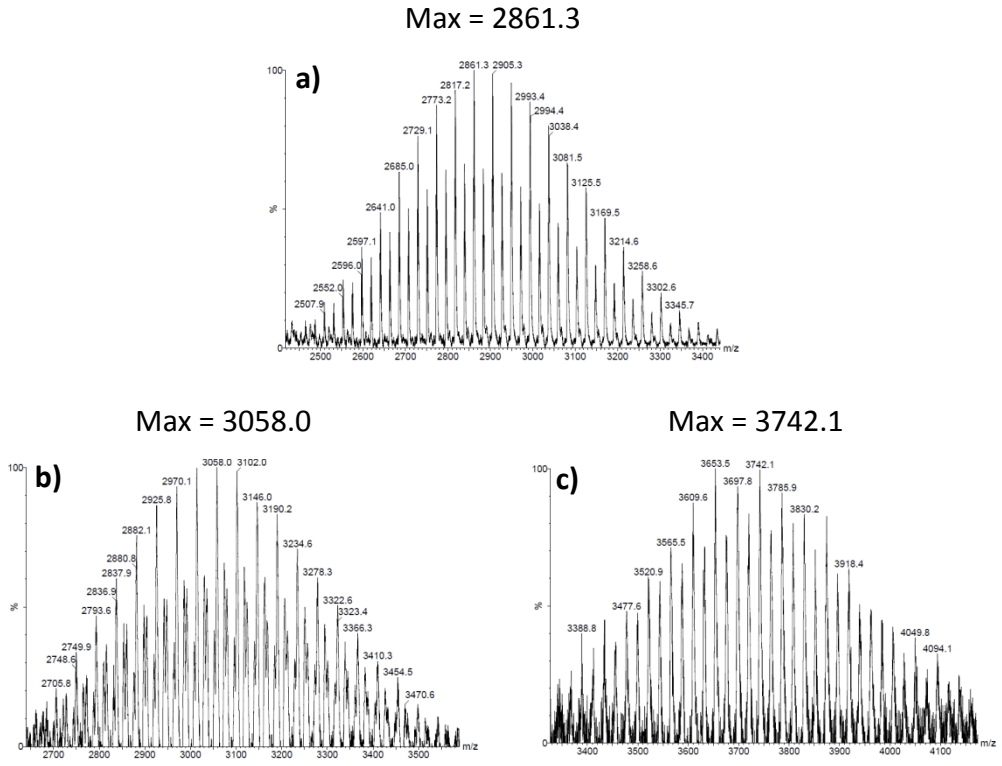


Figure 2.4: MALDI spectra in positive reflectron mode, matrix DHB. a) Unmodified DSPE-PEG_{2000}-NH_2; b) DSPE-PEG_{2000}-maleimide **2.1a**; c) DSPE-PEG_{2000}-cRGDfK **2.1**. Splitting pattern caused by PEG polymer chain.

Although a commonly used characterisation technique for phospholipids, effective crystallisation with the matrix and subsequent ionisation of the lipids is not always reliable and therefore this can be a time-consuming technique.

These lipids were also analysed by ultra-performance convergence chromatography (UPC^2), an alternative mass spectrometry technique which is not commonly used in literature. It was found that this consistently produced results and is therefore more routinely used in this thesis. The mass data obtained via UPC^2 is also slightly more accurate due to the equipment available. This technique provides a chromatogram of the intensity of the mass spectrum (average of all peaks) as a function of time, as shown in **Figure 2.5**. The spectra acquired from these major peaks are shown in **Figure 2.6**. As can be seen, the peaks observed are the result of multiply charged ions. This is due to the detector limit of 2000 m/z and the preferred charge state of the phospholipid under these conditions. This charge state can easily be determined by analysing the spacing between peaks, with an m/z of 22 indicating 2+, 14.7 a 3+ charge, 11 a 4+ ion etc. The peptide cRGDfK was also analysed by this technique, however no peak was observed.

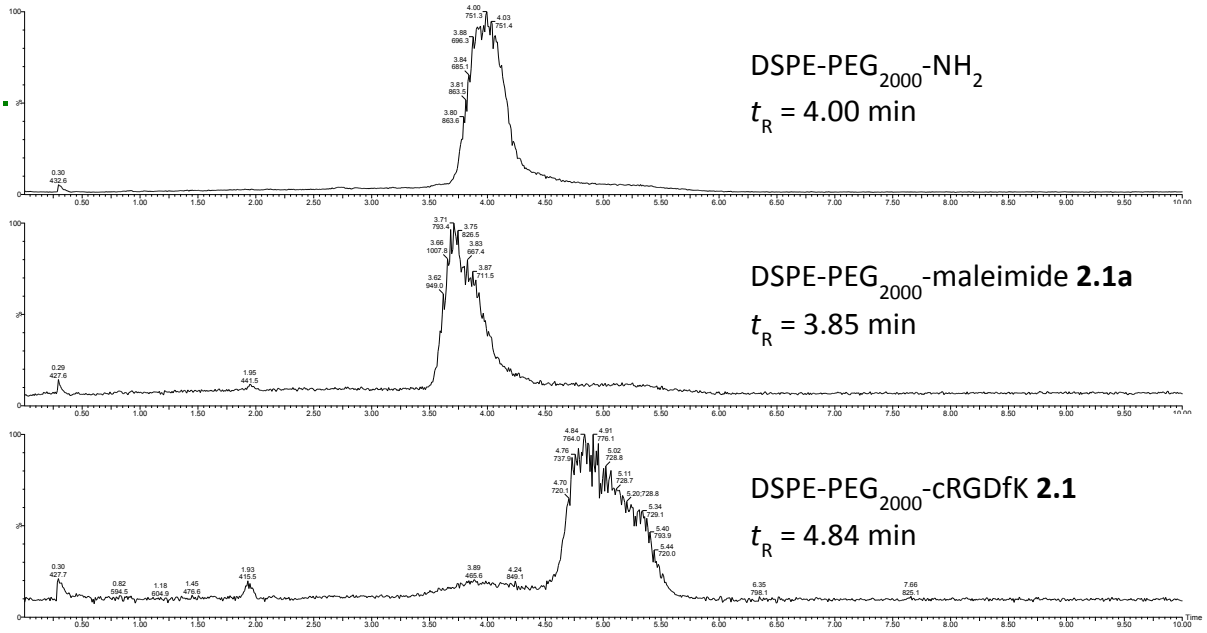


Figure 2.5: UPC^2 MS(ES+) chromatograms. Descending: unmodified DSPE-PEG$_{2000}$-NH$_2$, DSPE-PEG$_{2000}$-maleimide **2.1a** and DSPE-PEG$_{2000}$-cRGDfK **2.1**. Retention times 4.00, 3.85 and 4.84 min respectively.

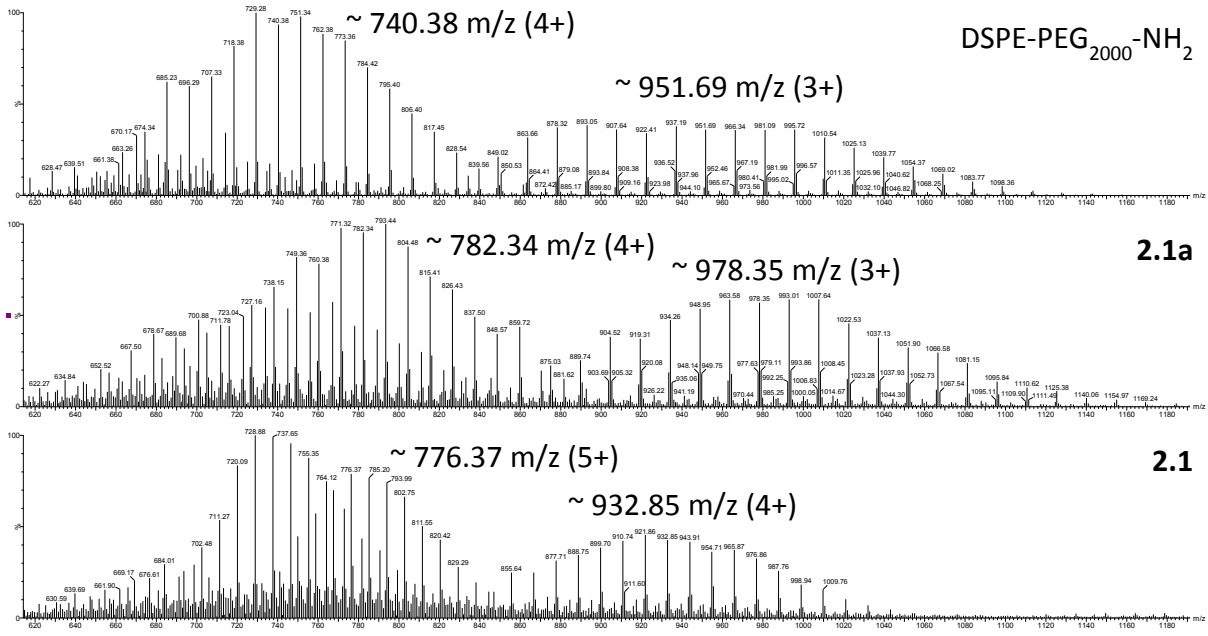


Figure 2.6: UPC^2 MS(ES+) spectra integrated over the major peaks observed in the chromatogram (**Figure 2.5**). Descending: DSPE-PEG$_{2000}$-NH$_2$, DSPE-PEG$_{2000}$-maleimide **2.1a** and product DSPE-PEG$_{2000}$-cRGDfK **2.1**.

It was also attempted to determine the purity of these phospholipids using LCMS after the success of UPC^2. HPLC chromatograms only showed a peak in the UV chromatogram of **2.1a**, however peaks in the ES(+) chromatogram were often observed, as shown in **Figure 2.7**. When the mass spectra of the major peaks were taken, mass distributions similar to those

observed in MALDI and UPC^2 were observed. However, the charge states calculated from the spacing between the peaks and the resulting absolute masses of the compounds did not correlate with the masses expected. An example of this is given in **Figure 2.8** for compound **2.1a** (the spectrum for **2.1** can be found in the Appendix **Figure A.7**). Here, the peak at 615.50 m/z fits well with the expected mass for the +5 charge state. However, the gap between PEG peaks is 5.5 m/z which would imply a +8 charge state. This would give a product of mass ~ 4924.00 g mol^{-1}, significantly too large for this molecule. If larger gaps are taken to allow for two overlapping distributions then a m/z gap of 11 is found, accounting for a +4 charge state. The calculated mass of ~ 2462.00 g mol^{-1} still does not correlate with other mass data. The peaks at 813.26 m/z exhibit the same problem.

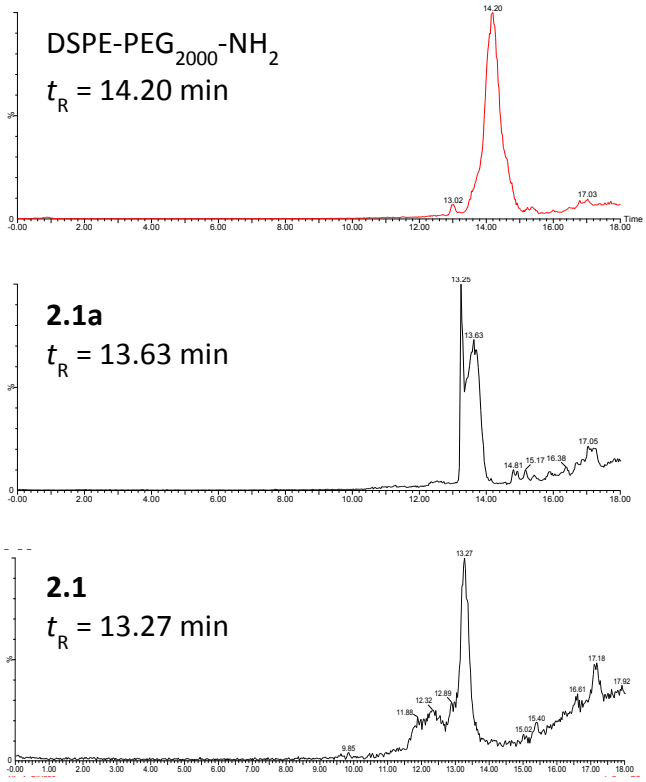


Figure 2.7: Comparison of LCMS ES+ chromatograms. Descending: unmodified DSPE-PEG$_{2000}$-NH$_2$, DSPE-PEG$_{2000}$-maleimide **2.1a** and product DSPE-PEG$_{2000}$-cRGDfK **2.1**. Peaks containing phospholipid distributions are at 14.20, 13.63 and 13.27 min respectively.

It is possible that these compounds are sticking to the column, without elution of the desired product, resulting in these unusual results. It was decided not to continue with this method of purification and characterisation. One piece of information that this chromatographic method did provide however, was the absence of residual cRGDfK. This was found to elute at 7.97 min, as shown in the Appendix (**Figures A.8** and **A.9**), and is not observed in **Figure 2.7**.

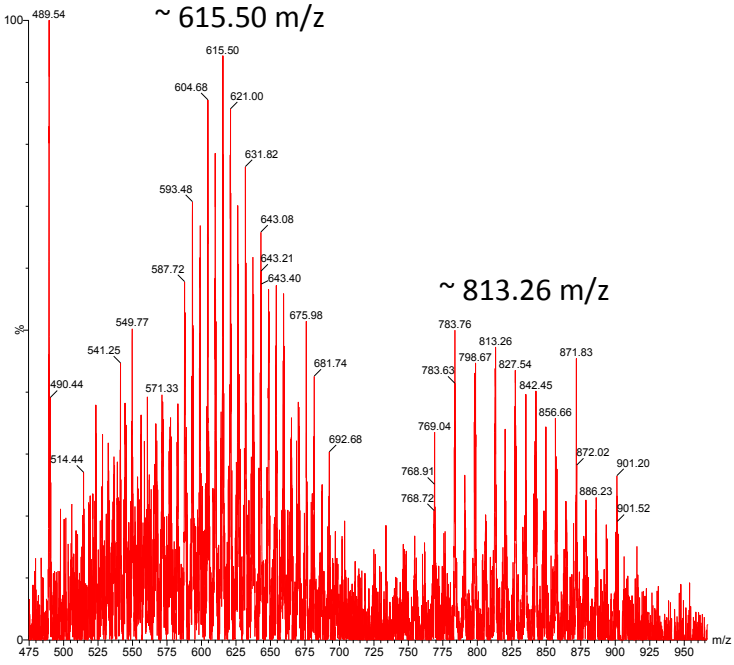


Figure 2.8: MS(ES+) spectrum for the peak at 13.63 min (**Figure 2.7**) for compound DSPE-PEG_{2000}-maleimide **2.1a**.

These samples were also analysed by NMR. This is not commonly used due to the small amounts of material typically synthesised and the insensitivity of the technique, however the combination of relatively large scale synthesis and high scan numbers allowed for this to be obtained. In these spectra, the appearance and disappearance of characteristic maleimide and aromatic (from the phenylalanine residue in cRGDfK) peaks is of interest and their relative integration intensity to the phospholipids peaks. This is most easily analysed using the terminal CH_3 groups from the phospholipid (integrates to 6 protons). These spectral regions are shown in **Figure 2.9**. Full interpretation was also performed with spectra shown in the Appendix (**Figures A.1-A.4**) and peak allocation in the Experimental section. The overlay of the cRGDfK aromatic peak in the lone peptide and phospholipid **2.1** is also shown in **Figure A.5** in the Appendix and confirms the identity of this peak as it maintains the same shape and chemical shift.

Proof that these groups were attached to the phospholipid scaffold was obtained by diffusion-ordered NMR spectroscopy (DOSY), where clear correlation of the maleimide and aromatic peaks with the other phospholipid peaks (they sit on a straight line at the same diffusion coefficient) implies that they are attached. These spectra are shown in **Figure 2.10**.

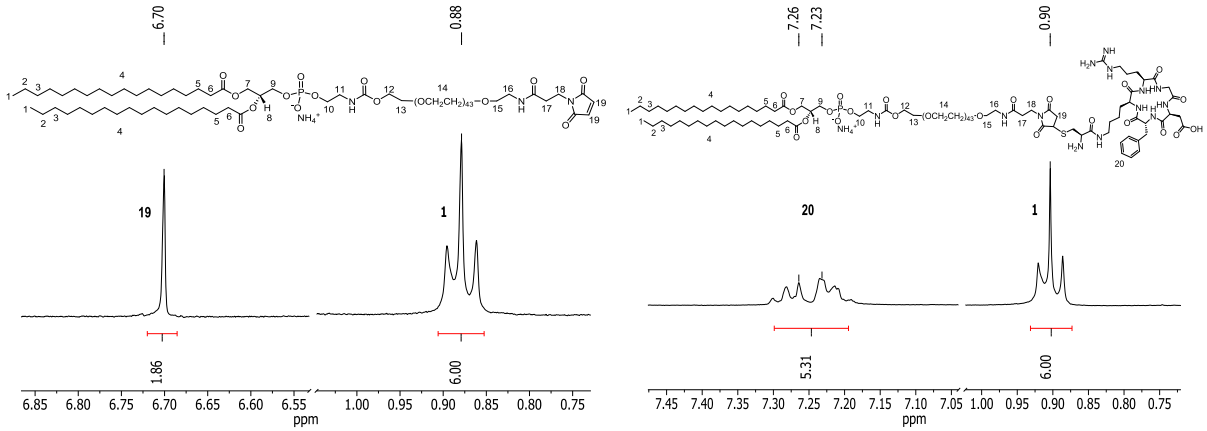


Figure 2.9: Significant peaks in the ^{1}H NMR spectra of DSPE-PEG$_{2000}$-maleimide **2.1a** (left) and DSPE-PEG$_{2000}$-cRGDfK **2.1** (right). Solvent $CDCl_3$ and CD_3OD respectively.

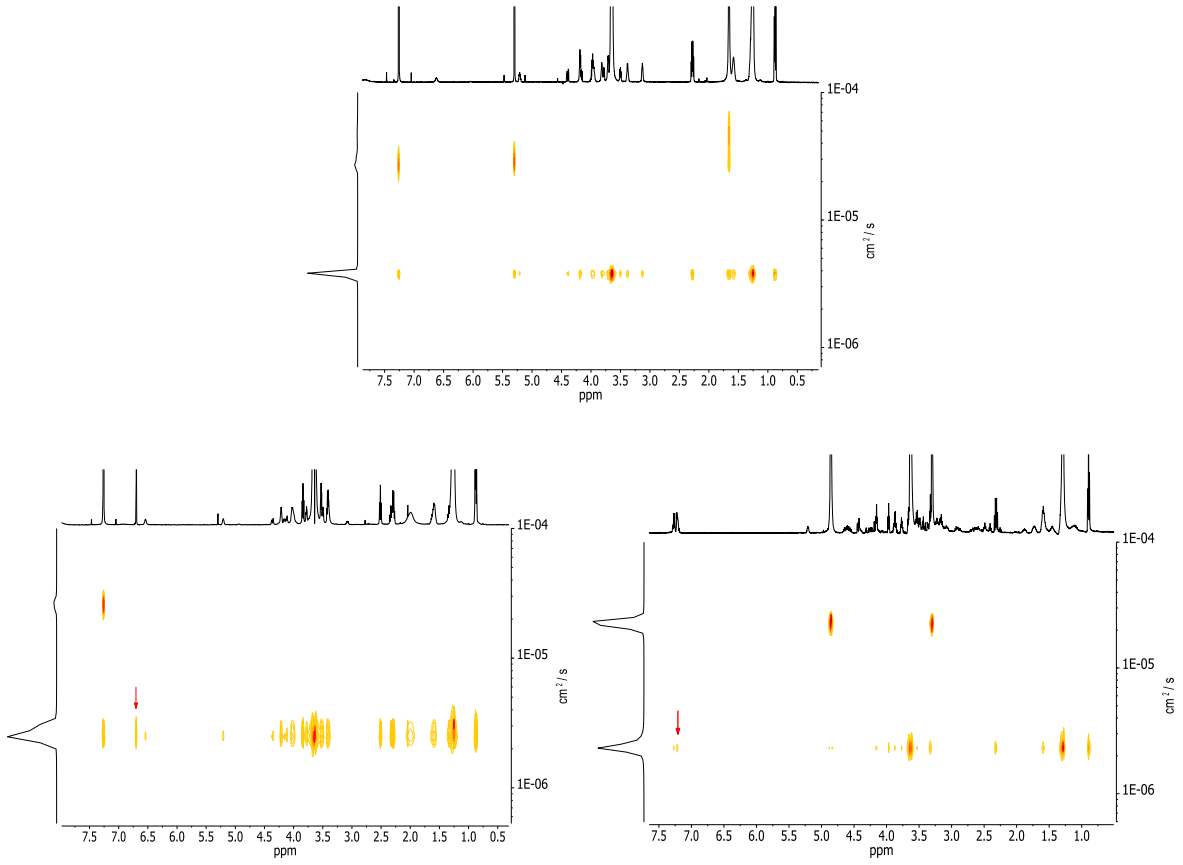


Figure 2.10: DOSY NMR spectra proving the attachment of maleimide and cRGDfK moieties (red arrows) to DSPE-PEG$_{2000}$-NH_2. Top: DSPE-PEG$_{2000}$-NH_2, solvent $CDCl_3$; Bottom left: DSPE-PEG$_{2000}$-maleimide **2.1a**, solvent $CDCl_3$; Bottom right: DSPE-PEG$_{2000}$-cRGDfK **2.1**, solvent CD_3OD.

Phospholipid **2.1a** was also made in sufficient quantities to allow for ^{13}C, HSQC and DEPT135 NMR. These show the appearance of a peak at 134.4 ppm in ^{13}C NMR which is in the correct region for a maleimide peak, this figure can be found in the Appendix (**Figure**

A.2). This correlates to the ^{1}H NMR maleimide peak using HSQC and DEPT135 proves that this is a CH or CH_3 group, supporting the allocation as a maleimide peak (**Figure A.3**).

All of this characterisation confirms that compounds **2.1a** and **2.1** were successfully synthesised. It also shows that UPC^2 provides correct and accurate information when compared to all other methods discussed. It was therefore deemed unnecessary to perform all characterisation methods on other phospholipid molecules.

2.2.2 Microbubble Formation and Characterisation

Phospholipid **2.1** was formed into microbubbles. According to the formulation, 10 mol% of the microbubble formulation may be a PEG-containing phospholipid. In order to achieve maximum targeting ability, it was decided to use the highest loading possible. This produced microbubbles on average of 1.96 μm at a concentration of 1.06 x 10^9 MB/ mL (n=3, see Appendix **Table A.2**). These size and concentration values are comparable to those of unmodified microbubbles with average values of 2.42 μm and 1.26 x 10^9 MB/ mL (n=3, see Appendix **Table A.1**).

2.2.2.1 Acoustic Characterisation

In order to confirm that these microbubbles remain acoustically active after modification, measurements were performed before and after their addition to water. This was performed by Shengtao Lin, Dept. of Bioengineering, Imperial College London. These results confirm acoustic contrast enhancement, as demonstrated in **Figure 2.11**. These measurements were performed three times, with all data shown in the Appendix (**Figure A.10**).

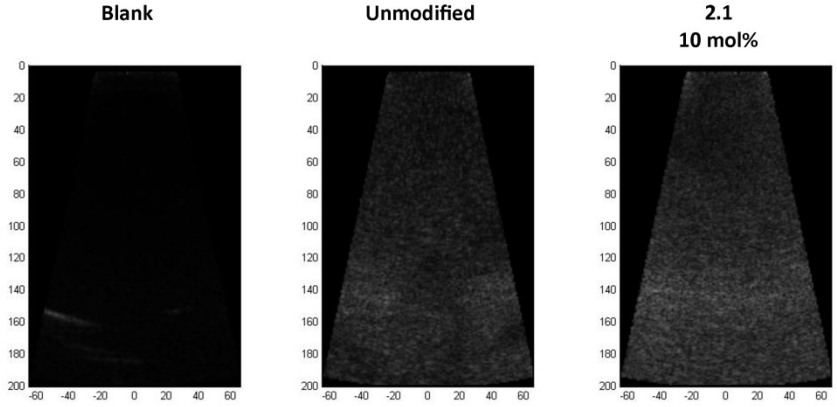


Figure 2.11: Acoustic measurements of solutions. Left to right: water, unmodified microbubbles and microbubbles containing 10 mol% **2.1**. Measurements performed on a Verasonics ultrasound imaging system equipped with a P4-2v probe (2 MHz imaging frequency at a Mechanical Index of 0.08). 1.7 L H_2O was rested for 5 min following which 20 μL of the microbubble solution was added.

2.2.3 In Vitro Characterisation

The selection of cell lines and all *in vitro* experiments were performed by Marta Braga, Dept. of Surgery and Cancer, Imperial College London, assisted by Javier Hernández-Gil, Dept. of Chemistry, Imperial College London. These results may be discussed in more detail in the thesis of Marta Braga (currently not submitted).[25]

In vitro work was performed using two different cell lines; MDA-MB-231 and M21. These are human breast cancer and melanoma cell lines respectively which are expected to have different expression of $\alpha_v\beta_3$ integrin. As this integrin is the target for these microbubbles, it was deemed useful to compare cell lines with different levels of expression. Expression of the β_3 subunit was assessed by Western Blot using a β_3 specific antibody. M21 cells were shown to have higher expression at all cell densities studied.

Confirmation that RGD-modified microbubbles adhered to these cell lines was performed using an Opticell chamber, which is illustrated in **Figure 2.12**. This is formed of two acoustically transparent membranes filled with media, with the cells adhered to the lower membrane. This chamber was used due to the buoyancy of microbubbles, which required incubation to be performed with the cells adhered to the top membrane. These membranes also allow for ultrasound images to be obtained; however, this was not deemed necessary at this stage.

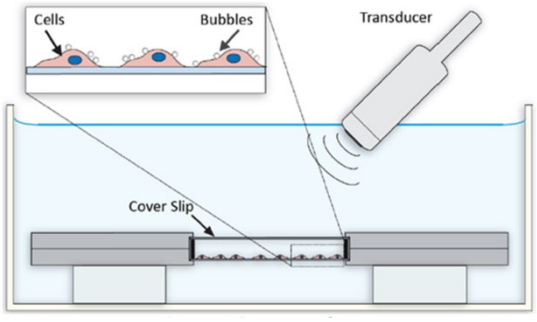


Figure 2.12: Diagram demonstrating the configuration and use of an Opticell unit. Reproduced with permission.[20]

All experiments were performed using the same protocol. Briefly, the plates were prepared with a density of 2 x 10^6 cells in 10 mL of media per Opticell 24 h prior to use. The microbubble solution was then diluted in media (1:100 dilution) and injected into the Opticell chamber. The Opticell was turned so that the cells were adhered to the top membrane, adjacent to the microbubbles. These were incubated for 10 min at 37 ^oC, following which the

membranes were turned again so that the cells were now adhered to the bottom membrane and observed using a microscope. Any microbubbles attached to the cells would then be observed at the bottom of the Opticell, whereas any not adhered would float in a different focal plane. Experiments were performed with both unmodified microbubbles and those containing 10 mol% phospholipid **2.1**.

Firstly, untargeted microbubbles were analysed using this method in order to prove that there is no unspecific binding caused by this microbubble formulation. As can be seen in **Figure 2.13**, no microbubbles bound to either cell line as all remained floating at the upper membrane after incubation. These results also show that the MDA-MB-231 cell line seems to have lower confluence under these conditions.

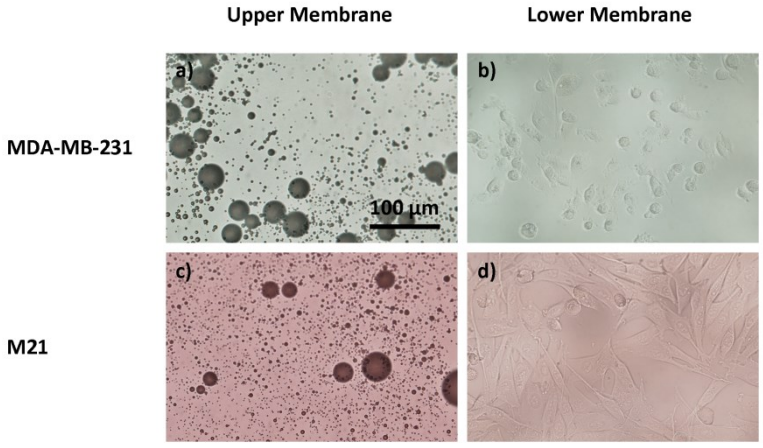


Figure 2.13: *In vitro* work performed with unmodified microbubbles on MDA-MB-231 (top) and M21 (bottom) cell lines using the incubation protocol described in the main text. a) Microbubbles that did not adhere to MDA-MB-231 cells floating near the upper membrane; b) MDA-MB-231 cells on the lower membrane showing no adhered microbubbles; c) microbubbles that did not adhere to M21 cells; d) M21 cells on the lower membrane. Initial microbubble concentrations of 8.90 x 10^8 MB/ mL for MDA-MB-231 and 1.67 x 10^9 MB/ mL for M21 experiments. Images obtained by Marta Braga.[25]

This protocol was then used to analyse microbubbles containing 10 mol% phospholipid **2.1**. These experiments were performed using the same microbubble solution for both cell lines to allow for accurate comparison. These results are shown in **Figure 2.14** for the M21 cell line and **Figure 2.15** for MDA-MB-231. **Figure 2.15** shows images taken at every stage of the experiment to clarify the process. In both instances, binding is observed. Additionally, those microbubbles not adhered to the MDA-MB-231 cells are significantly larger than those that adhere. This is good as these microbubbles are not relevant for ultrasound imaging because their acoustic properties are poor and their lifetime in the body will be significantly less.

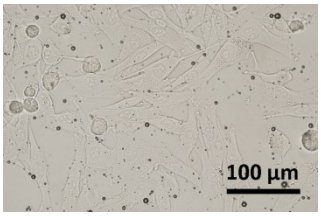


Figure 2.14: *In vitro* work performed with microbubbles containing 10 mol% phospholipid **2.1** and M21 cells. Image taken after incubation, showing only those microbubbles bound to the cells on the lower membrane. Initial microbubble concentration of 3.11 x 10^8 MB/ mL. Images obtained by Marta Braga.[25]

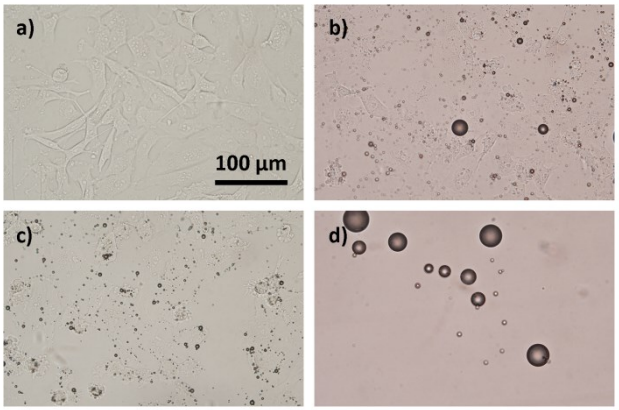


Figure 2.15: *In vitro* work performed with microbubbles containing 10 mol% phospholipid **2.1** and MDA-MB-231 cells. Images taken at different stages of the experiment. a) MDA-MB-231 cells adhered to lower membrane; b) incubation of cells with microbubbles with cells adhered to upper membrane; c) microbubbles adhered to cells on the lower membrane; d) microbubbles that did not adhere to cells floating near the upper membrane. Initial microbubble concentration of 3.11 x 10^8 MB/ mL. Images obtained by Marta Braga.[25]

It was attempted to compare the adhesion of microbubbles between the cell lines using the normal counting software. This is unlikely to be reliable data as the software may miss microbubbles due to cells obstructing the circumference. Additionally, it may count spherical cells as large microbubbles. When the data was compared between the two, it gave very similar results between the lines, with concentrations of 2.91 x 10^9 MB/ mL and 3.08 x 10^9 for M21 and MDA-MB-231 cells respectively. Interestingly, the initial concentration of microbubbles for this experiment was 3.11 x 10^8 MB/ mL and this was diluted by 100 times when added to the Opticell chamber. This implies that the cells are capturing and concentrating the microbubbles at the base of the chamber effectively. These results also show that binding is similar between the two cell lines, which is what can be generally determined visually. This could be due to the concentration of microbubbles being added not saturating the receptors in either cell line.

In order to determine whether this was the case, an experiment was performed with a higher initial microbubble concentration of 1.08 x 10^9 MB/ mL (3.5 times more concentrated). This was again diluted by 100 times before administration, with results shown in **Figure 2.16**. This experiment showed very clearly that the microbubbles adhered to the M21 cells much more effectively than MDA-MB-231 cells. Unfortunately, the MDA-MB-231 cells exhibited a low confluence and low binding in this study. Unspecific binding to the plate was also observed, but only in regions near cell populations; this could be due to signalling molecules between cells. This has been observed in literature, however these microbubbles were removed after washing.[21] This behaviour was not significantly observed in M21 cells, however this could be due to the higher cell confluence and therefore fewer areas without cells. As this was not observed for unmodified microbubbles, this clearly results from the addition of the targeting peptide. This experiment was repeated in a higher confluence MDA-MB-231 plate and it was found that although binding increased, it still did not match the M21 cell line.

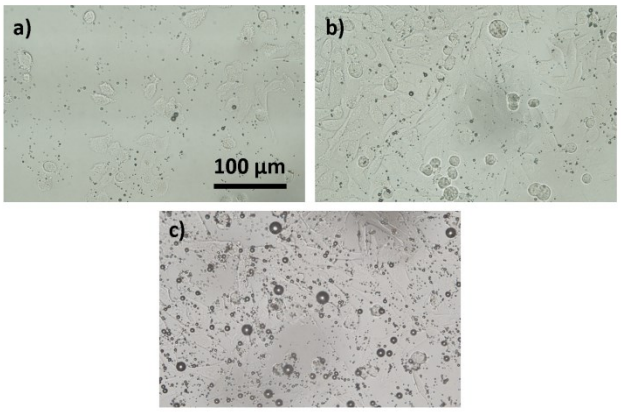


Figure 2.16: *In vitro* work performed with a higher concentration of microbubbles containing 10 mol% phospholipid **2.1** and MDA-MB-231 (top) or M21 (bottom) cells. a) Binding of microbubbles to the MDA-MB-231 cell line exhibiting low confluence; b) binding of microbubbles to the MDA-MB-231 cell line exhibiting higher confluence; c) binding of microbubbles to the M21 cell line. Images taken after incubation, showing only those microbubbles bound to the cells on the lower membrane. Initial microbubble concentration of 1.08 x 10^9 MB/ mL. Images obtained by Marta Braga.[25]

2.2.4 *In Vivo* Experiments

It was attempted to gain ultrasound images of tumour-bearing mice using these targeted microbubbles. An example image is shown in **Figure 2.17**, where the tumour can be clearly observed. Unfortunately, it was found that the equipment available was inappropriate for use on animal models due to transducer type (designed for human imaging) or other factors (the

procedures and image reconstruction codes required were different from those used in models outside animals). These experiments were not continued as image quality and microbubble enhancement were poor. These studies were performed by collaborator Marta Braga.[25]

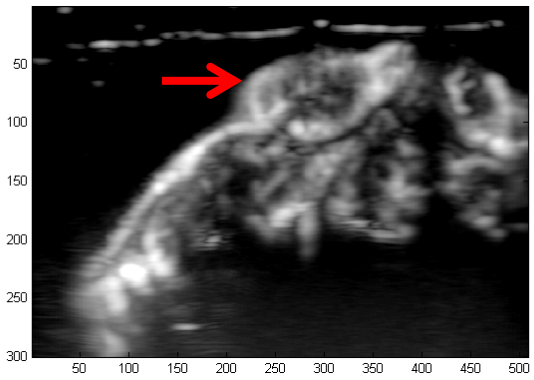


Figure 2.17: Microbubble-enhanced ultrasound image obtained of a tumour (red arrow) in an immune-compromised mouse. Microbubbles used contained 10 mol% phospholipid **2.1**, however little enhancement was observed. Image provided by Marta Braga.[25]

2.3 Pre-Targeting of Microbubbles

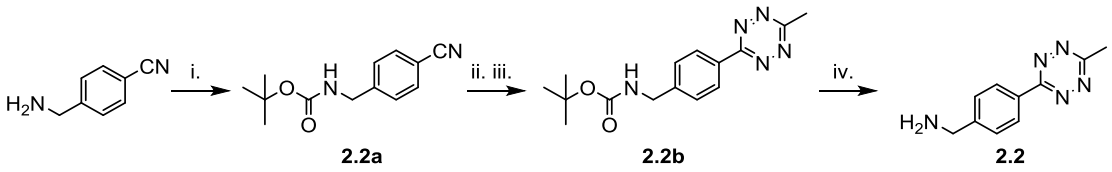
After successful targeting of microbubbles using direct labelling, it was decided to develop an analogous pre-targeting methodology. This has the potential to improve targeting as more peptide can be concentrated at the desired tumour location than can be attached to the surface of each microbubble (maximum 10 % modified lipid). This will hopefully allow for greater signal enhancement in the desired region.

2.3.1 Synthesis and Characterisation

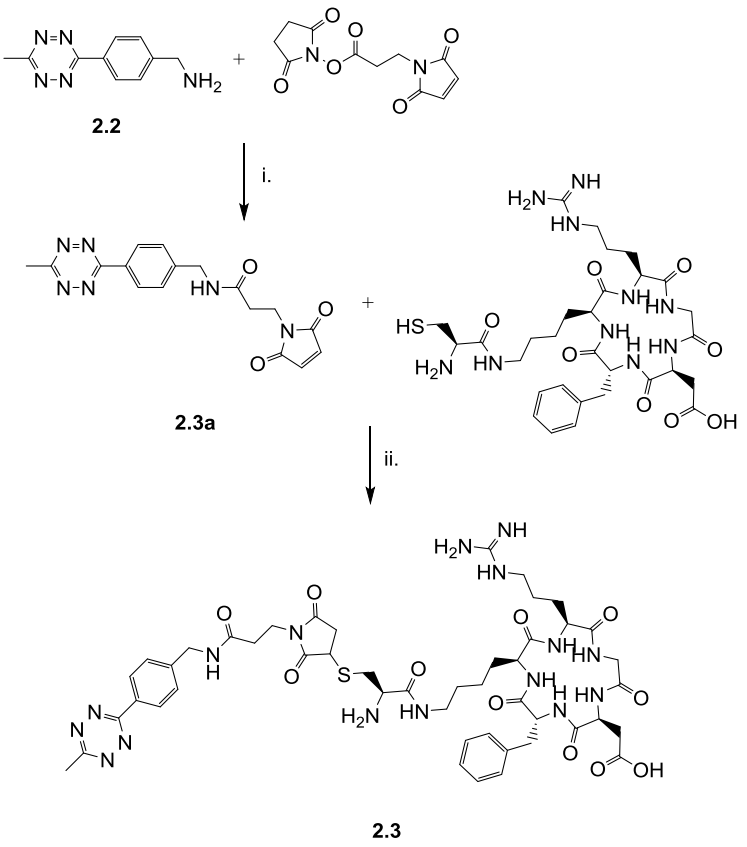
This method of microbubble capture required two molecules to be synthesised: a peptide and a phospholipid with cross reactive groups to allow for *in vitro* and *in vivo* capture. Due to the tetrazine-TCO reaction having been used previously and proving effective, in addition to being bio-orthogonal and biocompatible, this was chosen for microbubble capture. This required the synthesis of tetrazine, which was performed according to literature protocols[26, 27] as shown in **Scheme 2.2**.

The syntheses devised for these molecules are shown in **Schemes 2.3** and **2.4**, with the RGD peptide being attached to tetrazine and the phospholipid conjugated to the TCO moiety. This was chosen initially due to the desire to minimise the number of reagents required to react with the phospholipid. Tetrazine conjugation to the phospholipid would require peptide coupling and therefore an agent to be added to the reaction which would then have to be

removed. The efficiency of this purification is unknown. Therefore a pre-activated NHS-TCO molecule was purchased to minimise phospholipid manipulation.

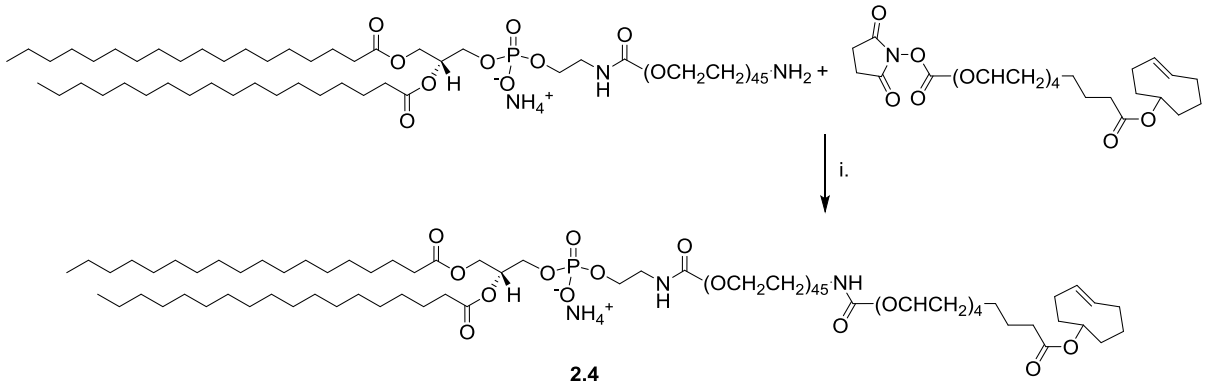


Scheme 2.2: Synthesis of tetrazine reagent **2.2**. i. Boc_2O, NEt_3, DCM, 16 h, RT, 84 % yield; ii. hydrazine hydrate, $Ni(OTf)_2$, CH_3CN, 72 h, 60 ^oC, not isolated; iii. $NaNO_2$, 1M HCl, RT, 62 % yield; iv. TFA, DCM, 2 h, RT, 84 % yield.



Scheme 2.3: Synthesis of RGD-tetrazine **2.3**. i. EDC.HCl, NEt_3, DCM, 3 h, RT, 48 % yield; ii. PBS, 5 h, RT, 99 % yield.

The tetrazine molecule was modified to attach a maleimide moiety in order to react with the cRGDfK peptide. This was then purified by dialysis using a membrane with a 300 MW cutoff, producing RGD-tetrazine **2.3**. The conjugation of tetrazine to RGD peptides has been explored previously for ^{18}F radiolabeling.[28] Reaction of the phospholipid DSPE-PEG_{2000}-NH_2 with NHS-TCO was performed as for molecules **2.1** and **2.2**, producing DSPE-PEG_{2000}-TCO **2.4** in a good yield.



Scheme 2.4: Synthesis of DSPE-PEG$_{2000}$-TCO **2.4**. i. NEt_3, $CHCl_3$, 48 h, RT, 99 % yield.

The peptide **2.3** was characterised predominantly by mass spectrometry, however as with phospholipid **2.1** the aromatic region of the ^{1}H NMR could be analysed to confirm the ratio between the peptide and tetrazine peaks. This is shown in **Figure 2.18**. Similarly, the characteristic peak of the TCO moiety[29] could be observed by ^{1}H NMR in phospholipid **2.4**, allowing for integration with the terminal CH_3 groups, as shown in **Figure 2.19** (full NMR can be found in the Appendix, **Figure A.6**). This phospholipid was also characterised by MALDI and UPC[2]. This data can be found in the Appendix (**Figures A.10** and **A.13**).

Unfortunately, no further work was carried out on pre-targeting microbubbles due to time constraints. The next step would require synthesis of microbubbles containing 10 mol% **2.4** and *in vitro* work to confirm whether this peptide can be used for this purpose.

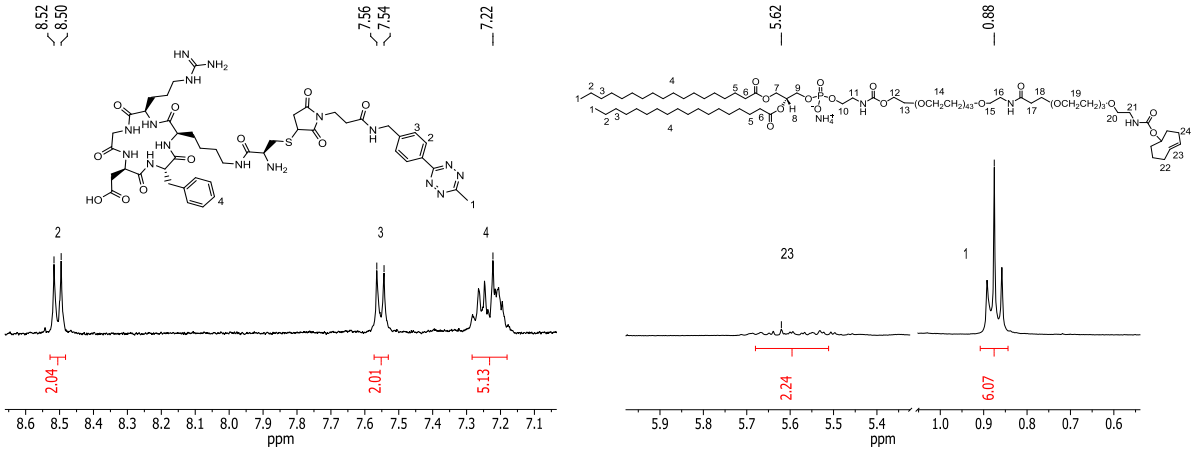


Figure 2.18: ^{1}H NMR of **2.3** (left) and **2.4** (right) with significant peaks assigned. Solvent CD_3OD and $CDCl_3$ respectively.

2.4 Conclusions

A phospholipid containing the peptide cRGDfK has been successfully synthesised and fully characterised using techniques such as MALDI, UPC^2-ES(+) and NMR. All of these techniques proved that the desired products had been synthesised, confirming that UPC^2 is a reliable, reproducible characterisation method for use in later chapters. This is important as not all syntheses involving peptides or phospholipids will be performed on a large enough scale for NMR analysis, therefore proving that techniques such as mass spectrometry are accurate will provide a solid basis for future characterisation.

This phospholipid was then incorporated into microbubbles which were shown to target human cancer cells *in vitro*. This will allow for all microbubble contrast agents in the rest of this thesis to be targeted to cancer, resulting in the formation of dual-modal targeted contrast agents.

In vivo work was also attempted, however improvement in ultrasound equipment and processing is required before further experiments can be performed. Research is currently being undertaken in this area with the aim of obtaining *in vivo* images of sufficient quality. This will allow for testing of these targeted microbubbles and determination of targeting efficiency.

Further work has begun in the attempt to allow for pre-targeting of microbubbles in order to build upon literature research. This makes use of the reaction between tetrazine and TCO, with tetrazine attached to the RGD peptide and TCO to the microbubbles. These molecules have been synthesised, however they have not yet been tested *in vitro*. Testing of these components will hopefully allow for improved targeting efficiency when compared to directly targeted microbubbles as the concentration of targeting peptide will be higher at the cancer location than ordinarily on the microbubble surface. The rapid reaction between TCO and tetrazine should allow for microbubble capture, as has been observed in literature.

2.5 References

1. T.-L. Pan, P.-W. Wang, S. A. Al-Suwayeh, Y.-J. Huang and J.-Y. Fang, *Food Chem. Toxicol.*, 2012, **50**, 3892-3901.
2. T.-L. Hwang, C.-L. Fang, S. A. Al-Suwayeh, L.-J. Yang and J.-Y. Fang, *Toxicol. Lett.*, 2011, **203**, 172-180.
3. L. Mai, A. Yao, J. Li, Q. Wei, M. Yuchi, X. He, M. Ding and Q. Zhou, *PLoS One*, 2013, **8**, e61224.

4. S. K. Hobbs, W. L. Monsky, F. Yuan, W. G. Roberts, L. Griffith, V. P. Torchilin and R. K. Jain, *Proc. Natl. Acad. Sci.*, 1998, **95**, 4607-4612.
5. J. Gallo, N. J. Long and E. O. Aboagye, *Chem. Soc. Rev.*, 2013, **42**, 7816-7833.
6. K. K. Wong, I. Huang, Y. R. Kim, H. Tang, E. S. Yang, K. K. Kwong and E. X. Wu, *Magn. Reson. Med.*, 2004, **52**, 445-452.
7. C. A. Janeway, P. Travers, M. Walport and M. J. Shlomchik, *Immunobiology 5: The Immune System in Health and Disease*, Garland Publishing, New York, 2001.
8. B. A. Kaufmann, *Cardiovasc. Res.*, 2009, **83**, 617-625.
9. W.-b. Zhang, J.-M. Navenot, B. Haribabu, H. Tamamura, K. Hiramatu, A. Omagari, G. Pei, J. P. Manfredi, N. Fujii, J. R. Broach and S. C. Peiper, *J. Biol. Chem.*, 2002, **277**, 24515-24521.
10. P. Brooks, R. Clark and D. Cheresh, *Science*, 1994, **264**, 569-571.
11. J. Folkman, *Nat. Med.*, 1995, **1**, 27-30.
12. S. Liu, *Bioconjugate Chem.*, 2009, **20**, 2199-2213.
13. D. Zhou, G. Zhang and Z. Gan, *J. Control. Release*, 2013, **169**, 204-210.
14. N. Nasongkla, X. Shuai, H. Ai, B. D. Weinberg, J. Pink, D. A. Boothman and J. Gao, *Angew. Chem. Int. Ed.*, 2004, **43**, 6323-6327.
15. X.-y. Liu, L.-m. Ruan, W.-w. Mao, J.-Q. Wang, Y.-q. Shen and M.-h. Sui, *Int. J. Med. Sci.*, 2010, **7**, 197-208.
16. F. Yan, X. Xu, Y. Chen, Z. Deng, H. Liu, J. Xu, J. Zhou, G. Tan, J. Wu and H. Zheng, *Ultrasound Med. Biol.*, 2015, **41**, 2765-2773.
17. C. R. Anderson, X. Hu, J. Tlaxca, A.-E. Decleves, R. Houghtaling, K. Sharma, M. Lawrence, K. Ferrara and J. J. Rychak, *Invest. Radiol.*, 2011, **46**, 215-224.
18. M. A. Borden, J. E. Streeter, S. R. Sirsi and P. A. Dayton, *Mol. Imaging*, 2013, **12**, 357-363.
19. H. Y. Jun, S. H. Park, H. S. Kim and K.-H. Yoon, *Acad. Radiol.*, 2010, **17**, 54-60.
20. P. S. Sheeran, J. E. Streeter, L. Mullin, T. O. Matsunaga and P. A. Dayton, *Ultrasound molecular imaging with customizable nanoscale phase-change contrast agents: An in-vitro feasibility study*, IEEE International Ultrasonics Symposium, 2012.
21. A. Zlitni, N. Janzen, F. S. Foster and J. F. Valliant, *Angew. Chem. Int. Ed.*, 2014, **53**, 6459-6463.
22. M. Chinol, C. Grana, R. Gennari, M. Cremonesi, J. G. Geraghty and G. Paganelli, in *Radioimmunotherapy of Cancer*, eds. P. G. Abrams and A. R. Fritzberg, CRC Press, Boca Raton, 2000, p. 181.
23. D. Marshall, R. B. Pedley, J. A. Boden, R. Boden, R. G. Melton and R. H. Begent, *Br. J. Cancer*, 1996, **73**, 565-572.
24. N. Deshpande, A. Needles and J. K. Willmann, *Clin. Radiol.*, 2010, **65**, 567-581.
25. M. Braga, Thesis, Not Submitted, Imperial College London.
26. H. L. Evans, L. Carroll, E. O. Aboagye and A. C. Spivey, *J. Labelled Compd. Radiopharm.*, 2014, **57**, 291-297.
27. H. L. Evans, Q.-D. Nguyen, L. S. Carroll, M. Kaliszczak, F. J. Twyman, A. C. Spivey and E. O. Aboagye, *Chem. Commun.*, 2014, **50**, 9557-9560.

28. J. M. Fox, M. Hassink, M. Blackman, Z. Li, P. S. Conti and R. Selvaraj, *Patent, US 20130266512 A1*, 2013.

29. B. Nichols, Z. Qin, J. Yang, D. R. Vera and N. K. Devaraj, *Chem. Commun.*, 2014, **50**, 5215-5217.

Chapter 3

PET Labelling of Microbubbles

People that have contributed to this chapter:

Marta Braga

Javier Hernández-Gil

Shengtao Lin

3.1 Introduction

Multimodality imaging is a growing area of research.[1] The nature of the microbubble architecture makes it an ideal scaffold for the attachment of multiple moieties to allow for dual-modal, targeted imaging. The selection of complementary modalities must take into account the microbubble concentration (small numbers of microbubbles can allow for good signal[2]) and short lifetime (minutes[3]). As such MRI is ill suited due to its low sensitivity and long imaging times, however contrast agents have still been developed in this area.[4, 5] Positron emission tomography (PET) exhibits exceptional sensitivity and can therefore be ideally matched to ultrasound properties.

3.1.1 PET-Labelled Microbubbles

These dual-modal probes will allow for whole-body pharmacokinetics of the microbubbles to be determined, something that is not widely performed with ultrasound alone. These biodistribution studies are of paramount importance in the evaluation of the usefulness of contrast agents and in uncovering possible side effects. All studies that could be found in literature are summarised in **Table 3.1** and are discussed briefly below.

Initial work used human serum albumin- (HSA-) coated air-filled microspheres labelled with ^{125}I or ^{123}I in *ex vivo* animal (**I**)[6] or *in vivo* human (**II**)[7] biodistribution studies respectively. These studies were improved upon using ^{18}F to PET-label microbubbles 14 years later by two separate groups. In one study, the radiolabel was attached to the lipid 1,2-dipalmitoyl-*sn*-glycerol (**III**) and incorporated into phospholipid microbubbles.[8] In the other, pre-formed, phospholipid-stabilised, streptavidin-coated microbubbles were targeted to cancer using antibodies (**IV**).[3] These provided the first ultrasound images and molecular targeting data respectively.

More recently this targeting approach has been extended to albumin-coated, targeted microbubbles, which have been radiolabelled with ^{18}F and targeted to cancer using the same antibodies (**V**).[9] This combined ultrasound images and tumour targeting with PET into one study. Finally, an alternative study has used ^{99m}Tc for SPECT imaging.[10] This was performed by labelling a biotin-modified chelate with ^{99m}Tc and subsequent reaction with pre-formed microbubbles which were used in an abovementioned ^{18}F study (**VI**). ^{99m}Tc is the most widely used radionuclide in diagnostic imaging, making it accessible to more imaging centres.

Table 3.1: Details of microbubble radiolabelling and biodistribution studies.[3, 6-10]

Microbubble	Isotope	Animal	Targeted[a]	US	Accumulation (% ID/ g)
I[6]	^{125}I	Rat, pig	×	×	**Rat 3 min (% only)**
Albunex[b]		*Ex vivo*			Liver (60 %)
HSA*					Spleen (7 %)
Air[†]					Lungs (3 %)
II[7]	^{123}I	Human	×	×	**60 min (% only)**
Quantison[c]		*In vivo*			Liver (41.8 %)
HSA*					Spleen (11.0 %)
Air[†]					Lungs (4.0 %)
III[8]	^{18}F	Rat	×	✓	**4 min**
In house		*In vivo*			Lung (~ 2.5)
Lipid*					Spleen (~ 1.8)
Perfluorobutane[†]					Blood (~ 1.0)
					Liver (~ 0.8)
IV[3]	^{18}F	Mouse	✓	×	**4 min**
MicroMarker[d]		*In vivo*			Liver (34.4)
Lipid*					Spleen (11.4)
Perfluorocarbon[†]					Blood (8.8)
					Tumour (1.1)
V[9]	^{18}F	Mouse	✓	✓	**5 min (blood 4.5 min)**
In house		*In vivo*			Liver (17.2)
HSA*					Blood (10.7)
Perfluoropropane[†]					Lung (5.8)
					Tumour (1.0)
VI[10]	^{99m}Tc	Mouse	×	×	**4 min**
MicroMarker[d]		*In vivo*			Liver (68.2)
Lipid*					Spleen (214.2)
Perfluorocarbon[†]					Blood (15.6)

[a]To cancer (VEGFR2). [b]NYCOMED Imaging AS, Oslo, Norway. [c]Upperton Limited, Nottingham, UK. [d]VisualSonics, Toronto, Canada. *Surface coating. [†]Core gas.

The number of microbubbles in the blood stream were found to decrease between 4 minute and 60 minute time-points.[10] This, in addition to the known short lifetime of microbubbles, means that the data shown in **Table 3.1** is for short time periods (~ 4 min post injection when available) when microbubbles will be available for ultrasound imaging. At 60 min, all microbubbles should be destroyed, therefore this distribution marks their metabolism (see references for these values).

In all of these instances, spleen and liver uptake are among the highest (see **Table 3.1**), particularly at 60-90 minutes post-injection. In the liver, microbubbles are phagocytosed by Kupffer cells[3, 6] corroborating with the elevated radiolabel accumulation observed. It has been postulated that large microbubbles (1-10 μm) may cause the elevated spleen signal owing to the small diameter of channels in this organ (200-500 nm).[8] However, it has also been commented that in the spleen microbubbles are taken up by macrophages, resulting in the observed signal.[3] For comparison, small non-targeted radiolabels accumulate in the kidneys and bladder.[3, 10] Another interesting area of accumulation is the lungs, although the reason for this has not been sufficiently elucidated.

In both of the targeting instances using antibodies, radiolabelling was performed in the presence of the antibody, therefore addition of ^{18}F to the antibody may affect the targeting efficiency.[9] These both showed slightly elevated uptake in tumorous areas when compared to surrounding tissue, however this was dramatically lower than uptake in other regions. This limits the areas that can be imaged as high background signal could mask tumour uptake.

Although these studies have paved the way for microbubble radiolabelling, there are clearly many areas that have been left unexplored. The advantages of phospholipid microbubbles have been discussed in Chapter 1, with the majority such PET studies using commercially available MicroMarker microbubbles which make use of the streptavidin-biotin interaction. Although this is useful in preclinical work, adverse side effects preclude its translation into the clinic (see Chapter 2). The advantages of PET over SPECT have also been mentioned in Chapter 1, with generator-produced isotopes being of key importance in the wide availability of tracers; this led to the selection of ^{68}Ga for radiolabelling experiments.

3.1.2 ^{68}Ga Microbubble Radiolabelling Methods

Although radiolabelling of microbubbles is relatively understudied, work with liposomes has been performed extensively. This has been studied with molecules containing ^{18}F,[11, 12] ^{15}O[13] and ^{125}I,[14] and with chelated metals such as ^{64}Cu,[15, 16] ^{99m}Tc,[17, 18] ^{67}Ga,[19] ^{111}In[14, 20] and ^{89}Zr[21]

for PET or SPECT. This labelling can be achieved by attachment to phospholipids or by encapsulation in the aqueous interior, the latter of which cannot be applied in microbubble labelling. The increased stability of liposomes means that only some of the radiolabelling methods are transferrable.

For use with metals such as ^{64}Cu,[16] ^{111}In[20] and Gd[5, 22] phospholipids have been modified with DOTA. This is also known to be effective for gallium chelation and has already been used in microbubble formation (dual-modal MRI-ultrasound).[5] This makes it an ideal choice for use in ^{68}Ga-labelled microbubbles. The majority of studies used the phospholipid DSPE-PEG$_{2000}$-DOTA however the PEG chain has been omitted on occasion.[22]

The only radiolabelling methodology suitable for microbubble labelling using this phospholipid is gallium chelation followed by microbubble formation as DOTA does not effectively chelate Ga^{3+} unless heated under conditions that would destroy microbubbles (see Chapter 1 **Table 1.4**).[23] This has been undertaken with ^{18}F-labelled phospholipid microbubbles (discussed above),[8] however the longer half-life of ^{18}F will make this manipulation easier.[24] Owing to this issue, it was decided to explore alternative methods for radiolabelling microbubbles.

The reaction of prosthetic radiolabelled groups onto microbubbles has been achieved for both ^{18}F and ^{99m}Tc using streptavidin and biotin interactions. Thiol-maleimide chemistry has been used as a replacement for this reaction in the conjugation of peptides and ^{64}Cu chelators to liposomes,[15] however the shorter half-life of ^{68}Ga is ill-matched to this reaction time. Recent literature has shown that the reaction between TCO and tetrazine (shown in **Figure 3.1**) can be used as a biocompatible substitute, with excellent reaction kinetics and selectivity under mild conditions.[25, 26] This reaction has also been used to pre-target microbubbles, highlighting its compatibility with these contrast agents.[27] The attachment of tetrazine to DOTA and chelation with ^{68}Ga has been shown to be effective,[25, 28] with subsequent radiolabelling of TCO-modified antibodies.[25] Therefore, the use of this ligand with microbubbles functionalised with TCO should allow for radiolabelling of preformed microbubbles.

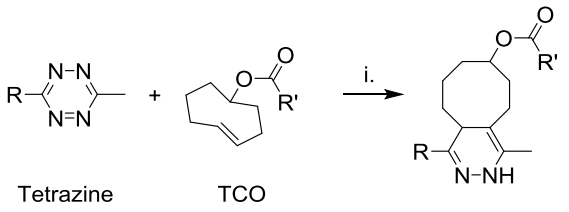


Figure 3.1: Reaction between tetrazine and TCO. i. RT or 37 ^{o}C, minutes.

An alternative chelator, NOTA, has been shown to chelate ^{68}Ga under much milder conditions than DOTA and to form more stable complexes (see Chapter 1 **Table 1.4**).[23] This macrocycle has not been used in lipid-containing molecules as DOTA has, however it could be used to replace DOTA in the methodologies discussed. The improved chelation properties could also allow for reaction directly onto the microbubble surface.

3.2.3 Aims

The aim of this chapter is to synthesise radiolabelled microbubbles using ^{68}Ga in order to allow for whole body monitoring of microbubbles using an easily accessible isotope. The combination of this with the cRGDfK-containing phospholipid **2.1** will also allow for targeting of these microbubbles, with the hope of improving upon the accumulation found in literature.

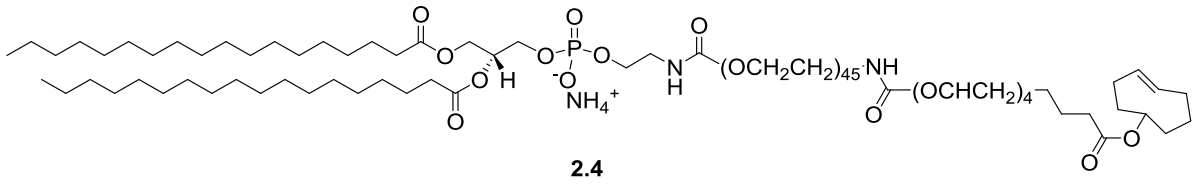
Literature has demonstrated the effective radiolabelling of antibodies using the reaction between a ^{68}Ga-labelled DOTA-tetrazine molecule and a TCO-modified antibody. Initial work aimed to use this reaction to radiolabel microbubbles containing TCO-functionalised phospholipids. Literature has used the phospholipid DSPE-PEG$_{2000}$-DOTA in the modification of microbubbles, however this was not initially employed as this method requires microbubble synthesis post-labelling. There is also the possibility to use alternative chelators such as NOTA which are less studied in this field but are known to react more effectively and form more stable complexes than DOTA.

3.2 Radiolabelling of Microbubbles Using the TCO-Tetrazine Reaction

Initial work involved the synthesis and radiolabelling of DOTA-tetrazine and subsequent reaction with TCO-functionalised microbubbles.

3.2.1 Characterisation of TCO-Containing Microbubbles

The synthesis of TCO-bearing phospholipid DSPE-PEG$_{2000}$-TCO **2.4** has been described in Chapter 2, however no other work or characterisation was performed on this phospholipid. In order to determine the viability of this approach, these microbubbles were characterised before any further work was carried out. The structure of this phospholipid is shown in **Figure 3.2**.



2.4

Figure 3.2: The structure of phospholipid DSPE-PEG_{2000}-TCO **2.4.**

3.2.1.1 In Vitro Characterisation

The selection of cell lines and all *in vitro* experiments were performed by Marta Braga, Dept. of Surgery and Cancer, Imperial College London, assisted by Javier Hernández-Gil, Dept. of Chemistry, Imperial College London. These results may be discussed in more detail in the thesis of Marta Braga (currently not submitted).[29]

In order to determine how addition of **2.4** affects microbubble targeting, *in vitro* work was performed. As discussed previously, the microbubble formulation allows for 10 mol% PEG-containing phospholipid to be used. In order to radiolabel and target these microbubbles, two PEG-containing phospholipids must be included: DSPE-PEG_{2000}-cRGDfK **2.1** and DSPE-PEG_{2000}-TCO **2.4**. It was initially decided to use 5 mol% of each. As radiolabelling requires few reactions for sufficient activity, this should be adequate for PET imaging. This formulation produced microbubbles on average of 1.86 μm at a concentration of 1.69 x 10^9 MB/ mL (n=3, see Appendix **Table A.3**), similar to unmodified microbubbles (see Appendix **Table A.1**). The effect of the reduction in targeting lipid was determined *in vitro*, as shown in **Figure 3.3**.

As can be seen from **Figure 3.3**, no unspecific binding was observed for microbubbles containing 5 mol% **2.4**, implying that the TCO does not interact with the cells. Those microbubbles containing 5 mol% **2.1** and 5 mol% **2.4** showed good binding to both cell lines, therefore the reduction in targeting groups has not affected this interaction. Similar trends were observed in binding of these microbubbles to those discussed in Chapter 2.

Washing and blocking experiments were also performed using these microbubble formulations, with the results shown in the Appendix (**Figure A.27**). Washing showed a decrease in microbubble concentration in both cell lines, however microbubbles were retained to a greater extent in the M21 cell line. This is expected as this has higher $\alpha_v\beta_3$ integrin expression. Blocking experiments showed reduced binding to the M21 cell line but were not as successful in the MDA-MB-231 cell line, with microbubble binding despite

linear RGD being administered. This could be due to the protocols used or due to the greater affinity of the cyclic RGD for the receptors.

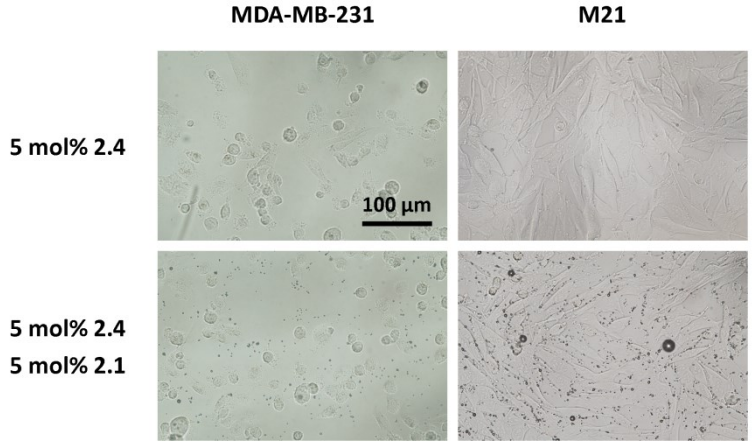


Figure 3.3: *In vitro* work performed with microbubbles containing 5 mol% phospholipid **2.4** (top) and 5 mol% phospholipid **2.1** and 5 % phospholipid **2.4** (bottom) on MDA-MB-231 (left) and M21 (right) cell lines using the incubation protocol described in Chapter 2. The same microbubble solution was used in all experiments with an initial concentration of 1.08 x 10^9 MB/ mL. Images obtained by Marta Braga.[29]

These experiments prove that the addition of TCO to the microbubble formulation and the reduction of cRGDfK do not significantly affect the microbubble properties and targeting. As a result, this route was pursued and appropriate gallium chelators synthesised.

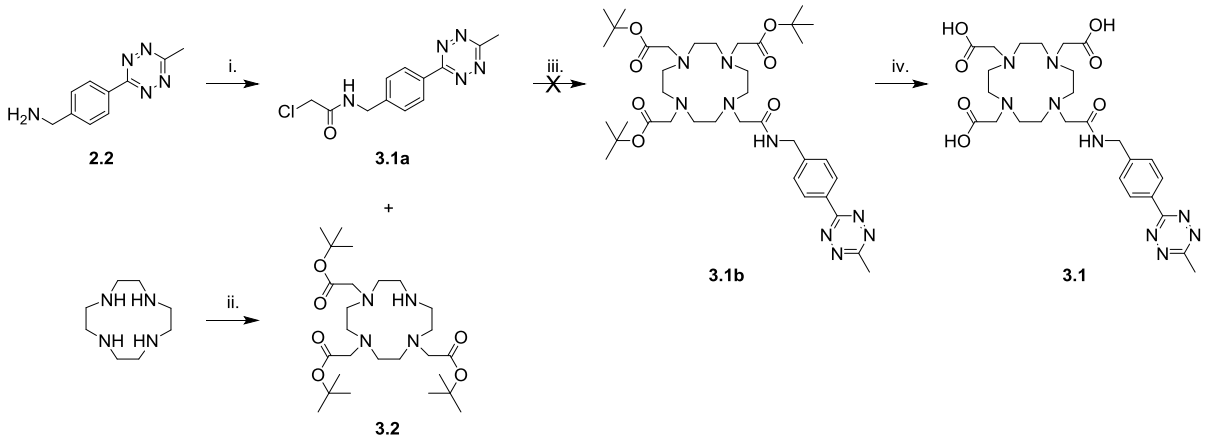
3.2.2 Synthesis and Characterisation of Tetrazine-Containing Ga Chelators

Tetrazine-bearing gallium chelators were required in order to react with phospholipid **2.4**. Two such chelators have been discussed in literature, based upon a DO3A[28] and a DOTAGA[25] scaffold. Both molecules were synthesised here in order to determine the best option for microbubble radiolabelling.

3.2.2.1 DO3A-Tetrazine

Although DO3A-tetrazine **3.1** has been synthesised in literature, this synthesis used expensive commercially available DOTA-NHS. It was decided here to synthesise all reagents, thus an alternative route was utilised.

Chloroacetyl chloride is a versatile bifunctional reagent used extensively in organic synthesis.[30] This reagent has been used for DOTA functionalisation, with initial modification of the arm and subsequent reaction with tri-*tert*-butyl DO3A (^{t}Bu-DO3A) **3.2**.[31, 32] The synthetic route developed using this reagent is shown in **Scheme 3.1**.



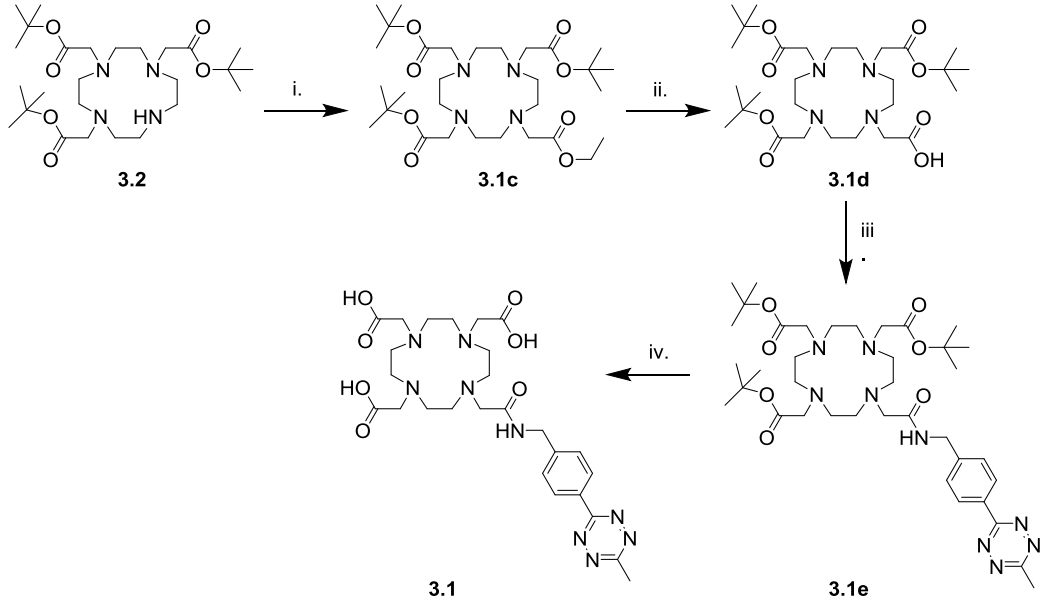
Scheme 3.1: Attempted synthesis of DO3A-tetrazine **3.1**. i. chloroacetyl chloride, NEt_3, DCM, 1 h, 0 ^oC, 53 % yield; ii. *tert*-butyl bromoacetate, NaOAc, DMA, 24 h, RT, 84 % yield; iii. DO3A, K_2CO_3, CH_3CN, 24 h, 82 ^oC, unsuccessful; iv. TFA, DCM, 16 h, RT, not performed.

The synthesis of **3.1a** proceeded as expected under the stated conditions in acceptable yields, with the identity and purity confirmed by NMR and mass spectrometry (ES+). The reaction to form **3.1b** was performed according to literature in acetonitrile under reflux with K_2CO_3. This is typically performed for > 24 h, however upon commencing the reaction, the bright pink solution resulting from the colour of tetrazine rapidly (within minutes) changed to orange, implying degradation of the tetrazine. After reaction, the crude material was analysed, with no aromatic tetrazine peaks observed in the NMR and no product in the mass spectrum. Purification was performed, however no tetrazine was recovered.

It has been postulated that tetrazines could react with acetonitrile,[28] therefore the solvent was determined to be the problem. Similar reactions were performed in chloroform, ethyl acetate and DMF. In the former two solvents little or no product was obtained, likely due to the lower reaction temperatures that can be achieved. The reaction in DMF was performed at 82 ^oC to mimic that in acetonitrile, however again an orange product was obtained within 5 minutes.

It was also attempted to react tetrazine with acetonitrile, both at reflux and at room temperature. This was performed for 3 days, after which no change was observed. This implies that the solvent is not the cause of the unwanted reaction, as confirmed by the same degradation reaction occurring in DMF. In an alternative synthetic route (not discussed), it was attempted to deprotect an ester using 1 M NaOH in CH_3OH (1:1 v/v) at room temperature in the presence of tetrazine. This resulted in the same colour change, implying that tetrazine is sensitive to basic conditions.

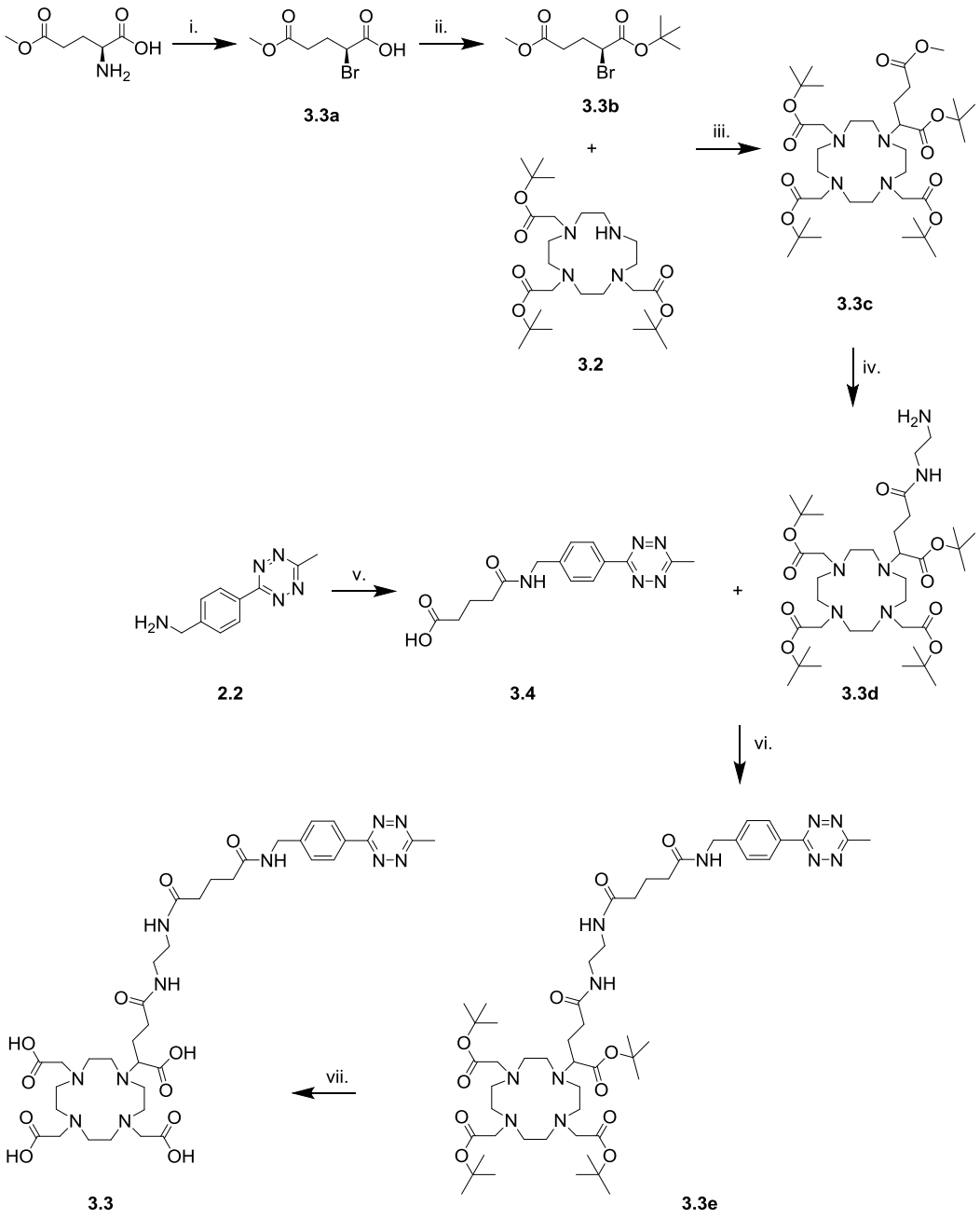
Due to these complications, an alternative synthetic route was developed, as shown in **Scheme 3.2**. This involved the synthesis of tri-protected DO3A-COOH **3.1d**, followed by peptide coupling between this and tetrazine **2.2**. This route proved effective, if low yielding in latter stages, with the identity and purity of all samples confirmed by NMR and mass spectrometry (ES+). The low yield in the final stage can be attributed to the use of LCMS for purification, which typically loses a significant proportion of product to waste at the expense of high purity. As only small quantities are required for radiolabelling applications, this was deemed an acceptable compromise.



Scheme 3.2: Alternative synthesis of DO3A-tetrazine **3.1**. i. ethyl bromoacetate, K_2CO_3, CH_3CN, 24 h, 82 ^oC, 77 % yield; ii. 1 M NaOH, MeOH, 48 h, RT, 78 % yield; iii. **2.2**, HBTU, NEt_3, DCM, 48 h, RT, 55 % yield; iv. TFA, DCM, 8 h, RT, 20 % yield.

3.2.2.2 DOTAGA-Tetrazine

As with **3.1**, the synthesis of **3.3** has been achieved in literature using commercially available DOTAGA-NH_2,[25] therefore an alternative synthetic route was developed, as shown in **Scheme 3.3**. This successfully produced **3.3** in moderate yields suitable for radiochemistry. The purity and identity of all intermediates and products were confirmed by mass spectrometry (ES+) and NMR.



Scheme 3.3: Synthesis of DOTAGA-tetrazine **3.3**. i. 2 M HBr, NaBr, $NaNO_2$, H_2SO_4, 4 h, 0 ^oC, 69 % yield; ii. *tert*-butyl acetate, 70 % perchloric acid, N_2, 24 h, RT, 51 % yield; iii. K_2CO_3, CH_3CN, 24 h, 82 ^oC, 61 % yield; iv. ethylenediamine, 72 h, RT, 73 % yield; v. glutaric anhydride, THF, 4 h, 70 ^oC, 25 % yield; vi. HBTU, NEt_3, DCM, 48 h, RT, 32 % yield; vii. TFA, DCM, 16 h, RT, 31 % yield.

3.2.3 TCO-Tetrazine Reactivity

In order to determine whether this route would work for radiolabelling microbubbles, the reactivity of TCO with molecules **3.1** and **3.3** was monitored, following which the reaction of phospholipid **2.4** with these molecules was performed.

The monitoring of this reaction was performed using the characteristic tetrazine absorbance peak at ~520 nm which disappears upon reaction with dienophiles.[26, 33] Initial concentration trials on tetrazine **3.4** showed a concentration of 0.4-1 mM and gave absorbance maximum high enough to observe the change upon reaction without requiring excessive amounts of TCO. This graph is shown in **Figure 3.4**, which can also be used to calibrate subsequent solutions. Measurements taken at 5 and 10 mM displayed distorted peak shapes due to detector saturation (see Appendix **Figure A.21**) and were therefore not included.

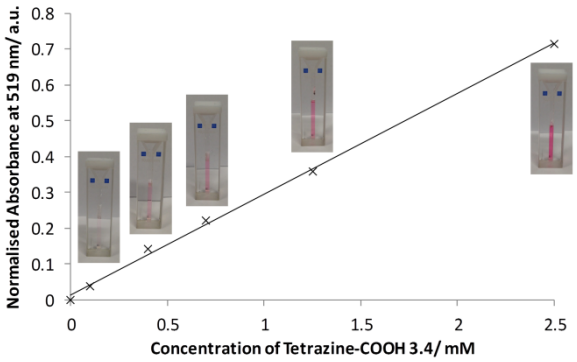


Figure 3.4: UV-vis. absorption spectra showing the linear correlation between the concentration of tetrazine-COOH **3.4** and the absorbance at 519 nm. Gradient of the trend line = 0.2813.

Reactions were then performed between DO3A-tetrazine **3.1** or DOTAGA-tetrazine **3.3** and TCO-PEG_4 (this was purchased as TCO-PEG_4-NHS however this was hydrolysed in the buffer used for the measurements). TCO-PEG_4 was added at a concentration of 8 mol/ dm^3 in 5 µL aliquots in order to minimise the dilution effects of addition and incubated for 1 min prior to measurement. In order to ensure that this was not causing the reduction in signal observed, experiments adding the same volume of PBS alone were performed. These results are shown in **Figure 3.5**. As can be seen, after the addition of 1 equivalent of TCO in both instances, the concentration of tetrazine has dramatically decreased but does not reach the baseline, indicating that the reaction is not complete. As this reaction is stoichiometrically 1:1, it implies that the efficiency is below 100 % (16 % and 9 % remaining after the addition of 1 eq. and 1.2 eq. respectively for **3.1** and 15 % after 1.3 eq. in **3.3**). After the addition of 1.5/2 equivalents, the value falls to the baseline and flattens out, indicating completion of the reaction. This is promising as it shows the reactivity of these materials.

The lower efficiency of this reaction could be due to degradation of the TCO reagent into the less reactive *cis* isomer.[34] This transformation can be induced thermally,[35] by exposure to light[36] or by storage in serum with copper-containing proteins.[37]

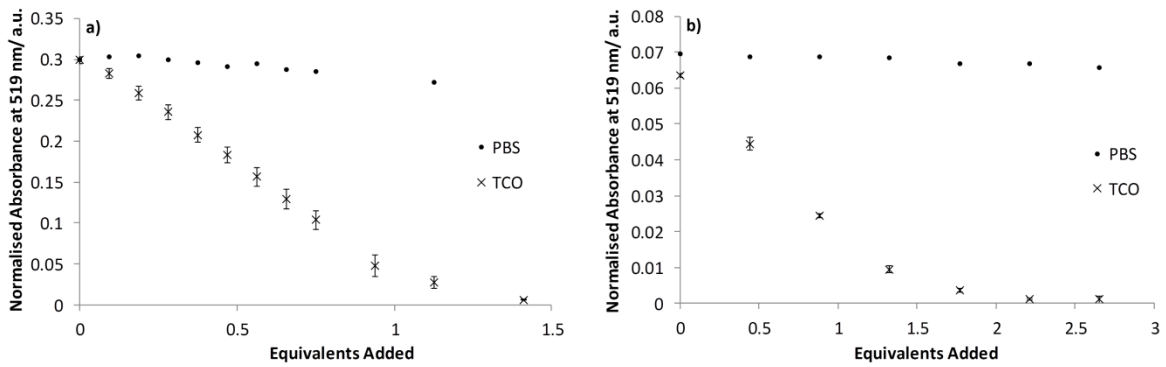


Figure 3.5: UV-vis. tetrazine absorption at 519 nm upon the addition of TCO-PEG$_4$. All measurements were taken in PBS pH 7.6 by gradual addition of an 8 M TCO solution, with control experiments performed by addition of the same volume of PBS. a) DO3A-tetrazine **3.1** 1.06 mM concentration (determined from **Figure 3.4**), n=3; b) DOTAGA-tetrazine **3.3** 0.23 mM concentration (determined from **Figure 3.4**), n=3.

These reactions were then performed with phospholipid **2.4**. This phospholipid was found to cause the solution to become turbid; this effect became more noticeable at higher concentrations, resulting in increased background signal in the UV-vis. spectra. This can be clearly observed in **Figure 3.6** for reaction with DOTAGA-tetrazine **3.3**. Although visually the peak at 519 nm is disappearing with increasing amounts of **2.4**, the absolute intensity at this wavelength is not always changed due to the increasing background. The same features were observed for the reaction of DOTA-tetrazine **3.1** and can be observed in **Figure A.22** (see Appendix).

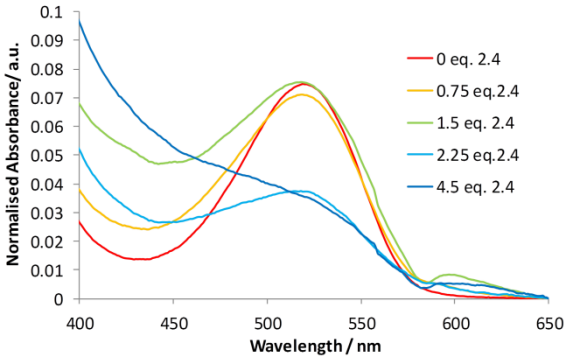


Figure 3.6: UV-vis. absorption spectra of DOTAGA-tetrazine **3.3** upon the addition of DSPE-PEG$_{2000}$-TCO **2.4**. All measurements were taken in PBS pH 7.6 by gradual addition to the dry phospholipid.

Due to the problems encountered with characterisation of the phospholipid reaction using UV-vis. absorption, it was decided to attempt characterisation by mass spectrometry. This method is not quantitative, however it can determine whether the product is being formed.

In UPC^2, the chromatograms show the appearance of an additional peak after reaction with both DO3A-tetrazine **3.1** (see Appendix **Figure A.14**) and DOTAGA-tetrazine **3.3** (**Figure 3.7**). This analysis was performed on the same samples used for the UV-vis. analysis described above, but 24 hours after the reaction was performed. Integration over the earlier peaks (~3.8 min) shows the same mass distribution observed for phospholipid **2.4**. The mass' observed in the later peak (~4.8 min) correlates well with the mass expected after addition of **3.1**, however little could be observed for **3.3**, likely due to the low concentrations of lipid. The reaction was repeated (with 2 equivalents of **3.3**) and integration of the product peak produced a weak spectrum at the correct mass for the desired product. Important regions of these mass spectra are shown in **Figure 3.8**.

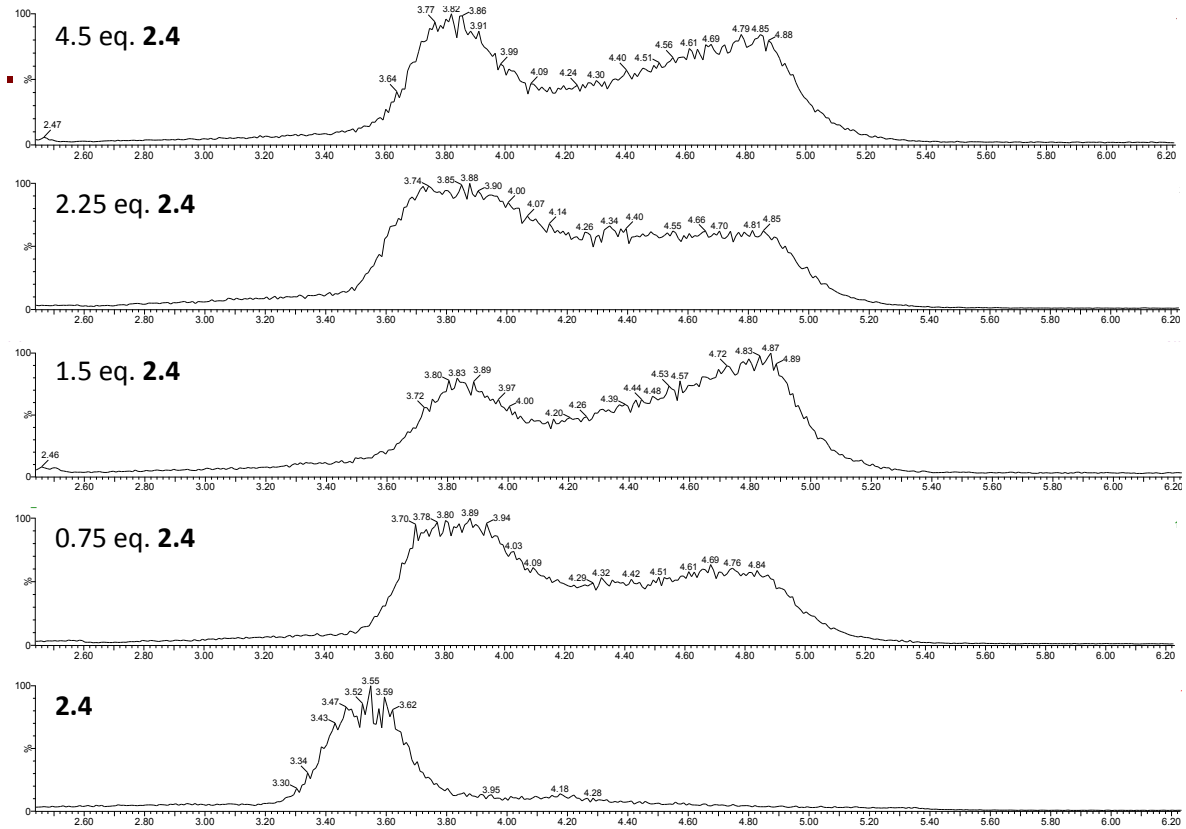


Figure 3.7: UPC^2 MS(ES+) chromatograms upon reaction of DSPE-PEG$_{2000}$-TCO **2.4** with DOTAGA-tetrazine **3.3**. Bottom: unreacted **2.4**. Ascending: Addition of 0.75, 1.5, 2.25 and 4.5 equivalents of **2.4** to a solution of **3.3**. Retention times of the two peaks are ~3.80 min for the unreacted phospholipid (~3.55 min in the pure lipid) and ~4.80 min after reaction.

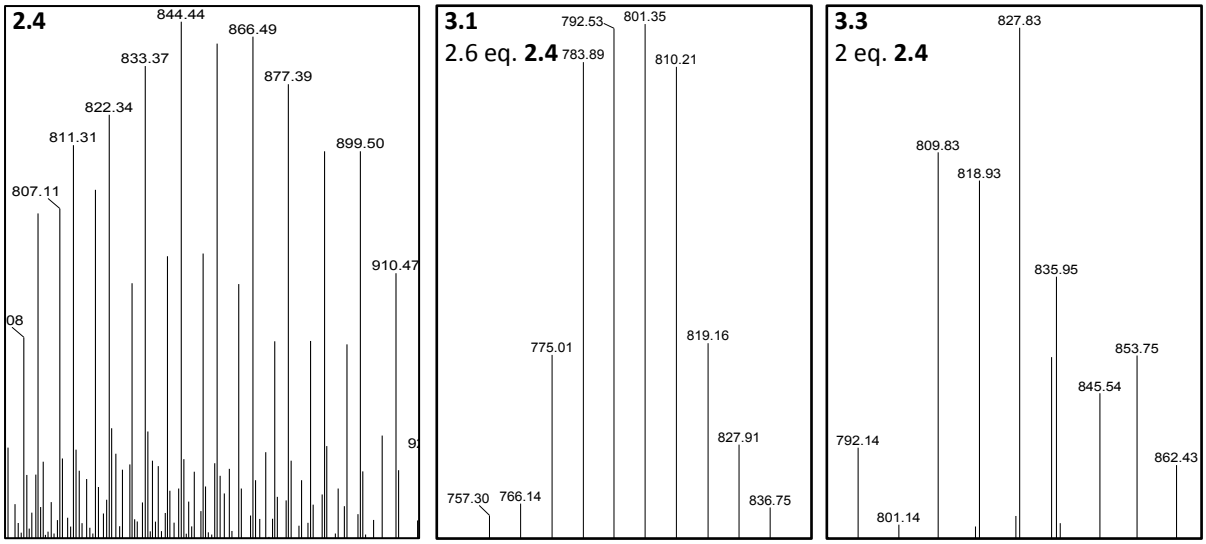


Figure 3.8: Section of MS(ES+) spectra integrated over the product peaks observed in the UPC^2 chromatograms (**Figure 3.7** and **A.14**). Left to right: unreacted **2.4,** reaction with **3.1** and reaction with **3.3**. Major distributions 4+ for the former and 5+ in the latter two.

Interestingly, in the chromatograms obtained over the course of these reactions the relative intensity of the product peak compared to the starting material **2.4** peak increases with the amount of **2.4** added. This is contrary to the expected result, where all of **2.4** will react when there is a lot of tetrazine present. This indicates that reaction of the TCO is hindered by the lipid, likely due to folding of the PEG chain. This means that relatively large concentrations of the lipid in comparison to the radiolabelled fragment will be required for reaction, contrary to what has been observed in literature in analogous radiolabelling experiments using the thiol-maleimide reaction.[15] This is unlikely to be a problem for radiochemistry, where the radiolabel is at much lower concentrations than the other reagents.

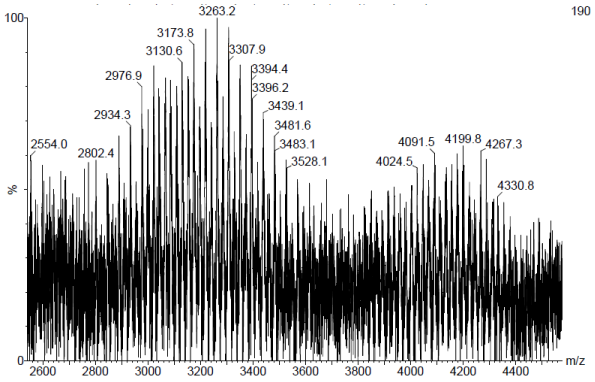


Figure 3.9: MALDI spectrum of DSPE-PEG$_{2000}$-DOTAGA after reaction between **2.4** and **3.3**.

In order to confirm the appearance of product in the reaction with **3.3**, the sample was also analysed using MALDI. This result, shown in **Figure 3.9**, clearly shows the appearance of an additional peak distribution at the mass expected for successful reaction (~ 4190. 8 m/z). Unreacted **2.4** is also observed (~ 3263.2 m/z), as expected from UPC^2 analysis. This confirms that this reaction is occurring at acceptable stoichiometric ratios.

3.2.4 Radiolabelling

In order to radiolabel microbubbles, protocols for radiolabelling of **3.1** and **3.3** were developed. Due to a change in generator type during the course of this project, this was performed for two different models producing different gallium activities for **3.3**. Initial work focused upon the radiolabelling of **3.3**, which was later employed in the labelling of **3.1**.

Labelling using both generator types was performed using two elution methods: elution in HCl (0.1 M or 1 M) and acidified saline (NaCl/ HCl). The former method was automated to collect only those fractions containing the highest content of ^{68}Ga in order to limit other metal impurities.[38] Cartridge purification after complexation removes unreacted ^{68}Ga and ^{68}Ge breakthrough, which does not complex to these chelators.[39] The final formulation in ethanol is acceptable, provided it is diluted to < 10 % in the injected formulation. In the latter, ^{68}Ga is trapped on a resin and eluted separately to impurities, concentrating the ^{68}Ga in the process. NaCl/HCl was chosen for this purpose in order to eliminate organic solvents, allowing for direct use of the labelled compound without purification (if radiolabel incorporation is sufficiently efficient).[40]

Conversion was determined using the relative areas of free gallium and product regions of interest (ROI) in crude HPLC mixtures. Radiochemical yields (RCY) were non-decay-corrected (n.d.c) and calculated relative to the amount of activity added at the beginning of the reaction.

3.2.4.1 DOTAGA-Tetrazine

When radiolabelling is performed for a given molecule, the temperature, reaction time, pH and labelling media must be optimised.[41] As this molecule has been labelled previously, this provided initial reaction conditions, although some experimentation was required.[25]

Initial optimisation on the Eckert & Ziegler generator showed reaction at pH 4.5 to result in reproducibly high radiolabel incorporation when the HCl elute was added directly to the reaction solution, as shown in **Table 3.2**. Reaction using NaCl/ HCl resulted in product

formation, however conversion and n.d.c RCYs were on average poorer (**Table 3.3**). As can be seen, these reactions can be variable even under the same conditions. It was decided that this could be due to subtle variations in the pH (measured using pH strips) and therefore a pH meter was purchased to minimise these effects. The age of the buffer could also cause discrepancies, therefore it was decided that new solutions should be used (not stored for over 1 week).

Table 3.2: A selection of radiolabelling experiments performed on **3.3** using $^{68}GaCl_3$ produced in 0.1 M HCl on an Eckert & Ziegler Generator.

Buffer pH	Reaction pH	Conversion/ %	RCY (n.d.c)/ %
4.5	4.5	87	33
6	4.5	97	46
6	4.5	99	49
6	4.5	76	45
6	5	71	42

All reactions performed at 90 °C for 10 min using 25 μg of **3.3**, 2 mL $^{68}GaCl_3$ solution in 0.1 M HCl and 2 mL 0.2 M NaOAc buffer at the specified pH.

Table 3.3: A selection of radiolabelling experiments performed on **3.3** using $^{68}GaCl_3$ produced in NaCl/ HCl on an Eckert & Ziegler Generator.

Reaction pH	Conversion/ %	RCY (n.d.c)/ %[b]
4.5[a]	68	-
4.5	96	-
4.5	36	13
4.5	87	46
4.5	52	20

All reactions performed at 90 °C for 10 min using 25 μg of **3.3**, 0.5 mL $^{68}GaCl_3$ solution in NaCl/ HCl, 0.35 mL 1 M pH 4.5 NaOAc buffer and 0.3 mL H_2O (unless otherwise stated). [a]Reaction using 12.5 μg of **3.3**, half the volume of $^{68}GaCl_3$ and half the quantity of all solvents.

While radiolabelling using the NaCl/HCl elute remained similar between the two generators, the difference in HCl concentration when eluted directly meant that the elute from the iThemba generator required partial neutralisation prior to use. This higher HCl concentration

also required the elute to be diluted prior to addition to the cartridge for the NaCl/ HCl elution.

Neutralisation of this HCl elute was attempted for individual reaction solutions using 1 M and 0.6 M HCl to elute the generator (it was found that the buffers appropriate for this reaction could not successfully modify such strong acid to an acceptable reaction pH) and to the stock eluent prior to use. The latter method was found to result in more reproducible reaction conditions, however in both instances the reactions were low yielding, as shown in **Table 3.4**. This is surprising considering the results shown in **Table 3.2** and could be due to the higher salt concentration present in these reactions.

Table 3.4: A selection of radiolabelling experiments performed on **3.3** using $^{68}GaCl_3$ produced in 1 M or 0.6 M HCl on an iThemba Generator and neutralised for each reaction (post) or in the stock solution (pre) before heating.

Neutralisation	Volume/ mL	Reaction pH	Conversion/ %	RCY (n.d.c)/ %
Post	2[a]	4.5	14	3
	2.5	4.5	29	9
Pre	1.5	4.5	32	13
	1.5	4.5	38	17
Pre 0.6 M	2.8	4	76	-
	2.8	5	13	-
	2.8	6	4	-

All reactions performed at 90 ^{o}C for 10 min using 25 µg of **3.3** neutralised using 2 M NaOAc and dissolved in 0.2 M pH 4.5 NaOAc buffer. [a]Reaction performed with half the amount of **3.3**

In this instance, the use of the NaCl/ HCl elution proved much more effective due to the increased reproducibility between elutions and between generators, as demonstrated in **Table 3.5**. It was found that the optimal conditions used 0.5 mL of the ^{68}Ga elute in NaCl/ HCl, 0.75 mL 0.2 M pH 5 NaOAc buffer and 25 µg **3.3**, resulting in a reaction pH between 4.4 and 4.6. This was heated to 90 ^{o}C for 10 minutes, resulting in 93-97 % incorporation of the radiolabel. After purification, this resulted in a RCY between 35-47 %. Although not as high as quoted in literature, this value remains acceptable.

Table 3.5: A selection of radiolabelling experiments performed on **3.3** using $^{68}GaCl_3$ produced in NaCl/ HCl on an iThemba Generator.

^{68}Ga Vol/ mL	Buffer pH	Buffer Vol/ mL	Conversion/ %	RCY (n.d.c)/ %
0.1	4.5	1	25	-
0.1	4.5	1	19	-
0.5	5	0.75	93	43
0.5	5	0.75	97	35
0.5	5	0.75	96	47

All reactions performed at 90 ^{o}C for 10 min using 25 µg of **3.3** and dissolved in 0.2 M pH 4.5 NaOAc buffer with a final reaction pH of 4.4-4.6.

Figure 3.10a demonstrates the appearance of the HPLC traces for this compound. Although the UV chromatograms display noise, a small shift in retention time can be observed upon complexation, with little residual Ga in the crude mixture. After purification, no free ^{68}Ga is observed (**Figure 3.10b**).

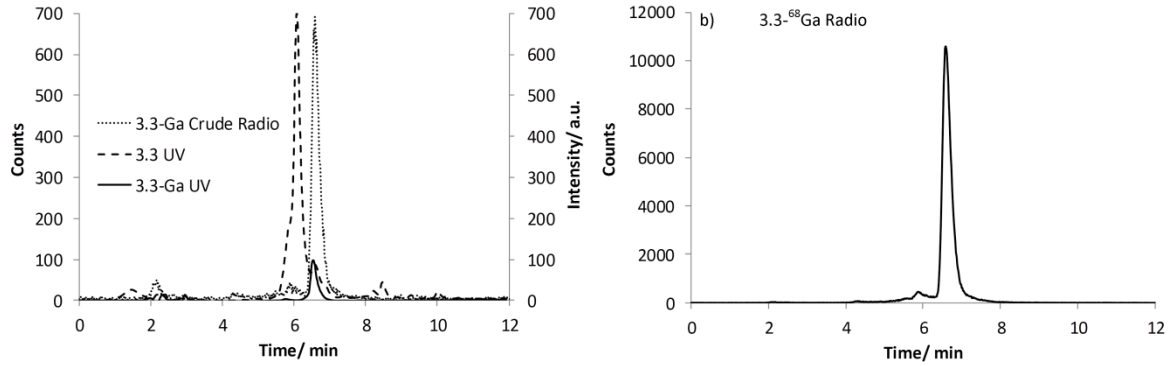


Figure 3.10: HPLC chromatograms showing the radiolabelling of **3.3** to form **3.3-^{68}Ga**. a) Chromatograms showing the retention times of **3.3** and **3.3-^{68}Ga** upon UV detection (right axis) and the corresponding radio chromatogram of the crude reaction mixture (left axis); b) radio chromatogram of purified **3.3-^{68}Ga**. UV peak expected at slightly earlier retention time than radio due to detectors set up.

3.2.4.2 DO3A-Tetrazine

This molecule was found to radiolabel effectively under conditions analogous to those used for DOTAGA-tetrazine **3.3** using the iThemba generator, as shown in **Table 3.6**. 98 % radiolabel incorporation was achieved reproducibly using 0.5 mL of the NaCl/ HCl eluent, following which the reaction solution was buffered to pH 4.4-4.6 using 750 µL 0.2 M pH 5 NaOAc buffer and heated to 90 ^{o}C for 10 min. According to European Pharmacopeia

legislation, when ^{68}Ga-DOTATOC is prepared for *in vivo* application the radiochemical purity must be ≥ 91 %. However, when this peak area is taken in comparison to the entire chromatogram this incorporation falls to 83-87 %, as such purification was deemed prudent.[41]

Table 3.6: A selection of radiolabelling experiments performed on **3.1** using $^{68}GaCl_3$ produced in NaCl/ HCl (unless otherwise specified) on an iThemba Generator.

^{68}Ga Vol/ mL	Buffer pH	Buffer Vol/ mL	Conversion/ %	RCY (n.d.c)/ %
0.1[a]	4.5	0.9	98	64
0.1	4.5	1	95	-
0.5	5	0.75	98	43
0.5	5	0.75	98	50
0.5	5	0.75	98	38

All reactions performed at 90 °C for 10 min using 25 µg of **3.1** and dissolved in 0.2 M NaOAc buffer at the specified pH with a final reaction pH of 4.4-4.6. [a]Reaction performed using the 1 M HCl elution with twice the amount of **3.1**

These reactions were never performed under time pressure, therefore maximum radiochemical yields could not be calculated. Radiochemical yields of 38-50 % were achieved despite this, with a final activity of 664 µCi. The HPLC traces for the radiolabelled (radio and UV chromatograms) and unlabelled (UV chromatogram) products can be found in **Figure 3.11a**, demonstrating a shift in retention time upon complexation and the high incorporation of ^{68}Ga. The purified sample is shown in **Figure 3.11b**.

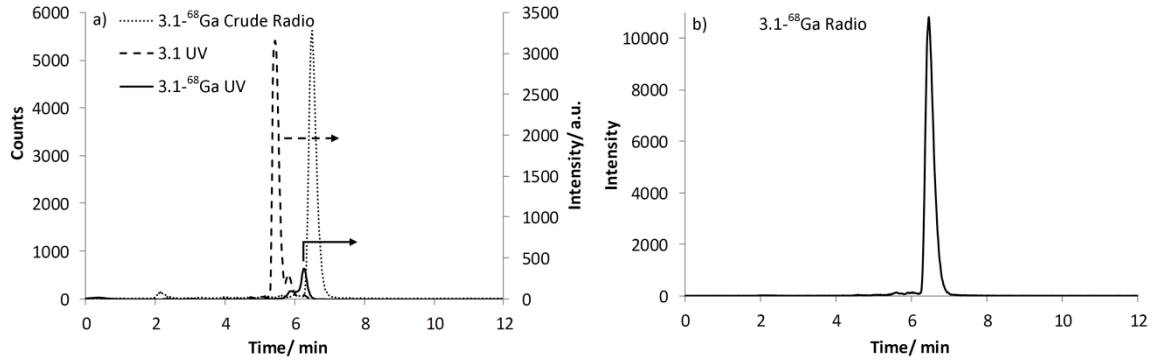


Figure 3.11: HPLC chromatograms showing the radiolabelling of **3.1** to form **3.1-^{68}Ga**. a) Chromatograms showing the retention times of **3.1** and **3.1-^{68}Ga** upon UV detection (right axis) and the corresponding radio chromatogram of the crude reaction mixture (left axis); b) radio chromatogram of purified **3.1-^{68}Ga**. UV peak expected at slightly earlier retention time than radio due to detectors set up.

3.2.4.3 Reaction with Microbubbles

The reaction of **3.1-^{68}Ga** and **3.3-^{68}Ga** was then tested with TCO-containing microbubbles. This was analysed using size-exclusion chromatography (SEC), where small molecules such as **3.1-^{68}Ga** and **3.3-^{68}Ga** are eluted at approximately 10 minutes and large phospholipids around 6 minutes.

Previous reports have used radiometal (^{99m}Tc) chelation followed by reaction with preformed microbubbles. It was found that reaction for 2 h was required to achieve > 98 % yield, however 45 min incubation resulted in 30 % labelling.[10] The longer labelling time is acceptable for this long-lived radioisotope (6 h half-life) however the short ^{68}Ga half-life is better suited to the shorter reaction time.

Initially, the reaction was performed between **3.1-^{68}Ga** as purified in ethanol and the amount of phospholipid **2.4** present in one microbubble vial (136.0 μg) for 45 minutes at ambient temperature. It was found that this resulted in a small shift in HPLC retention time, as can be seen in **Figure 3.12a**.

In order to confirm this reaction, **3.1** and **3.3** were heated to dryness to remove organic solvents and incubated for 45 minutes at room temperature with 408 μg **2.4**, three times the quantity used in a single vial of microbubbles. These solutions were then heated to 90 ^{o}C for 45 minutes to determine whether this increased product formation. As can be seen in **Figures 3.12a** and **3.12b**, there is a shift in the retention time upon reaction, indicating formation of a larger molecule. However this does not shift as far as expected from the UV trace of **2.4**, therefore it is unclear whether this is the desired product. Heating further did not affect the position of the peaks, however it did result in loss of the shoulder observed in both reactions. Although the retention time of this shoulder is not identical to that of unreacted **3.1-^{68}Ga** or **3.3-^{68}Ga**, the differences could be caused by marginal differences in HPLC conditions and therefore these shoulders could result from detection of the unreacted radiolabel. As the initial reaction of **3.1-^{68}Ga** with 136 μg of **2.4** overlays well with this shoulder in the latter reaction, it is possible that this reaction was not successful at this lower concentration.

Following this, **3.1-^{68}Ga** and **3.3-^{68}Ga** were reacted with microbubbles containing 5 mol% **2.4** under the same conditions. The analysis showed that no reaction had occurred, even after heating the reaction with **3.1-^{68}Ga** to 90 ^{o}C for 45 min (this may also destroy microbubbles) as shown in **Figures 3.12c** and **3.12d**.

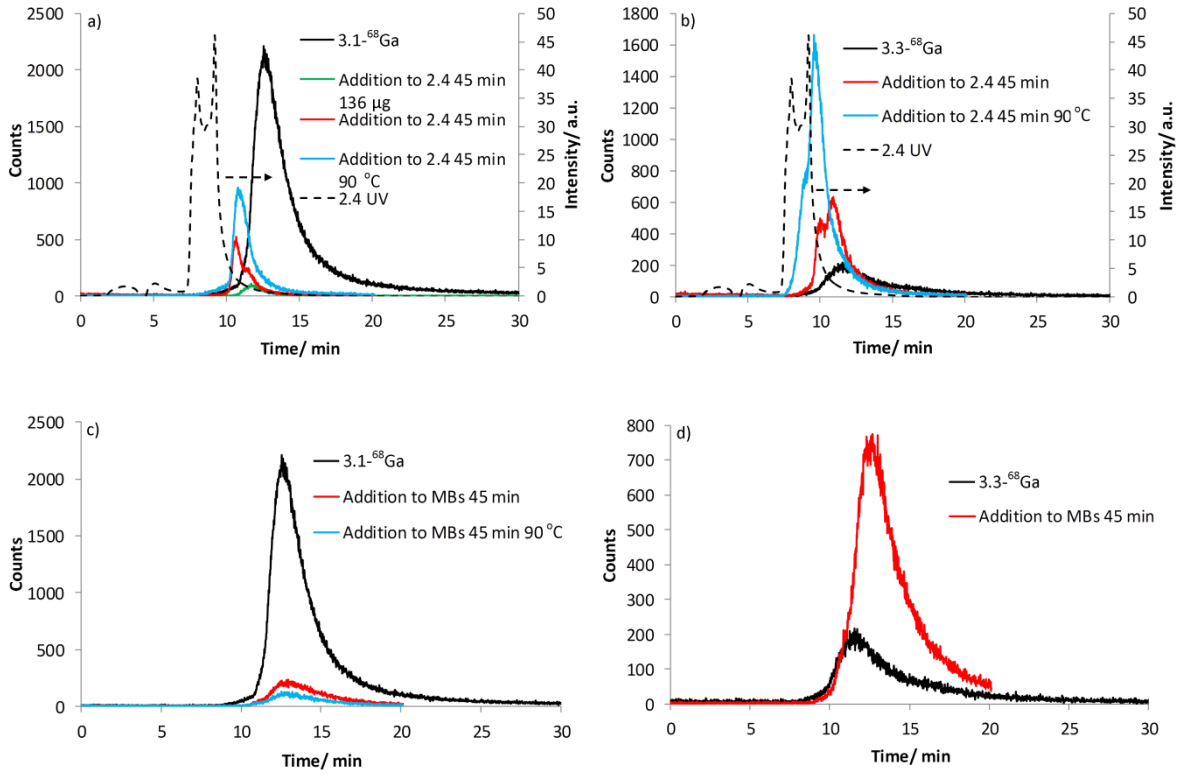


Figure 3.12: HPLC chromatograms showing the reaction of **3.1-^{68}Ga** **3.3-^{68}Ga** with DSPE-PEG$_{2000}$-TCO **2.4** (415 µg unless otherwise stated) and microbubbles containing 5 mol% **2.4**. Reactions were performed at ambient temperature for 45 minutes followed by 45 minutes at 90 °C. HPLC performed using SEC. a) Reaction between **3.1-^{68}Ga** and **2.4**; b) reaction between **3.3-^{68}Ga** and **2.4**; c) reaction between **3.1-^{68}Ga** and microbubbles containing 5 mol% **2.4**; d) reaction between **3.3-^{68}Ga** and microbubbles containing 5 mol% **2.4**.

Although it has been demonstrated that phospholipid **2.4** and molecules **3.1** or **3.3** will react with gallium reagents under normal conditions and in concentrated radiochemical situations, the change in conditions when radiolabelling microbubbles has clearly impacted their reactivity. In literature, low radiolabelling efficiency has been accounted for by entropic effects relating to the small quantities of radiolabel ligand,[10] which can be applied to this instance. After evaluation of these results, it was decided that this approach would not result in effectively radiolabelled microbubbles and therefore another methodology was developed.

3.3 Direct Radiolabelling of Microbubbles

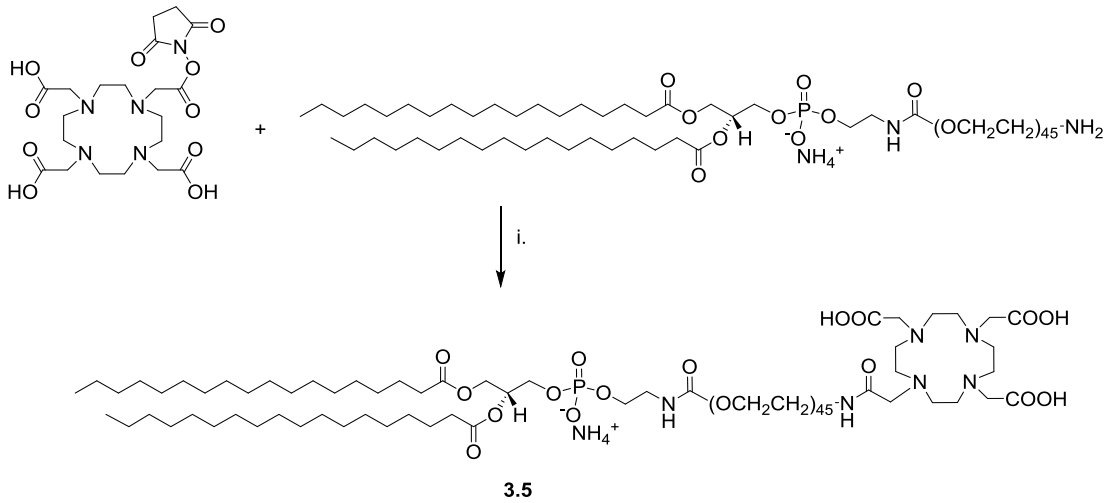
Owing to the lack of reactivity between tetrazine and TCO in microbubble radiolabelling, it was decided to attempt direct radiolabelling of the phospholipids. As discussed above, the phospholipid DSPE-PEG$_{2000}$-DOTA has been used to chelate metals for PET, SPECT and MRI and has been incorporated into microbubbles. It was therefore decided to synthesise this

phospholipid for ^{68}Ga chelation. It was also decided to synthesise the phospholipid DSPE-PEG_{2000}-NOTA for comparison as NOTA is known to chelate gallium more effectively.

3.3.1 Synthesis and Characterisation of Chelating Phospholipids

3.3.1.1 DSPE-PEG_{2000}-DOTA

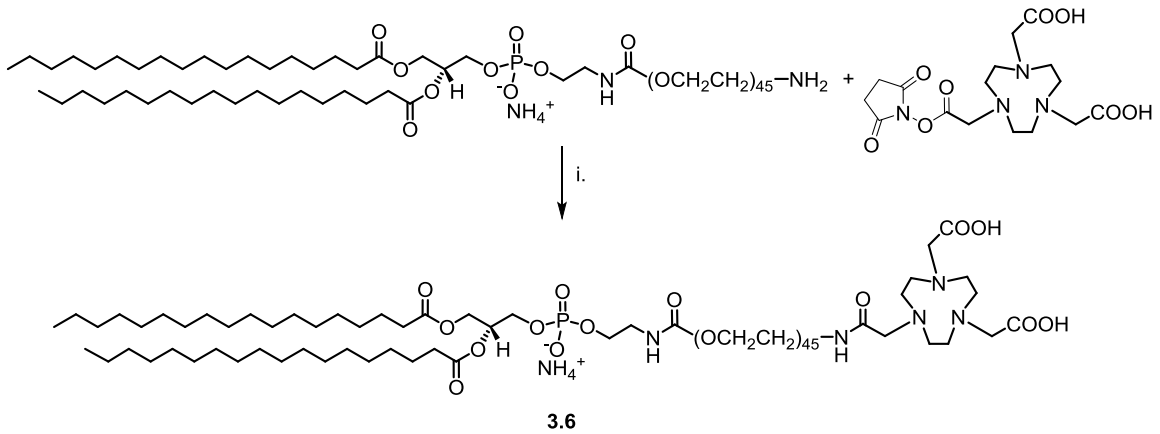
It was decided to develop synthetic protocols analogous to those from literature using the pre-activated, commercially available DO3A-NHS ester and DSPE-PEG_{2000}-NH_2 to synthesise DSPE-PEG_{2000}-DOTA **3.5**.[16, 20] This synthesis is shown in **Scheme 3.4** and was analysed by both MALDI and UPC^2 (see Appendix **Figures A.11** and **A.15**). The MALDI spectra match those observed in literature,[16, 20] and UPC^2 shows a shift in the retention time in addition to an increase in the observed mass.



Scheme 3.4: Synthesis of DSPE-PEG_{2000}-DOTA **3.5**. i. NEt_3, $CHCl_3$, 24 h, RT, 99 % yield.

3.3.1.2 DSPE-PEG_{2000}-NOTA

The synthesis of DSPE-PEG_{2000}-NOTA **3.6** was performed using analogous reagents, as shown in **Scheme 3.5**. This was analysed by UPC^2, confirming product formation (see Appendix **Figure A.16**). This displayed some unreacted phospholipid despite a three times excess of NOTA-NHS. It was decided not to add further NOTA-NHS as purification by dialysis may not be sufficient for the removal of large amounts of unreacted material.



Scheme 3.5: Synthesis of DSPE-PEG_{2000}-NOTA **3.6**. i. NEt_3, $CHCl_3$, 24 h, RT, 82 % yield.

3.3.2 Radiolabelling

As discussed above, the radiolabelling conditions are too harsh to maintain the integrity of the microbubbles,[3] therefore this method required subsequent formation of the microbubbles.

3.3.2.1 DSPE-PEG_{2000}-DOTA

This molecule has not been labelled using ^{68}Ga, therefore a new protocol was developed. When conjugating ^{64}Cu, the activity was eluted in HCl and buffered to the required pH using 0.2 M NaOAc buffer, in an analogous fashion to the protocols developed for the radiolabelling of **3.1** and **3.3**.[16] All reactions were performed using the iThemba generator and due to the increased reproducibility observed for **3.3** radiolabelling, all experiments were performed using the NaCl/ HCl elution.

Test reactions were performed on a small scale using 1 M and 0.2 M buffers and indicted an optimal reaction pH of ~4.3, as shown in **Table 3.7**. It was found that higher concentration buffers resulted in no labelling whereas some product was formed when using 0.2 M buffer, therefore the pH of the buffer as opposed to the strength of the buffer was modified in later reactions in order to attain the correct reaction pH.

In these reactions, an additional radiolabelled peak was observed. This has the same retention time as free DOTA (shown in **Figures 3.13** and **3.14**) therefore it was assumed to be unreacted DOTA that had not been removed during dialysis. This was not expected as DOTA is both water soluble and small enough to permeate through the dialysis membrane (3500-5000 MWCO). This retention could be due to the aggregates formed by lipids in aqueous solution trapping unreacted DOTA. In the attempt to combat this, the lipid was dialysed for 2 weeks prior to use, however the additional peak remained.

Table 3.7: A selection of small scale radiolabelling experiments performed on **3.5** using $^{68}GaCl_3$ produced in NaCl/ HCl on an iThemba Generator.

Buffer pH	Buffer Vol/ mL	^{68}Ga Vol/ mL	p	Crude Result
4[a]	1	0.1	4.46	Some product
4.5	1	0.1	4.26	Some product
4.5	1	0.1	4.31	Some product
4.5 (1 M)	1	0.1	4.14	No product
5	1	0.1	5.03	No product

All reactions performed at 90 ^{o}C for 10 min using 110 μg of **3.5** and dissolved in 1 mL 0.2 M NaOAc buffer (unless otherwise specified) at the specified pH. [a]55 μg of **3.5** used.

Centrifugal filters (3000 MWCO, 15 mL, Amicon Ultra-4 Centrifugal Filters, UFC9003) were subsequently used in the attempt to purify the lipid from free DOTA, with the residue analysed by mass spectrometry and HPLC (**Figure 3.13**). MALDI showed the phospholipid to be both trapped on and having gone through the filter. MS(ES+) did not show any DOTA peaks from the product trapped on the filter, however this could be clearly observed in the filtrate. HPLC did not show any lipid having travelled through the filter, whilst DOTA-like peaks were observed. The final lipid retained some DOTA but the proportion of lipid was improved. Radiolabelling of this additionally purified sample retained the unwanted DOTA peak, but it was hoped that further centrifugal purification after radiolabelling would remove this impurity.

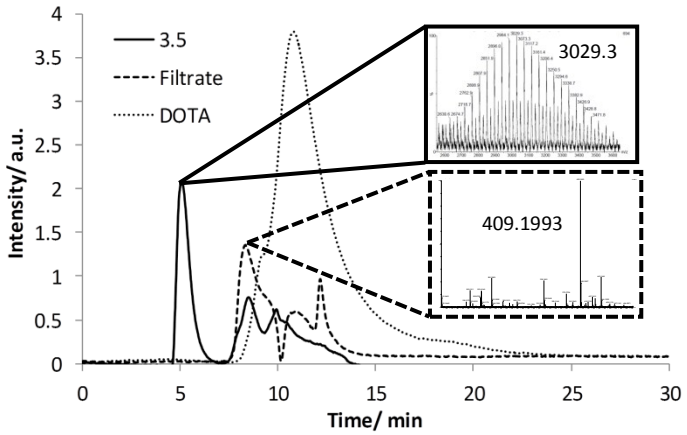


Figure 3.13: HPLC UV chromatograms showing the products from centrifugation of **3.5**. The MALDI spectrum is shown after analysis of the product retained on the filter (mostly **3.5**) and MS(ES+) for the filtrate collected after purification.

It was also difficult to quantify the incorporation efficiency for these reactions by HPLC as free gallium cannot be observed using SEC and the phospholipid could not be observed using other column types (HILIC, C4, C8 and C18 were attempted). The use of centrifugal filters to purify the product can also allow for quantification of radiolabel incorporation as activity trapped on the filter can be considered to be coordinated to **3.5** (filter ratio is the ratio of unincorporated to incorporated activity whilst conversion is the percentage of activity trapped on the filter to that added to the reaction solution). In this instance, 0.5 mL 3000 MWCO filters (Amicon Ultra-0.5 Centrifugal Filters, UFC5003) were selected in order to ensure as much free gallium and DOTA side product were removed as possible (**3.5** ~ 3200, **3.6** ~ 3100 g mol^{-1}), with the volume selected due to the centrifuge available behind lead shielding.

After reaction, samples were placed in 0.5 mL centrifuge filters. The amount of starting material, the centrifugation time and the incorporation of washing steps were all analysed, as shown in **Table 3.8**. It was found that none of these produced pure **3.5-^{68}Ga** as all were contaminated with DOTA-^{68}Ga after centrifugation, however additional starting material did seem to improve conversion and the proportion of activity trapped on the filter (at the expense of specific activity). The centrifugation time did not affect the purity, however the addition of a washing step did improve this somewhat.

Table 3.8: Small scale radiolabelling experiments performed on **3.5** using 2 0.5 mL 3000 MWCO filters for purification and $^{68}GaCl_3$ produced in NaCl/ HCl on an iThemba Generator.

Reaction pH	3.5/ µg	Centrifugation Time/ min	Filter Ratio
4.30	27.5	15 + 15[a]	1:0.2
4.30	55	15 + 15[a]	1:0.9
4.30	550	15 + 15[a]	1:1.0
4.31	27.5	30	1:0.3
4.31	27.5	30 + 30[a]	1:0.2

All reactions performed at 90 °C for 10 min using 0.225 mL 0.2 M pH 5 NaOAc buffer and 0.15 mL $^{68}GaCl_3$ solution. Purification performed using 2 3000 MWCO 0.5 mL centrifugal filters. [a]400 µL of PBS pH 7.6 was added between the two rounds of centrifugation.

In order to allow for use in microbubble formation, these reactions were scaled up to allow for the maximum amount of activity to be incorporated. It was found that the use of 0.5 mL of pH 5 0.2 M NaOAc buffer in combination with 1 mL ^{68}Ga in NaCl/ HCl resulted in the desired pH of ~ 4.3. These samples were heated to 90 °C for 10 min, following which they

were purified by centrifugation. These results are shown in **Table 3.9**. The scale up of these syntheses proved effective, however centrifugation for 5+5 minutes proved too little for the removal of free DOTA while 15+15 min was too long and dried out these filters. 10+10 min resulted in retrieval of the pure compound in a desirable volume of solvent (~ 0.1 mL per filter), as shown in **Figure 3.14**.

In this instance, the pure solution was diluted to 0.8 mL in PBS and used in microbubble synthesis, with 23 % of the original activity being incorporated into the final microbubble solution. This resulted in 99.9 MBq activity in 1 mL microbubbles (typical concentration 1 x 10^9 MB/ mL), which is acceptable for further use.

Table 3.9: Large scale radiolabelling experiments performed on **3.5** using 6 0.5 mL 3000 MWCO filters for purification and $^{68}GaCl_3$ produced in NaCl/ HCl on an iThemba Generator.

Centrifugation/ min	Conversion/ %	Filter Ratio	MB/ MBq[d]	MB/ %[e]
5 + 5[a]	29	1:1.0	-	-
10 + 10[b]	37	1:1.7	99.9	23
15 + 15[c]	21	1:0.7	-	-

All reactions performed at 90 °C for 10 min using 110 µg of **3.5** and dissolved in 0.5 mL 0.2 M pH 5 NaOAc buffer and 1 mL $^{68}GaCl_3$ solution. Final reaction pH 4.38-4.39. [a] 200, [b]300 or [c]400 µL PBS pH 7.6 addition between rounds of centrifugation. [d]Total activity present in final MB formulation. [e]Percentage of initial activity present in the final MB formulation.

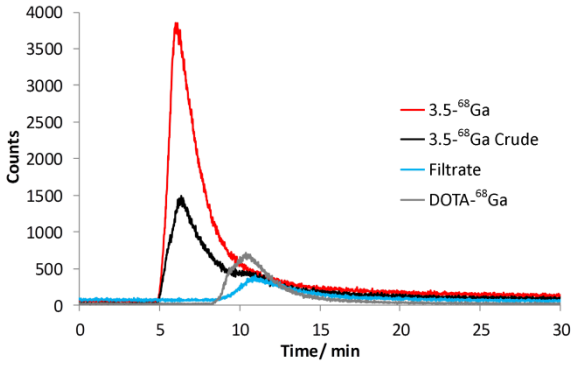


Figure 3.14: HPLC radio chromatograms for the radiolabelling of **3.5** showing the product purified by centrifugation using 0.5 mL filters, the discarded filtrate, the crude reaction mixture and DOTA-^{68}Ga for comparison.

It was found that for large scale synthesis the small 0.5 mL filters were problematic as 6 were required to contain the entire volume (including vial washings). This resulted in activity and time loss due the increased number of surfaces requiring manipulation. In addition, loss

during removal from the filters was large as further centrifugation was required for product retrieval.

The large (15 mL) filters used in lipid purification were not used in radiochemical syntheses due to a lack of shielding around this centrifuge, however it was decided that for large scale synthesis these may reduce the problems mentioned. Initial experiments were performed by decaying the activity prior to reaction to allow for safe use of this machine. It was found that two rounds of 15 min centrifugation with addition of 1 mL PBS (pH 7.6) produced the desired product in an appropriate volume of PBS, as shown in **Table 3.10**. Due to this success, it was deemed worthwhile to modify the equipment to allow for use with higher activities. A test reaction without decaying the product showed good gallium incorporation (49 %) and purity, as shown in **Table 3.10**.

Table 3.10: Large scale radiolabelling experiments performed on **3.5** using a 15 mL 3000 MWCO filter for purification and $^{68}GaCl_3$ produced in NaCl/ HCl on an iThemba Generator. Decayed prior to centrifugation unless otherwise stated.

Reaction pH	Centrifugation Time/ min	Conversion/ %	Filter Ratio
4.34	15 + 15	-	1:4.8
4.36[a]	15 + 15	49	1:2.5

All reactions performed at 90 °C for 10 min using 110 µg of **3.5** (unless otherwise stated) dissolved in 0.5 mL 0.2 M pH 5 NaOAc buffer and 1 mL $^{68}GaCl_3$ solution. [a]Not decayed prior to centrifugation.

This purification method was then used to synthesise microbubbles incorporating the phospholipid **3.5-^{68}Ga**, as shown in **Table 3.11**, with final activities of 98.8 MBq achieved in 1 mL of microbubbles. These reactions produced **3.5-^{68}Ga** with the same retention time as that shown in **Figure 3.14**. Although this final activity is no higher than that achieved using small filters, this method is more reproducible and requires less manipulation of radioactive substances by the user, minimising user exposure.

3.3.2.2 DSPE-PEG$_{2000}$-NOTA

After the successful radiolabelling of **3.5**, similar methods were employed for the radiolabelling of **3.6**. After centrifugal purification **3.6** appeared more pure than **3.5**, however during radiolabelling experiments it proved difficult to remove radiolabelled NOTA. It is likely that ^{68}Ga chelation with NOTA is kinetically more favourable than with DOTA under these conditions, causing it to be a larger radiolabelled impurity and thus more difficult to remove.

Table 3.11: Large scale radiolabelling experiments performed on **3.5** using a 15 mL 3000 MWCO filter for purification and $^{68}GaCl_3$ produced in NaCl/ HCl on an iThemba Generator. Product used to form radiolabelled microbubbles.

Reaction pH	Conversion/ %	Filter Ratio	MB Activity/ MBq	MB Activity/ %[b]
4.65	41	1:2.9	45.4	18
4.08	39	1:1.9	98.8	21
4.35[a]	37	1:2.1	98.8	22

All reactions performed at 90 °C for 10 min using 110 µg of **3.5** (unless otherwise stated) dissolved in 0.5 mL 0.2 M pH 5 NaOAc buffer and 1 mL $^{68}GaCl_3$ solution. [a]220 µg of **3.5** used. [b]Percentage of activity remaining that was added after initial elution in 1 mL NaCl/HCl eluent.

Purification was attempted on small scale reactions with both 0.5 mL and 15 mL filters, using the optimal centrifugation times determined above and longer times, however no pure product was obtained. A selection of experiments performed are shown in **Table 3.12** with example chromatograms in **Figure 3.15**. Due to this, no further work was performed using this phospholipid.

Table 3.12: A selection of radiolabelling experiments performed on **3.6** using 0.5 mL (or 15 mL when specified) 3000 MWCO filters for purification and $^{68}GaCl_3$ produced in NaCl/ HCl on an iThemba Generator.

Total Vol/ mL	Reaction pH	Centrifugation Time/ min	Filter Ratio
0.375	4.31	10 + 10	1:0.6
0.375	4.31	30 + 30	1:3.3
0.375	4.31	30 + 30	1:3.5
0.625[a]	4.4	10 + 10	1:1.7
0.625 [a]	4.33	10 + 10	1:1.5
0.625 [a]	4.47	10 + 10	1:1.1
0.375	4.31	15 + 15[b]	1:16.4
0.375	4.31	15 + 15 [b]	1:11.2
0.375	4.31	15 + 15 [b]	1:11.0

All reactions performed at 90 °C for 10 min using 27.5 µg of **3.6** (unless otherwise stated) dissolved in 0.2 M pH 5 NaOAc buffer. [a]82.5 µg of **3.6** used. [b]Purification performed using 15 mL centrifugal filters.

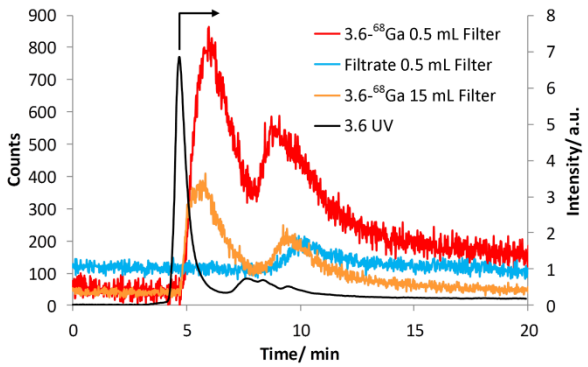


Figure 3.15: HPLC radio chromatograms for the radiolabelling of **3.6** showing the reaction mixture purified by centrifugation using 0.5 mL and 15 mL filters, the discarded filtrate and the comparison to unlabelled UV chromatogram of **3.6**.

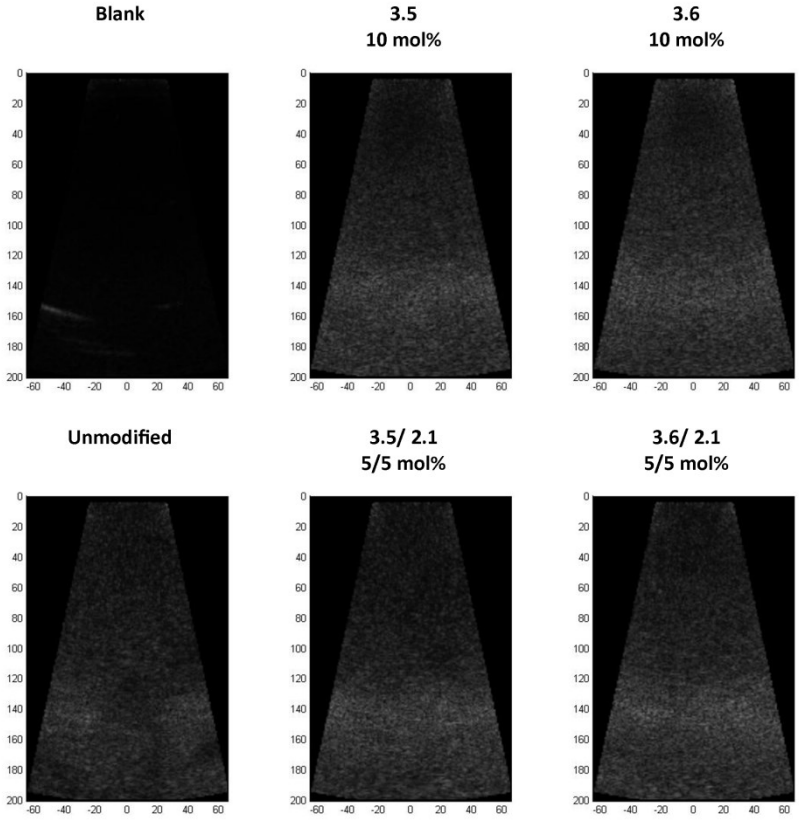


Figure 3.16: Acoustic measurements of solutions. Top (left to right): water, microbubbles containing 10 mol% **3.5** and microbubbles containing 10 mol% **3.6**; Bottom (left to right): unmodified microbubbles, microbubbles containing 5 mol% **3.5** and 5 mol% **2.1** and microbubbles containing 5 mol% **3.6** and 5 mol% **2.1**. Measurements performed on a Verasonics ultrasound imaging system equipped with a P4-2v probe (2 MHz imaging frequency at a Mechanical Index of 0.08). 1.7 L H_2O was rested for 5 min following which 20 µL of the microbubble solution was added.

3.3.3 Acoustic Characterisation

Microbubbles containing phospholipids **3.5** and **3.6** at 10 mol% loading were synthesised, showing larger size distributions of 4.74 and 4.11 μm and lower concentrations of 6.08 x 10^8 MB/ mL and 8.09 x 10^8 MB/ mL respectively when compared to unmodified microbubbles (n=3, see Appendix **Tables A.4** and **A.5**). Formulations containing 5 mol% **3.5** or **3.6** and 5 mol% of the targeting phospholipid **2.1** were also synthesised with similar sizes (4.72 and 4.44 μm respectively) and lower concentrations (4.98 x 10^8 and 4.47 x 10^8 MB/ mL respectively, n=3). These are shown in the Appendix (**Tables A.6** and **A.7**).

As in Chapter 2, measurements were taken by Shengtao Lin, Dept. of Bioengineering, Imperial College London, before and after addition of these microbubbles to water in order to confirm that they retained their acoustic properties despite these changes in size and concentration. These results display acoustic contrast enhancement, as demonstrated in **Figure 3.16**. Additional data is shown in the Appendix (**Figure A.20**).

3.4 Conclusions

Work has been undertaken to radiolabel microbubbles using two different methods. Initially, labelling was attempted using TCO-functionalised microbubbles and a radiolabel functionalised with tetrazine. Although initial reactions proved promising, once the reaction was performed on microbubbles, no radiolabelling was observed. This is likely due to the low concentration of TCO in microbubble solutions. It does appear that a reaction is occurring when the TCO lipid **2.4** is directly reacted with **3.1-^{68}Ga** or **3.3-^{68}Ga**, however the use of this reaction to radiolabel microbubbles seems inefficient when compared to direct radiolabelling of the phospholipids.

In order to combat this, phospholipids attached to the chelators DOTA and NOTA were synthesised and directly radiolabelled. It was found that free DOTA and NOTA were contaminating these samples despite numerous purification attempts. Although the efficiency of these reactions could not be confirmed by HPLC, purification by centrifugation allowed for quantification in addition to purification. DSPE-PEG_{2000}-DOTA **3.5** was successfully radiolabelled, purified and incorporated into microbubbles at sufficient activities for further work. Radiolabelling of the NOTA containing lipid **3.6** was abandoned due to the difficulty of removing free NOTA.

Although direct radiolabelling has been achieved, the necessity of centrifugal purification for > 30 min and the inability to remove unreacted chelator is a significant limitation. One solution to this problem is to use a phospholipid without the PEG polymer chain to chelate the radiolabel. This has been undertaken in literature for Gd coordination[22] and will make purification easier as these lipids can be purified using normal column chromatography and by cartridge under radiochemical conditions. This should also allow for regular C18 HPLC analysis for purity determination and incorporation quantification.

3.5 References

1. G.-L. Law and W.-T. Wong, in *The Chemistry of Molecular Imaging*, eds. N. J. Long and W.-T. Wong, John Wiley & Sons, Inc, 2014, pp. 1-24.
2. A. L. Klibanov, P. T. Rasche, M. S. Hughes, J. K. Wojdyla, K. P. Galen, J. H. Wible and G. H. Brandenburger, *Invest. Radiol.*, 2004, **39**, 187-195.
3. J. K. Willmann, Z. Cheng, C. Davis, A. M. Lutz, M. L. Schipper, C. H. Nielsen and S. S. Gambhir, *Radiology*, 2008, **249**, 212-219.
4. N. Teraphongphom, P. Chhour, J. R. Eisenbrey, P. C. Naha, W. R. T. Witschey, B. Opasanont, L. Jablonowski, D. P. Cormode and M. A. Wheatley, *Langmuir*, 2015, **31**, 11858-11867.
5. J. A. Feshitan, F. Vlachos, S. R. Sirsi, E. E. Konofagou and M. A. Borden, *Biomaterials*, 2012, **33**, 247-255.
6. P. Walday, H. Tolleshaug, T. Gjøen, G. M. Kindberg, T. Berg, T. Skotland and E. Holtz, *Biochem. J*, 1994, **299**, 437-443.
7. A. C. Perkins, M. Frier, A. J. Hindle, P. E. Blackshaw, S. E. Bailey, J. M. Hebden, S. M. Middleton and M. L. Wastie, *Br. J. Radiol.*, 1997, **70**, 603-611.
8. M. S. Tartis, D. E. Kruse, H. Zheng, H. Zhang, A. Kheirolomoom, J. Marik and K. W. Ferrara, *J. Control. Release*, 2008, **131**, 160-166.
9. A.-H. Liao, S.-Y. Wu, H.-E. Wang, C.-H. Weng, M.-F. Wu and P.-C. Li, *Ultrasonics*, 2013, **53**, 320-327.
10. N. Lazarova, P. W. Causey, J. A. Lemon, S. K. Czorny, J. R. Forbes, A. Zlitni, A. Genady, F. S. Foster and J. F. Valliant, *Nucl. Med. Biol.*, 2011, **38**, 1111-1118.
11. N. Oku, Y. Tokudome, H. Tsukada, T. Kosugi, Y. Namba and S. Okada, *Biopharm. Drug Disposition*, 1996, **17**, 435-441.
12. A. T. I. Jensen, T. Binderup, T. L. Andresen, A. Kjær and P. H. Rasmussen, *J. Liposome Res.*, 2012, **22**, 295-305.
13. V. Awasthi, S.-H. Yee, P. Jerabek, B. Goins and W. T. Phillips, *J. Appl. Physiol.*, 2007, **103**, 28-38.
14. M. Mougin-Degraef, C. Bourdeau, E. Jestin, C. Saï-Maurel, M. Bourgeois, P. R.-L. Saëc, P. Thédrez, J. F. Gestin, J. Barbet and A. Faivre-Chauvet, *Int. J. Pharm.*, 2007, **344**, 110-117.
15. J. W. Seo, L. M. Mahakian, A. Kheirolomoom, H. Zhang, C. F. Meares, R. Ferdani, C. J. Anderson and K. W. Ferrara, *Bioconjugate Chem.*, 2010, **21**, 1206-1215.

16. C. M. Kang, H.-J. Koo, S. Lee, K. C. Lee, Y.-K. Oh and Y. S. Choe, *Nucl. Med. Biol.*, 2013, **40**, 1018-1024.
17. A. Bao, B. Goins, R. Klipper, G. Negrete, M. Mahindaratne and W. T. Phillips, *J. Pharm. Sci.*, 2003, **92**, 1893-1904.
18. W. T. Phillips, A. S. Rudolph, B. Goins, J. H. Timmons, R. Klipper and R. Blumhardt, *Int. J. Rad. Appl. Instrum. B*, 1992, **19**, 539-547.
19. M. C. Woodle, *Nucl. Med. Biol.*, 1993, **20**, 149-155.
20. W. C. Hsu, I. T. Chiang, L. C. Chen, S. P. Chiu, T. W. Lee and J. J. Hwang, 2015.
21. J. W. Seo, L. M. Mahakian, S. Tam, S. Qin, E. S. Ingham, C. F. Meares and K. W. Ferrara, *Nucl. Med. Biol.*, 2015, **42**, 155-163.
22. S. Jung, K. Na, S. Lee, S. Cho, H. Seong and B. Shin, *Nanoscale Res. Lett.*, 2012, **7**, 462.
23. E. W. Price and C. Orvig, *Chem. Soc. Rev.*, 2014, **43**, 260-290.
24. P. W. Miller, N. J. Long, R. Vilar and A. D. Gee, *Angew. Chem. Int. Ed.*, 2008, **47**, 8998-9033.
25. H. L. Evans, Q.-D. Nguyen, L. S. Carroll, M. Kaliszczak, F. J. Twyman, A. C. Spivey and E. O. Aboagye, *Chem. Commun.*, 2014, **50**, 9557-9560.
26. N. K. Devaraj and R. Weissleder, *Acc. Chem. Res.*, 2011, **44**, 816-827.
27. A. Zlitni, N. Janzen, F. S. Foster and J. F. Valliant, *Angew. Chem. Int. Ed.*, 2014, **53**, 6459-6463.
28. H. L. Evans, L. Carroll, E. O. Aboagye and A. C. Spivey, *J. Labelled Compd. Radiopharm.*, 2014, **57**, 291-297.
29. M. Braga, Thesis, Not Submitted, Imperial College London.
30. G. A. Olah, G. K. Surya Prakash, Q. Wang, X.-y. Li and T. Ziegler, in *Encyclopedia of Reagents for Organic Synthesis*, John Wiley & Sons, Ltd, 2001.
31. C. Rivas, G. J. Stasiuk, M. Sae-Heng and N. J. Long, *Dalton Trans.*, 2015, **44**, 4976-4985.
32. C. Rivas, G. J. Stasiuk, J. Gallo, F. Minuzzi, G. A. Rutter and N. J. Long, *Inorg. Chem.*, 2013, **52**, 14284-14293.
33. M. R. Karver, R. Weissleder and S. A. Hilderbrand, *Bioconjugate Chem.*, 2011, **22**, 2263-2270.
34. F. Thalhammer, U. Wallfahrer and J. Sauer, *Tetrahedron Lett.*, 1990, **31**, 6851-6854.
35. U. H. Andrews, J. E. Baldwin and M. W. Grayston, *J. Org. Chem.*, 1982, **47**, 287-292.
36. Y. Inoue, T. Kobata and T. Hakushi, *J. Phys. Chem.*, 1985, **89**, 1973-1976.
37. R. Rossin, S. M. J. van Duijnhoven, W. ten Hoeve, H. M. Janssen, F. J. M. Hoeben, R. M. Versteegen and M. S. Robillard, *Bioconjugate Chem.*, 2016, DOI: 10.1021/acs.bioconjchem.6b00231.
38. W. A. P. Breeman, M. de Jong, E. de Blois, B. F. Bernard, M. Konijnenberg and E. P. Krenning, *Eur. J. Nucl. Med. Mol. Imaging*, 2005, **32**, 478-485.
39. J. Šimeček, P. Hermann, H.-J. Wester and J. Notni, *ChemMedChem*, 2013, **8**, 95-103.
40. D. Mueller, W. A. P. Breeman, I. Klette, M. Gottschaldt, A. Odparlik, M. Baehre, I. Tworowska and M. K. Schultz, *Nat. Protocols*, 2016, **11**, 1057-1066.
41. J. Seemann, E. Eppard, B. P. Waldron, T. L. Ross and F. Roesch, *Appl. Radiat. Isot.*, 2015, **98**, 54-59.

Chapter 4

Fluorescent Microbubbles and Nanodroplets

People that have contributed to this chapter:

Shengtao Lin

4.1 Introduction

Fluorescence can also be used for dual-modal visualisation of microbubbles alongside ultrasound. It is well matched to the advantages of ultrasound as it is easy to use, flexible, inexpensive and data can be collected rapidly. It also has the advantage of being ionising-radiation free.[1] It is particularly useful *in vitro* as it is easy to visualise in tissue cultures with a much higher resolution than PET (~1 μm for intravital microscopy,[2, 3] as opposed to 1-2 mm in PET[2]).

4.1.1 Fluorescent Phospholipid Structures

Historically fluorescent phospholipids have been studied in order to determine the nature,[4] exchangeability[5] and processing[6, 7] of phospholipids in various membranes. In the majority of these studies, 4-nitrobenzo-2-oxa-1,3-diazole (NBD) or sulforhodamine B (Rh) functionalised phospholipids (NBD-PC and N-Rh-PE) were purchased and no further functionalisation was performed. More recently, fluorescent modification has also been undertaken using other labels such as boron-dipyrromethene (BODIPY)[8] and pyrene.[8, 9] The structures of these are shown in **Figure 4.1**. In general, it has been found that headgroup-modified lipids are non-exchangeable between membranes whereas acyl chain-labelled lipids can undergo spontaneous transfer.[7]

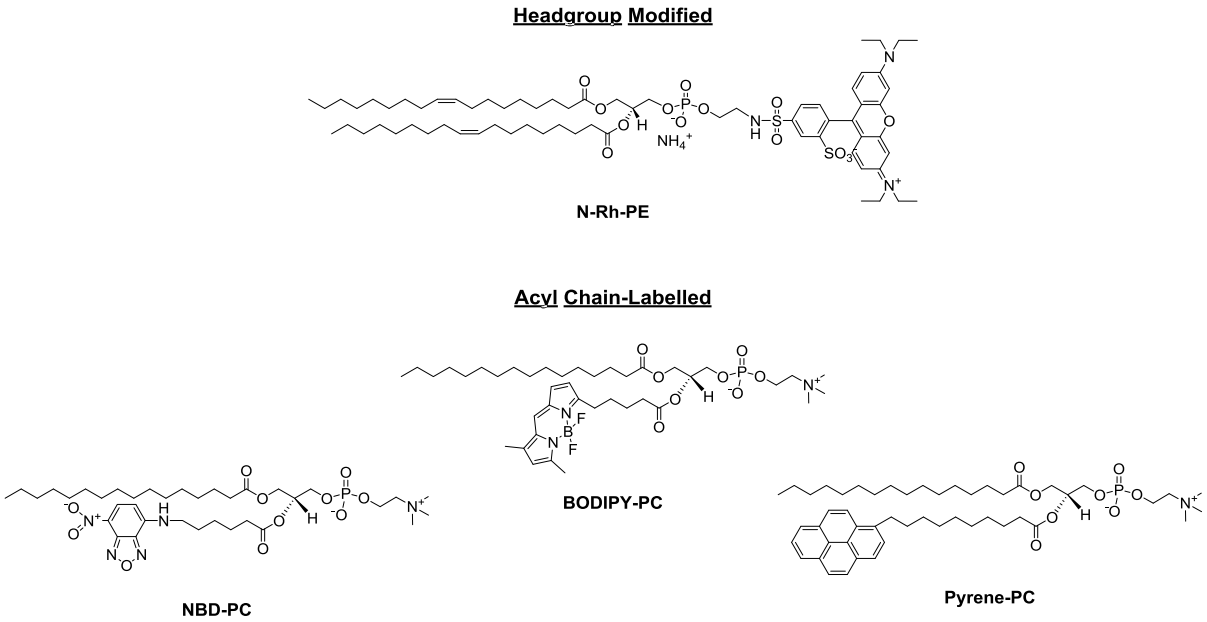


Figure 4.1: Example structures of fluorescent phospholipids containing rhodamine, NBD, BODIPY and pyrene.

The incorporation of fluorescent moieties into 3D lipid structures can also be performed by noncovalent encapsulation or association of the desired molecules. Examples of noncovalent probes include diphenylhexatriene (DPH)[10] and 1-anilino-8-napthalene sulfonate (ANS),[11] the structures of which are shown in **Figure 4.2**. These reside in non-polar and polar regions of membranes respectively and interact via hydrophobic and coulombic interactions as appropriate. Although this method of incorporation is synthetically much simpler, the exact locations of noncovalent probes in lipid membranes cannot unambiguously be determined as factors such as compartmentalisation may also be important.[12] This could affect the collection and interpretation of results.[13]

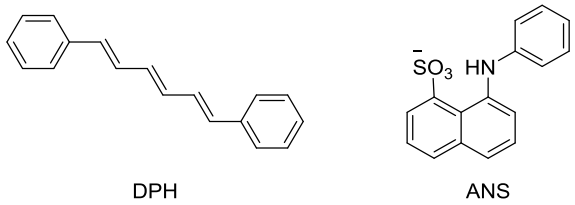


Figure 4.2: Structures of noncovalent probes DPH and ANS which reside on the inside and outside of lipid membranes respectively.

The effect of incorporating fluorescent phospholipids into 3D structures such as vesicles[14, 15] has also been analysed. It is expected that these molecules could self-quench due to the enforced close proximity of the fluorophores. For example, a sharp increase in quenching was observed in vesicles containing 1-20 mol% of an NBD-lipid.[5] When composed of 100 mol% NBD-lipid, vesicles were found to have 120 times lower fluorescence than when at non-quenching concentrations.[14]

Self-quenching was also observed for N-Rh-PE and related rhodamine-containing molecules. After analysis, the degree of quenching was found to depend upon the formation nonfluorescent dimers.[15] Pyrene functionalised phospholipids are also well known to form aggregates in the form of excimers, which have been used to analyse the lateral organisation of membranes.[9]

Fluorophores have also been incorporated into microbubbles for dual-modal ultrasound-fluorescence imaging. Fluorescence imaging usually only provides 2D signals,[16] therefore its combination with ultrasound will enhance the information obtained. Cyanine dyes have been used for dual-modal cancer imaging using microbubbles (Cy 7)[17] and nanobubbes (microbubbles below 500 nm diameter, Cy 5.5).[18] Interestingly, in the latter case it was found that fluorescence signal was retained for over 24 h, whereas unconjugated dyes were quickly

excreted.[18] This implies that modified lipids can be used post microbubble destruction for further imaging, proving both short-term ultrasound imaging and longer-term fluorescence of the same area.

The use of fluorophores in microbubbles has recently focussed around ultrasound modulated fluorescence and uses the aforementioned self-quenching of fluorophores at high concentrations. When ultrasound pulses are applied to these microbubbles, the pressure wave causes oscillations in the phospholipid shell; during expansion the fluorophores are further apart and therefore quenching is reduced, whilst self-quenching occurs at any other time.[19] This causes a blinking of the fluorescence which is much more distinguishable from background signals. This technique has the advantage of combining the environment-sensitive information provided by different fluorophores but with ultrasonic resolution and imaging depth.[19] For this purpose, lipophilic dye molecules with long aliphatic chains (such as the cyanine fluorophore DiI) have been inserted into microbubble membranes[19] and fluorophores have been covalently attached to the microbubble surface (such as Atto-532).[20]

4.1.2 Nanodroplets

Work in the area of fluorescent microbubbles has recently been included into nanodroplet research, as briefly described in Chapter 1. These have a number of advantages including increased circulation time and the ability to extravasate through tumorous vasculature due to the EPR effect.[21] These nanodroplets can then be vaporised in order to enhance ultrasound contrast in cancerous regions.

Nanodroplets can have a similar variety of surface coatings to microbubbles, including proteins,[22] phospholipids[23-25] and polymers.[26, 27] It has been found that albumin forms droplets that vaporise more rapidly than lipid stabilised analogues, however the latter represent homogeneous encapsulation while heterogeneous patterns in albumin-coated droplets suggest areas of diminished coating. This, in addition to the stability and toxicity issues discussed in Chapter 1, suggests that phospholipid coatings are the most advantageous.

Through the use of fluorescence microscopy, it was determined that after vaporisation these microbubbles retained the original surface coating and any non-covalently bound molecules remained associated.[28] In order for this to occur, bilayer strands form during microbubble condensation which become unzipped upon vaporisation.[29, 30] Phospholipid nanodroplets can also be targeted to cancer using cyclic RGD and have shown a statistically significant increase in binding of microbubbles after vaporisation using ultrasound.[23] This agrees with

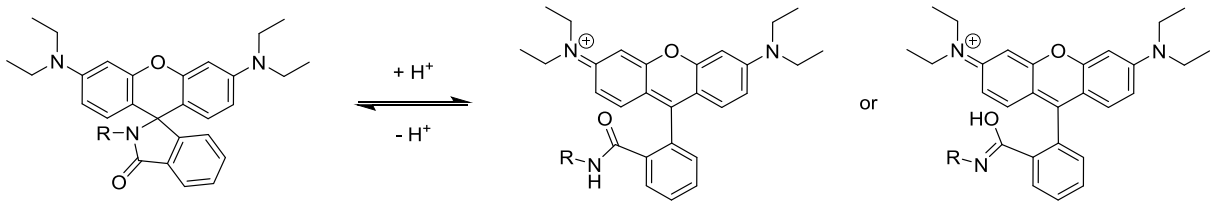
findings that the original shell is retained after vaporisation and means that functionalisation of the original membrane will be retained in resultant nanodroplets and microbubbles.

The use of optical vaporisation is advantageous as it can be used in gaseous areas that acoustic signals cannot traverse.[27] The laser fluence required to vaporise these nanodroplets varies greatly depending upon nanodroplet composition and fluorophore.[31] One study quoted a 50% threshold fluence of 10.6 ± 5.1 mJ/ cm^2,[24] however higher minimum fluences of 1.4 J/ cm^2 have been quoted in an alternative system.[27] The laser fluence heavily depends upon the core material, with lower molecular weight perfluorocarbons requiring lower laser fluence.

4.1.3 Fluorophore Selection

When selecting an appropriate fluorophore for microbubble modification, many factors must be taken into account. Although visible probes are often considered less ideal for *in vivo* use than NIR dyes due to low tissue penetration, visible fluorophores have higher emission efficiency and target-to-background ratios and are therefore superior to higher wavelength fluorophores for surface imaging.[32] This, in combination with the wavelength compatibility of available analytical equipment, make these fluorophores desirable for initial analysis and *in vitro* experiments. In particular, rhodamine-derivatives exhibit good photostabilities, high extinction coefficients and high fluorescence quantum yields.[33]

One advantage of using rhodamine fluorophores is their sensitivity to the surrounding environment, resulting in the switching on or off of fluorescence.[34] This modulation can be induced by numerous stimuli from pH[35, 36] to metal ions.[37] Many of these probes use the spyrolacam ring-opening in order to moderate fluorescence; this requires rhodamine to be modified to include an amide or other nucleophile that can attack the xanthene fluorescent structure,[34] as shown below in **Scheme 4.1** for rhodamine B.



Scheme 4.1: Amine-modified rhodamine B pH-controlled spyrolactam ring opening. Ring opened form (right) is fluorescent whilst the ring closed (left) is non-fluorescent.

As discussed in Chapter 1, tumorous tissue has a more acidic microenvironment than healthy cells, in the range of 5.6-7.6 as opposed to 7.2-7.6 for normal tissue.[38] The pH switching of

rhodamine fluorophores occurs around this range, between pH 4 and 7[35, 36] dependent upon the structure; this can cause a 100-fold fluorescence increase.[36]

Rhodamines can also be functionalised to prevent this ring-closing reaction in order to retain fluorescence over the entire pH range. One synthetic method is to use an ester as opposed to an amide functionality, as employed in the commercial dye Rhodamine 6G.[39] Alternatively, the nitrogen moiety can be functionalised with two R groups. While some probes have used methyl-functionalisation of the amine,[35] many examples of pH insensitive rhodamine fluorophores are based upon modification of the carboxylic acid with piperazine, as shown in **Figure 4.3**.[40, 41] In rhodamine B derivatives, a slight fluorescence increase at pH 11 was observed, however fluorescence was maintained over a wide pH range (**Figure 4.3**).[41]

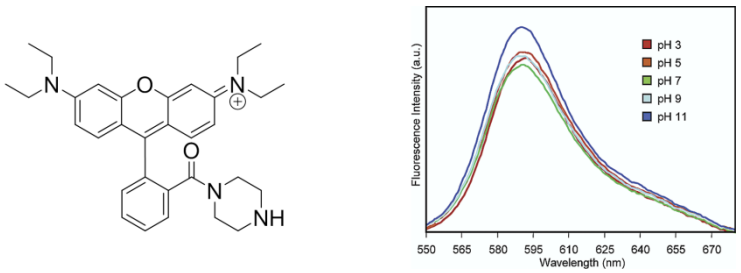


Figure 4.3: The structure and pH sensitivity of rhodamine B functionalised with piperazine at the 2' position. Graph reproduced with permission.[41]

Rhodamine dyes unmodified at the 2' position experience little pH sensitivity in the range 4-10.[42] Due to steric hindrance at the 3' and 6' positions, most functionalisation occurs at the 4' and 5' positions. These are often sold as mixtures of isomers and are expensive.[34] There are many examples of these derivatives in the functionalisation of biomolecules where the expense of the dye is limited by the small quantities required. Of these, the rhodamine 101 derivative 5(6)-carboxy-X-rhodamine (ROX) and sulforhodamine 101 (Texas Red) are popular due to their high quantum yields[34] and relative pH insensitivity.[43] The structures of these are shown in **Figure 4.4**.

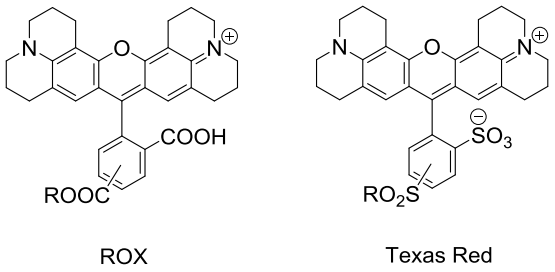


Figure 4.4: Structures of rhodamine dyes functionalised at the 4' or 5' positions. Left: 5(6)-carboxy-X-rhodamine (ROX); Right: sulforhodamine 101 (Texas Red).

Fluorescence switching in rhodamines is not always a result of spyrolactam formation. There are a number of mechanisms by which quenching can occur. This includes dynamic quenching from mechanisms such as Förster resonance energy transfer (FRET), static contributions through the formation of ground state complexes such as H-dimers and other effects including photoinduced electron transfer (PeT). These have all been implicated in rhodamine quenching.[44, 45]

4.1.4 Aims

This chapter aims to functionalise the phospholipid DSPE-PEG_{2000}-NH_2 with a fluorophore and to incorporate this into microbubbles. Formation of these fluorescent microbubbles can be used to prove that modified lipids are being incorporated into the microbubble shell in this formulation and will allow for their use as dual-modal contrast agents. In addition, these microbubbles can also be condensed into nanodroplets and their absorbance properties used to induce vaporisation.

In many of the fluorescent microbubble syntheses mentioned above, microbubbles were modified post formation. This means that there is no proof as to how the dyes are incorporated into the microbubbles (i.e. whether they are covalently attached or otherwise associated) and the dye loading is unknown.[17, 20] In order to improve the method of functionalisation, fluorescent phospholipids will be synthesised and characterised prior to microbubble synthesis.

Fluorophore selection for this project is important. Rhodamine B provides many features such as good photophysical properties, synthetic versatility and low cost (£15.20 for 25 g, Sigma Aldrich 2017). This will also allow for pH sensitivity to be incorporated into the microbubbles with the hope of detecting cancer through fluorescence switching and selective nanodroplet vaporisation.

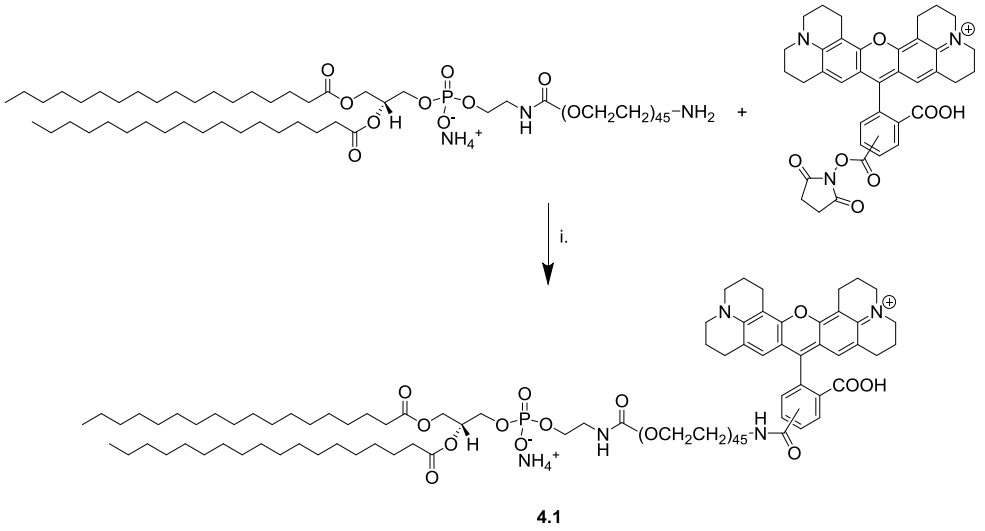
4.2 Synthesis and Characterisation of Fluorescent Phospholipids

The initial purpose of these phospholipids was to prove that modified phospholipids incorporate into microbubbles. As such, preliminary synthesis was performed using commercially available rhodamine derivative ROX, following which rhodamine B was modified in order to allow for selective pH sensitivity.

4.2.1 ROX Phospholipid

4.2.1.1 Synthesis

This synthesis was accomplished using an NHS-activated ROX. This allowed for reaction using peptide coupling, analogous to synthetic methods used in previous chapters; this is shown in **Scheme 4.2**. Phospholipid **4.1** (DSPE-PEG_{2000}-ROX) was analysed by MALDI and UPC^2 to confirm product formation (see Appendix **Figures A.12** and **A.17**). The latter also indicated the presence of unreacted DSPE-PEG_{2000}-NH_2, however this was not problematic for providing the initial proof that these phospholipids are incorporated into the microbubble shell.



Scheme 4.2: Synthetic scheme for DSPE-PEG_{2000}-ROX **4.1**. i. $CHCl_3$, NEt_3, 24 h, RT, 100 % yield.

4.2.1.2 pH Titration

Microbubbles are formulated predominantly in PBS with a pH of 7.6, therefore the pH-dependence of fluorescence was determined to ensure that fluorescence would be observable from microbubbles under these conditions. As discussed above, ROX should not display significant pH dependence, however this was confirmed by monitoring absorbance as a function of pH. The absorbance band with λ_{max} = 580 nm is indicative of the fluorescent form of this rhodamine and disappears when rhodamines convert to the spyrolactam form. These results are shown in **Figure 4.5**, with measurements taken in 0.1 M KCl in order to maintain a constant ionic strength and to compare with analogous literature. These results show that fluorescence intensity increases linearly with pH. This does not follow the pattern previously described for rhodamines.[42]

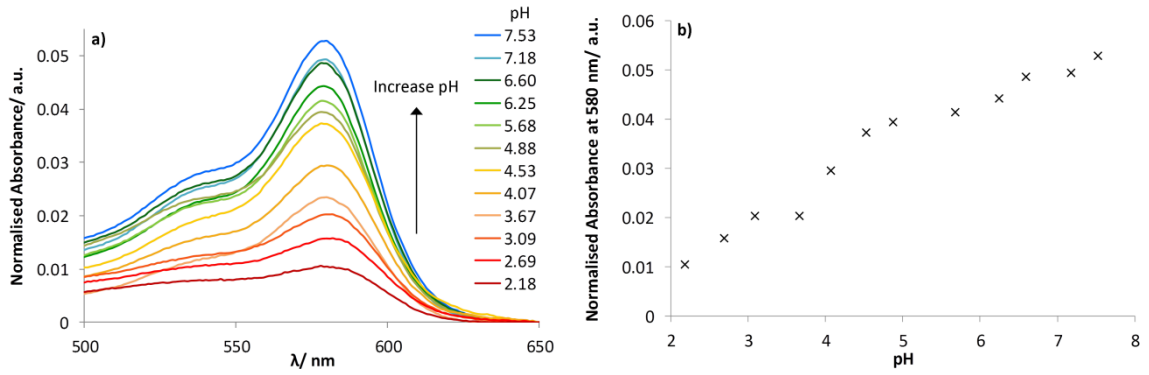


Figure 4.5: Graphs showing the pH dependence of DSPE-PEG_{2000}-ROX **4.1** absorbance. 10 µM solution in 0.1 M KCl. a) Overlay of normalised UV-vis. spectra over a pH range. pH of each solution shown in legend; b) plot of the normalised absorbance intensity at 580 nm as a function of pH.

Phospholipid attachment could be the cause of this observation. In solution, phospholipids appear as aggregates above the critical micelle concentration (cmc). This concentration is generally quite low and depends on the chain length and head group; the cmc of DSPE-PEG_{2000} has been reported as 1.1 x 10^{-5} M[46] (alternative reports state a concentration of 0.5-1 x 10^{-3} M[47]). This approximately the concentration used in these experiments (10 µM), therefore micelles are likely to have formed. These aggregates could be causing self-quenching, which has been previously noted for rhodamine.[45, 48] It may be that different pH values cause disruption or formation of aggregates which modifies the fluorescence.

This could also be a result of repeated illumination of this sample. In this experiment the same sample was used and the pH adjusted for each measurement from acid to base. It could be that in this instance we are noticing the effect of irradiation on the fluorophore (this effect has been noticed for pH sensitive probes).

In order to confirm this hypothesis, fluorescence spectra were obtained for three pH values, as shown in **Figure 4.6**. This also demonstrates a slight increase of emission λ_{max} at 600 nm with pH, although this is much less pronounced. Repeated sample irradiation at each pH did not change the emission, therefore this does not affect the results obtained.

The low emission intensities observed could be due to aggregation as this sample had low solubility in 0.1 M KCl. This is supported by the appearance of a large excitation band at 500 nm, with corresponding emission at 530 nm (not shown). The solubility of this lipid in chloroform or methanol was good, with low concentrations required for microbubble formation, therefore this is unlikely to be a problem in the future.

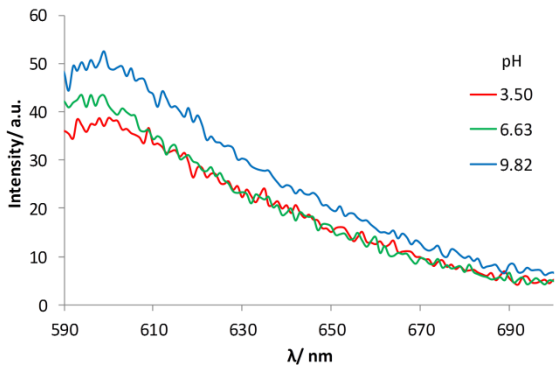


Figure 4.6: Graphs showing the pH dependence of DSPE-PEG$_{2000}$-ROX **4.1** fluorescence. pH of each solution shown in legend. 10 µM solution in 0.1 M KCl, λ_{ex} = 580 nm.

Although some variation has been observed in the absorbance and emission of this phospholipid, fluorescence at pH 7.6 is clear and therefore fluorescence from microbubbles at the pH synthesised should be observable.

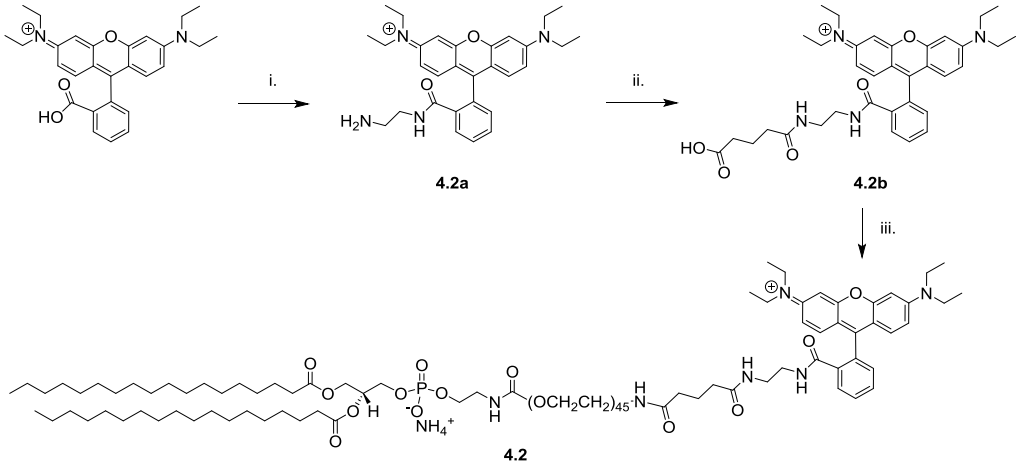
4.2.2 pH Sensitive Rhodamine Phospholipid

4.2.2.1 Synthesis

Many methods exist for the functionalisation of an amine with a desired molecule. Peptide coupling is popular, using a coupling agent to facilitate reaction between a carboxylic acid and an amine under mild conditions. Many coupling agents are available with different properties, however 1-ethyl-3-(3-dimethylaminopropyl)carbodiimide **(**EDC) is particularly favoured due to the water solubility of both the unreacted reagent and the side products.[49] This is important as purification was performed by dialysis, requiring water solubility.

This requires modification of rhodamine to incorporate a free carboxylic acid to facilitate reaction with phospholipid DSPE-PEG$_{2000}$-NH$_2$. Although rhodamine B has an available carboxylic acid, this is close to ring systems which could sterically hinder attack from the large phospholipid. In order to overcome this, a longer chain was attached (**4.2b**). The synthetic scheme is shown in **Scheme 4.3**.

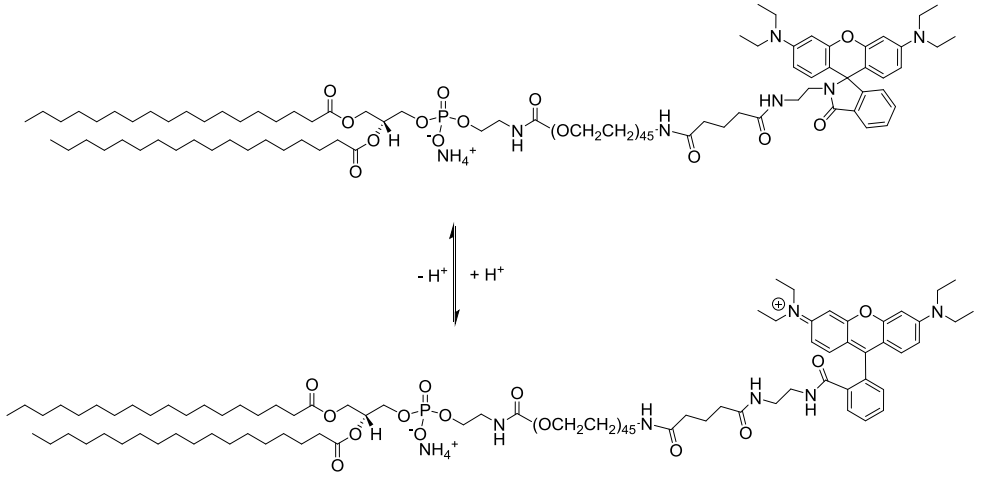
Synthesis of **4.2a** was performed according to literature[50] and **4.2b** was synthesised using a known reaction with glutaric anhydride. Reaction with DSPE-PEG$_{2000}$-NH$_2$ produced **4.2** (DSPE-PEG$_{2000}$-Rh) in high yield (98 %). This was confirmed by UPC^2 (see Appendix **Figure A.18**), however as before some starting material remained.



Scheme 4.3: Synthetic scheme for DSPE-PEG_{2000}-Rh **4.2**. i. Ethylenediamine, EtOH, 25 h, 100 ^{o}C, 84 % yield; ii. glutaric anhydride, THF, 4 h, 70 ^{o}C, 60 h, 50 ^{o}C, 54 % yield; iii. DSPE-PEG_{2000}-NH_2, EDC, NEt_3, $CHCl_3$, 3 d, RT, 98 % yield.

4.2.2.2 pH Titration

The pH sensitivity of this lipid was then determined by pH titration, as previously described. The expected ring-opening and closing reaction is shown in **Scheme 4.4**, with results shown in **Figures 4.7** and **4.8**. Visual inspection can also be used as the solution appears colourless when in the ring closed form and pink when ring open.



Scheme 4.4: Scheme showing the fluorescence pH dependence of DSPE-PEG_{2000}-Rh **4.2**.

Previous experiments brought into question the results obtained through gradual pH change of the same sample. In order to ensure accurate results, pH titration was performed in two ways: gradual pH change (in order to compare with previous results) and the use of discrete samples at each pH. The latter method was not used previously as more sample is required and these phospholipids are typically made in small quantities. These titrations were

monitored by UV-vis. and fluorescence (excitation and emission) spectroscopy in order to confirm correlation of the absorbance band with fluorescence intensity. The former measurements were performed in 0.1 M KCl in order to compare with previous experiments, however later measurements were obtained in PBS to replicate the conditions that these phospholipids will be formed, analysed and used in. Here the concentration of NaCl is about 0.11 M.[51] All results corroborated well between conditions and measurement techniques, with a selection shown in **Figures 4.7** and **4.8**.

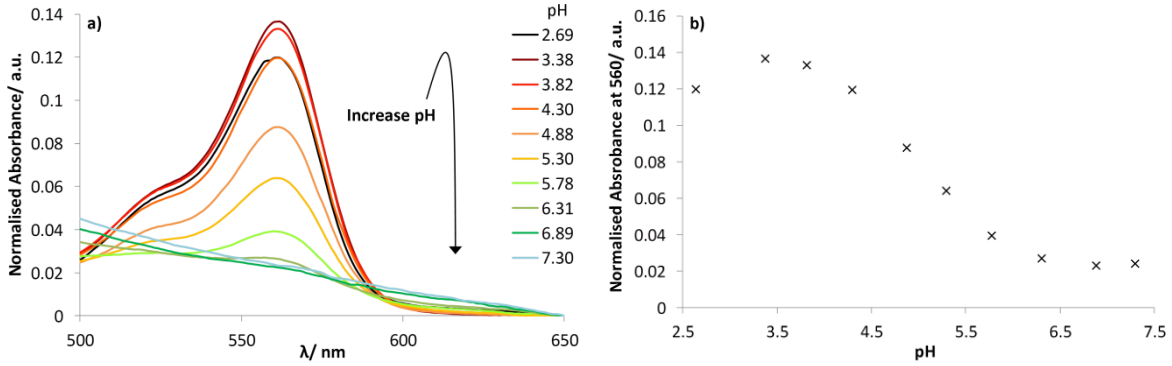


Figure 4.7: Graphs showing the pH dependence of DSPE-PEG$_{2000}$-Rh **4.2** absorbance. Measurements were taken by gradual pH change using 1 M NaOH/ HCl. 10 µM solution in 0.1 M KCl. a) Overlay of normalised UV-vis. spectra over a pH range, pH of each solution shown in legend; b) plot of the normalised absorbance intensity at 560 nm as a function of pH.

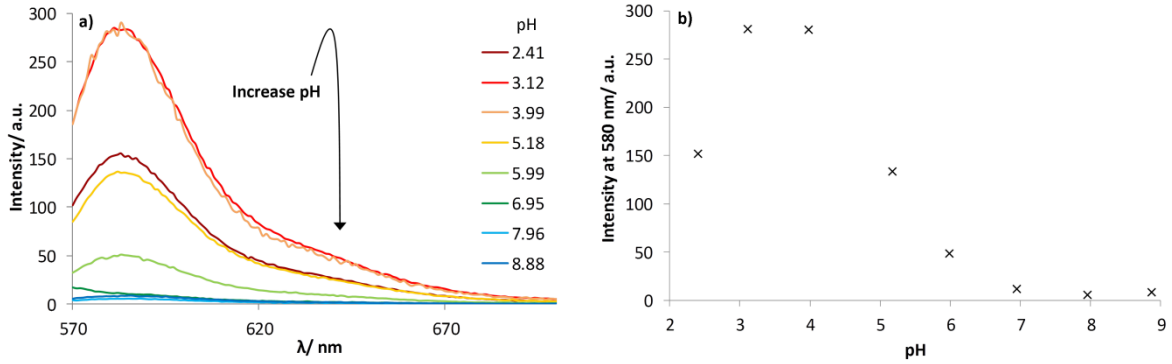


Figure 4.8: Graphs showing the pH dependence of DSPE-PEG$_{2000}$-Rh **4.2** fluorescence emission. All measurements taken on individual samples which had been equilibrated at the desired pH for 24 h. 10 µM solution in PBS. a) Overlay of emission spectra over a pH range, λ_{ex} = 560 nm, pH of each solution shown in legend; b) plot of emission intensity at 580 nm as a function of pH, λ_{ex} = 560.

From these data we can obtain an approximate absorbance (and excitation) λ_{max} at 560 nm and emission λ_{max} at 580 nm. As can be seen in **Figures 4.7b** and **4.8b** there is a clear reduction in the absorbance and emission peak as pH is increased. Once the pH increases

above about 6.5 fluorescence is effectively 'switched off' and no absorbance is observed. This is the trend expected for lactone formation.[52]

In all measurements, emission/ excitation/ absorbance intensity decreased below approximately pH 3. Fluorescence decrease at low pH has been observed in literature for rhodamine B and was ascribed to formation of the lactone form.[42] This has also been reported for fluorescein.[53-56] This behaviour has also been noted for various rhodamine dyes conjugated to large albumin structures at pH 2.3,[33] although no explanation for this observation was given. This has not been noted in all instances in literature,[35, 37] therefore this phenomenon may be caused by the lipid as opposed to the rhodamine moiety.

In order to determine whether the fluorophore alone exhibits similar fluctuation with pH, the same studies were performed on **4.2b**, as shown in **Figures 4.9** and **4.10**. The general pH dependence observed is analogous to that of phospholipid **4.2** (compare **Figures 4.9b** and **4.8b**). A small change in peak shape and an accompanying shift of emission and absorbance λ_{max} was also observed between pH 2.34 and 4.01. This indicates that structure changes are likely to occur within this pH range; this was not observed for phospholipid **4.2**.

The absorbance, excitation and emission values are all lower in the case of **4.2b** when compared to **4.2** at the same concentration (10 μM), which could be due to increased quenching of fluorescence when molecules can easily orient themselves in molecular form.[45] Another difference between these spectra is the observation of absorbance and emission in **4.2b** even at high pH; this is not observed for **4.2** above pH 6.95. This again implies that the two are not acting identically.

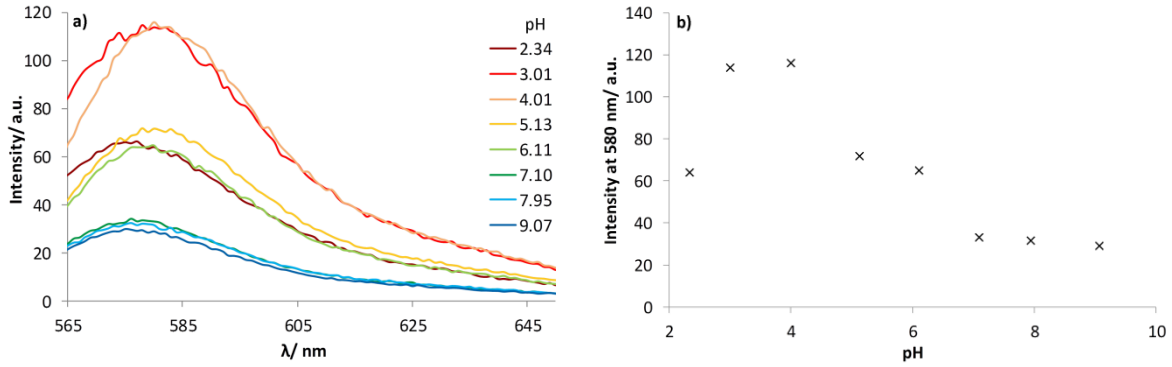


Figure 4.9: Graphs showing the pH dependence of **4.2b** emission. All measurements taken on individual samples which had been equilibrated at the desired pH for 24 h. 10 μM solutions in PBS. a) Overlay of normalised emission spectra over a pH range, λ_{ex} = 555 nm, pH of each solution shown in legend; b) plot of the emission intensity at 580 nm as a function of pH, λ_{ex} = 555 nm.

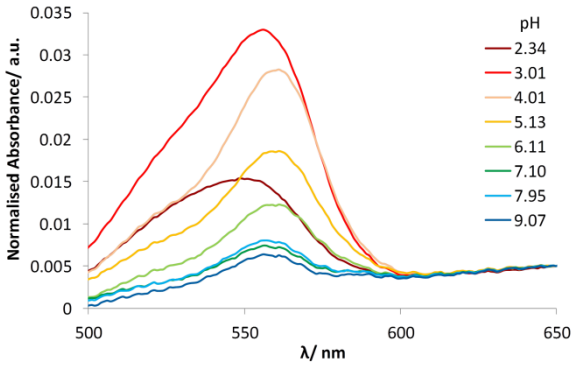


Figure 4.10: Graphs showing the pH dependence of **4.2b** absorbance. Overlay of normalised UV-vis. spectra over a pH range, pH of each solution shown in legend. All measurements taken on individual samples which had been equilibrated at the desired pH for 24 h. 10 μM solutions in PBS.

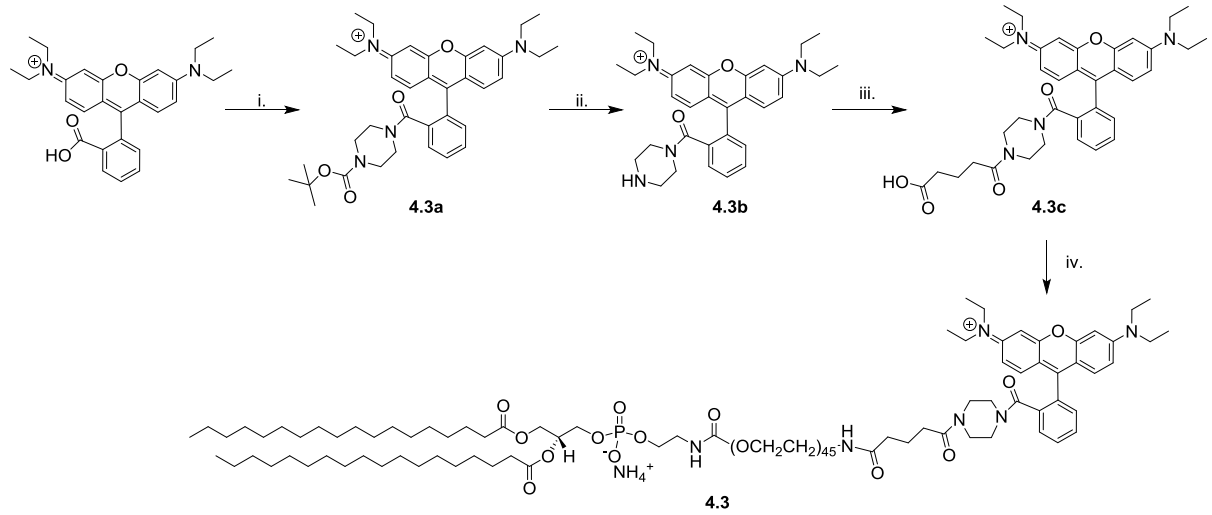
Overall, phospholipid **4.2** shows very similar pH dependence to molecule **4.2b**, indicating that the properties observed are likely a result of the fluorophore and not due to phospholipid attachment. The pH sensitivity of **4.2** between 7 and 3 is very good, with an increase in emission intensity of about 300 times. In the pH range 7-5, which is relevant to cancer imaging, there is a 100 times increase in emission intensity.

4.2.3 pH Insensitive Rhodamine Phospholipid

4.2.3.1 Synthesis

In order to be able to compare the characteristics of a pH sensitive and insensitive phospholipid, it seemed prudent to synthesise a rhodamine B-functionalised phospholipid that was pH insensitive. This would also eliminate the need to use phospholipid **4.1** which displayed unusual pH activity in further work. This utilised the piperazine structure discussed in the introduction as opposed to the ethylene bridge used in phospholipid **4.2**. This should have a minimal effect on the structure. The scheme for this synthesis is shown in **Scheme 4.5**.

This synthesis closely mimics that of **4.2** shown in **Scheme 4.3**, with successful synthesis of **4.3** (DSPE-PEG_{2000}-Rh+) in 94 % yield confirmed by UPC[2] (see Appendix **Figure A.19**). Interestingly, upon NMR analysis of intermediates **4.3a-c**, four ^{13}C peaks were often observed for the piperazine ring as opposed to the expected two. This has two possible explanations: firstly that rotation about the amide bonds is limited, resulting in all four carbon atoms existing in different environments, or that there is a switching between chair and boat conformations.



Scheme 4.5: Synthetic scheme for DSPE-PEG_{2000}-Rh+ **4.3**. i. Boc-piperazine, HBTU, NEt_3, DCM, 2 h, RT, 84 % yield; ii. TFA, DCM, 16 h, RT, 55 % yield; iii. glutaric anhydride, THF, 16 h, 70 ^oC, 88 % yield; iii. DSPE-PEG_{2000}-NH_2, EDC, NEt_3, $CHCl_3$, 16 h, RT, 94 % yield.

4.2.3.2 pH Titration

The excitation and emission spectra were measured, with approximate excitation and emission λ_{max} values of 565 nm and 590 nm respectively. These are slightly shifted in comparison to those values for phospholipid **4.2**.

The effect of pH on emission intensity was determined by pH titration, as shown in **Figure 4.11a**. These fluctuate about a straight line, indicating that any differences are due to random error. All spectra retained the same shape and λ_{max}. This experiment was performed by gradual pH change and measurement of the same sample, with no significant effect caused by repeated experiments. This implies that the effect noted above for **4.1** is a result of the ROX fluorophore.

In order to compare the properties of this phospholipid and the dye alone, the effect of pH on molecule **4.3c** was also investigated (**Figure 4.11b**). The trend was similar to that of **4.3**; however, there are two differences between these results. Firstly, a small shift in emission λ_{max} to 585 nm was observed for molecule **4.3c**. Secondly, the concentration required to get a similar emission intensity was 16 times less for **4.3c**. This implies that either not all of the phospholipid molecules are functionalised with a rhodamine moiety or that quenching is occurring to a large degree when the phospholipid forms micelles. Unfortunately this is difficult to prove due to the small quantities of phospholipid synthesised. UPC^2 appears to have only one peak, but a high background could be masking unreacted phospholipid.

Interestingly, the opposite trend, although to a lesser degree, was observed for phospholipid **4.2** when compared to **4.2b**. Additionally, at all pH values the emission of **4.3** is higher than **4.2**.

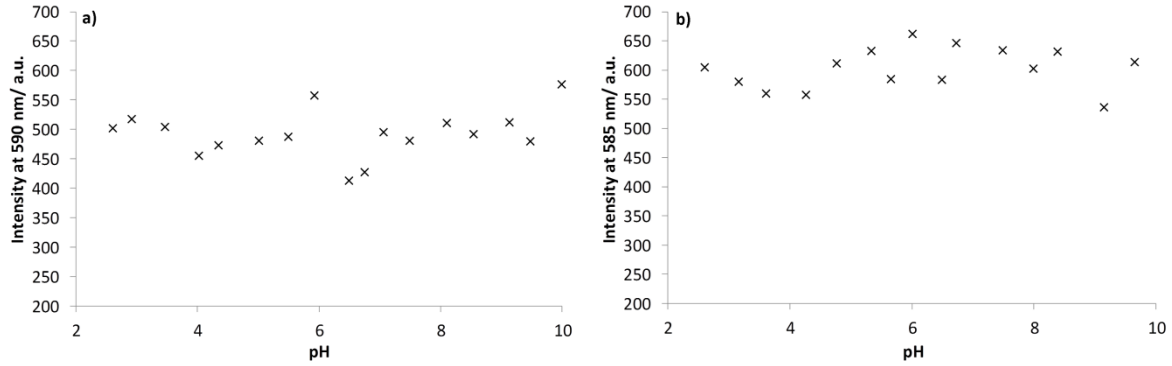


Figure 4.11: Graphs showing the pH dependence of **4.3** and **4.3c** emission. Measurements were taken by gradual pH change using 1 M NaOH/ HCl. a) Plot of emission intensity of phospholipid **4.3** at 590 nm, λ_{ex} = 565 nm, 10 μM, PBS; b) plot of emission intensity of molecule **4.3c** at 585 nm, λ_{ex} = 565 nm, 0.625 μM, PBS.

These properties make this molecule an ideal comparison for phospholipid **4.2**, and potentially a model when pH prevents characterisation.

4.3 Microbubble Formation and Characterisation

4.3.1 N-Rh-PE Phospholipid

The first experiment was performed using the commercial fluorescent lipid N-Rh-PE, as shown in **Figure 4.12**. This was selected as a control as it has been used extensively in literature studies and is known to incorporate into phospholipid membranes.

The concentration of phospholipid incorporated into microbubbles is important in order to get the desired fluorescence without reducing microbubble stability or inducing fluorescence quenching. In one study, analysis was carried out using DPPC membranes (vesicles) containing 0.5-10 mol% C_{18}-Rh.[15] Quenching was shown to increase exponentially with increasing dye content. In another study using a cyanine dye, significant quenching was observed above 2 mol% of dye.[19] Finally, work incorporating modified phospholipids into nanodroplets used 2 mol% dye.[25] These results indicate that lower dye concentrations are desirable, therefore they were performed with only 1 mol% fluorescent lipid.

The lipid composition was kept the same as in previous studies in order to draw accurate comparisons, containing DPPC, DPPA, DSPE-PEG_{2000}-NH_2 and N-Rh-PE in the molar ratio

82:8:9:1. This produced microbubbles of 1.40 µm at a concentration of 3.07 x 10^8 MB/ mL (measurement only performed once, see Appendix **Table A.8**). This size is smaller than typically observed, with unmodified microbubbles giving an average size of 2.42 µm. The concentration is also quite low when compared to 1.26 x 10^9 for unmodified microbubbles (see Appendix **Table A.1**).

In order to determine whether this phospholipid has been incorporated into microbubbles, fluorescence was visualised using laser excitation and appropriate filters, as shown in **Figure 4.12**. It should be noted that in all instances laser illumination was not homogenous throughout the entire field-of-view, but more intense around the centre. These microbubbles were quite homogeneous in size, however fluorescence was easier to observe in the few large microbubbles produced, therefore images showing these larger microbubbles have also been included (**Figure 4.12d**).

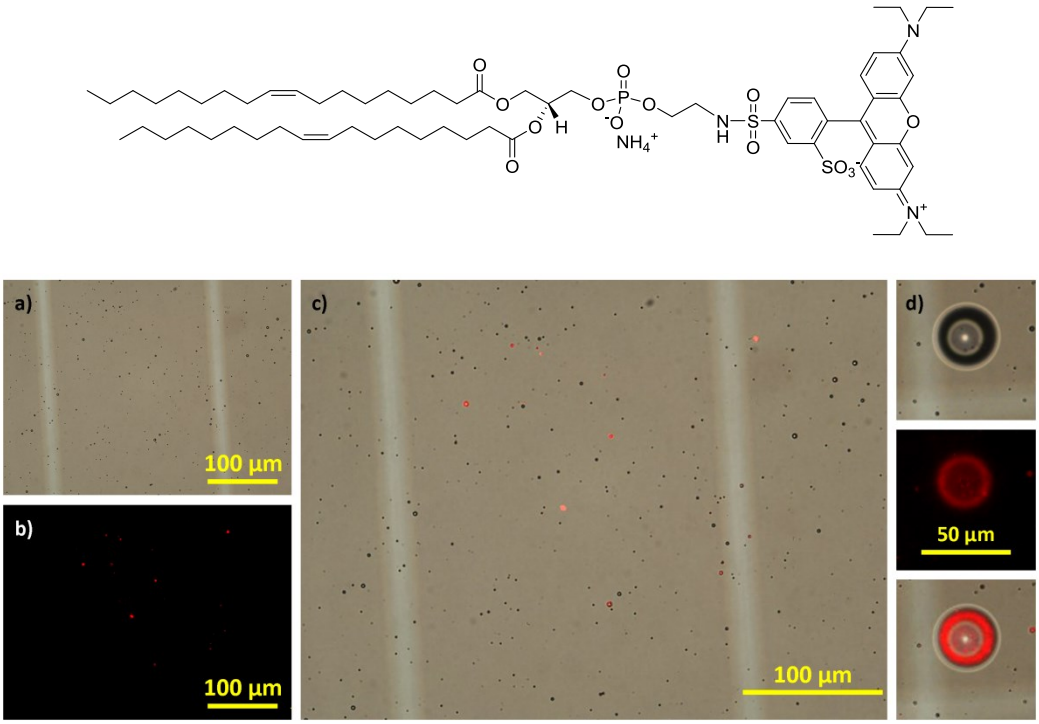


Figure 4.12: Top: Structure of N-Rh-PE. Bottom: Images of microbubbles containing 1 mol% fluorescent lipid N-Rh-PE**.** a) Brightfield illumination; b) fluorescent image of the same field-of-view; c) merge of brightfield and fluorescent images a and b; d) large microbubble brightfield image (top), fluorescence image (middle) and merged (bottom) showing fluorescence from microbubble core, proving incorporation of dye into microbubbles. 100 times dilution with PBS.

While fluorescence appears well-matched with the microbubbles, it has previously been noted that even non-fluorescent microbubbles will appear with a bright ring due to reflection

off the gas/ liquid boundary. The observation of fluorescence from the middle of the microbubble confirms that the fluorophore is incorporated into the micobubble.[19, 57] This can be more clearly observed in the larger microbubbles as there is more distinction between the edge and center. This proves that this phospholipid is incorporated into the microbubbles.

4.3.2 ROX Phospholipid

The original purpose of this phospholipid was to prove that these modified phospholipids incorporate into microbubbles before further syntheses and studies were performed. Phospholipid **4.1** includes the PEG chain used in other formulations (as shown in **Figure 4.13**) and therefore more accurately mimics their incorporation properties than N-Rh-PE. Microbubbles were formulated containing DPPC, DPPA, DSPE-PEG_{2000}-NH_2 and **4.1** in the molar ratio 82:8:9:1 in order to compare with lipid incorporation discussed previously. This produced microbubbles with an average size of 2.13 µm and a concentration of 3.94 x 10^8 MB/ mL (n=3, see Appendix **Table A.9**). Again the concentration is a little low when compared to unmodified microbubbles, but it is more similar than that noted for N-Rh-PE.

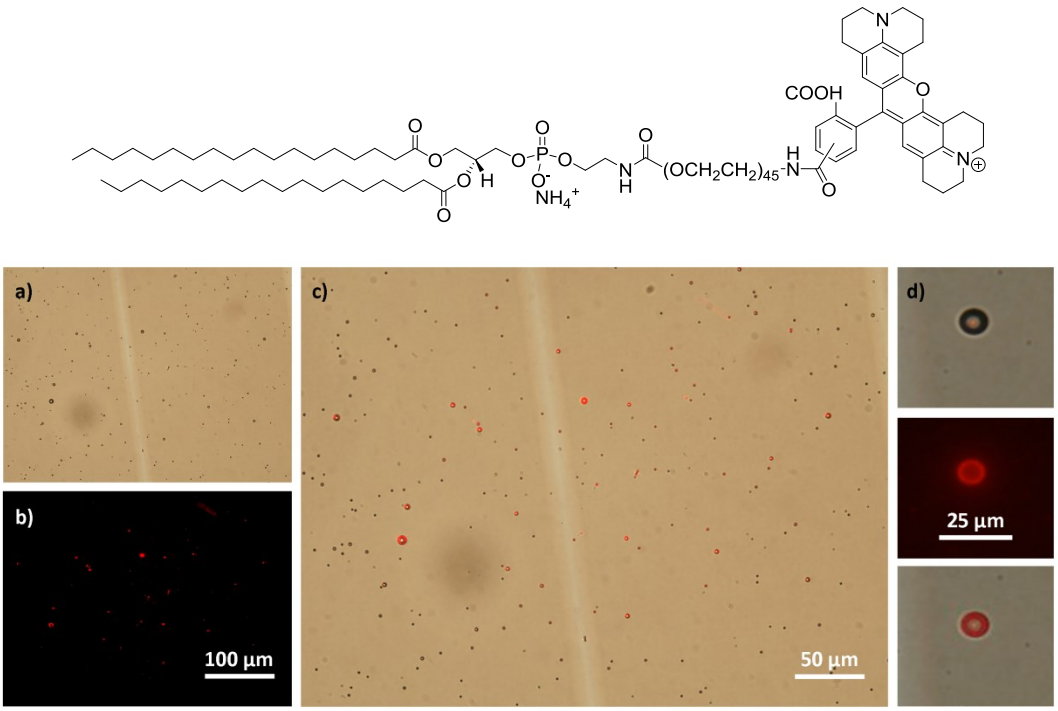


Figure 4.13: Top: Structure of **4.1**. Bottom: Images of microbubbles containing 1 mol% fluorescent lipid **4.1** (40 x magnification)**.** a) Brightfield illumination; b) fluorescent image of the same field-of-view; c) merge of brightfield and fluorescent images a and b; d) large microbubble brightfield image (top), fluorescence image (middle) and merged (bottom) showing fluorescence from microbubble core, proving incorporation of dye into microbubbles. 100 times dilution with PBS.

Phospholipid incorporation was determined as described above. As can be seen in **Figure 4.13** this lipid shows qualitatively the same incorporation as N-Rh-PE, indicating that both are acting in the same way despite obvious structural differences. Visually, N-Rh-PE seems to be incorporated into fewer microbubbles, however this is likely to be due to differences in quality of fluorescent image obtained and the merging procedure between brightfield and fluorescent images.

This phospholipid was not continued into further studies as phospholipids **4.2** and **4.3** have similar structures and provide all necessary information, making any comparisons between them more valid.

4.3.3 pH Sensitive and pH Insensitive Rhodamine Phospholipids

One purpose for these phospholipids was to form pH-sensitive and pH-insensitive nanodroplets. Previous studies using phospholipid stabilised nanodroplets have used mixtures of only DPPC and DSPE-PEG_x with desired photoabsorbers.[25, 26] In one study, formulations analogous to those discussed previously for microbubble formation have been used (DPPC with 10 mol% DSPE-PEG_x).[25] It was therefore decided to use a formulation containing DPPC, DSPE-PEG_{2000}-OMe and DSPE-PEG_{2000}-rhodamine (**4.2** or **4.3**) in a molar ratio of 90:9:1 mol%. This formulation produced unmodified microbubbles 4.76 μm and 9.55 x 10^8 MB/mL upon averaging of three syntheses (n=3, see Appendix **Table A.10**).

Formulations containing **4.2** produced average microbubbles of 3.83 μm at 7.84 x 10^8 MB/ mL and **4.3** formed microbubbles of average size 4.07 μm and concentration of 1.53 x 10^9 MB/ mL (n=3, see Appendix **Tables A.11** and **A.12**). Although these size and concentration values are not identical to those for unmodified microbubbles, they are of the same order of magnitude and within expected fluctuation.

It was also decided to synthesise microbubbles containing a higher concentration of **4.3** in the hope that this would allow for easier characterisation. In one study, only 1 mol% PEG lipid was required to stabilise nanodroplets as opposed to the 10 mol% used previously.[26] As a result, the formulation for the higher rhodamine loading used only DPPC and DSPE-PEG_{2000}-Rh+ **4.3** in a ratio of 96:4 mol%. This produced average microbubbles of 4.21 μm and 7.07 x 10^8 MB/ mL (n=3, see Appendix **Table A.13**).

Images were taken on the fluorescent microscope as described for N-Rh-PE and **4.1**. Interestingly, laser irradiation of these microbubbles modified the microbubble properties; an example of this effect is shown in **Figure 4.14** for phospholipid **4.3** at 1 mol% loading (for 4

mol% loading see Appendix **Figure A.23**). Initial microbubble distribution appeared normal, shown in **Figure 4.14a**. Upon irradiation however these microbubbles seemed to grow and coalesce, as can be seen in fluorescent images **c** and **d** which were taken in immediate succession after the laser was focussed on the sample. Interestingly fluorescence from the microbubbles is much more intense immediately after irradiation and decreases in subsequent images. This could be due to photobleaching or changes occurring in the microbubble shell. This can be most clearly observed in **Figure A.23** where the contrast and brightness of images has not been adjusted. In both formulations fluorescence occurs from the whole microbubble initially, proving incorporation of the phospholipid into the microbubble shell. This decreases rapidly such that in later image acquisitions (**Figure 4.14d**) only reflection from the microbubble rim is visible.

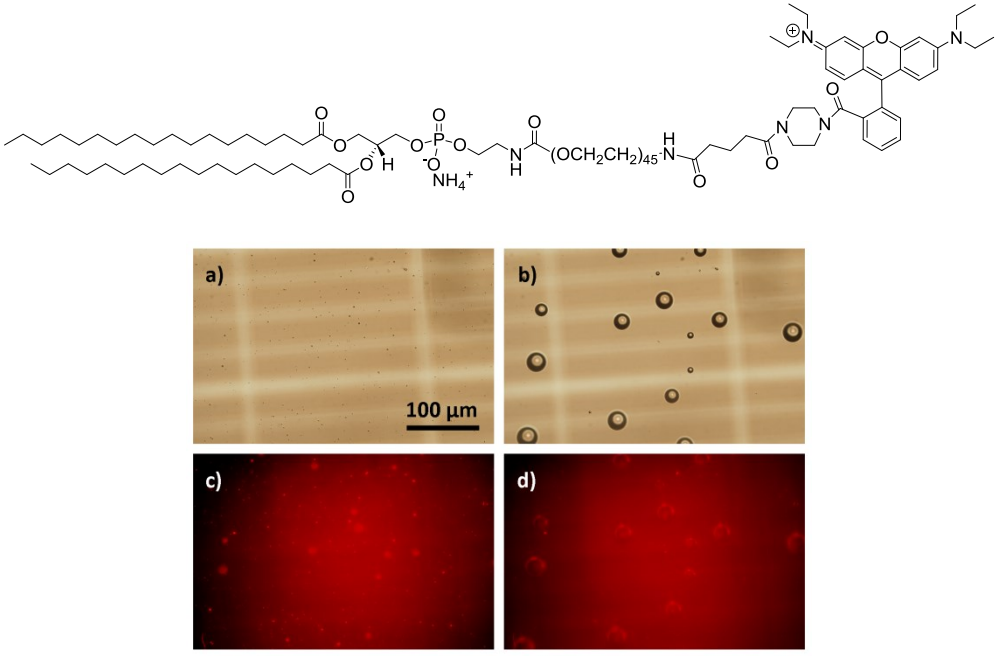


Figure 4.14: Top: Structure of **4.3**. Bottom: Images of microbubbles containing 1 mol% **4.3** (40 x magnification). a) and b) show brightfield images before and after laser irradiation respectively. c) and d) are fluorescent images of the same field-of-view taken in immediate succession during irradiation. 100 times dilution with PBS.

It was expected that no fluorescence would be observed for **4.2** until the pH was decreased, therefore measurements were taken before and after adjustment to pH 3.5 for this phospholipid. Minor changes were observed at neutral pH (see Appendix **Figure A.24**), however at pH 3.5 the same phenomenon was noted as that described above. This is shown in the **Figure 4.15**. The size of these microbubbles were analysed after pH change to ensure that this did not affect the results. These microbubbles (individual results) changed from 2.05 to

2.14 µm in size and increased in concentration from 5.33 x 10^8 to 1.26 x 10^9 MB/ mL (see Appendix **Table A.14**). There is no reason for this increase in concentration and is likely the result of different fields-of-view showing random microbubble numbers. These values can be loosely labelled as unchanged.

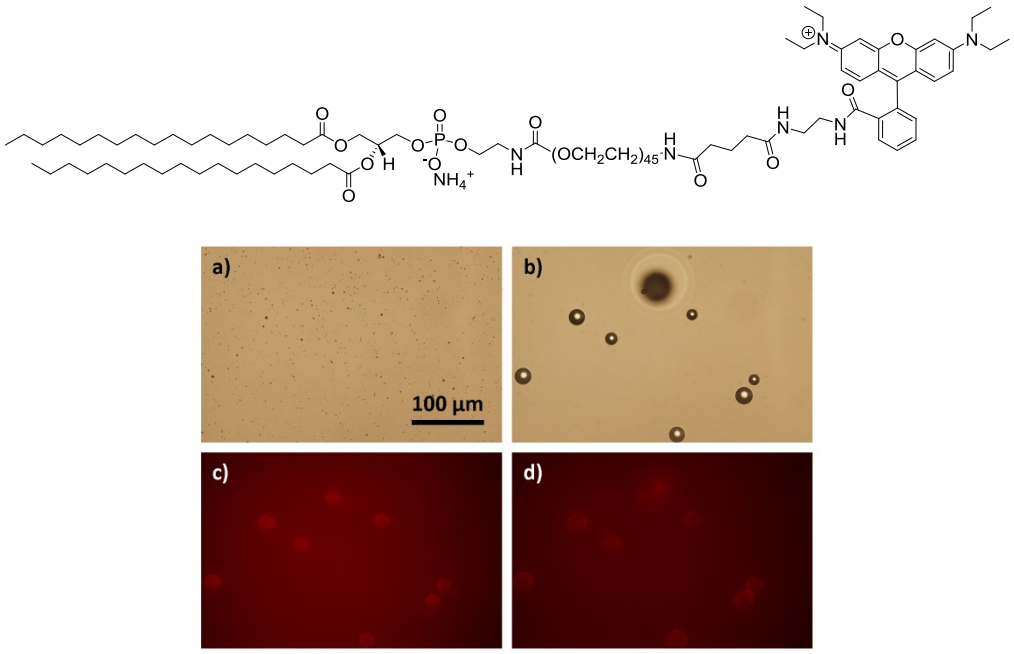


Figure 4.15: Top: Structure of **4.2**. Bottom: Images of microbubbles containing 1 mol% **4.2** at pH 3.5 (40 x magnification). a) and b) show brightfield images before and after laser irradiation respectively. c) and d) are fluorescent images of the same field-of-view taken in immediate succession during irradiation. 100 times dilution with PBS. The dark circle observed in b) is caused by a microbubble adhered to the base of the hemocytometer and out of the focal zone.

The reason for this effect upon irradiation must be due to the absorbance by the rhodamine moiety. This is promising for future nanodroplet work as it indicates that this rhodamine can induce expansion of the surface.

In order to confirm fluorophore incorporation into the microbubbles, 1 mol% **4.3** microbubbles were purified by centrifugation. Due to the buoyancy of microbubbles, they float under these conditions, forming a cake. The liquid underneath was removed and replaced by approximately the same volume.[58, 59]

The microbubbles could not be measured immediately after centrifugation as they scatter laser light, preventing accurate fluorescent measurements. The solutions were therefore left open to air for 3 weeks until all bubbles had disappeared and the solution was translucent before measurement. The results, displayed in **Figure 4.16**, show clearly that the fluorophore

is retained in the solution after purification and is therefore incorporated into the microbubbles. The reduction in fluorescence after purification can be attributed to two things. First, the process of centrifugation will destroy some microbubbles, resulting in the loss of some incorporated fluorophore. Secondly, the volume of solvent removed and added will contain an error, therefore the concentration cannot be assumed to be constant.

Irrespective of this reduction in fluorescence intensity, it is clear that these modified phospholipids are incorporated into microbubbles.

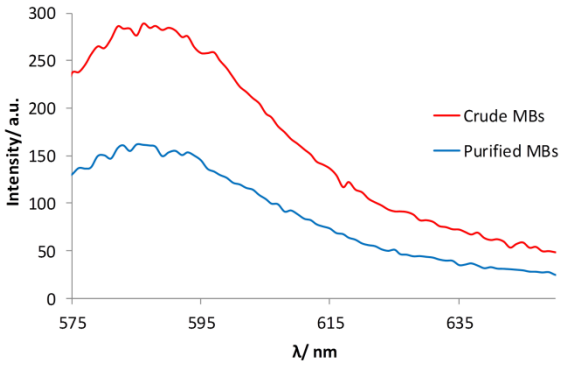


Figure 4.16: Fluorescence emission of microbubbles containing 1 mol% **4.3** with and without centrifugal purification. Measurements taken after microbubble destruction. No dilution, λ_{ex} 565 nm.

4.3.4 Acoustic Characterisation

The acoustic properties of these formulations were confirmed by ultrasound measurements performed by Shengtao Lin, Dept. of Bioengineering, Imperial College London. The results are shown in **Figure 4.17** and prove that all microbubble formulations are acoustically active.

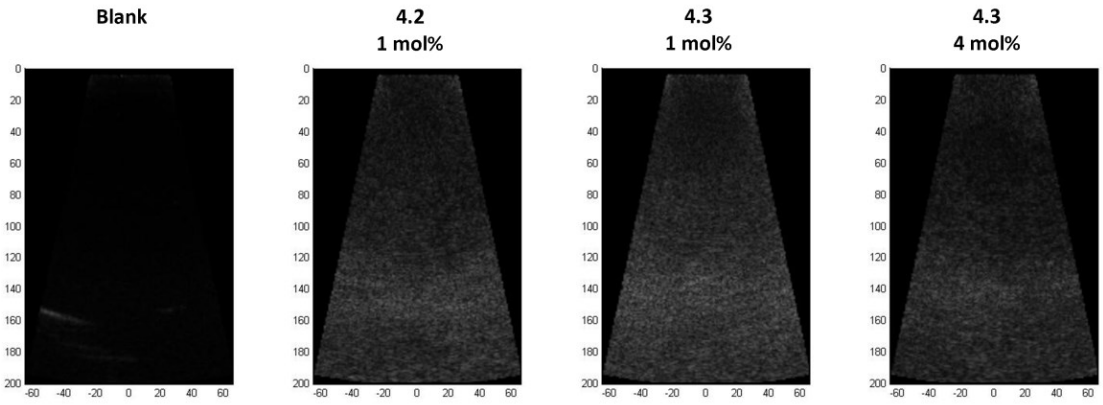


Figure 4.17: Acoustic measurements of solutions. Left to right: water, microbubbles containing 1 mol% **4.2**, microbubbles containing 1 mol% **4.3** and microbubbles containing 4 mol% **4.3**. Measurements performed on a Verasonics ultrasound imaging system equipped with a P4-2v probe (2 MHz imaging frequency at a Mechanical Index of 0.08). 1.7 L H_2O was rested for 5 min following which 20 µL of the microbubble solution was added.

4.4 Nanodroplet Formation and Characterisation

As discussed in the introduction, nanodroplets can be synthesised by condensation of microbubbles.[60] Briefly, microbubbles were synthesised as previously. These were cooled in a brine ice bath for 2 min and pressurised by 60 mL of air using a syringe. The visual change from moving between physical forms of these formulations can be seen in **Figure 4.18**. Microbubbles form an opaque milky solution (colour dependent upon lipid composition) whereas nanodroplets form a turbid translucent solution. These droplets were shown to routinely have a diameter of 200-300 nm in literature and subsequently yield microbubbles of the order of 1-5 µm.[60]

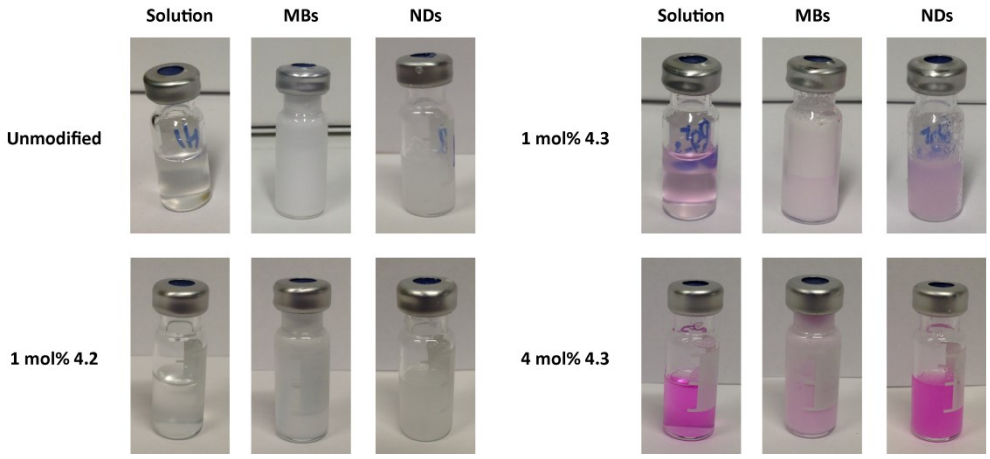


Figure 4.18: Pictures of phospholipid solutions (left), microbubble solutions (middle) and nanodroplet solutions (right) of various formulations. Left Top: unmodified nanodroplet formulation; Left Bottom: 1 mol% **4.2** formulation; Right Top: 1 mol% **4.3** formulation; Right Bottom: 4 mol% **4.3** formulation. These images show the visual difference between formulations and phospholipid structures.

4.4.1 Microscope Images

In order to prove that microbubbles were no longer present in these samples, they were analysed under a microscope, as performed above. The size of nanodroplets means that they should not be visible using this technique. In addition, while microbubbles float, nanodroplets sink and therefore will not be in the same focal plane.[22]

The nanodroplet formulation containing 4 mol% **4.3** was chosen for this test as it is always fluorescent and provides the greatest opportunity to observe fluorescence from nanodroplets. Little could be observed at the typical 100 times dilution, therefore images were taken of the concentrated sample. A few large bubbles were present on the surface and a number of

objects on the bottom which are likely large droplets (**Figure 4.19a** and **b**). In order to determine whether these droplets contained fluorescent phospholipid, images were taken during laser excitation.

Upon irradiation, large microbubbles immediately started forming and grew over time, as shown by **Figure 4.19c**. When brightfield images were taken after irradiation, very large bubbles were observed both floating (**d**) and adhered to the bottom (**e**). When gently agitated, those adhered to the bottom detached and floated to the top. This shows that some nanodroplets are vaporising into microbubbles. This phenomenon is not unexpected as large nanodroplets require less energy to vaporise than smaller ones. This explains the formation of very large microbubbles as large nanodroplets will result in large microbubbles.

It should be noted that due to the concentration being 100 times that usually measured, the number of nanodroplets vaporising is very small in comparison to the normal number of microbubbles in a solution.

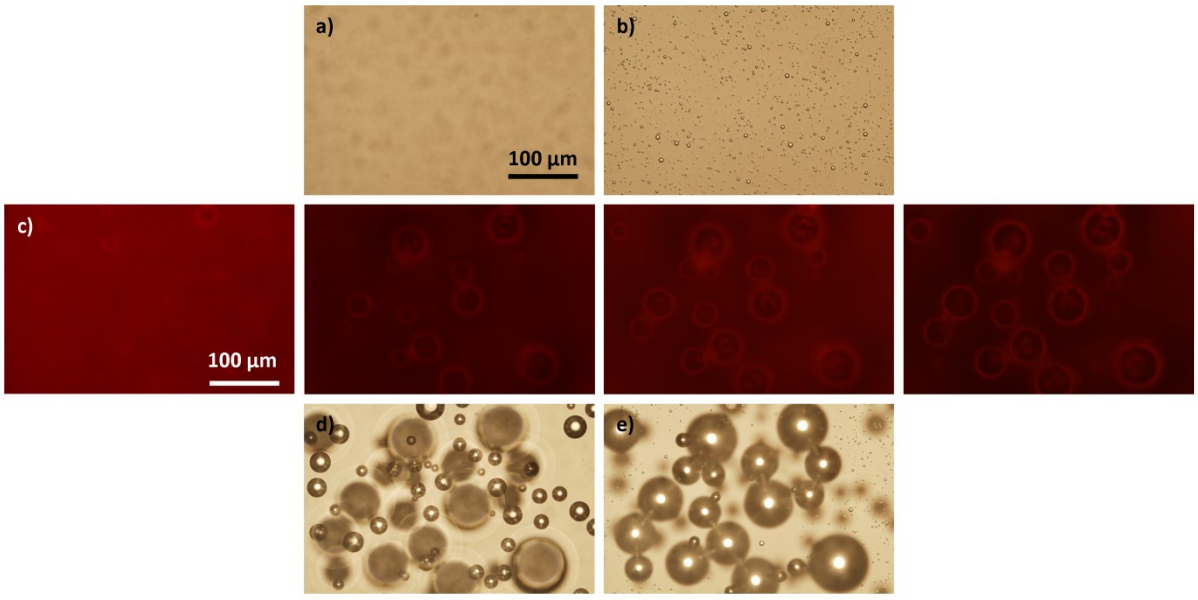


Figure 4.19: Images of nanodroplets formed from 4 mol% **4.3** before (top), during (middle) and after (bottom) fluorescence measurement. a) Brightfield surface image (where microbubbles are expected); b) brightfield image focussed on the base (where nanodroplets are expected); c) focus on base during fluorescence measurements. Left to right over time; d) brightfield surface image after irradiation; e) brightfield image focussed on the base after irradiation. Solution used at concentration synthesised.

Unmodified nanodroplets were also tested in order to determine whether this vaporisation was the result of fluorophore incorporation. These images (see Appendix **Figure A.25**) show that some vaporisation also occurs in this instance. This implies that it is not the absorbance

of light that is causing this vaporisation. It could be that the laser increases the temperature, causing the least stable (largest) nanodroplets to vaporise.[61] In both instances a large number of droplets persist even after irradiation, indicating that this laser is not sufficient to vaporise the majority of nanodroplets.

4.4.2 DLS Measurement

The sizes of these nanodroplets were determined by dynamic light scattering (DLS). The values quoted are an average of three measurements. Unfortunately this is not an ideal method for characterisation of these nanodroplets as a laser is used to measure the scattering and determine size. After the measurement was performed, it was noticed that gas bubbles had formed on the outside of the chamber as demonstrated in **Figure 4.20**. This was unexpected as the laser wavelength used was outside the fluorophore range (830 nm) and this technique has been used in literature to characterise fluorophore-labelled nanodroplets.[22, 25]

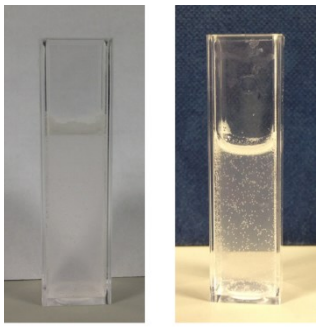


Figure 4.20: Example of a sample a) before and b) after DLS measurement.

In order to minimise this effect, DLS measurement times were decreased from 300 s to 60 s in some instances, with results shown in **Figure 4.21**.The size of all of these nanodroplets is small enough to allow for the EPR effect to cause accumulation in cancerous tissues (< 780 nm).[21] Strangely, those nanodroplets containing **4.2** are approximately twice the size of others, however due to the issues with measurement this data is not overly reliable. Repeatable data could not be obtained for samples containing 4 mol% **4.3**.

These problems with laser irradiation make these samples difficult to size using alternative methods. For example confocal microscopy is often used on fluorescent samples, however the sensitivity of these nanodroplets to laser irradiation could also present problems when using this technique.

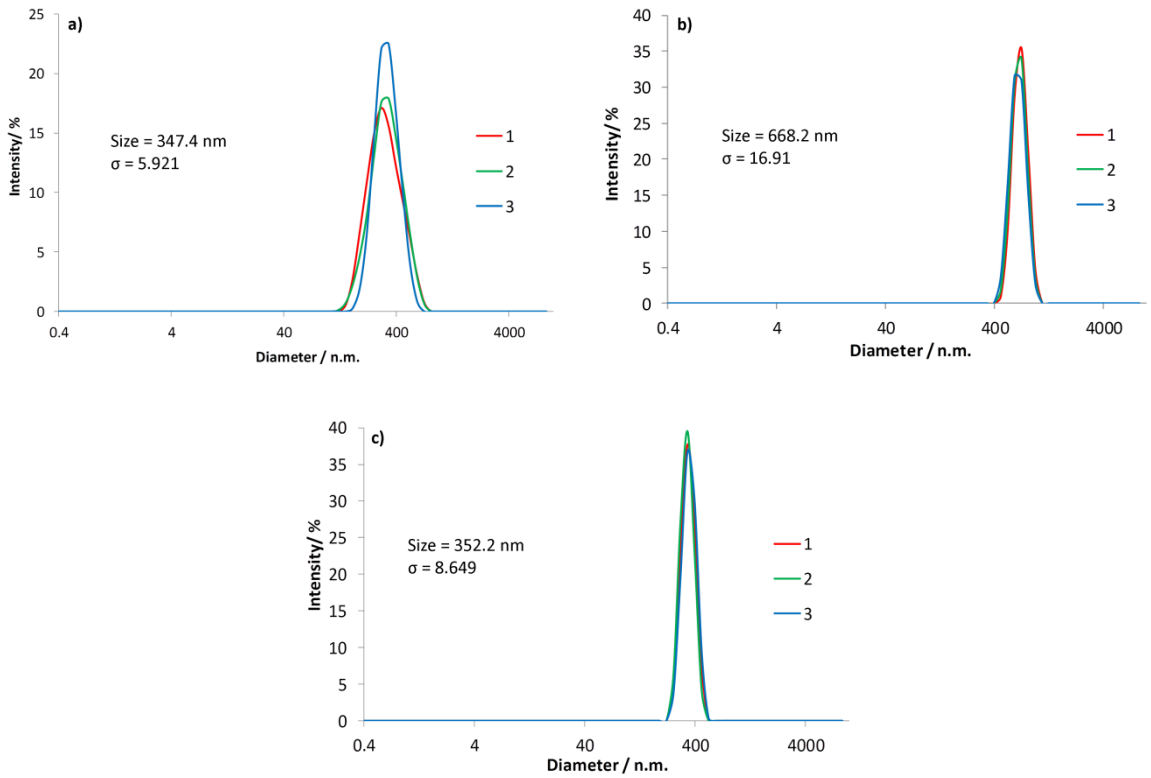


Figure 4.21: DLS measurements of nanodroplet solutions. a) Unmodified nanodroplets, measurements run for 300 s; b) 1 mol% **4.2** nanodroplets, measurements run for 60 s; c) 1 mol% **4.3** nanodroplets, measurements run for 60 s. Average sizes and standard deviations given.

4.5 Nanodroplet Vaporisation

In order to determine whether these nanodroplets can be vaporised using laser irradiation, a compatible laser was sought. The requirements were that it could excite the fluorophore in these nanodroplets at the absorbance wavelength (560 and 565nm for **4.2** and **4.3** respectively) using nanosecond pulses. The energy requirements for this laser are unknown, however similar systems have used a fluence of 22.6 mJ/ cm^2,[25] however this used a different fluorophore.

The closest laser system that could be found was a Nd:YAG solid state laser which had a pulse length of 5 ns, an energy of 1.8 mJ per pulse and a light guide of 3 mm diameter, resulting in a fluence of approximately 6.4 mJ/ cm^2. The samples were analysed after 30 s irradiation at 1 Hz using brightfield microscopy.

As these were preliminary experiments, it was decided only to test nanodroplets containing **4.3** as these should respond to laser irradiation at all pH values, eliminating one variable. 1 mol% and 4 mol% samples were diluted by 10 times, following the concentration used in

relevant literature.[25] No discernible difference was observed between control and irradiated samples (images of these samples after irradiation and comparisons to control samples are shown in the Appendix, **Figure A.26**). In order to determine whether this was due to a problem with nanodroplet concentration, the 1 mol% sample was also irradiated at the actual nanodroplet concentration. The results, shown in **Figure 4.22**, show no noticeable change between the two samples.

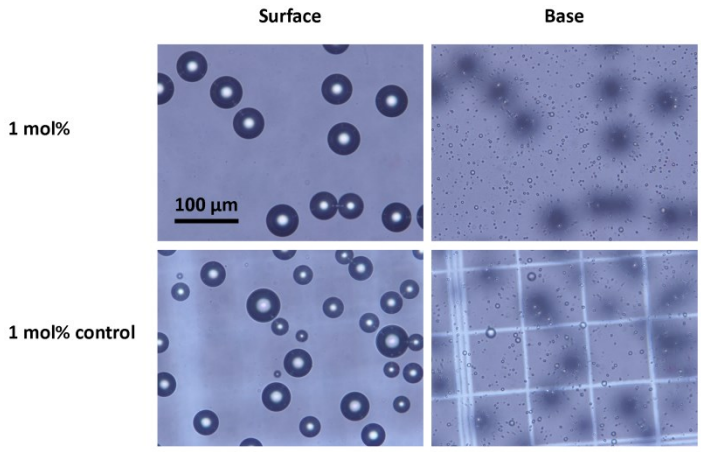


Figure 4.22: Brightfield images taken of nanodroplet solutions containing 1 mol% of **4.3** with and without (control) laser irradiation. All experiments performed without dilution of nanodroplet solution. Images taken without further dilution. Left: Surface image where microbubbles are expected; Right: base images where nanodroplets are expected. Top: nanodroplets after laser irradiation; Bottom: nanodroplets without laser irradiation.

While disappointing, this does not mean that these nanodroplets will not vaporise under the correct conditions. As discussed, the laser fluence was low in comparison to those used in literature. These measurements were also taken at ambient temperature, approximately 21 ^{o}C, however *in vivo* the temperature will be increased to about 37 ^{o}C. It has been suggested that at higher temperatures, the core gas becomes more volatile, resulting in the same laser fluence vaporising a larger proportions of droplets.[22]

Additionally, in literature imaging was performed with 5 ns laser pulses with 20 pulses/ s and a fluence of 20 mJ cm^{-2}.[22] This is significantly different from the conditions used in this study. Reviewing this information, there seem to be two solutions: increase the temperature to induce vaporisation at the same laser fluence, or increase the power/ pulse length or pulse number.

Due to the experimental set up, it would be difficult to heat the sample in the laser laboratory. Additionally, the laser fluence was at the maximum for this piece of equipment at the desired

wavelength. While the number of pulses and the duration of irradiation could be changed, it has been noted that almost all vaporisation events occur during the first laser pulse,[22] therefore the fact that none have been observed indicates that this laser is not appropriate for these droplets.

Due to these results with this equipment, other samples were not analysed using this technique.

4.6 Conclusions

Fluorescent phospholipids which are both pH sensitive and pH insensitive have been synthesised. The structural similarity of the fluorophore (based upon rhodamine B) in both of these will allow for direct comparison of their properties and distribution in future work. These phospholipids have provided evidence that modified DSPE-PEG_{2000}-X phospholipids are incorporated into microbubbles; this is relevant to all phospholipids discussed in this thesis and proved their utility in imaging.

The pH sensitive phospholipid **4.2** has a pH switching range between about 6.5 and 3 that is potentially relevant to the pH difference between tumorous and normal tissue. This pH switching ability has also been observed in microbubbles, where fluorescent images were taken at pH 7.6 and 3.5.

These microbubbles were formed into nanodroplets, which exhibited potential for vaporisation due to their sensitivity to laser irradiation. Further attempts to characterise these nanodroplets using confocal microscopy may provide evidence of smaller droplets which may not be sensitive to the lasers used in this characterisation method.

Future work in determining the vaporisation of these droplets requires a laser better suited to the properties of these nanodroplets. This is problematic because the known lasers designed for nanodroplet vaporisation, which can be combined with ultrasound and photoacoustic imaging, are tuneable only in the NIR due to the deeper imaging depth allowed by these wavelengths. It may be possible to find an individual laser with the required properties to vaporise the nanodroplets, however additional information will be difficult to obtain.

In order to combat this problem but maintain the properties of these phospholipids, future work should aim to develop NIR dyes that exhibit the same pH switching ability. Recently, silicon derivatives of rhodamine dyes have been developed that fit this description,[62, 63] a

selection of which are shown in **Figure 4.23**. At the Institute of Cancer Research, the range of excitation wavelengths for the relevant equipment is 680-980 nm, therefore not all of these are suitable. Determination of the pH sensitivity of silicon-rhodamine probes has also been performed, and a turning on of fluorescence in the pH range 7-5 was observed.[64]

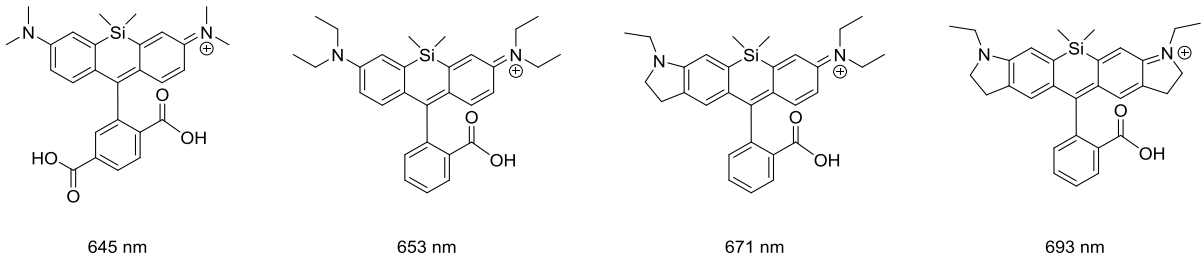


Figure 4.23: Silicon-rhodamine derivatives and their absorbance λ_{max} values.

Clearly, the synthesis and characterisation of the phospholipids described above is only the beginning of this work. Their applications in dual-modal (pH sensitive) fluorescence-ultrasound imaging, selective fluorescence imaging (through the blinking of fluorescence) and determination of phospholipid fate are clear. Biological studies in these areas will hopefully elucidate how the addition of a PEG chain into the fluorescent phospholipid alters its properties.

The application of these phospholipids in the formation of pH sensitive nanodroplets is very exciting but requires further work.

4.7 References

1. H. Chen and S. H. Thorne, in *Current Protocols in Cytometry*, John Wiley & Sons, Inc., 2001.
2. M. Rudin and R. Weissleder, *Nat. Rev. Drug Discov.*, 2003, **2**, 123-131.
3. A. Masedunskas, O. Milberg, N. Porat-Shliom, M. Sramkova, T. Wigand, P. Amornphimoltham and R. Weigert, *Bioarchitecture*, 2012, **2**, 143-157.
4. C. Gutierrez-Merino, I. C. B. de Romanelli, L. I. Pietrasanta and F. J. Barrantes, *Biochemistry*, 1995, **34**, 4846-4855.
5. J. W. Nichols and R. E. Pagano, *Biochemistry*, 1981, **20**, 2783-2789.
6. Y. Cen, Y.-M. Wu, X.-J. Kong, S. Wu, R.-Q. Yu and X. Chu, *Anal. Chem.*, 2014, **86**, 7119-7127.
7. R. Pagano and R. Sleight, *Science*, 1985, **229**, 1051-1057.
8. A. Moumtzi, M. Trenker, K. Flicker, E. Zenzmaier, R. Saf and A. Hermetter, *J. Lipid Res.*, 2007, **48**, 565-582.
9. M. Koivusalo, J. Alvesalo, J. A. Virtanen and P. Somerharju, *Biophys. J.*, **86**, 923-935.
10. B. R. Lentz, *Chem. Phys. Lipids*, 1993, **64**, 99-116.
11. A. B. Dhanikula and R. Panchagnula, *Lipids*, 2008, **43**, 569.

12. J. H. Fendler, *J. Phys. Chem.*, 1980, **84**, 1485-1491.
13. R. W. Sinkeldam, N. J. Greco and Y. Tor, *Chem. Rev.*, 2010, **110**, 2579-2619.
14. J. W. Nichols, *J. Biol. Chem.*, 1987, **262**, 14172-14177.
15. R. I. MacDonald, *J. Biol. Chem.*, 1990, **265**, 13533-13539.
16. Z. Chen, S. Yang and D. Xing, *Opt. Lett.*, 2016, **41**, 1636-1639.
17. E. Qu, Z. Dai, X. Liang, Y. Qian, S. Wang, H. Ke and J. Wang, *Ultrasound Med. Biol.*, 2015, **41**, 1905-1912.
18. L. Mai, A. Yao, J. Li, Q. Wei, M. Yuchi, X. He, M. Ding and Q. Zhou, *PLoS One*, 2013, **8**, e61224.
19. M. J. Benchimol, M. J. Hsu, C. E. Schutt, D. J. Hall, R. F. Mattrey and S. C. Esener, *Soft Matter*, 2013, **9**, 2384-2388.
20. Y. Liu, J. A. Feshitan, M.-Y. Wei, M. A. Borden and B. Yuan, *J. Biomed. Opt.*, 2014, **19**, 0850051-0850059.
21. S. K. Hobbs, W. L. Monsky, F. Yuan, W. G. Roberts, L. Griffith, V. P. Torchilin and R. K. Jain, *Proc. Natl. Acad. Sci.*, 1998, **95**, 4607-4612.
22. A. Hannah, G. Luke, K. Wilson, K. Homan and S. Emelianov, *ACS Nano*, 2014, **8**, 250-259.
23. P. S. Sheeran, J. E. Streeter, L. Mullin, T. O. Matsunaga and P. A. Dayton, *Ultrasound molecular imaging with customizable nanoscale phase-change contrast agents: An in-vitro feasibility study*, IEEE International Ultrasonics Symposium, 2012.
24. J. D. Dove, P. A. Mountford, T. W. Murray and M. A. Borden, *Biomed. Opt. Express*, 2014, **5**, 4417-4427.
25. S. Lin, A. Shah, J. Hernández-Gil, A. Stanziola, B. I. Harriss, T. O. Matsunaga, N. Long, J. Bamber and M.-X. Tang, *Photoacoustics*, 2017, **6**, 26-36.
26. G. P. Luke, A. S. Hannah and S. Y. Emelianov, *Nano Lett.*, 2016, **16**, 2556-2559.
27. E. Strohm, M. Rui, I. Gorelikov, N. Matsuura and M. Kolios, *Biomed. Opt. Express*, 2011, **2**, 1432-1442.
28. R. Nikita, S. Minseok, W. Ross, B.-P. Eleonora, L. Mike, M. Naomi, G. Jean, F. S. Foster and N. B. Peter, *Phys. Med. Biol.*, 2012, **57**, 7205.
29. P. A. Mountford, S. R. Sirsi and M. A. Borden, *Langmuir*, 2014, **30**, 6209-6218.
30. P. A. Mountford, A. N. Thomas and M. A. Borden, *Langmuir*, 2015, **31**, 4627-4634.
31. Y. Ma, S. Tong, G. Bao, C. Gao and Z. Dai, *Biomaterials*, 2013, **34**, 7706-7714.
32. Y. Hama, Y. Urano, Y. Koyama, M. Bernardo, P. L. Choyke and H. Kobayashi, *Bioconjugate Chem.*, 2006, **17**, 1426-1431.
33. M. R. Longmire, M. Ogawa, Y. Hama, N. Kosaka, C. A. S. Regino, P. L. Choyke and H. Kobayashi, *Bioconjugate Chem.*, 2008, **19**, 1735-1742.
34. M. Beija, C. A. M. Afonso and J. M. G. Martinho, *Chem. Soc. Rev.*, 2009, **38**, 2410-2433.
35. Q. A. Best, R. Xu, M. E. McCarroll, L. Wang and D. J. Dyer, *Org. Lett.*, 2010, **12**, 3219-3221.
36. W. Zhang, B. Tang, X. Liu, Y. Liu, K. Xu, J. Ma, L. Tong and G. Yang, *Analyst*, 2009, **134**, 367-371.
37. C. Rivas, G. J. Stasiuk, M. Sae-Heng and N. J. Long, *Dalton Trans.*, 2015, **44**, 4976-4985.
38. J. R. Griffiths, *Br. J. Cancer*, 1991, **64**, 425-427.
39. K. H. Drexhage, *J. Res. Natl. Stand. Sec. A*, 1976, **80A**, 421-428.

40. L. Bi, *Patent, WO2014063033 A3*, 2014.
41. T. Nguyen and M. B. Francis, *Org. Lett.*, 2003, **5**, 3245-3248.
42. I. L. Arbeloa and P. R. Ojeda, *Chem. Phys. Lett.*, 1981, **79**, 347-350.
43. M. S. T. Gonçalves, *Chem. Rev.*, 2009, **109**, 190-212.
44. M. K. Johansson and R. M. Cook, *Chem. Eur. J.*, 2003, **9**, 3466-3471.
45. K. Zhou, H. Liu, S. Zhang, X. Huang, Y. Wang, G. Huang, B. D. Sumer and J. Gao, *J. Am. Chem. Soc.*, 2012, **134**, 7803-7811.
46. A. N. Lukyanov, Z. Gao, L. Mazzola and V. P. Torchilin, *Pharm. Res.*, 2002, **19**, 1424-1429.
47. B. Ashok, L. Arleth, R. P. Hjelm, I. Rubinstein and H. Önyüksel, *J. Pharm. Sci.*, 2004, **93**, 2476-2487.
48. K. Zhou, Y. Wang, X. Huang, K. Luby-Phelps, B. D. Sumer and J. Gao, *Angew. Chem. Int. Ed.*, 2011, **50**, 6109-6114.
49. T. I. Al-Warhi, H. M. A. Al-Hazimi and A. El-Faham, *J. Saudi Chem. Soc.*, 2012, **16**, 97-116.
50. X. Zhang, Y. Shiraishi and T. Hirai, *Org. Lett.*, 2007, **9**, 5039-5042.
51. S. Kim, M. Fujitsuka, N. Tohnai, T. Tachikawa, I. Hisaki, M. Miyata and T. Majima, *Chem. Commun.*, 2015, **51**, 11580-11583.
52. C. Rivas, G. J. Stasiuk, J. Gallo, F. Minuzzi, G. A. Rutter and N. J. Long, *Inorg. Chem.*, 2013, **52**, 14284-14293.
53. A. Minta, J. P. Kao and R. Y. Tsien, *J. Biol. Chem.*, 1989, **264**, 8171-8178.
54. R. Sjöback, J. Nygren and M. Kubista, *Spectrochim. Acta A Mol. Biomol. Spectrosc.*, 1995, **51**, L7-L21.
55. M. J. Doughty, *Ophthalmic Physiol. Opt.*, 2010, **30**, 167-174.
56. M. Adamczyk and J. Grote, *Bioorg. Med. Chem. Lett.*, 2003, **13**, 2327-2330.
57. C. E. Schutt, S. D. Ibsen, M. J. Benchimol, M. J. Hsu and S. C. Esener, *Small*, 2014, DOI: 10.1002/smll.201302786, n/a-n/a.
58. M. A. Borden, J. E. Streeter, S. R. Sirsi and P. A. Dayton, *Mol. Imaging*, 2013, **12**, 357-363.
59. C. R. Anderson, X. Hu, J. Tlaxca, A.-E. Decleves, R. Houghtaling, K. Sharma, M. Lawrence, K. Ferrara and J. J. Rychak, *Invest. Radiol.*, 2011, **46**, 215-224.
60. P. S. Sheeran, S. Luois, P. A. Dayton and T. O. Matsunaga, *Langmuir*, 2011, **27**, 10412-10420.
61. P. S. Sheeran, V. P. Wong, S. Luois, R. J. McFarland, W. D. Ross, S. Feingold, T. O. Matsunaga and P. A. Dayton, *Ultrasound Med. Biol.*, 2011, **37**, 1518-1530.
62. G. Lukinavičius, K. Umezawa, N. Olivier, A. Honigmann, G. Yang, T. Plass, V. Mueller, L. Reymond, I. R. Corrêa Jr, Z.-G. Luo, C. Schultz, E. A. Lemke, P. Heppenstall, C. Eggeling, S. Manley and K. Johnsson, *Nat. Chem.*, 2013, **5**, 132-139.
63. T. Wang, B. Wang, X. CHAI and Q. WU, *Patent, WO 2016029671 A1*, 2016.
64. W. Zhu, X. Chai, B. Wang, Y. Zou, T. Wang, Q. Meng and Q. Wu, *Chem. Commun.*, 2015, **51**, 9608-9611.

Chapter 5

Ultrasound Mediated Delivery of Contrast Agents

People that have contributed to this chapter:

Sophie Morse

Michael Coogan

Charlotte Rivas

5.1 Introduction

The human body uses a complex system of vessels and capillaries which allow for the exchange of molecules between the blood and surrounding tissue through porous endothelial walls. This is facilitated by open interendothelial junctional spaces and active pinocytosis which allows for transcellular diffusion.[1] The blood-brain barrier (BBB) is designed to restrict extravasation of molecules from the blood stream into the brain in order to maintain the environment necessary for cerebral function.[2] This is made up of tight endothelial junctions and has minimal pinocytosis in addition to other features,[1, 2] excluding almost 100 % of large molecules and 98 % of small molecules.[3] Various transport mechanisms across the BBB are demonstrated in **Figure 5.1a**. Many factors affect the vascular permeability of a molecule across the BBB, such as size, charge, polarizability, hydrogen bonding ability and lipophilicity. In general, charged molecules or those with hydrogen bonding potential (> 10 donors/ acceptors) are unable to leave the blood stream due to strong intermolecular forces retaining them in the polar environment.[3, 4] In addition, brain efflux transporters such as P-glycoprotein (P-gp) are known to transport molecules out of the brain that have a positive charge at pH 7.4, high lipophilicity and multiple aromatic groups.[5] As many drugs and contrast agents fit into this category, rapid removal from the brain can prevent use of these agents.

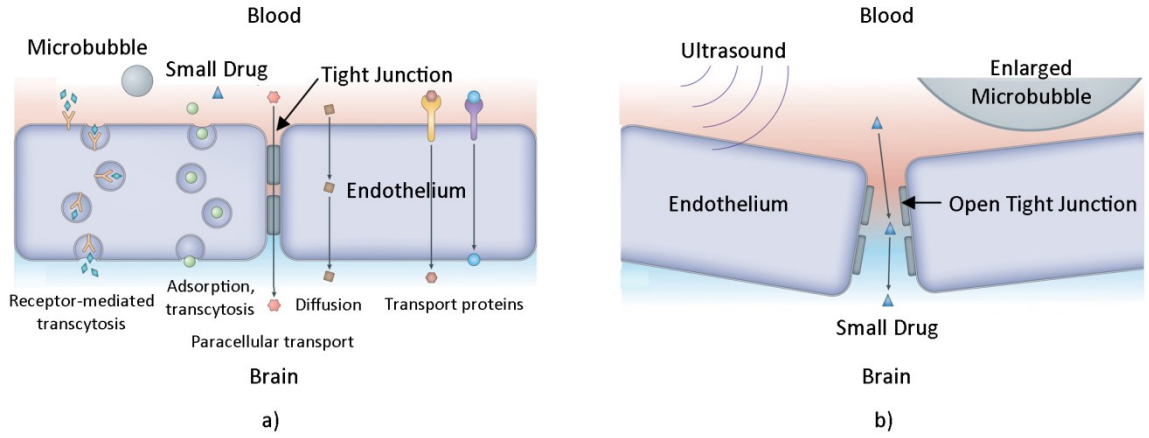


Figure 5.1: Diagrammatic representation of the methods that can be used to cross the BBB. a) Endogenous mechanisms that enable transport across the BBB. Tight junctions prevent passage of small-molecule drugs; b) the use of ultrasound in combination with microbubbles causes oscillations which transiently open tight junctions, allowing for small-molecule drugs to enter the brain. Reproduced with permission[2, 6] and modified prior to use.

Numerous methods have been researched to overcome this barrier in order to deliver drugs or contrast agents to the brain without using invasive techniques. The modification of drugs to increase lipophilicity increases their permeability across membranes, however this results in rapid removal from the blood and minimises the increase in brain uptake. The design of molecules to use endogenous transport systems results in non-targeted and diffuse distributions, while chemical disruption the blood brain barrier also causes a generalised increase in uptake of all plasma components which can be toxic to brain cells.[1, 3, 7]

It has been found that localised transient opening of the BBB can be achieved using a focused ultrasound (FUS) beam.[8-10] FUS allows for the concentration of acoustic energy into a spot of a few millimetres in size deep in the body.[11, 12] The addition of microbubbles has been shown to reduce the energy required to disrupt the BBB when used in combination with FUS, reducing thermal effects and potential tissue damage.[11, 13] The exact mechanism of BBB opening using microbubbles is unknown, with several proposed mechanisms. These include acoustic radiation forces which cause microbubbles to move in the direction of wave propagation, forcing them into contact with the vessel,[14] and the shear stress exerted on surrounding cells when microbubbles oscillate in an ultrasound field.[11] This results in multiple methods for transport through the BBB such as the widening of tight junctions between cells and channel formation.[15] This is demonstrated in **Figure 5.1b**. This ambiguity limits the application of this technique as it makes the development of methods to enhance delivery without causing damage difficult.

Initial work demonstrated that the use of high pressure FUS improved delivery but also increased tissue damage,[16] with subsequent research performed to reduce these side effects. It has been shown that BBB disruption can last for 4 hours after sonication,[17] with no delayed effects noted by MRI or histological analysis up to 4 weeks after sonication.[18] Work has been undertaken to minimise adverse effects through the use of low frequencies[19] and the development of extremely short (2.3 μs) pulse sequences that use low peak-rarefactional pressures (PRP).[20, 21] It has also been shown that high power ultrasound can damage the endothelium.[15]

Many studies are performed using MRI to observe BBB opening both with and without[12, 13] the use of contrast agents such as Magnevist (Berlex Laboratories Inc., Wayne, USA)[12, 19] and Omniscan (Amersham Health, Oslo, Norway).[22] This has developed into MRI-guided FUS as this allows for image-guided target planning and real-time temperature mapping.[12, 23, 24]

Alternative studies use fluorescently tagged molecules to allow for detection post-sonication. These are typically dextran polymers of 3-70 kDa.[20, 25]

While useful to quantify the opening of the BBB, these molecules are not useful for therapeutic or selective imaging. Using this technique, antibody agents have been used to target dopamine[12] and HER2/neu receptors,[24] the latter of which are indicative of breast cancer and can also cause brain metastases. In both instances, an MRI contrast agent was administered after sonication and it was found that the MRI signal change correlated well with the amount of antibody delivered. Recently, the chemotherapeutic drug doxorubicin (DOX) has been studied for application with this technique. This allowed for therapeutic concentrations to be reached which could not be achieved under normal conditions, with low accumulation in untreated brain tissue.[23] These show the promise of this delivery method for cancer therapy.

5.1.1 Modalities for Brain Imaging

The use of gadolinium in the brain is of questionable value owing to safety concerns. Of particular importance are the deposits that have been observed in the brain of patients that have undergone numerous MRI scans, as discussed in Chapter 1. With these safety concerns in the imaging community, it may be appropriate to consider alternative imaging modalities that do not use gadolinium and require much lower concentrations of contrast agent.

Fluorescence staining is currently used for *ex vivo* work owing to the high sensitivity and resolution available. Fluorescence is also able to detect changes in the local environment that other modalities cannot; this was discussed in Chapter 4. The pH of the brain is known to be important in normal brain activity and has been monitored using various MRI techniques.[26, 27] Due to the sensitivity of fluorescence emission, it may be possible to use this method for analysis. The depth penetration *in vivo* is poor however, particularly when performing imaging through the skull, which may limit this application.

An alternative modality is PET, where low concentrations are required and the signal can penetrate through the skull. PET is most commonly applied to brain studies using ^{18}F-FDG to study glucose metabolism.[28] This is transported across the BBB by the glucose transporter, after which it is phosphorylated and trapped within the brain.

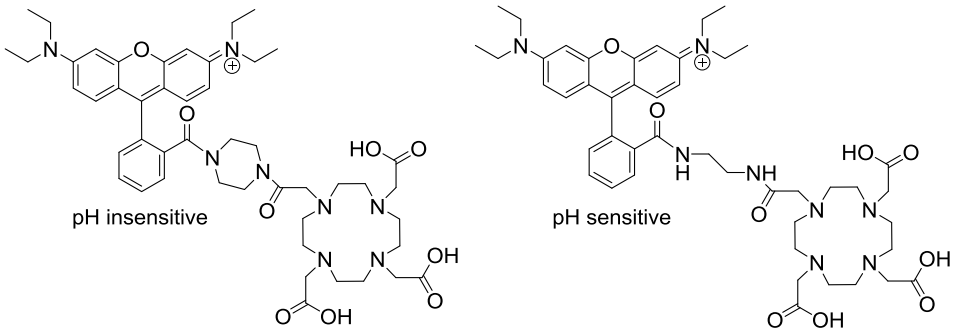
The development of new PET tracers is slowed by the difficulty of crossing the BBB, as described above for general contrast agent and drug molecule design. Of those that show acceptable uptake, the majority are ^{11}C- and ^{18}F-based.[28, 29]

5.1.2 Aims

Imaging of the brain using FUS BBB disruption has been limited to MRI and fluorescently-tagged contrast agents. These differ significantly from each other in structure, being small and large (macro)molecules respectively. In addition, the use of different imaging modalities for detection creates the opportunity for discrepancies between the results. This project aims to synthesise a small molecule incorporating the ability to image simultaneously using MRI and fluorescence in order to combine the ability to image effectively *in vivo* and *ex vivo*. This can then be compared to the distribution of both types of contrast agent in literature.

The use of PET and fluorescence may also be able to provide information that MRI cannot. A mean baseline pH of 7.05 has been reported for the brain,[27] with the pH of brain cancer reported to be more alkaline than in other regions.[30] Therefore, the pH sensitive rhodamine derivative from Chapter 4 may be applicable to the monitoring of pH inside the brain, although the pH range is not ideal. In addition, work using ^{68}Ga to visualise cerebral activity as an alternative to ^{11}C and ^{18}F would be interesting.

These goals have led to the design of molecules **5.1** and **5.2** shown in **Figure 5.2**. These incorporate a macrocyclic ligand in order to safely chelate gadolinium[31] and to coordinate ^{68}Ga. In addition, a pH sensitive rhodamine fluorophore has been incorporated in order to determine whether the pH change in the brain can be detected using the 'on-off' switch. A pH insensitive rhodamine derivative has also been used in order to obtain comparable, reliable fluorescence results. These structures are very similar in order to allow for comparison of the data obtained.

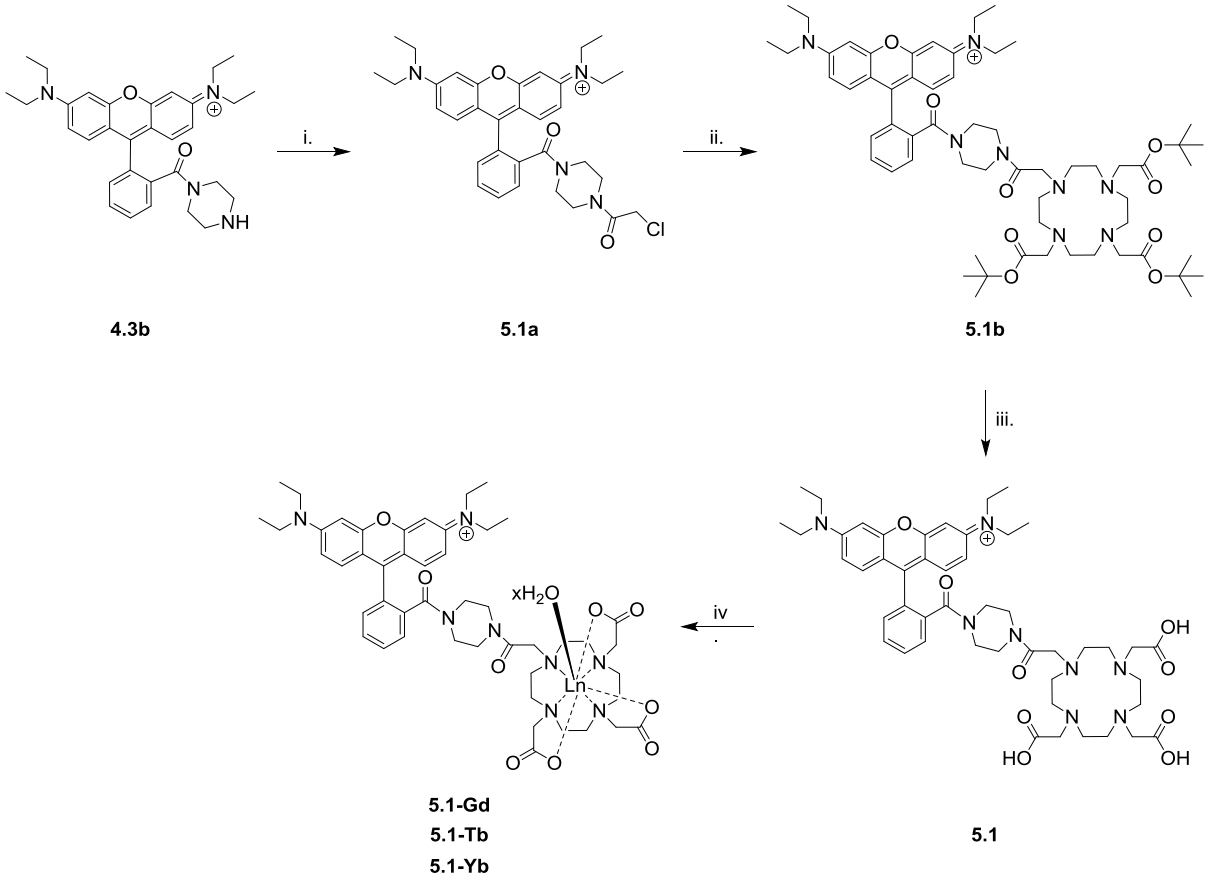


5.1 **5.2**

Figure 5.2: Structures of the probes designed for delivery across the BBB using FUS. **5.1** can be used as a pH insensitive fluorescence probe whilst **5.2** can be used in pH sensitive fluorescence imaging. Both can be coordinated to Gd for MRI or ^{68}Ga for PET dual-modal imaging.

5.2 Dual-Modal MRI-Fluorescence Probe

The probe designed for dual-modal MRI-fluorescence incorporated a pH insensitive rhodamine B moiety to ensure signal from any complex that crosses the BBB. This design incorporates 17 hydrogen bond donors/ acceptors and a positive charge, which should prevent transport across the BBB without sonication. In addition, this molecule presents characteristics that are likely to be recognised by P-gp, resulting in removal from the brain. This is desirable as it will reduce potential side effects of the contrast agent which could occur if it became trapped within the brain. This effect is a compromise as the lifetime within the brain must be sufficient for imaging prior to efflux.



Scheme 5.1: Synthesis of DO3A-Rh+ **5.1** and the complexation of various lanthanides. i. Chloroacetyl chloride, NEt_3, DCM, 3 h, 0 ^oC, 62 % yield; ii. **3.2**, K_2CO_3, CH_3CN, 48 h, 82 ^oC, 66 % yield; iii. TFA, DCM, 16 h, RT, 74 % yield; iv. $LnCl_3.6H_2O$, pH 5.5, 24 h, RT, 65-87 % yield.

5.2.1 Synthesis

The synthesis of DO3A-Rh+ **5.1** used the rhodamine B derivative **4.3b** from Chapter 4 and a synthetic protocol similar to that used in literature for **5.2-Gd** (shown in **Figure 5.2**), as shown in **Scheme 5.1**.[32] These syntheses proceeded in good yields and could be monitored using conventional techniques. Purification of the final complex was performed by LCMS or reverse phase chromatography and analysed my mass spectrometry.

5.2.2 Characterisation

5.2.2.1 Fluorescence Measurements

The absorbance and emission spectra of compound **5.1-Gd** were determined by UV-vis. and fluorescence measurements respectively, as shown in **Figure 5.3a**. These gave a rhodamine absorbance λ_{max} of 565 nm and a corresponding emission λ_{max} of 585 nm. No emission from Gd is observed as it emits in the UV range (312 nm).[33]

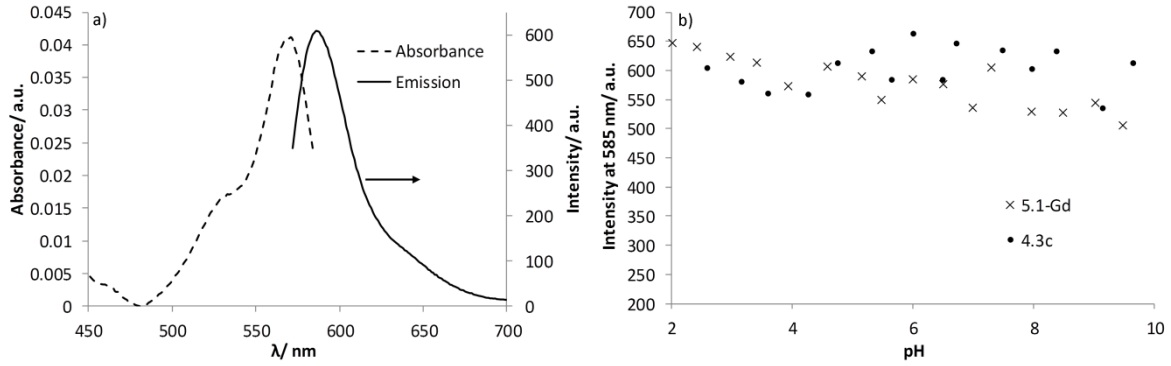


Figure 5.3: a) Absorbance (left axis) and emission (right axis) spectra of **5.1-Gd**, 0.625 μM, PBS pH 7.3; b) graphs showing the pH dependence of **5.1-Gd** emission, with comparison to **4.3c** emission. Measurements taken by gradual pH change using 1 M NaOH/ HCl. λ_{ex} = 565 nm, 0.625 μM, PBS.

In order to confirm that the emission of this molecule is pH independent, the fluorescence intensity was measured over a pH range, as shown in **Figure 5.3b**. This shows that there is little change in the emission with pH, which correlates well with the emission from the rhodamine component alone (molecule **4.3c**).

5.2.2.2 T_1 Relaxation Studies – Determination of Relaxivity (r_1)

The T_1 of **5.1-Gd** at different concentrations was determined by Peter Haycock, Dept. of Chemistry, Imperial College London. These values were used to determine the relaxivity (r_1) of this compound, as shown in **Figure 5.4**. This produced an r_1 of 7.8 mM^{-1} s^{-1} at 400 MHz,

which is unexpectedly high, particularly as the analogous compound **5.2-Gd** has a reported r_1 of 3.8 mM^{-1} s^{-1} at 400 MHz.[32] There are a few possible explanations for this such as an increase in the hydration number (q), an increase in rotational correlation time (τ_R) or a decrease in the water residence lifetime (τ_m).

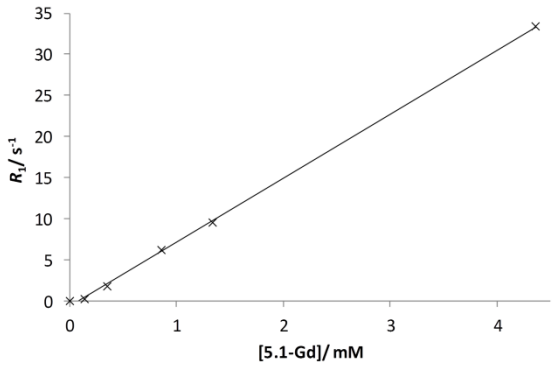


Figure 5.4: Graph showing the change in longitudinal relaxation (R_1) as a function of concentration for **5.1-Gd**. Gradient = r_1 = 7.77 ± 0.10 mM^{-1} s^{-1}.

The modification of rhodamine in order to prevent ring closing has increased the steric bulk around the amide that coordinates to the lanthanide centre in **5.2-Gd**, which could prevent binding. If this does not coordinate, an additional water molecule may interact with the metal. A similar compound with q = 2 exhibited an r_1 of 8.8 mM^{-1} s^{-1} at 400 MHz.[32] In DOTA complexes using the same piperazine linker, it has been found that q = 1, implying that in molecule **5.1-Gd** this linker should not change the hydration number.[34]

The size of the molecule is largely unchanged from **5.2-Gd**, therefore this is unlikely to increase τ_R and therefore r_1. One explanation for an increase in this parameter is if these molecules aggregate in solution due to low solubility or strong intramolecular interactions. The linear relationship between concentration and R_1 shown in **Figure 5.4** indicates that there is no change in aqueous form between these concentrations. This would mean that aggregates would have to form below a concentration of 0.14 mM; this phenomenon has been observed in literature.[35] Alternatively, the piperazine linker in **5.1-Gd** could inhibit independent rotation of the DOTA-Gd section of the complex when compared to **5.2-Gd**, which has a freely rotating ethylene linker. This would mean that the DOTA-Gd moiety would rotate at the speed of the entire molecule in **5.1-Gd**, which would cause an increase in τ_R and a resulting increase in r_1. This effect of the piperazine linker when compared to a flexible bridge has been observed in literature.[34]

Finally, τ_m is typically decreased by increasing the steric crowding around the water coordination site,[36] however the small modification of the structure from the literature compound makes this unlikely. This can also be affected by the residual charge, with positive charges decreasing the exchange rate and therefore r_1; this is the opposite to the observed effect.[37]

5.2.2.3 Luminescence Studies – Determination of Hydration Number (q)

In order to determine the *q* value of **5.1-Gd**, ligand **5.1** was coordinated with luminescent lanthanides. Measurement and analysis of the luminescent lifetimes of these complexes in H_2O and D_2O has been shown to effectively determine the *q* value of the Gd analogue.[38] This analysis cannot be performed directly on Gd as the HOMO-LUMO gap is too large to allow for efficient quenching of the excited state by the OH vibrational states in H_2O (the cause of the lifetime differences observed in H_2O and D_2O).[38] Lanthanides such as Tb, Eu and Yb are typically used, however with compound **5.2-Eu** difficulties with Tb contamination were found,[39] therefore this metal was omitted.

As discussed in Chapter 1, a sensitiser is often used in order to excite the lanthanide and promote fluorescence. Rhodamine moieties have been used in literature as sensitisers for lanthanides, making **5.1** an acceptable ligand for this measurement.[32, 40]

The longer lifetime of Tb^{3+} makes it more compatible with the equipment available than Yb^{3+},[33] therefore this metal was coordinated initially; in these experiments no Tb^{3+} emission was observed. This could be due to incompatible energy levels of Tb^{3+} and rhodamine, with the former reported at ~ 20,500 cm^{-1} ($^5D_4$ state)[41] whilst the triplet state of ring-open rhodamine 6G has been reported at ~17,000 cm^{-1}.[40] Although the structure of this rhodamine differs from the molecule in question, these indicate that either no transfer or thermally activated back transfer could occur.[33]

In order to determine whether this energy transfer is occurring, additional experiments attempting to excite the terbium directly were performed by Michael Coogan, Dept. of Chemistry, University of Lancaster. Test samples of $TbCl_3$ in methanol at similar concentrations to those used for **5.1-Tb** were run to optimise these measurements, with the characteristic Tb^{3+} emission observed (**Figure 5.5a**). This was then exchanged for the sample and measurements taken with 300-370 nm excitation, however only rhodamine emission was observed (and a harmonic of the excitation wavelength). No rhodamine absorption peak was

observed at these wavelengths in the UV-vis. spectra (not shown), implying that little rhodamine emission should occur with excitation at this wavelength.

These measurements were also performed with a time gate as the long lifetime of the lanthanide emission allows for removal of background fluorescence using this method. In these measurements, no emission was observed, as shown in **Figure 5.5b**. Lifetime measurements showed only short-lived fluorescence attributed to rhodamine, as shown in **Figure 5.6**. There are a number of explanations for this. Firstly, it could be that the rhodamine emission is so strong and direct excitation of terbium so weak that it could not be detected; however, the ability to observe excitation of $TbCl_3$ indicates that this should be possible. It is also possible that the Tb^{3+} in this complex may not be excited under the same conditions as 'naked' Tb^{3+} due to the absorption of rhodamine (the inner filter effect[42]). The most likely explanation however is that upon excitation Tb^{3+} is undergoing energy transfer to the rhodamine moiety due to the overlap between Tb^{3+} emission and rhodamine excitation in this molecule.

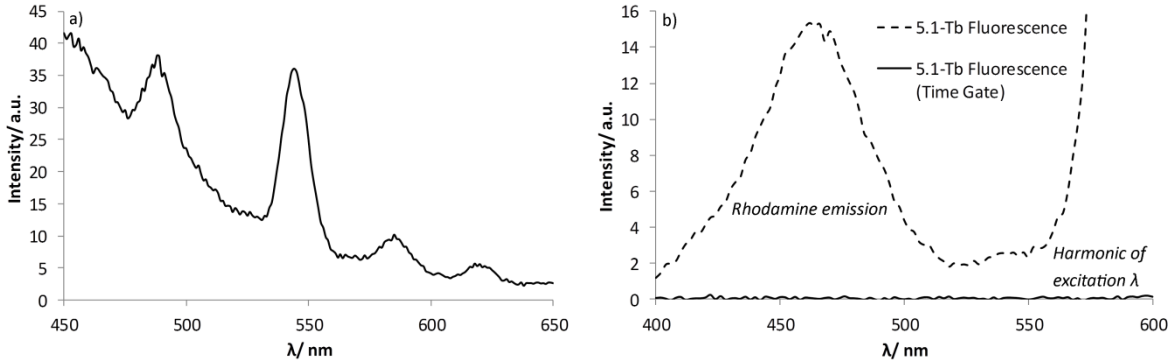


Figure 5.5: Emission spectra of Tb^{3+}. a) $TbCl_3$ emission in MeOH upon excitation at 370 nm; b) **5.1-Tb** emission in H_2O upon excitation at 360 nm both with and without a time gate.

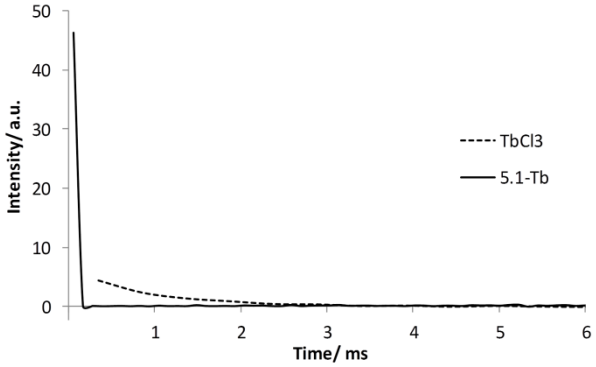


Figure 5.6: Lifetime measurements performed on $TbCl_3$ and **5.1-Tb** showing the absence of Tb emission in the latter.

It was subsequently decided to form the complex **5.1-Yb**. Due to the much lower energy level of Yb (~ 10,200 cm^{-1})[38] this backwards energy transfer should not occur, however shorter emission lifetimes (μs as opposed to ms for Eu and Tb) are typical for this metal.[38] Yb emission is expected at 980 nm, with sensitisation using rhodamine derivatives having been performed in literature.[40] No Yb emission could be observed when measurements were performed with or without a time gate. This was attributed to rhodamine fluorescence dominating the fluorescence spectrum and the inability to set a time gate short enough on the equipment available.

For this reason, this sample was also analysed by Michael Coogan. Although some emission could be observed in the NIR, the lifetime of this was found to be very short (1.8 ns) and identical in both H_2O and D_2O. This indicates that either this emission is not from Yb or that it is also being quenched by the rhodamine (this would not be a normal energy transfer process due to the locations of the energy levels).

Owing to these problems, the q value of this complex could not been confirmed, however comparison to similar literature compounds incorporating the same piperazine modification on DOTA indicates that **5.2-Gd** should have $q = 1$.[34]

5.2.2.4 NMRD Profile – Aggregate Analysis

In literature, aggregate formation was determined through observation of a change in slope of the correlation between concentration and R_1 (as shown in **Figure 5.4**). This change was observed for compounds at concentrations of 0.3-0.4 mM.[35] As can be seen in **Figure 5.4**, the value at 0 mM does not fit in a straight line observed for points above 0.14 mM. It is possible that at a concentration between 0-0.14 mM (the lowest two measurement points) a change in slope could occur, indicting aggregate formation; this feature could also be caused by natural error. It should be noted that the Gd-containing compounds found to exhibit this behaviour in literature either contain hydrophobic chains[43] or large aromatic substituents[35] which cause micellation.

Nuclear magnetic relaxation dispersion (NMRD) profiles for **5.1-Gd** at 0.1 mM and 1.5 mM were obtained in order to determine whether this sample aggregates in solution, these are shown in **Figure 5.7**. This method requires fewer samples to be made up than analysis of R_1 values at many concentrations and can provide more detailed information.

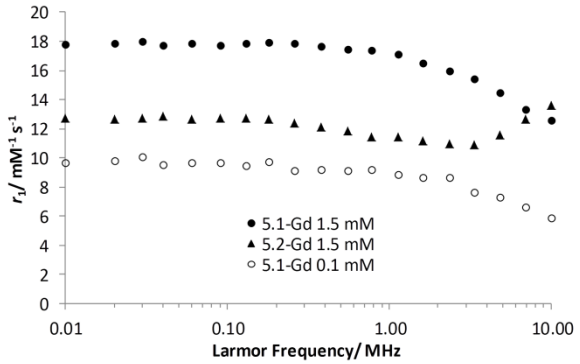


Figure 5.7: NMRD profiles of 5**.1-Gd** and **5.2-Gd** at 37 ^{o}C in H_2O (1.5 mM shaded symbols and 0.1 mM hollow symbols). Data for **5.2-Gd** obtained by Charlotte Rivas.[39]

Initially, it was observed that the relaxivity was lower at 0.1 mM than at 1.5 mM, indicating that there is aggregate formation at the higher concentration. However, the shape of both of these profiles is characteristic of small molecule Gd^{3+} compounds in which relaxivity is limited by τ_R. The relaxivity is higher at low fields, with a decrease from around 1 MHz (this decrease slows but continues from ~ 10-100 MHz).[44] The shape of these two curves are also almost identical across the entire frequency range, with an offset of ~ 10 mM^{-1} s^{-1}. This indicates that the difference between these profiles cannot be caused by a parameter that is field dependent, which includes the τ_R and water τ_m. The parameters which could apply are a change in q and the Gd-H_2O distance, which should not change with concentration[35] unless concentration dependent aggregation modifies the hydration state.[45] There is also the possibility of differences at field values of 10-100 MHz (cannot be measured by this equipment), however it is likely that these differences would be observed prior to this, as can be seen for **5.2-Gd** at 1.5 mM.

It should be noted however that aggregates (confirmed by DLS) exhibiting high relaxivities have displayed this shape profile within the field range assessed in **Figure 5.7**.[46] Monomeric complexes have also been shown to exhibit the same profile shape with high relaxivities, which has been accounted for by strong π-π intermolecular interactions which slow rotation (τ_R) without causing aggregate formation.[35] Both of these examples could be used to explain the observed concentration dependent relaxivity difference: in the former instance, aggregate formation at high concentrations could cause the increased relaxivity without an observed effect on the NMRD profile. In the latter case, the increased concentration could enhance the intermolecular interactions, slowing τ_R and increasing r_1. DLS measurements on the sample at the concentrations used in **Figure 5.7** would be able to determine whether aggregation is

the origin of these results, however this was not performed due to time constraints. These explanations do not account for the higher relaxivities observed for **5.2-Gd** than **5.1-Gd**.

In profiles containing slowly tumbling aggregates, a high field 'hump' is observed between 10-100 MHz. Although this equipment cannot measure above 10 MHz, the beginning of this increase can be observed for **5.2-Gd** in **Figure 5.7**[35] (this data was obtained by Charlotte Rivas in our group). As can be seen, not only does this molecule exhibit significantly reduced relaxivity when compared to **5.1-Gd** at the same concentration, it also displays different behaviour as the magnetic field strength increases. This implies that it is unlikely that **5.1-Gd** forms aggregates in solution. As the only differences between molecules **5.1-Gd** and **5.2-Gd** are the charge state of the rhodamine and the linker to the DO3A chelate, it is likely that the neutral rhodamine in **5.2-Gd** is acting as a hydrophobic moiety and causing micelle formation. This is surprising considering the lower relaxivity observed for this molecule, as aggregation would be expected to increase this value.

Although the origin of the high relaxivity has not been completely elucidated due to difficulty in quantifying *q* values, there seems to one explanation that can be hypothesised using the data obtained and literature precedence. The change in linker from ethylenediamine in **5.2-Gd** to piperazine in **5.1-Gd** inhibits independent rotation of the DOTA-Gd moiety and causes the entire molecule to rotate as one, increasing the rotational correlation time without aggregation and thus increaseing r_1.

5.2.3 In Vivo Studies

This probe was then used in combination with FUS and microbubbles to mediate delivery into a mouse brain, with all *in vivo* work performed by collaborator Sophie Morse and colleagues, Dept. Bioengineering, Imperial College London. These results may be discussed in more detail in the thesis of Sophie Morse (currently not submitted).[47]

As the size distribution and stability of the microbubbles is important for successful BBB opening (they must oscillate under the ultrasound fields used) SonoVue (Bracco SpA, Milan, Italy) microbubbles were selected. The spray-drying procedure used in the synthesis of commercial microbubbles provides a more homogenous distribution of sizes when compared to in house microbubbles, making them better suited to this application.[48, 49]

The protocol used for FUS-mediated delivery is similar to that described in literature, with ultrasound focussed on the left hippocampus[21] and the right hippocampus used as a control. After delivery, the animal was sacrificed and the brain analysed by microscopy. Preliminary

results obtained for this molecule using short pulse sequences at 0.66 MPa are shown in **Figure 5.8**. These show that probe **5.1-Gd** does not penetrate the BBB without sonication, with uniform delivery upon sonication. There appears to be no damage under these conditions, which would cause a strong accumulation of the contrast agent along large vessels. In order to confirm this, staining experiments must be performed to prove that red blood cells are not present in the brain.

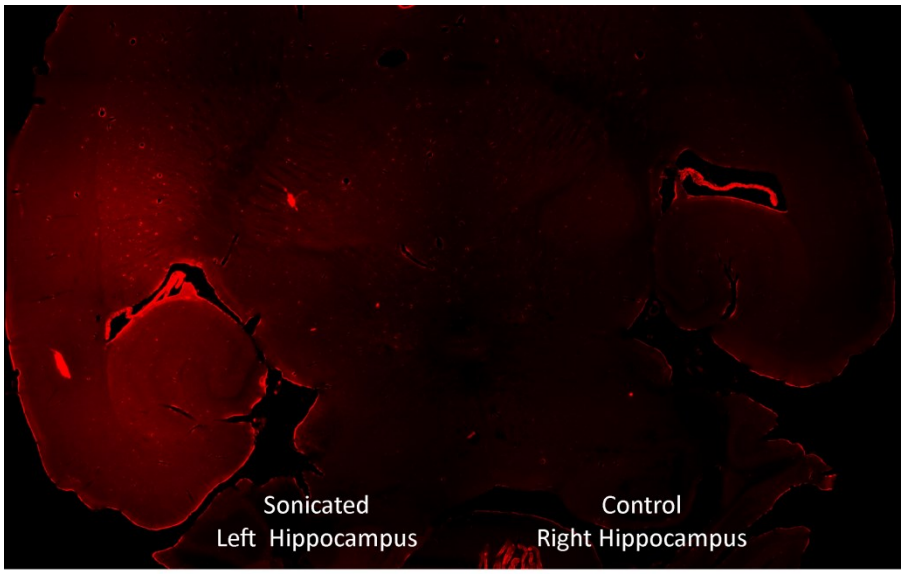


Figure 5.8: Fluorescence images of the sonicated and control sides of a mouse brain after sonication in the presence of microbubbles and **5.1-Gd**. Short pulse sequences at 0.66 MPa. x5 magnification. Image provided by Sophie Morse.[47]

The delivery of this contrast agent differed from fluorescently tagged dextran delivered under the same conditions (data not published and not shown). Further work is being performed to replicate this (n=3), confirm that there is no damage, quantify the increase in fluorescence between the two hemispheres and perform the same experiment with standard long pulse sequences to determine the effect on delivery.

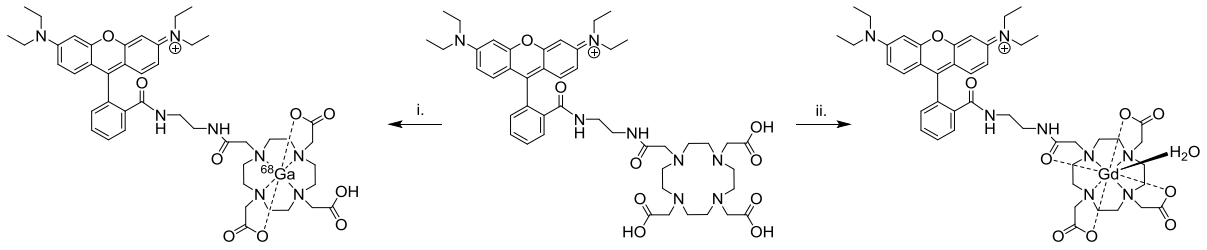
Due to the equipment available, no MRI studies have been performed on these samples, with the measurement of fluorescence deemed sufficient to determine delivery of the probe at this stage.

5.3 Dual-Modal PET-Fluorescence pH Sensitive Probe

This probe was designed as an extension of that discussed above in an attempt to incorporate pH sensitivity into the fluorescence emission, which may provide more detailed environmental information. In addition, the use of ^{68}Ga for PET as opposed to Gd MRI will avoid the use of potentially toxic Gd and will require lower concentrations for imaging purposes.

5.3.1 Synthesis and Characterisation

This work focussed on the use of a DO3A chelate attached to unmodified, pH sensitive rhodamine B, as shown in **Scheme 5.2**. This was used for three reasons: firstly synthetic protocols have been developed in our research group and published in literature for **5.2** (DO3A-Rh) and **5.2-Gd**,[32] allowing for facile synthesis. Secondly, it allows for the stable chelation of numerous metals (importantly Gd and ^{68}Ga), facilitating multiple imaging methods. Finally, it is structurally similar to probe **5.1**, allowing for reasonable comparison.



Scheme 5.2: Synthesis of ^{68}Ga or Gd chelates of DO3A-Rh **5.2**. i. $^{68}GaCl_3$, 0.2 M NaOAc buffer, 10 min, 90 ^{o}C, 25 % incorporation; ii. $GdCl_3.6H_2O$, pH 5.5, 24 h, RT, 74 % yield.

5.3.2 Radiolabelling

Extensive radiolabelling studies were not performed on this molecule, however ^{68}Ga was successfully incorporated into the molecule. Radiolabelling was performed using the iThemba generator eluted in 1 M HCl under similar conditions to those described in Chapter 4. Briefly, 0.5 mL $^{68}GaCl_3$ in 1 M HCl was added to 25 µg **5.2** in 1 mL 0.2 M pH 4.5 NaOAc buffer. This was heated to 90 ^{o}C for 10 min with 25 % incorporation, following which cartridge purification produced **5.2-^{68}Ga**. This has clearly not been optimised, but indicates that radiolabelling can be performed. The chromatograms are shown in **Figure 5.9**.

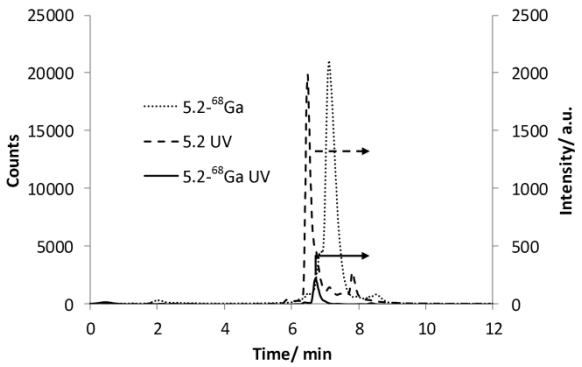


Figure 5.9: HPLC chromatograms showing the radiolabelling of **5.2** to form **5.2-^{68}Ga**. Chromatograms showing the retention times of **5.2** and **5.2-^{68}Ga** upon UV detection (right axis) and the corresponding radio chromatogram of **5.2-^{68}Ga** (left axis). UV peak expected at slightly earlier retention time than radio due to detectors set up.

5.3.3 *In Vivo* Studies

Ultrasound-mediated delivery of **5.2** was performed as discussed for probe **5.1-Gd** by Sophie Morse and colleagues. These results may be discussed in more detail in the thesis of Sophie Morse (currently not submitted).[47]

Due to the equipment available, it was not possible to perform this analysis on radioactive **5.2-^{68}Ga**, therefore initial studies using the ligand **5.2** only were performed in order to determine the viability of this approach. This analysis was performed using standard long pulse sequences at 0.98 MPa. This was repeated three times, with one example shown in **Figure 5.10**. Again, delivery can be observed with no obvious signs of damage and no unwanted probe diffusion into the mouse brain. Haematoxylin and Eosin (H&E) staining was performed in these experiments, with no sign of haemorrhage or red blood cell extravasation, confirming that no damage occurred.

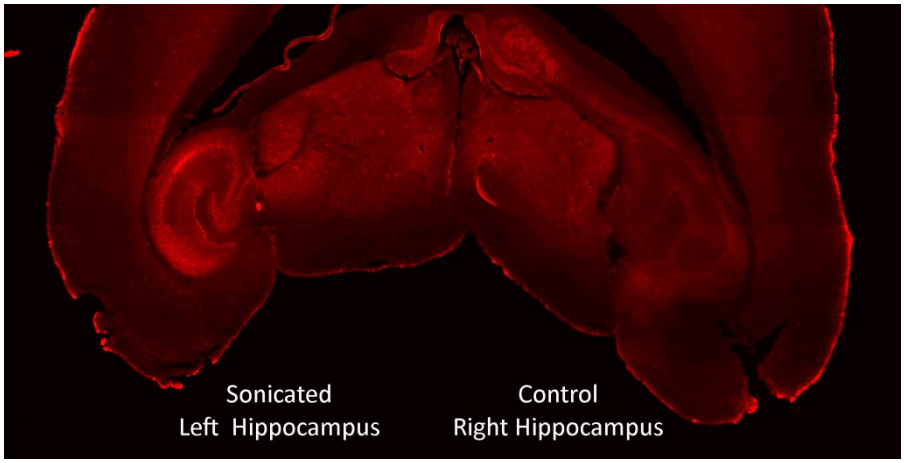


Figure 5.10: Fluorescence images of the entire mouse brain after sonication in the presence of microbubbles and **5.2** Long pulse sequences at 0.98 MPa. x5 Magnification. Image provided by Sophie Morse.[47]

The observation of fluorescence in the left hippocampus indicates that this brain environment must be acidic. In literature, **5.2-Gd** has displayed a pK_a of 5.11, with minimal fluorescence from about pH 7.[32] This value is not expected to vary significantly for **5.2** alone and implies that this region of the brain is more acidic than the typical values measured in literature.[27] This could be due to a number of biological factors such as the effect of sonication on the brain; however, due to the method used to fix the brain, it is also likely that the pH was modified during this process. This makes the pH sensitivity of questionable use in combination with this method of analysis. Despite this, delivery of **5.2** has proved effective under these conditions.

The increase in fluorescence between the sonicated and control regions was quantified in all three mouse brains, as shown in **Figure 5.11**. All of these show an increase, with the variability observed likely being caused by the exact location of sonication and the quality of the microbubbles injected.

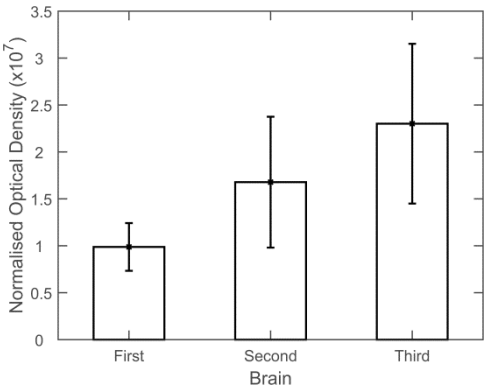


Figure 5.11: The increase in fluorescence from **5.2** on the targeted side of the brain when compared to the control region. Image provided by Sophie Morse.[47]

5.4 Conclusions

Two different contrast agents have been synthesised and successfully delivered into a mouse brain using focused ultrasound pulses. Neither probe was found to cross the BBB in the control region, indicating that these probes cannot diffuse across this membrane without aid. Two different pulse sequences were used, both of which showed delivery to the desired region and no obvious damage. Short pulse sequences are of interest due to their increased safety profile, therefore this result is positive for future work.

Future work will involve increasing the size of the data set (n = 3) and performing experiments using long pulse sequences to deliver **5.1-Gd**. This will allow for direct comparison of different pulse sequences using the same probe. Additional experiments are

being performed using large molecules under these conditions in order to form comparisons. Additional MRI studies will hopefully allow for corroboration of fluorescence and MRI delivery, confirming that Gd is chelated in this molecule.

Owing to the problems with the detection of pH sensitive fluorescence under the conditions used, it seems that radiolabelling of **5.1** could provide a useful alternative to MRI-based techniques. The pH insensitive fluorescence will eliminate complications that could arise from the use of **5.2**.

Finally, it would be advantageous to observe delivery of both **5.1** and **5.2** in live animals. This could allow for use of pH sensitive fluorescence from **5.2**, with facile monitoring also possible using MRI. This would also allow for determination of the lifetime of the probe in the brain as animals are rapidly sacrificed after delivery in this work. This could also be performed by delivering the probe and waiting set time intervals before sacrifice.

While cancer-related drug and antibody delivery has been achieved in literature (*vida supra*), the imaging of brain cancer *in vivo* has not been addressed in these studies. In addition, the advantages of peptides over antibodies (discussed in Chapter 1) could be extended to use in the brain, with peptides used to target the contrast agents discussed above to specific regions.

5.5 References

1. W. M. Pardridge, *Neuron*, 2002, **36**, 555-558.
2. N. J. Abbott, L. Ronnback and E. Hansson, *Nat. Rev. Neurosci.*, 2006, **7**, 41-53.
3. W. M. Pardridge, *NeuroRx*, 2005, **2**, 3-14.
4. M. D. Habgood, D. J. Begley and N. J. Abbott, *Cell. Mol. Neurobiol.*, 2000, **20**, 231-253.
5. T. J. Raub, *Mol. Pharm.*, 2006, **3**, 3-25.
6. G. Leinenga, C. Langton, R. Nisbet and J. Gotz, *Nat. Rev. Neurol.*, 2016, **12**, 161-174.
7. W. M. Pardridge, *Drug Discovery Today*, 2007, **12**, 54-61.
8. L. L. Bakay, T. F. Hueter, H. T. Ballantine, Jr and D. D. Sosa, *AMA Arch. Neurol. Psychiatry*, 1956, **76**, 457-467.
9. J. H. T. Ballantine, Eugene Bell and Jesus Manlapaz, *J. Neurosurg.*, 1960, **17**, 858-876.
10. A. H. Mesiwala, L. Farrell, H. J. Wenzel, D. L. Silbergeld, L. A. Crum, H. R. Winn and P. D. Mourad, *Ultrasound Med. Biol.*, 2002, **28**, 389-400.
11. N. Vykhodtseva, N. McDannold and K. Hynynen, *Ultrasonics*, 2008, **48**, 279-296.
12. M. Kinoshita, N. McDannold, F. A. Jolesz and K. Hynynen, *Biochem. Biophys. Res. Commun.*, 2006, **340**, 1085-1090.
13. N. Vykhodtseva, V. Sorrentino, F. A. Jolesz, R. T. Bronson and K. Hynynen, *Ultrasound Med. Biol.*, 2000, **26**, 871-880.

14. P. A. Dayton, J. S. Allen and K. W. Ferrara, *J. Acoust. Soc. Am.*, 2002, **112**, 2183-2192.
15. N. Sheikov, N. McDannold, N. Vykhodtseva, F. Jolesz and K. Hynynen, *Ultrasound Med. Biol.*, 2004, **30**, 979-989.
16. K. Hynynen, N. McDannold, N. Vykhodtseva and F. A. Jolesz, *Radiology*, 2001, **220**, 640-646.
17. N. Sheikov, N. McDannold, S. Sharma and K. Hynynen, *Ultrasound Med. Biol.*, 2008, **34**, 1093-1104.
18. N. McDannold, N. Vykhodtseva, S. Raymond, F. A. Jolesz and K. Hynynen, *Ultrasound Med. Biol.*, 2005, **31**, 1527-1537.
19. K. Hynynen, N. McDannold, N. Vykhodtseva, S. Raymond, R. Weissleder, F. A. Jolesz and N. Sheikov, *J. Neurosurg.*, 2006, **105**, 445-454.
20. J. J. Choi, K. Selert, F. Vlachos, A. Wong and E. E. Konofagou, *Proc. Natl. Acad. Sci.*, 2011, **108**, 16539-16544.
21. B. Baseri, J. J. Choi, Y.-S. Tung and E. E. Konofagou, *Ultrasound Med. Biol.*, 2010, **36**, 1445-1459.
22. J. J. Choi, M. Pernot, T. R. Brown, S. A. Small and E. E. Konofagou, *Phys. Med. Biol.*, 2007, **52**, 5509.
23. L. H. Treat, N. McDannold, N. Vykhodtseva, Y. Zhang, K. Tam and K. Hynynen, *Int. J. Cancer*, 2007, **121**, 901-907.
24. M. Kinoshita, N. McDannold, F. A. Jolesz and K. Hynynen, *Proc. Natl. Acad. Sci.*, 2006, **103**, 11719-11723.
25. T. Nhan, A. Burgess, E. E. Cho, B. Stefanovic, L. Lilge and K. Hynynen, *J. Control. Release*, 2013, **172**, 274-280.
26. V. A. Magnotta, H.-Y. Heo, B. J. Dlouhy, N. S. Dahdaleh, R. L. Follmer, D. R. Thedens, M. J. Welsh and J. A. Wemmie, *Proc. Natl. Acad. Sci.*, 2012, **109**, 8270-8273.
27. S. Vorstrup, K. E. Jensen, C. Thomsen, O. Henriksen, N. A. Lassen and O. B. Paulson, *J. Cereb. Blood Flow Metab.*, 1989, **9**, 417-421.
28. E. Salmon, C. Bernard Ir and R. Hustinx, *Semin. Nucl. Med.*, 2015, **45**, 541-551.
29. V. W. Pike, *Trends Pharmacol. Sci.*, 2009, **30**, 431-440.
30. J. B. Arnold, R. P. Kraig and D. A. Rottenberg, *J. Cereb. Blood Flow Metab.*, 1986, **6**, 435-440.
31. G. W. White, W. A. Gibby and M. F. Tweedle, *Invest. Radiol.*, 2006, **41**, 272-278.
32. C. Rivas, G. J. Stasiuk, J. Gallo, F. Minuzzi, G. A. Rutter and N. J. Long, *Inorg. Chem.*, 2013, **52**, 14284-14293.
33. D. Parker and J. A. G. Williams, *J. Chem. Soc., Dalton Trans.*, 1996, 3613-3628.
34. D. H. Powell, O. M. N. Dhubhghaill, D. Pubanz, L. Helm, Y. S. Lebedev, W. Schlaepfer and A. E. Merbach, *J. Am. Chem. Soc.*, 1996, **118**, 9333-9346.
35. S. Avedano, M. Botta, J. S. Haigh, D. L. Longo and M. Woods, *Inorg. Chem.*, 2013, **52**, 8436-8450.
36. S. Laus, R. Ruloff, É. Tóth and A. E. Merbach, *Chem. Eur. J.*, 2003, **9**, 3555-3566.
37. S. Faulkner and O. A. Blackburn, in *The Chemistry of Molecular Imaging*, eds. N. J. Long and W.-T. Wong, John Wiley & Sons, Inc, 2014, pp. 179-197.
38. A. Beeby, I. M. Clarkson, R. S. Dickins, S. Faulkner, D. Parker, L. Royle, A. S. de Sousa, J. A. Gareth Williams and M. Woods, *J. Chem. Soc. Perk. Trans. 2*, 1999, 493-504.
39. C. Rivas, Thesis, Dual-Modal Imaging Agents for Zinc Ion Sensing, Imperial College London, June 2015.

40. W. Huang, D. Wu, D. Guo, X. Zhu, C. He, Q. Meng and C. Duan, *Dalton Trans.*, 2009, **12**, 2081-2084.
41. D. Parker, *Coord. Chem. Rev.*, 2000, **205**, 109-130.
42. T. Larsson, M. Wedborg and D. Turner, *Anal. Chim. Acta*, 2007, **583**, 357-363.
43. K. C. Briley-Saebo, S. Geninatti-Crich, D. P. Cormode, A. Barazza, W. J. M. Mulder, W. Chen, G. B. Giovenzana, E. A. Fisher, S. Aime and Z. A. Fayad, *J. Phys. Chem. B*, 2009, **113**, 6283-6289.
44. R. B. Lauffer, *Chem. Rev.*, 1987, **87**, 901-927.
45. J. Costa, E. Balogh, V. Turcry, R. Tripier, M. L. Baccon, F. Chuburu, H. Handel, L. Helm, É. Tóth and A. E. Merbach, *Chem. Eur. J.*, 2006, **12**, 6841-6851.
46. H. Li, B. I. Harriss, A. Phinikaridou, S. Lacerda, G. Ramniceanu, B.-T. Doan, K.-L. Ho, C.-F. Chan, W.-S. Lo, R. M. Botnar, R. Lan, C. Richard, G.-L. Law, N. J. Long and K.-L. Wong, *Nanotheranostics*, 2017, **1**, 186-195.
47. S. Morse, Thesis, Not Submitted, Imperial College London.
48. E. G. Schutt, D. H. Klein, R. M. Mattrey and J. G. Riess, *Angew. Chem. Int. Ed.*, 2003, **42**, 3218-3235.
49. J. Alter, C. A. Sennoga, D. M. Lopes, R. J. Eckersley and D. J. Wells, *Ultrasound Med. Biol.*, 2009, **35**, 976-984.

Chapter 6

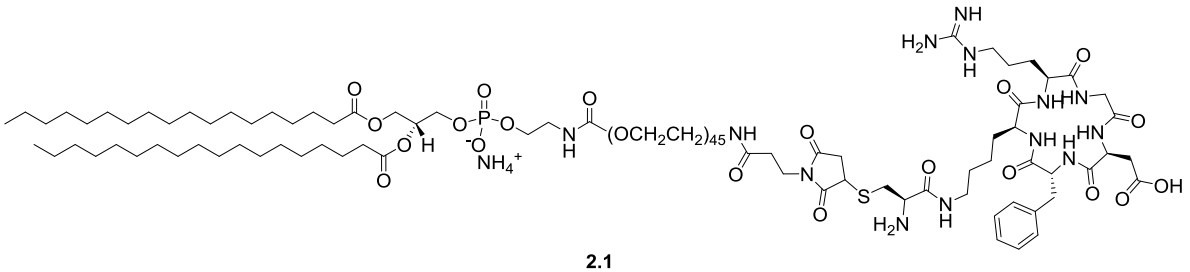
Conclusions and Future Work

In this thesis, numerous imaging modalities have been combined with microbubble ultrasound contrast agents to allow for dual-modal imaging of desired regions. Although a range of microbubbles are approved for clinical use, these cannot be used for molecular imaging as they do not target biological processes. For this reason, the initial goal of this work was to target microbubbles to cancer biomarkers. This was then combined with compatible modalities to allow for dual-modal, targeted imaging. This can enrich the information obtained and provide additional data such as whole-body biodistribution and extravascular imaging. Finally, an alternative use for microbubbles was explored in order to transiently open the blood-brain-barrier. This facilitates contrast agent delivery to desired regions of the brain only, providing selective contrast and reducing possible side effects. Dual-modal contrast agents were synthesised for this purpose.

All of these projects have shown success and expanded the area of microbubble-based contrast agents. Importantly, a range of synthetic methods and characterisation techniques for phospholipid manipulation have been developed which can be used in future studies. The current status and the next steps that should be taken in each area are detailed below.

6.1 Targeting

Microbubbles were targeted to cancer through the synthesis of a phospholipid containing the cancer-targeting peptide cRGDfK (DSPE-PEG_{2000}-cRGDfK **2.1**), as shown in **Figure 6.1**. This was fully characterised and used to successfully target cancer *in vitro*. *In vivo* work was attempted, however problems with the equipment available prohibited further studies. This requires further *in vivo* development by collaborators in the Dept. of Surgery and Cancer, Imperial College London.

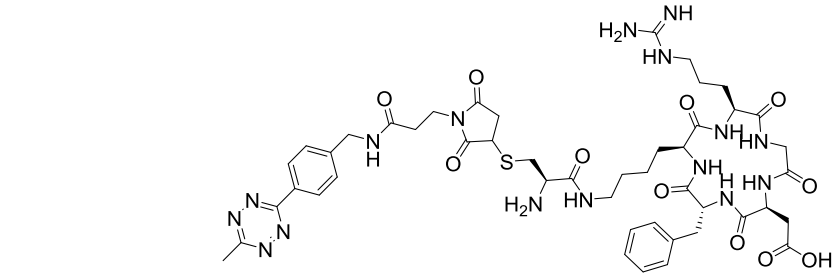


2.1

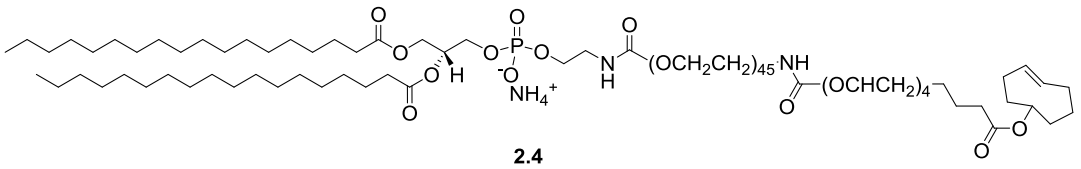
Figure 6.1: Structure of cancer-targeting phospholipid DSPE-PEG_{2000}-cRGDfK **2.1**.

An alternative pre-targeting method was also developed using the reaction between TCO and tetrazine. This reaction has been shown to be capable of 'catching' microbubbles *in vivo*,[1] with excellent reaction kinetics and selectivity under mild conditions.[2, 3] This should allow

for enhanced ultrasound contrast in desired regions. This methodology could also be developed to allow for the combination of ultrasound with currently incompatible modalities such as MRI through initial pre-targeted MRI imaging followed by administration of microbubbles and ultrasound imaging. The synthesis of the required tetrazine-modified cRGDfK peptide (RGD-tetrazine **2.3**) and TCO-functionalised phospholipid (DSPE-PEG_{2000}-TCO **2.4**) was achieved, as shown in **Figure 6.2**, however no *in vitro* or *in vivo* testing has yet been performed. Subsequent studies involving PET-labelling of microbubbles has demonstrated poor reaction between this lipid and small-molecules containing tetrazine, therefore it is possible that this may not be an achievable goal in this formulation. Future testing will confirm whether this is a viable route.



2.3



2.4

Figure 6.2: Structure of pre-targeting molecules RGD-tetrazine **2.3** and DSPE-PEG_{2000}-TCO **2.4**.

Additional work assessing the viability of other cancer-targeting peptides and small molecules would be useful for the targeting of alternative biomarkers expressed in different cancer types. For this reason, the peptide T140,[4] which targets the CXCR4 receptor, is being researched by collaborators in the Dept. of Surgery and Cancer, Imperial College London. Research into small peptides (Pentixafor) and small molecules (AMD3100) that also target this receptor[5] could provide valuable comparisons of the compatibility of these targeting groups with microbubbles. These are shown in **Figure 6.3**.

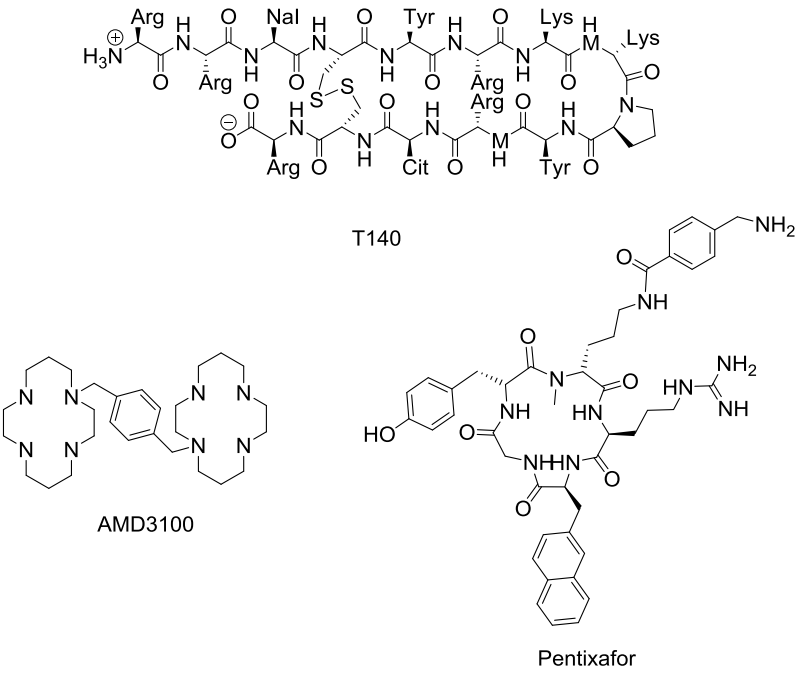


Figure 6.3: Structures of CXCR4-targeting peptides T140 and Pentixafor and small molecule AMD3100.

6.2 Dual-Modal PET-Ultrasound

The radiolabelling of microbubbles is little studied, with only 6 examples having been found in literature. These are summarised in **Figure 6.4**. For PET, only the isotope ^{18}F has been used in combination with microbubbles. In this thesis, extensive work was performed in the attempt to form ^{68}Ga-labelled microbubbles. This has been achieved, however further development is necessary.

This initially utilised the TCO-tetrazine reaction discussed above, using the TCO-functionalised phospholipid **2.4** shown in **Figure 6.2** and two tetrazine-modified ^{68}Ga chelators: DO3A-tetrazine **3.1** and DOTAGA-tetrazine **3.3** shown in **Figure 6.5**. The reaction between these was hypothesized to allow for direct radiolabelling of preformed microbubbles.

Radiolabelling strategies were developed for **3.1** and **3.3** using multiple generators, with elution in acidified saline (modified protocol from reference[6]) found to be the most transferrable and highest yielding. Reaction between **3.1** or **3.3** and **2.4** was monitored by UV-vis., mass spectrometry and radio-HPLC. All of these indicated that the reaction was effective and achievable short time periods (1 min). Unfortunately, once **2.4** was incorporated into microbubbles, this reaction did not occur (this was monitored by radio-HPLC).

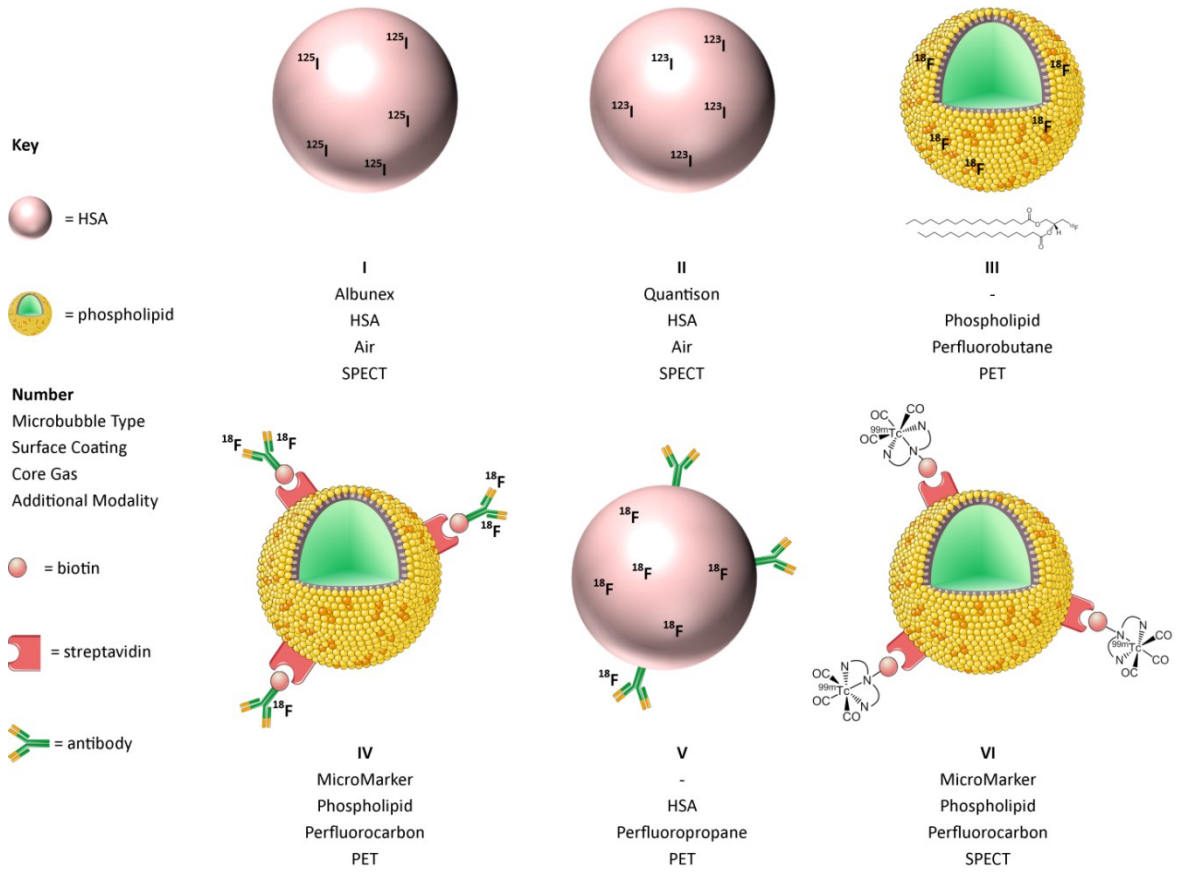
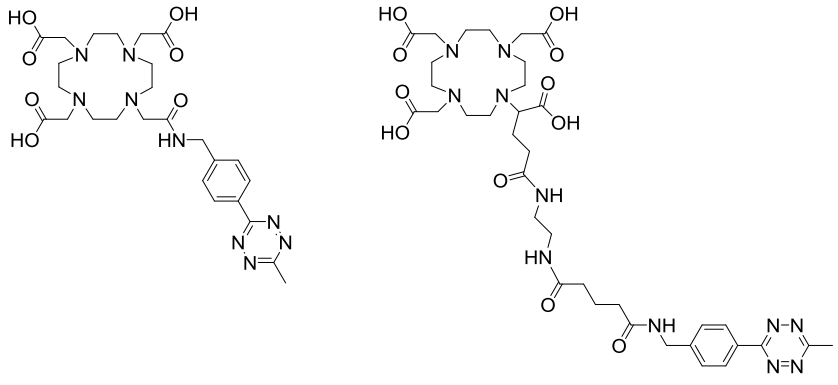


Figure 6.4: Details of all radiolabelled microbubbles that could be found in literature.[7-12]



3.1 **3.3**

Figure 6.5: Structures of tetrazine-modified ^{68}Ga chelators DO3A-tetrazine **3.1** and DOTAGA-tetrazine **3.3**.

Due to this, an alternative method was developed involving direct labelling of phospholipids and subsequent formation of microbubbles. For this purpose, phospholipids containing the chelators DOTA (DSPE-PEG$_{2000}$-DOTA, **3.5**) and NOTA (DPSE-PEG$_{2000}$-NOTA, **3.6**) were synthesised, as shown in **Figure 6.6**, and radiolabelled with ^{68}Ga. Radiolabelling and microbubble formation was achieved with DOTA-containing **3.5** at sufficient activity for further work, however no *in vivo* work was performed. Future work by collaborators in the

Dept. of Surgery and Cancer, Imperial College London, will determine the biodistribution of these microbubbles by PET and ultrasound imaging.

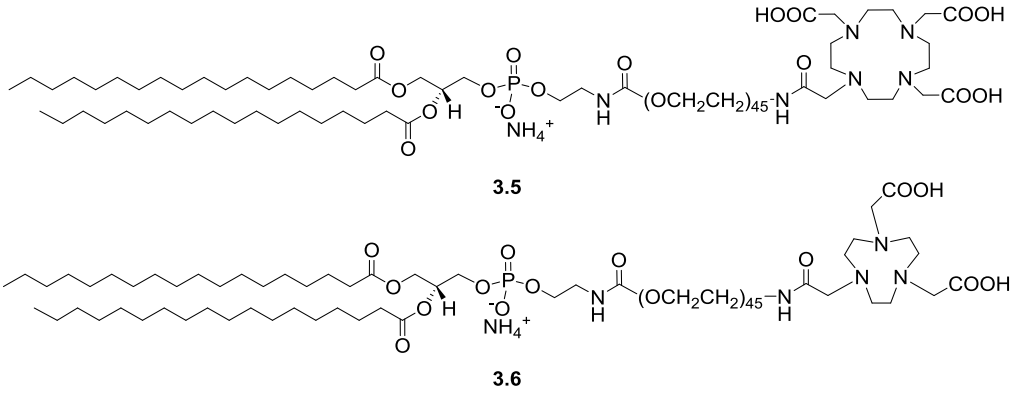


Figure 6.6: Structures of ^{68}Ga-chelating phospholipids DSPE-PEG_{2000}-DOTA **3.5** and DSPE-PEG_{2000}-NOTA **3.6**.

Unfortunately, radiolabelled free DOTA and NOTA was observed in both instances, which could not be removed from the phospholipids prior to radiolabelling. Difficulties in purification could be overcome by using a phospholipid that does not contain the PEG chain; this has already been performed with DOTA for MRI imaging in literature.[13] This phospholipid can be purified and manipulated in a similar fashion to other small molecules, making purification more effective.

6.3 Dual-Modal Fluorescence-Ultrasound

The initial focus of this work was to prove incorporation of modified phospholipids into microbubbles. This was achieved through the synthesis of a phospholipid containing the commercial dye ROX (DSPE-PEG_{2000}-ROX, **4.1**), shown in **Figure 6.7**. Comparison of the fluorescence properties of microbubbles containing 1 mol% of this phospholipid with those containing N-Rh-PE, a commercially available, well studied fluorescent phospholipid, proved incorporation.

The use of fluorescent phospholipids in dual-modal optical-ultrasound imaging was also explored. For this purpose, two fluorophores were synthesised and attached to phospholipids; one pH sensitive (DSPE-PEG_{2000}-Rh, **4.2**) and an analogous pH insensitive rhodamine derivative (DSPE-PEG_{2000}-Rh+, **4.3**). These are shown in **Figure 6.7**. The pH sensitivity of **4.2** was shown to span the range 3-7, with an increase of about 100 times in the range 5-7. This overlaps with the pH difference of cancerous tissue (5.6-7.6) when compared to healthy cells (7.2-7.6).[14]

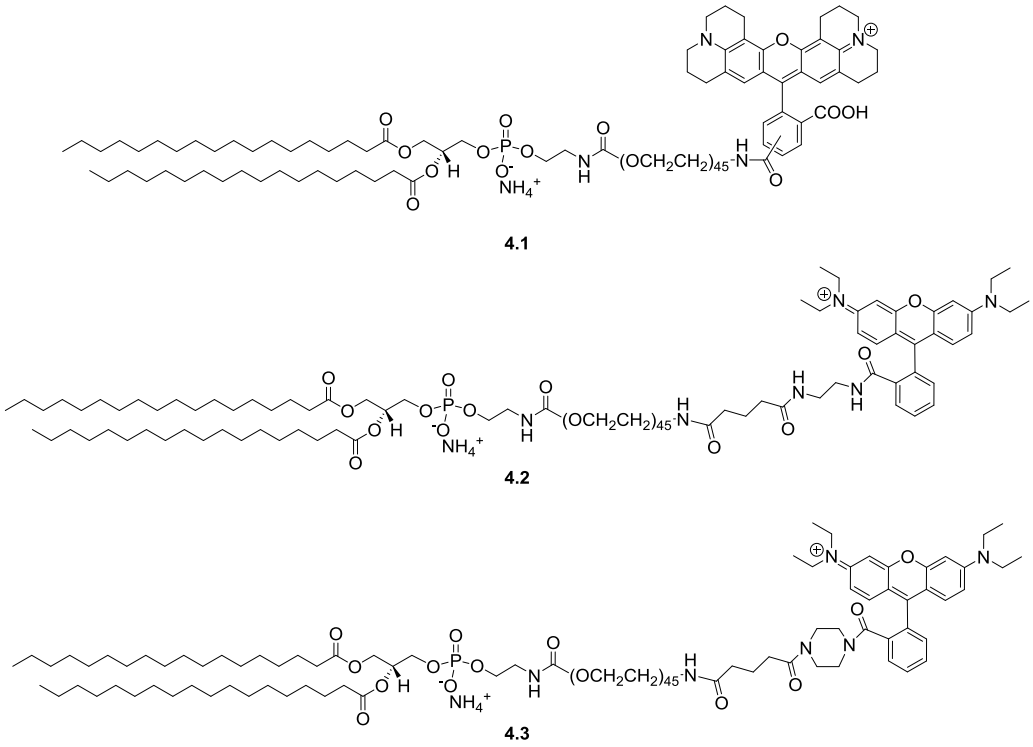


Figure 6.7: Structures of fluorescent phospholipids DSPE-PEG_{2000}-ROX **4.1**, DSPE-PEG_{2000}-Rh **4.2** and DSPE-PEG_{2000}-Rh+ **4.3**.

These microbubbles were also formed into nanodroplets; these are condensed microbubbles that can be vaporised using optical absorbers[15] such as rhodamine. The size of these droplets allows for them to leave the blood stream and accumulate in tumorous tissue. The pH sensitivity of phospholipid **4.2** has the potential to only allow for vaporisation of these in cancerous regions where the pH is sufficiently acidic to allow for absorption at 560 nm. This would result in selective ultrasound imaging as microbubbles would only form in these regions. These nanodroplets were synthesised and characterised, however a suitable laser for vaporisation experiments could not be found, therefore proof-of-concept was not obtained.

No *in vitro* or *in vivo* work was performed on these samples, however their combination with targeting lipid **2.1** would allow for fluorescent images of microbubbles and nanodroplets adhered to cells. As nanodroplets are too small to be observed ordinarily under a microscope, the observation of their fluorescence from cell membranes could be used to prove their attachment. An example of this type of experiment performed in literature is shown in **Figure 6.8**, where the green fluorescence of targeted microbubbles is clearly visible.[16]

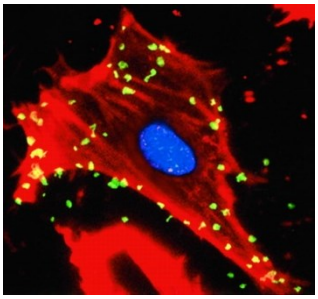


Figure 6.8: Fluorescent images of cells after exposure to targeted green fluorescent microbubbles. F-actin stained red and nuclei stained blue. Reproduced with permission.[16]

Further work using these nanodroplets will require the appropriate laser to be found for their vaporisation. Alternatively, the equipment is currently available for use with absorbing wavelengths in the range 680-980 nm. As discussed in Chapter 4, similar pH sensitivity could be obtained from silicon-rhodamine derivatives which can be excited up to 693 nm.[17] Additional synthesis and characterisation would be required to determine their suitability, but this provides an alternative route if the correct equipment cannot be found for current fluorophores.

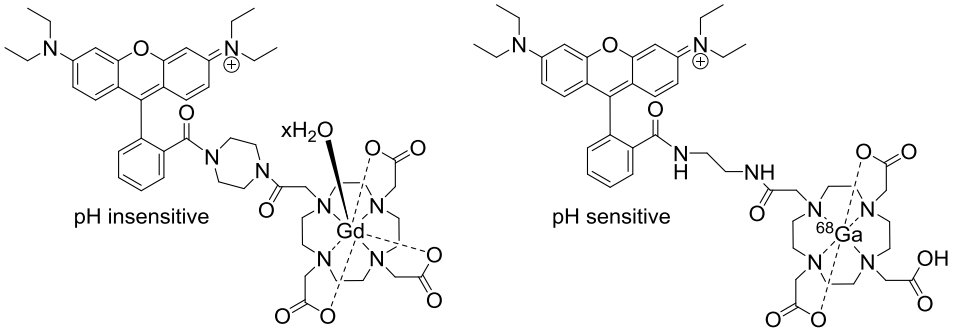
6.4 Sonoporation

The dual-modal fluorescence-MRI (Gd-DO3A-Rh+, **5.1-Gd**) and fluorescence-PET (^{68}Ga-DO3A-Rh, **5.2-^{68}Ga**) probes that were developed for this work are shown in **Figure 6.9**. These probes were designed to contain features which should prevent them from crossing the BBB unassisted.[18] This was confirmed by *in vivo* experiments, where the probes only entered the brain in the sonicated regions. Two different pulse sequences were employed in the hope of reducing damage to the BBB.[19] These preliminary experiments indicate no damage has been caused, however further studies, currently being performed by collaborator Sophie Morse and colleagues, Dept. Bioengineering, Imperial College London, are required for confirmation. Interestingly, these probes appear to have a different distribution in the brain than larger dextran molecules, a feature which will also be investigated further.

Analysis of **5.1-Gd** found that it had an unexpectedly high r_1 value, implying that the piperazine linker is increasing the rotational correlation time. The hydration number could not be confirmed using fluorescent lanthanide studies due to incompatible excited-state energy levels, therefore further experimentation and stability studies are required.

It was found that fluorescence pH sensitivity provides little additional information due to the method of brain analysis, therefore this should only be used as and when *in vivo* live animal

imaging is performed. As such, ^{68}Ga radiolabelling of **5.1** should be performed to obtain an optical-PET probe with properties appropriate for current analysis.



5.1-Gd **5.2-Ga**

Figure 6.9: Structures of dual-modal probes Gd-DO3A-Rh+ **5.1-Gd** and ^{68}Ga-DO3A-Rh **5.2-^{68}Ga**.

Further development of these probes to target specific biological processes will also enhance the image quality and allow for detection of diseases such as cancer or Alzheimer's.

6.5 References

1. A. Zlitni, N. Janzen, F. S. Foster and J. F. Valliant, *Angew. Chem. Int. Ed.*, 2014, **53**, 6459-6463.
2. H. L. Evans, Q.-D. Nguyen, L. S. Carroll, M. Kaliszczak, F. J. Twyman, A. C. Spivey and E. O. Aboagye, *Chem. Commun.*, 2014, **50**, 9557-9560.
3. N. K. Devaraj and R. Weissleder, *Acc. Chem. Res.*, 2011, **44**, 816-827.
4. H. Tamamura, Y. Xu, T. Hattori, X. Zhang, R. Arakaki, K. Kanbara, A. Omagari, A. Otaka, T. Ibuka, N. Yamamoto, H. Nakashima and N. Fujii, *Biochem. Biophys. Res. Commun.*, 1998, **253**, 877-882.
5. J. Kuil, T. Buckle and F. W. B. van Leeuwen, *Chem. Soc. Rev.*, 2012, **41**, 5239-5261.
6. D. Mueller, W. A. P. Breeman, I. Klette, M. Gottschaldt, A. Odparlik, M. Baehre, I. Tworowska and M. K. Schultz, *Nat. Protocols*, 2016, **11**, 1057-1066.
7. P. Walday, H. Tolleshaug, T. Gjøen, G. M. Kindberg, T. Berg, T. Skotland and E. Holtz, *Biochem. J*, 1994, **299**, 437-443.
8. A. C. Perkins, M. Frier, A. J. Hindle, P. E. Blackshaw, S. E. Bailey, J. M. Hebden, S. M. Middleton and M. L. Wastie, *Br. J. Radiol.*, 1997, **70**, 603-611.
9. M. S. Tartis, D. E. Kruse, H. Zheng, H. Zhang, A. Kheirolomoom, J. Marik and K. W. Ferrara, *J. Control. Release*, 2008, **131**, 160-166.
10. J. K. Willmann, Z. Cheng, C. Davis, A. M. Lutz, M. L. Schipper, C. H. Nielsen and S. S. Gambhir, *Radiology*, 2008, **249**, 212-219.
11. A.-H. Liao, S.-Y. Wu, H.-E. Wang, C.-H. Weng, M.-F. Wu and P.-C. Li, *Ultrasonics*, 2013, **53**, 320-327.
12. N. Lazarova, P. W. Causey, J. A. Lemon, S. K. Czorny, J. R. Forbes, A. Zlitni, A. Genady, F. S. Foster and J. F. Valliant, *Nucl. Med. Biol.*, 2011, **38**, 1111-1118.
13. S. Jung, K. Na, S. Lee, S. Cho, H. Seong and B. Shin, *Nanoscale Res. Lett.*, 2012, **7**, 462.

14. J. R. Griffiths, *Br. J. Cancer*, 1991, **64**, 425-427.
15. S. Lin, A. Shah, J. Hernández-Gil, A. Stanziola, B. I. Harriss, T. O. Matsunaga, N. Long, J. Bamber and M.-X. Tang, *Photoacoustics*, 2017, **6**, 26-36.
16. F. S. Villanueva, R. J. Jankowski, S. Klibanov, M. L. Pina, S. M. Alber, S. C. Watkins, G. H. Brandenburger and W. R. Wagner, *Circulation*, 1998, **98**, 1-5.
17. T. Wang, B. Wang, X. CHAI and Q. WU, *Patent, WO 2016029671 A1*, 2016.
18. M. D. Habgood, D. J. Begley and N. J. Abbott, *Cell. Mol. Neurobiol.*, 2000, **20**, 231-253.
19. J. J. Choi, K. Selert, F. Vlachos, A. Wong and E. E. Konofagou, *Proc. Natl. Acad. Sci.*, 2011, **108**, 16539-16544.

Chapter 7

Experimental

7.1 General

All solvents and commercially available chemicals were used without further purification, unless otherwise stated. No precautions were taken to remove water or air from reactions unless otherwise stated. All lipids were purchased from Avanti® Polar Lipids Inc.

TLC was performed on Merck Kieselgel 60 F_{254} or Aluminium Oxide 60 F_{254} plates and visualised by the quenching of UV fluorescence (254 and 366 nm) or using I_2 vapour. Silica, alumina (Brockman activity I, 0 % H_2O) or reverse phase C18 silica were used for chromatographic purification.

Compounds, ^{t}Bu-DO3A **3.2**,[1] ^{t}Bu-DOTAGA-NH_2 **3.3a-d**,[2-4] tetrazine-COOH **3.4**,[5] Rh-NH_2 **4.2a**,[6] Rh+ **4.3a-b**[7] and DO3A-Rh **5.2**[8] were prepared *via* literature methods from commercially available starting materials.

7.2 Equipment and Instrumentation

7.2.1 NMR

^{1}H, ^{13}C{^{1}H} and 2D COSY, HSQC and HMBC NMR spectra were recorded at ambient temperature on Bruker 400 MHz spectrometers. Specialist NMR experiments were performed at the Imperial College London, Department of Chemistry, NMR Service Facility by Mr. P. Haycock on either a Bruker AV 500 or a DRX-400 spectrometer. All NMR spectra were processed using MestReNova and referenced to the residual solvent peaks, as reported by Fulmer et. al.[9] Chemical shifts are reported in parts per million (ppm) with coupling constants quoted in hertz (Hz) to the nearest 0.1 . Multiplicities are abbreviated as follows: s = singlet, d = doublet, t = triplet, q = quartet, m = multiplet, br = broad, s_{br} = broad singlet.

7.2.2 Mass Spectrometry

High resolution ES+ mass spectra were collected by Dr. L. Haigh in the Department of Chemistry Mass Spectrometry Service Facility on a Waters LCT Premier spectrometer. Other spectra were recorded on open-access machines. MALDI spectra were collected on a low resolution Micromass MALDI-ToF machine in positive reflectron mode using the matrix 2,5-dihydroxybenzoic acid (DHB). UPC^2(ES+) chromatograms and spectra were recorded on a low resolution Waters Acquity UPC^2 using an Acquity BEH 2EP (1.7 μM, 3 x 100 mm) column. A flow rate of 1.85 mL/ min was used in combination with the following gradient:

95-60 % A over 5 min, 60 % A to 95 % A over 0.5 min and 95 % A for 4.5 min. Solvent A = CO_2 and B = CH_3OH (1 % NH_4OAc). MassLynx (Waters) software was used to analyse these spectra.

7.2.3 UV-Vis. Measurements

UV-vis. absorption spectra were recorded on a PerkinElmer 650 UV-vis. spectrometer using quartz cuvettes (10 x 10 mm or 10 x 2 mm). Concentrations were adapted to ensure absorbance in the range 0.05-0.3. Measurements were taken at 0.625 μM for Rh+-COOH **4.3c** and Gd-DO3A-Rh+ **5.1-Gd**. All other measurements were performed at 10 μM.

7.2.4 LCMS

LCMS was performed on a Waters 2767 HPLC system equipped with a photodiode array and a Waters 3100 mass detector (ES+ and ES-). A Waters XBridge C18 5 μm column (4.6 x 100 mm) was used for analytical HPLC, whilst a Waters XBridge Prep C18 5 μm OBD column (19 x 100 mm) was used for purification. A flow rate of 1.20 mL/ min or 20 mL/ min was used for analytical and semi-preparative runs respectively with the following gradient: 95-2 % A over 10 min, 2 % A for 2 min, 2-95 % A over 1 min and 95 % A for 5 min. A = H_2O (0.1% FA) B = MeOH (0.1% FA). MassLynx software (Waters) was used to analyze HPLC chromatograms.

7.2.5 T_1 Measurements at 400 MHz

T_1 measurements were performed on a Bruker DRX-400 spectrometer. The complexes were dissolved in H_2O at a range of 5 concentrations and placed in 1.7 mm diameter capillary tubes, which were sealed with Parafilm. These were placed in 5 mm NMR tubes and filled with D_2O and 1/ T_1 measurements were performed.

The concentration of Gd^{3+} in these samples was confirmed using the Evans method.[10] Briefly, ^1H NMR experiments of the above samples were performed at a fixed temperature (298 K) on a Bruker AV 500. The chemical shift difference between the HOD and H_2O signals induced by the paramagnetic Gd^{3+} was then used to calculate the sample concentration.

7.2.6 Relaxometer

Nuclear magnetic relaxation dispersion (NMRD) profiles were measured on a fast-field-cycling Stelar SMARtracer relaxometer (Stelar, s.r.l., Pavia, Italy) in the field range from 200 μT – 0.25 T, corresponding to proton Larmor frequencies of 0.01 – 10 MHz. Measurements

were taken at 37 ^{o}C (± 0.1 ^{o}C temperature resolution) under full computer control using pre-programmed experiments. NMRD acquisition was fully automated.

7.2.7 Photophysical Measurements

Fluorescence spectra and lifetime analysis were recorded on a Varian Cary Eclipse fluorescence spectrophotometer using quartz cuvettes (10 x 10 mm or 10 x 2 mm).

Standard fluorescence measurements were taken using 5:5 nm excitation and emission slits and the concentrations adapted to prevent saturation. Measurements were taken at 0.625 μM for Rh+-COOH **4.3c** and Gd-DO3A-Rh+ **5.1-Gd**. All other measurements were taken at 10 μM.

Lanthanide luminescence measurements were taken using 5:5 nm excitation and emission slits and the concentrations adapted to prevent saturation. Rh+-DO3A-Gd was measured at 0.625 μM, Rh+-DO3A-Tb was performed at 0.67 mg/ mL (0.95 mM) and Rh+-DO3A-Yb were taken at 1 mg/ mL.

Lanthanide lifetime measurements on Yb were taken using 20:20 excitation and emission slits with 0 ms delay time and 0.001 ms time gate. Five flashes were used to excite the fluorophore at 455 nm, with emission at 901 nm measured. The PMT detector was set to high voltage. All results were averaged over 100 measurements.

The number of coordinated water molecules was determined using lifetime measurements of the Yb complex in H_2O and D_2O at 1 mg/ mL. The lifetimes were calculated by fitting a monoexponential first-order decay to the data.

7.2.8 Acoustic Characterisation

Acoustic enhancement caused by modified MBs was proved using a Verasonics ultrasound imaging system equipped with a P4-2v probe (2 MHz imaging frequency at a Mechanical Index of 0.08). 1.7 L H_2O was allowed to rest for 5 min, following which 20 μL MB solution was added and 3 US images taken.

7.2.9 Additional

Microanalyses were carried out by Stephen Boyer of the Science Centre, London Metropolitan University when deemed appropriate.

pH measurements were performed using a Jenway model 3510 pH/mV/temperature meter.

7.3 Microbubble Formation and Analysis

Microbubble images were taken with a Nikon digital camera DXM 1200C attached to a Nikon Eclipse 50i microscope. Images were taken using a 40 x lens and analysed using a MATLAB (The MathWorks, Natick, MA, USA) bespoke automatic application.[11]

Fluorescence and related brightfield images were taken on an Olympus BA51 microscope fitted with an Olympus DP70 camera. Laser excitation was performed using an Olympus 100 W mercury burner (peaks of emission intensity at 313, 334, 365, 406, 435, 546, and 578 nm) and a Texas Red filter (λ_{ex} = 596 nm, λ_{em} = 620 nm, excitation filter 545-580 nm, barrier filter 610IF).

7.3.1 General Procedure

The phospholipids DPPC, DPPA, DSPE-PEG_{2000}-NH_2 and any modified lipids (DSPE-PEG_{2000}-X) were measured out in the appropriate quantities to a total concentration of 0.849 μmol (per 1 vial) and the solvent removed. These were then dissolved in propylene glycol (160 μL) with gentle heating, PBS solution (800 μL) added slowly and finally glycerol (50 μL) was added. This mixture was then decanted in 1 mL portions into vials, the vial purged with perfluorobutane gas and shaken in an amalgamator for 60 s.[12]

7.3.2 Formulations

Control:

Lipid	Mw/ g mol^{-1}	Mass/ μg	Moles/ μmol	Mol%
DPPC	734.04	510.8	0.696	82
DPPA	670.87	45.6	0.068	8
DSPE-PEG_{2000}-NH_2	2790.49	236.8	0.085	10

10 mol% 2.1-Containing:

Lipid	Mw/ g mol^{-1}	Mass/ μg	Moles/ μmol	Mol%
DPPC	734.04	510.8	0.696	82
DPPA	670.87	45.6	0.068	8
DSPE-PEG_{2000}-cRGDfK **2.1**	3648.46	31.0	0.085	10

5 mol% 2.4-Containing:

Lipid	Mw/ g mol^{-1}	Mass/ µg	Moles/ µmol	Mol%
DPPC	734.04	510.8	0.696	82
DPPA	670.87	45.6	0.068	8
DSPE-PEG$_{2000}$-NH$_2$	2790.49	118.0	0.042	5
DSPE-PEG$_{2000}$-TCO **2.4**	3200.02	136.0	0.042	5

5 mol% 2.1 and 5 mol% 2.4-Containing:

Lipid	Mw/ g mol^{-1}	Mass/ µg	Moles/ µmol	Mol%
DPPC	734.04	510.8	0.696	82
DPPA	670.87	45.6	0.068	8
DSPE-PEG$_{2000}$-cRGDfK **2.1**	3648.46	154.8	0.042	5
DSPE-PEG$_{2000}$-TCO **2.4**	3200.02	136.0	0.042	5

10 mol% 2.4-Containing:

Lipid	Mw/ g mol^{-1}	Mass/ µg	Moles/ µmol	Mol%
DPPC	734.04	510.8	0.696	82
DPPA	670.87	45.6	0.068	8
DSPE-PEG$_{2000}$-TCO **2.4**	3200.02	271.6	0.085	10

10 mol% 3.5-Containing:

Lipid	Mw/ g mol^{-1}	Mass/ µg	Moles/ µmol	Mol%
DPPC	734.04	510.8	0.696	82
DPPA	670.87	45.6	0.068	8
DSPE-PEG$_{2000}$-DOTA **3.5**	3176.93	269.6	0.085	10

5 mol% 2.1 and 5 mol% 3.5-Containing:

Lipid	Mw/ g mol^{-1}	Mass/ µg	Moles/ µmol	Mol%
DPPC	734.04	510.8	0.696	82
DPPA	670.87	45.6	0.068	8
DSPE-PEG$_{2000}$-cRGDfK **2.1**	3648.46	154.8	0.042	5
DSPE-PEG$_{2000}$-DOTA **3.5**	3176.93	134.8	0.042	5

10 mol% 3.6-Containing:

Lipid	Mw/ g mol^{-1}	Mass/ µg	Moles/ µmol	Mol%
DPPC	734.04	510.8	0.696	82
DPPA	670.87	45.6	0.068	8
DSPE-PEG$_{2000}$-NOTA **3.6**	3075.82	261.1	0.085	10

5 mol% 2.1 and 5 mol% 3.6-Containing:

Lipid	Mw/ g mol^{-1}	Mass/ µg	Moles/ µmol	Mol%
DPPC	734.04	510.8	0.696	82
DPPA	670.87	45.6	0.068	8
DSPE-PEG$_{2000}$-cRGDfK **2.1**	3648.46	154.8	0.042	5
DSPE-PEG$_{2000}$-NOTA **3.6**	3075.82	130.5	0.042	5

1 mol% N-Rh-PE-Containing:

Lipid	Mw/ g mol^{-1}	Mass/ µg	Moles/ µmol	Mol%
DPPC	734.04	510.8	0.696	82
DPPA	670.87	45.6	0.068	8
DSPE-PEG$_{2000}$-NH$_2$	2790.49	213.2	0.076	9
N-Rh-PE	1301.72	11.0	0.008	1

1 mol% 4.1-Containing:

Lipid	Mw/ g mol^{-1}	Mass/ µg	Moles/ µmol	Mol%
DPPC	734.04	510.8	0.696	82
DPPA	670.87	45.6	0.068	8
DSPE-PEG$_{2000}$-NH$_2$	2790.49	213.2	0.076	9
DSPE-PEG$_{2000}$-ROX **4.1**	3352.48	28.5	0.008	1

7.4 Nanodroplet Formation and Analysis

Nanodroplet size distributions were measured by dynamic light scattering (DLS) using a Malvern Zetasizer µV. 300 µL of the nanodroplet sample was diluted into PBS (3 mL) in a disposable plastic cuvette (10 x 10 mm). Measurements were taken using a laser at 830 nm (max. 60 mW) after 30 s calibration at 25 ^{o}C. Measurements were either 60 or 300 s in duration and all values quoted are taken from an average of three runs. Data was analysed using Zetasizer (Malvern Instruments Ltd.) software.

7.4.1 General Procedure

The phospholipids DPPC, DSPE-PEG$_{2000}$-OMe and any modified lipids (DSPE-PEG$_{2000}$-X) were measured out in the appropriate quantities whilst maintaining the concentration of DPPC at 0.764 µM (per 1 vial) and the solvent removed. These were then dissolved in propylene glycol (160 µL) with gentle heating, PBS solution (800 µL) added slowly and finally glycerol (50 µL) was added. This mixture was then decanted in 1 mL portions into vials, the vial purged with perfluorobutane gas and shaken in an amalgamator for 60 s.

The solution was cooled to ambient temperature and placed in a brine ice bath (~ -6 ^{o}C) for 2 min. The vial was then removed and the sample pressurised with air (60 mL) using a 25 G needle, turning the original cloudy microbubble solution clear.[12, 13]

7.4.2 Formulations

Unmodified:

Lipid	Mw/ g mol^{-1}	Mass/ µg	Moles/ µmol	Mol%
DPPC	734.04	560.7	0.764	90
DSPE-PEG$_{2000}$-OMe	2805.50	238.1	0.085	10

1 mol% 4.2-Containing:

Lipid	Mw/ g mol^{-1}	Mass/ µg	Moles/ µmol	Mol%
DPPC	734.04	560.7	0.764	90
DSPE-PEG$_{2000}$-OMe	2805.50	210.4	0.076	9
DSPE-PEG$_{2000}$-Rh **4.2**	3372.26	28.6	0.085	1

4 mol% 4.2-Containing:

Lipid	Mw/ g mol^{-1}	Mass/ µg	Moles/ µmol	Mol%
DPPC	734.04	560.7	0.764	96
DSPE-PEG$_{2000}$-Rh **4.2**	3372.26	110.5	0.033	4

1 mol% 4.3-Containing:

Lipid	Mw/ g mol^{-1}	Mass/ µg	Moles/ µmol	Mol%
DPPC	734.04	560.7	0.764	90
DSPE-PEG$_{2000}$-OMe	2805.50	210.4	0.076	9
DSPE-PEG$_{2000}$-Rh+ **4.3**	3398.30	28.8	0.085	1

4 mol% 4.3-Containing:

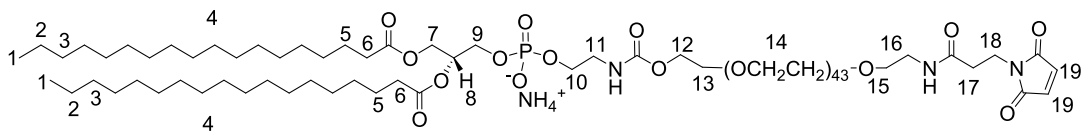
Lipid	Mw/ g mol^{-1}	Mass/ µg	Moles/ µmol	Mol%
DPPC	734.04	560.7	0.764	96
DSPE-PEG$_{2000}$-Rh+ **4.3**	3398.30	110.5	0.033	4

7.4.3 Laser Irradiation

An Opolette (HE) 355 II Nd:YAG solid state laser with a pulse length of 5 ns was used to irradiate NDs at a wavelength of 565 nm. 100 µL of sample (either at concentration synthesised or at 10 x dilution in PBS) was placed in a quartz cuvette (10 x 2 mm) and positioned in direct contact with the light guide (against the 2 mm edge), which had a diameter of ~3 mm. The sample was irradiated for 30 seconds at a frequency of 1 Hz (30 pulses in total) and an energy per pulse of 1.8 mJ, resulting in a fluence of approximately 6.4 mJ/ cm^2.

7.5 Synthesis of Compounds in Chapter 2

7.5.1 DSPE-PEG_{2000}-maleimide – 2.1a



$DSPE\text{-}PEG_{2000}\text{-}NH_2$ (15 mg, 5.4 µmol) was dissolved in chloroform (1 mL) following which NEt_3 (5.27 µL, 0.0378 mmol) and 3-(maleimido)propionic acid N-hydroxysuccinimide ester (5.8 mg, 22.6 µmol) were added. The solution was stirred for 48 h at RT, following which the solvent was removed under reduced pressure and the residue dissolved in H_2O (5 mL). This was purified by dialysis (Spectum Labs float-a-lyzer 3.5-5 kD, G235053) over 48 h. The resulting solution was lyophilised, producing **2.1a** (14.6 mg, 92 % yield) as a white powder.

^{1}H NMR (400 MHz, $CDCl_3$): 0.88 (6 H, t, $^3J_{H\text{-}H}$ = 7.0, C^1H_3), 1.25 (~56 H, s, C^4H_2), 1.54-1.67 (4 H, m, C^5H_2), 2.25-2.34 (4 H, m, C^6H_2), 2.52 (2 H, t, $^3J_{H\text{-}H}$ = 7.2, $C^{17}H_2$), 3.39-3.48 (4 H, m, 2 H $C^{11}H_2$ and 2 H $C^{16}H$), 3.54 (2 H, t, $^3J_{H\text{-}H}$ = 5.0, $C^{15}H_2$), 3.60-3.72 (~172 H, m, PEG^{14}), 3.79-3.88 (4 H, m, 2 H PEG^{14} and 2 H $C^{18}H_2$), 3.96-4.09 (4 H, m, C^9H_2 and $C^{10}H_2$), 4.18-4.26 (3 H, m, 1 H C^7H_2 and 2 H PEG^{14}), 4.38 (1 H, dd, $^3J_{H\text{-}H}$ = 12.0, 3.2, C^7H_2), 5.18-5.23 (1 H, m, C^8H), 6.37 (1 H, s_{br}, NH), 6.70 (2 H, s, $C^{19}H$).

^{13}C NMR (125 MHz, $CDCl_3$): 14.3 (C^1H_3), 22.9 (C^2CH_2), 24.9 (C^5CH_2), 25.1 (C^5CH_2), 29.3, 29.3, 29.4, 29.5, 29.6, 29.7, 29.8, 29.9 (C^4CH_2), 32.1 (C^3H_2), 34.2 (C^6H_2), 34.4 (C^6H_2), 34.5 (C^{17} or C^{18}), 34.7 (C^{17} or C^{18}), 39.4 ($C^{16}H_2$), 42.1 ($C^{11}H_2$), 62.5 (C^7H_2), 63.7 ($C^{9/10}H_2$), 65.4 ($C^{9/10}H_2$), 69.9 ($C^{15}H_2$), 70.3, 70.4, 70.7 ($C^{14}H_2$), 134.4 ($C^{19}H$), 169.9 ($C^{17}H_2\underline{C}ONH$), 170.7 (C=O mal), 173.2, 173.5 (C=O).

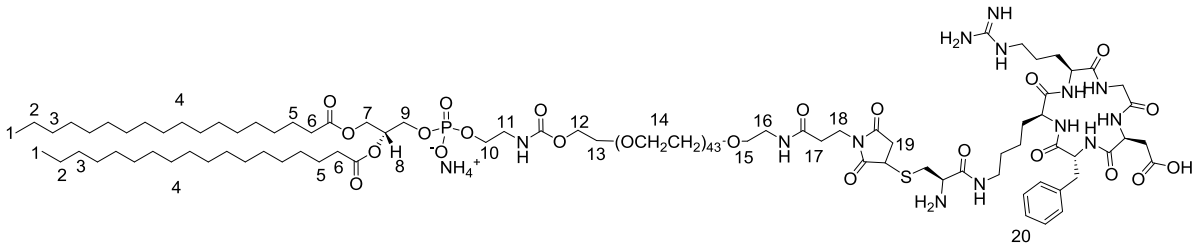
MS UPC^2(ES+) *m/z* calcd. for $C_{141}H_{282}N_5O_{59}P$ 755.73 $[M+4H+2H_{mal}+NH_4OAc]^{4+}$, found 756.07. t_R = 3.85 min.

MS(MALDI) *m/z* calcd. for $C_{139}H_{271}N_3O_{57}P$ 2925.8 $[M-NH_4^+ +2H+2H_{mal}]^+$, found 2925.8.

Also assigned in MeOD:

^{1}H NMR (400 MHz, CD_3OD): 0.92 (6 H, t, $^3J_{H-H}$ = 6.2, CH^1_3), 1.32 (~56 H, s, CH^4_2), 1.58-1.67 (4 H, m, CH^5_2), 2.26-2.40 (4 H, m, CH^6_2), 2.49 (2 H, t, $^3J_{H-H}$ = 7.0, CH^{17}_2), 3.35-3.39 (4 H, m, CH^{11}_2 and $C^{16}H_2$), 3.46-3.50 (1 H, m, PEG^{14}), 3.53 (2 H, t, $^3J_{H-H}$ = 5.4, $C^{15}H_2$), 3.60-3.72 (~172 H, m, PEG^{14}), 3.79 (2 H, t, $^3J_{H-H}$ = 7.0, CH^{18}_2), 3.82-3.86 (1 H, m, PEG^{14}), 3.87-3.95 (2 H, m, CH^{10}_2), 3.96-4.04 (2 H, m, CH^9_2), 4.16-4.22 (3 H, m, 1 H CH^7_2 and 2 H PEG^{14}), 4.43-4.48 (1 H, m, CH^7_2), 5.21-5.29 (1 H, m, CH^8), 6.85 (2 H, s, CH^{19}).

7.5.2 DSPE-PEG$_{2000}$-cRGDfK – 2.1



2.1a (12.5 mg, 4.3 µmol) was dissolved in degassed PBS (pH 7.27, 2 mL) under an N_2 atmosphere. cRGDfK-C (6.0 mg, 8.5 µmol) was added and the reaction stirred for 5 d at RT. This solution was then purified by dialysis (Spectum Labs float-a-lyzer 3.5-5 kD, G235053) over 48 h. The resulting solution was lyophilised, producing **2.1** (9.2 mg, 60 % yield) as a white powder.

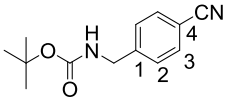
^{1}H NMR (400 MHz, CD_3OD): 0.90 (6 H, t, $^3J_{H-H}$ = 6.8, C^1H_3), 1.07-1.17 (2 H, m, RGD), 1.28-1.35 (~56 H, s, C^4H_2), 1.42-1.52 (4 H, m, RGD), 1.54-1.67 (8 H, m, 4 H C^5H_2, 4 H RGD), 1.68-1.80 (4 H, m, RGD), 1.84-1.94 (2 H, m, RGD), 2.29-2.37 (4 H, m, C^6H_2), 2.47-2.53 (2 H, m, $C^{17}H_2$), 2.55-3.25 (18 H, m, RGD), 3.44-3.48 (2 H, m, $C^{11}H_2$), 3.52-3.56 (3 H, m, PEG^{14}), 3.61-3.68 (~172 H, m, PEG^{14}), 3.75-3.84 (4 H, m, 2H $C^{18}H_2$ and PEG^{14}), 3.85-3.89 (4 H, m, 2 H $C^{10}H_2$), 3.95-4.01 (3 H, m), 4.13-4.21 (4 H, m, 1 H C^7H_2), 4.23-4.34 (2 H, m, RGD), 2.41-2.47 (2 H, m, 1 H C^7H_2), 4.53-4.69 (4 H, m), 5.19-5.24 (1 H, m, C^8H), 7.18-7.31 (5 H, m, $C^{20}H$).

MS UPC^2(ES+) *m/z* calcd. for $C_{171}H_{328}N_{15}O_{67}PS$ 931.80 $[M+4H+NH_4OAc]^{4+}$, found 932.82. t_R = 4.84 min.

MS(MALDI) *m/z* calcd. for $C_{169}H_{318}N_{14}O_{65}PS$ 3647.1 $[M+H]^+$, found 3653.5.

7.5.3 *Tert*-butyl (4-(aminomethyl)benzocarbamate) – 2.2a

Synthesis adapted from reference.[5]



4-(Aminomethyl)benzonitrile·HCl (5.0 g, 30.0 mmol) was dissolved in CH_2Cl_2 (4.0 mL), triethylamine (11.0 mL, 75.0 mmol) and Boc_2O (7.4 g, 33.0 mmol) were added and the resultant mixture stirred at RT for 16 h. The solvent was removed under reduced pressure, water added (100 mL) and the product extracted into DCM (3 x 100 mL). The organic layers were combined, washed with water (1 x 100 mL) and the solvent removed under reduced pressure to yield *tert*-butyl (4-(aminomethyl)benzocarbamate) **2.2a** (5.84, 84 % yield) as a white powder.

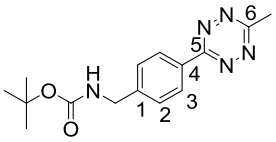
^{1}H NMR (400 MHz, $CDCl_3$) 1.46 (9 H, s, ^{t}Bu), 4.37 (2 H, d, $^3J_{H\text{-}H}$ = 6, CH_2), 4.97 (1 H, s_{br}, NH), 7.38 (2 H, d, $^3J_{H\text{-}H}$ = 8.4, C^2H), 7.62 (2 H, d, $^3J_{H\text{-}H}$ = 8.4, C^3H).

^{13}C NMR (100 MHz, $CDCl_3$) 28.5 (CH_3 ^{t}Bu), 44.4 (CH_2), 80.2 (4^o C ^{t}Bu), 111.3 (C^1), 118.9 (C^4 or CN), 127.9 (C^2H), 132.6 (C^3H), 144.8 (C^4 or CN), 156.0 (C=O).

MS (ES+) *m/z* calcd. for $C_{13}H_{16}N_2O_2$ 233.1290 $[M+H]^+$, found 233.1296.

7.4.4 *Tert*-butyl 4-(6-methyl-1,2,4,5-tetrazin-3-yl)benzylcarbamate – 2.2b

Synthesis adapted from reference.[5]



A high pressure reaction tube was treated with **2.2a** (464 mg, 2.0 mmol), CH_3CN (1050 µL, 20.0 mmol), $Ni(OTf)_2$ (356 mg, 1.0 mmol) and hydrazine hydrate (50-60% NH_2NH_2) (6.2 mL, 100.0 mmol). The tube was sealed and heated to 60°C for 72 h, following which H_2O (10 mL) and $NaNO_2$ (2.82 g, 40.0 mmol) were added to the mixture. HCl (1M) was added dropwise until the pH reached 3 and gases stopped evolving, at which point the mixture had turned bright red. The product was extracted with EtOAc (3 x 40 mL), and the combined organic layers were washed with H_2O (3 x 20 mL), dried over $MgSO_4$, filtered and concentrated under reduced pressure. The bright pink crude solid was purified by flash column chromatography (DCM/ Et_2O gradient 100:0 v/v to 96:4 v/v) to give *tert*-butyl 4-(6-methyl-1,2,4,5-tetrazin-3-yl)benzylcarbamate **2.2b** (0.37 g, 62% yield) as a bright pink solid. R_f = 0.39 (2% Et_2O/ DCM).

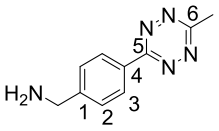
^{1}H NMR (400 MHz, $CDCl_3$) 1.46 (9 H, s, CH_3 ^{t}Bu), 3.07 (3 H, s, CH_3), 4.41 (2 H, d, $^3J_{H\text{-}H}$ = 5.6, CH_2), 5.09 (1 H, s_{br}, NH), 7.47 (2 H, d, $^3J_{H\text{-}H}$ = 8.4, C^2H), 8.51 (2 H, d, $^3J_{H\text{-}H}$ = 8.4, C^3H).

^{13}C NMR (100 MHz, $CDCl_3$) 21.2 (CH_3), 28.5 (CH_3 ^{t}Bu), 44.5 (CH_2), 79.9 (4^{o} C ^{t}Bu), 128.1 ($C^{2/3}H$), 128.3 ($C^{2/3}H$), 130.9 (C^1), 144.1 (C^4), 156.1 (C=O) 164.0 (C^5), 167.3 (C^6).

MS (LCMS-ES+) *m/z* calcd. for $C_{15}H_{20}N_5O_2$ 302.1617 $[M+H]^+$, found 302.1621.

7.5.5 4-(6-Methyl-1,2,4,5-tetrazin-3-yl)benzylamine (Tetrazine) – 2.2

Synthesis adapted from reference.[5]



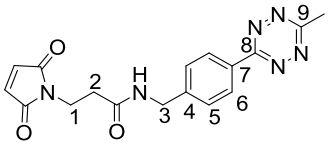
2.2b (30.4 mg, 0.15 mmol) was treated with TFA/CH_2Cl_2 (1/1, *v/v*, 3 mL) and stirred for 1.5 h at RT. The solvent was removed under reduced pressure to yield the TFA salt of 4-(6-methyl-1,2,4,5-tetrazin-3-yl)benzylamine **2.2** (26.4 mg, 84 % yield) as a bright pink solid.

^{1}H NMR (400 MHz, CD_3OD) 3.06 (3 H, s, CH_3), 4.26 (2 H, s, CH_2), 7.72 (2 H, d, $^{3}J_{H\text{-}H}$ = 8.4, C^2H), 8.62 (2 H, d, $^{3}J_{H\text{-}H}$ = 8.4, C^3H).

^{13}C NMR (100 MHz, CD_3OD) 21.1 (CH_3), 43.9 (CH_2), 129.4 (C^3H), 130.8 (C^2H), 134.3 (C^1), 138.8 (C^4), 164.9 (C^5), 169.1 (C^6).

MS (ES+) *m/z* calcd. for $C_{10}H_{12}N_5$ 202.1093 $[M+H]^+$, found 202.1083.

7.5.6 Tetrazine-maleimide – 2.3a



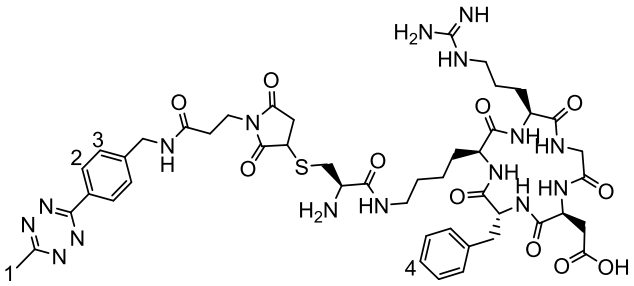
2.2 (16.2 mg, 0.091 mmol) was dissolved in DCM (2 mL) and 3-(maleimido)propionic acid N-hydroxysuccinimide ester (48.5 mg, 0.182 mmol) and NEt_3 (52.4 µL, 0.376 mmol) were added. The solution was stirred at RT for 3 h, following which H_2O (5 mL) was added, the product extracted with DCM (3 x 5 mL) and the combined organic layers washed with H_2O (1 x 5 mL). The organic layers were then dried over $MgSO_4$, filtered and the solvent removed under reduced pressure. The crude solid was purified by flash column chromatography (DCM/ MeOH gradient 100:0 v/v to 95:5 v/v) to give **2.3a** (15.4 mg, 48% yield) as a bright pink solid. R_f = 0.43 (10 % MeOH/ DCM).

^{1}H NMR (400 MHz, $CDCl_3$) 2.62 (2 H, t, $^{3}J_{H\text{-}H}$ = 7.0, C^2H_2), 3.09 (3 H, s, CH_3), 3.89 (2 H, t, $^{3}J_{H\text{-}H}$ = 7.2, C^1H_2), 4.52 (2 H, d, $^{3}J_{H\text{-}H}$ = 6, C^3H_2), 6.10 (1 H, s_{br}, NH), 6.99 (2 H, s, HC=CH), 7.46 (2 H, d, $^{3}J_{H\text{-}H}$ = 8.8, C^5H_2), 8.53 (2 H, d, $^{3}J_{H\text{-}H}$ = 8.4, C^6H_2).

^{13}C NMR (100 MHz, $CDCl_3$) 21.3 (CH_3), 34.4 (C^1H_2 or C^2H_2), 34.8 (C^1H_2 or C^2H_2), 43.5 (C^3H_2), 128.5 (C^5H or C^6H), 128.7 (C^5H or C^6H), 131.4 (C^4), 134.4 (HC=CH), 143.01 (C^7), 164.0 (C^8), 167.5 (C^9), 169.7 ($C^2H_2\underline{C}$=O), 170.6 (C=O mal).

MS (ES+) *m/z* calcd. for $C_{17}H_{17}N_6O_3$ 353.1362 $[M+H]^+$, found 353.1354.

7.5.7 RGD-tetrazine – 2.3

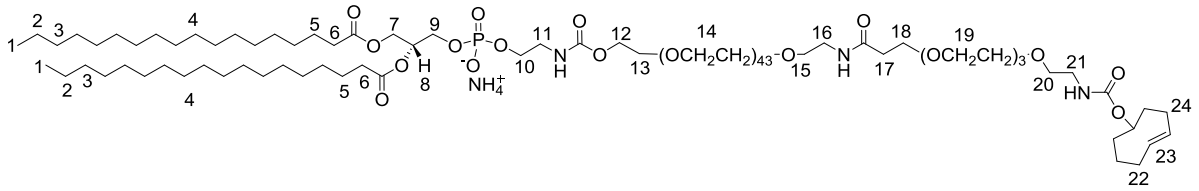


cRGDfK-C (0.4 mg, 0.57 µmol) and **2.3a** (0.3 mg, 0.85 µmol) were dissolved in PBS (pH 7.3 1 mL) under a N_2 atmosphere. The solution was stirred for 5 hours at RT, following which the product was purified by dialysis (Spectum Labs float-a-lyzer 0.1-0.5 kD, G235049) for 24 h. The resulting solution was lyophilised, producing **2.3** (0.6 mg, 99 % yield) as a pink powder.

^{1}H NMR (400 MHz, CD_3OD) 1.00-4.70 (a series of broad weak peaks), 3.04 (3 H, s, C^1H_3), 7.16-7.29 (5 H, m, C^4H), 7.55 (2 H, d, $^3J_{H\text{-}H}$ = 8.8, C^3H), 8.51 (2 H, d, $^3J_{H\text{-}H}$ = 8.4, C^2H).

MS (ES+) *m/z* calcd. for $C_{47}H_{63}N_{16}O_{11}S$ 1059.4583 $[M+H]^+$, found 1059.4674.

7.5.8 DSPE-PEG$_{2000}$-TCO – 2.4



DSPE-PEG_{2000}-NH_2 (10 mg, 7.2 µmol) was dissolved in $CHCl_3$ (500 µL) following which NEt_3 (3.76 µL, 0.06 mmol) and TCO-PEG_4-NHS ester (7.4 mg, 0.03 mmol) were added. The solution was stirred for 24 h at RT, following which the solvent was removed under reduced pressure and the residue dissolved in H_2O (5 mL). This was purified by dialysis (Spectum Labs float-a-lyzer 3.5-5 kD, G235053) over 48 h. The resulting solution was lyophilised, producing **2.4** (11.4 mg, 99 % yield) as a white powder.

^{1}H NMR (400 MHz, $CDCl_3$): 0.88 (6 H, t, $^3J_{H\text{-}H}$ = 6.8, C^1H_3), 1.25 (~56 H, s, C^4H_2), 1.59 (4 H, s, C^5H_2), 1.75-1.83 (2 H, m, TCO), 1.90-1.96 (2 H, m, $C^{22}H_2$ or $C^{24}H_2$), 2.07-2.16 (2 H, m, $C^{22}H_2$ or $C^{24}H_2$), 2.26-2.33 (6 H, m, C^6H_2 and TCO), 2.47 (2 H, t, $^3J_{H\text{-}H}$ = 6.2, $C^{17}H_2$), 2.60 (2 H, t, $^3J_{H\text{-}H}$ = 5.8, $C^{21}H_2$), 2.78-3.02 (8 H, m, TCO), 3.04-3.10 (2 H, m, TCO), 3.26-3.49 (12 H, m, $C^{11}H_2$, $C^{16}H_2$ and TCO), 3.55 (2 H, t $^3J_{H\text{-}H}$ = 5.2, $C^{15}H_2$), 3.57-3.70 (~178 H, m, PEG^{14} and PEG^{19}), 3.70-3.85 (6 H, m, $C^{18}H_2$, $C^{20}H_2$, PEG^{14}), 3.96-4.05 (4 H, m, C^9H_2 and $C^{10}H_2$),

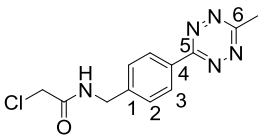
4.12-4.18 (1 H, m, C^7H_2), 4.19-4.23 (1 H, m), 4.36 (1 H, dd, $^3J_{H\text{-}H}$ = 12 3.6, C^7H_2), 5.17-5.23 (1 H, m, C^8H), 5.46-5.70 (2 H, m, $C^{23}H$), 6.65 (1 H, s_{br}, NH).

MS UPC^2(ES+) *m/z* calcd. for $C_{154}H_{312}N_5O_{63}P$ 817.78 $[M+4H+2H_{TCO}+NH_4OAc]^{4+}$, found 818.06. t_R = 3.55 min.

MS(MALDI) *m/z* calcd. for $C_{152}H_{299}N_3O_{61}P$ 3174.0 $[M\text{-}NH_4^+\text{+}2H\text{+}2H_{TCO}]^+$, found 3173.7

7.6 Synthesis of Compounds in Chapter 3

7.6.1 Tetrazine-Cl – 3.1a



2.2 (0.1137 g, 0.57 mmol) in CH_3CN (20 mL) was cooled to 0 ^oC in ice. NEt_3 (82.42 µL, 0.62 mmol) was added, the solution mixed for 5 min and chloroacetyl chloride (49.35 µL, 0.62 mmol) added dropwise. The solution was stirred for 2 h, warming to room temperature as the ice melted, following which the solvent was removed under reduced pressure. The crude pink oil was purified by flash column chromatography (DCM/ EtOAc gradient 100:0 v/v to 90:10 v/v) to give **3.1a** (82.8 mg, 53 % yield) as a pink solid. R_f = 0.59 (50% EtOAc/DCM).

^{1}H NMR (400 MHz, $CDCl_3$) 3.10 (3 H, s, CH_3), 4.15 (2 H, s, CH_2-Cl), 4.62 (2 H, d, $^3J_{H\text{-}H}$ = 6.0, NH-C$\underline{H_2}$), 7.02 (1 H, s_{br}, NH), 7.51 (2H, d, $^3J_{H\text{-}H}$ = 8.8, C^2H), 8.58 (2 H, d, $^3J_{H\text{-}H}$ = 8.4, C^3H).

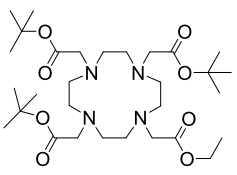
^{13}C NMR (100 MHz, $CDCl_3$) 21.3 (CH_3), 42.8 (CH_2-Cl), 43.6 (NH-$\underline{C}H_2$), 128.5 (C^2H or C^3H), 128.6 (C^2H or C^3H), 131.5 (C^1), 142.3 (C^4), 163.9 (C^5), 166.2 (C=O), 167.5 (C^6).

MS (ES+) *m/z* calcd. for $C_{12}H_{13}ClN_5O$ 278.0809 $[M+H]^+$, found 278.0817.

Elemental Analysis: calc ($C_{12}H_{12}ClN_5O$) C 51.90 %, H 4.36 %, N 25.22 %, found C 51.92 %, H 4.25 %, N 25.18 %.

7.6.2 ^{t}Bu-DO3A-COOEt – 3.1c

Synthesis adapted from reference.[14]



3.1a (1.00 g, 1.68 mmol) was dissolved in CH_3CN (15 mL), K_2CO_3 (0.46 g, 3.36) added and the solution stirred for 15 min. Following this, the mixture was heated to 82 ^oC whilst adding ethylbromoacetate (0.24 mL, 2.18 mmol) dropwise. The solution was refluxed for 24 h, filtered and the solvent removed under reduced pressure. The crude yellow oil was purified by flash column

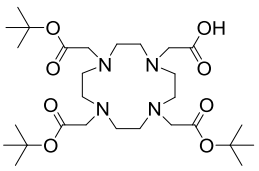
chromatography (DCM/ MeOH 100:0 v/v to 90:10 v/v), producing **3.1c** (1.00 g, 77 % yield) as a clear colourless oil. R_f = 0.53 (5 % MeOH/ DCM).

^{1}H NMR (400 MHz, $CDCl_3$) 1.27 (3 H, t, $^3J_{H\text{-}H}$ = 7.2, $CH_2C\underline{H}_3$), 1.44 (9 H, s, CH_3 ^{t}Bu), 1.45 (18 H, s, CH_3 ^{t}Bu), 1.84-3.75 (24 H, m), 4.11-4.23 (2 H, m, $C\underline{H}_2CH_3$).

^{13}C NMR (100 MHz, $CDCl_3$) 14.3 ($CH_2\underline{C}H_3$), 28.1 ($\underline{C}H_3$ ^{t}Bu), 28.2 ($\underline{C}H_3$ ^{t}Bu), 49.2 (br), 51.1 (br), 52.5 (br), 55.9, 56.3, 56.9, 57.2, 61.2 ($\underline{C}H_2CH_3$), 82.1 (C^{IV} ^{t}Bu) 82.1 (C^{IV} ^{t}Bu), 172.4 (C=O), 172.5 (C=O), 173.0 (C=O).

MS (ES+) *m/z* calcd for $C_{30}H_{57}N_4O_8$ 601.4176 $[M+H]^+$, found 601.4166.

7.6.3 DO3A-COOH – 3.1d



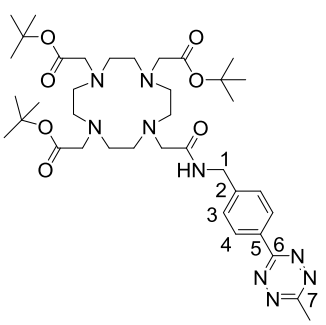
3.1c (0.82 g, 1.36 mmol) was dissolved in MeOH (10 mL) and NaOH solution (1 M, 10 mL) and stirred for 48 h at RT. MeOH was removed under reduced pressure and the residue extracted with DCM (3 x 15 mL). The organic extracts were washed with H_2O (1 x 25 mL), dried over Na_2SO_4, filtered and the solvent removed under reduced pressure, giving **3.1d** (0.61 g, 78 % yield) as a clear oil which solidified when *in vacuo*.

^{1}H NMR (400 MHz, $CDCl_3$) 1.39 (18 H, s, CH_3 ^{t}Bu), 1.40 (9 H, s, CH_3 ^{t}Bu), 2.22-3.34 (24 H, m).

^{13}C NMR (100 MHz, $CDCl_3$) 27.5 (CH_3 ^{t}Bu), 27.61 (CH_3 ^{t}Bu), 50.3 (br), 55.3, 55.8, 58.5, 81.0 (C^{IV} ^{t}Bu), 81.1 (C^{IV} ^{t}Bu), 171.6 (C=O), 172.5 (C=O), 174.9 (C=O).

MS (ES+) *m/z* calcd for $C_{28}H_{53}N_4O_8$ 573.3863 $[M+H]^+$, found 573.3888.

7.6.4 ^{t}Bu-DO3A-tetrazine – 3.1e



3.1d (209.4 mg, 0.366 mmol) was dissolved in DCM (5 mL) and HBTU (278.0 mg, 0.732 mmol) and **2.2** (81.0 mg, 0.4026 mmol) were added. The solution was stirred for 48 h at RT, following which H_2O (5 mL) was added, the product extracted with DCM (3 x 5 mL) and the combined organic layers washed with H_2O (1 x 5 mL). The organic layers were combined, dried over Na_2SO_4, filtered and the solvent removed under reduced pressure. The

crude solid was purified by flash column chromatography (DCM/ MeOH gradient 100:0 v/v to 98:2 v/v) to give **3.1e** (151.6 mg, 55% yield) as a pink solid. R_f = 0.65 (5 % MeOH/ DCM).

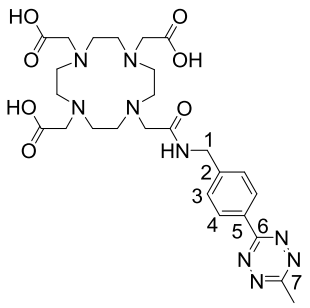
^{1}H NMR (400 MHz, $CDCl_3$) 1.37 (18 H, s, CH_3 ^{t}Bu), 1.42 (9 H, s, CH_3 ^{t}Bu), 2.01-2.98 (20 H, m), 3.04 (3 H, s, CH_3), 3.08-3.48 (4 H, m), 4.40-4.55 (2 H, m, C^1H_2), 6.89 (1 H, t, $^3J_{H\text{-}H}$ = 6.4, NH), 7.49 (2 H, d, $^3J_{H\text{-}H}$ = 8.4, C^3H), 8.43 (2 H, d, $^3J_{H\text{-}H}$ = 8.4, C^4H).

^{13}C NMR (100 MHz, $CDCl_3$) 21.2 (CH_3), 27.9 (CH_3 ^{t}Bu) 27.96 (CH_3 ^{t}Bu), 43.0 (C^1H_2), 48.40 (br, DO3A), 52.27 (br, DO3A), 55.7 (DO3A), 56.0 (DO3A), 81.8 (4^o C ^{t}Bu), 81.8 (4^o C ^{t}Bu), 128.0 (C^3H or C^4H), 128.7 (C^3H or C^4H), 130.3 (C^2), 144.3 (C^5), 164.0 (C^6), 167.1 (C^7), 172.1 (C=O), 172.4 (C=O), 172.7 (C=O).

MS (ES+) *m/z* calcd for $C_{38}H_{62}N_9O_7$ 756.4772 $[M+H]^+$, found 756.4767.

7.6.5 DO3A-tetrazine – 3.1

Synthesis adapted from reference.[15]



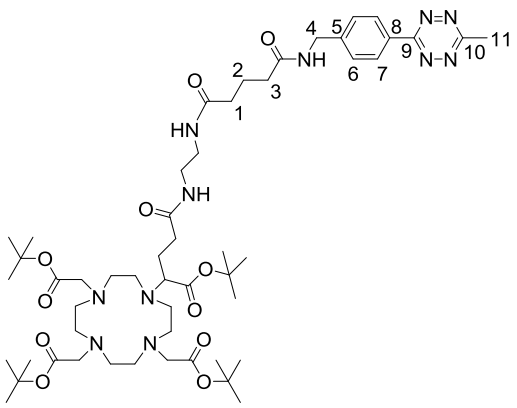
3.1e (151.6 mg, 0.201 mmol) was treated with TFA/CH_2Cl_2 (1/1 *v/v,* 2 mL) and stirred for 8 h at RT. The solvent was removed under reduced pressure and the residue taken up in H_2O (15 mL). This was washed with $CHCl_3$ (3 x 15 mL) and the H_2O removed under reduced pressure, producing the product as a TFA salt. This was finally purified by LCMS, yielding **3.1** (23 mg, 20 % yield) as a pink solid.

^{1}H NMR (400 MHz, CD_3OD) 3.03 (CH_3), 3.04-3.10 (4 H, m, DOTA), 3.11-3.16 (4 H, m, DOTA), 3.37-3.61 (12 H, m, DOTA), 3.75-3.80 (4 H, m, DOTA), 4.49 (2 H, s, C^1H_2), 7.58 (2 H, d, $^3J_{H\text{-}H}$ = 8.4, C^3H), 8.46 (2 H, d, $^3J_{H\text{-}H}$ = 8.4, C^4H).

^{13}C NMR (100 MHz, CD_3OD) 21.1 (CH_3), 44.0, (C^1H_2), 49.9 (DOTA), 50.2 (DOTA), 51.9 (DOTA), 52.6 (DOTA), 56.7 (DOTA), 57.6 (DOTA), 128.9 (C^3H or C^4H), 129.5 (C^3H or C^4H), 132.1 (C^2), 145.4 (C^5), 165.1 (C^6), 168.7 (C^7), 170.1 (C=O), 172.0 (NHC=O), 174.7 (C=O).

MS (ES+) *m/z* calcd for $C_{26}H_{38}N_9O_7$ 588.2894 $[M+H]^+$, found 588.2885.

7.6.6 ^{t}Bu-DOTAGA-tetrazine – 3.3e



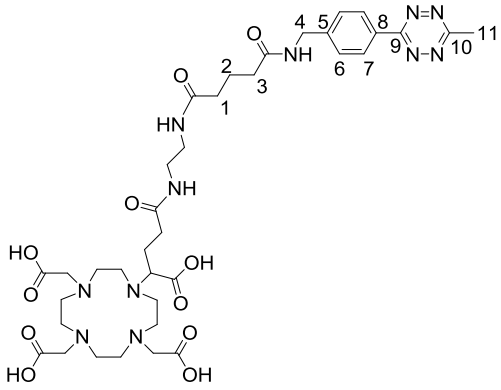
3.4 (14.0 mg, 44.4 µmol) was dissolved in DCM (4 mL) and HBTU (30.5 mg, 80.6 µmol), NEt_3 (19.7 µL, 141.1 µmol) and **3.3d** (29.9 mg, 40.3 µmol) were added. The solution was stirred for 40 h at RT, following which the solvent was removed under reduced pressure. The crude solid purified by LCMS, yielding **3.3e** (13.6 mg, 32 % yield) as a pink solid.

^{1}H NMR (400 MHz, $CDCl_3$) 1.43 (9 H, s, ^{t}Bu), 1.45 (27 H, s ^{t}Bu), 1.81 (2 H, s_{br}, NH), 1.95-2.11 (6 H, m, $C^{2}H_2$), 2.13-2.41 (8 H, m, $C^{1}H_2$ and $C^{3}H_2$), 2.47-2.72 (8 H, m), 2.77-2.91 (8 H, m), 3.09 (3 H, s, $C^{11}H_3$), 3.27-3.39 (7 H, m), 4.56 (2 H, d, $^{3}J_{H\text{-}H}$ = 6, C_1H_2), 7.53 (2 H, d, $^{3}J_{H\text{-}H}$ = 8.4, $C^{6}H$), 8.54 (2 H, d, $^{3}J_{H\text{-}H}$ = 8.4, $C^{7}H$).

^{13}C NMR (100 MHz, $CDCl_3$) 21.2 ($C^{11}H_3$), 21.8, 22.9 ($C^{2}H_2$), 27.9 (CH_3 ^{t}Bu), 28.0 (CH_3 ^{t}Bu), 35.1, 36.0 ($C^{1}H_2$ or $C^{3}H_2$), 36.2 ($C^{1}H_2$ or $C^{3}H_2$), 39.5, 39.8, 43.0 ($C^{4}H_2$), 44.4, 47.0, 48.2, 48.4, 48.6, 52.7, 52.8, 55.6, 55.9, 60.3, 82.0 (4^{o} C ^{t}Bu), 82.2 (4^{o} C ^{t}Bu), 82.3 (4^{o} C ^{t}Bu), 128.0 ($C^{7}H$), 128.5 ($C^{6}H$), 130.2 (C^{5}), 144.6 (C^{8}), 164.2 (C^{9}), 167.1 (C^{10}), 172.5 (C=O), 172.7 (C=O), 172.9 (C=O), 173.4 (C=O), 173.7 (C=O), 173.9 (C=O).

MS (ES+) *m/z* calcd for $C_{52}H_{86}N_{11}O_{11}$ 1040.6508 $[M+H]^{+}$, found 1040.6501.

7.6.7 DOTAGA-tetrazine – 3.3



3.3e (11.9 mg, 11.4 µmol) was treated with TFA/CH_2Cl_2 (1/1 *v/v,* 6 mL) and stirred for 5 h at RT. The solvent was removed under reduced pressure and the residue purified by LCMS, yielding **3.3** (2.9 mg, 31 % yield) as a pink solid.

^{1}H NMR (400 MHz, CD_3OD) 1.90-1.98 (2 H, m, $C^{2}H_2$), 2.25 (2 H, t, $^{3}J_{H\text{-}H}$ = 7.6, $C^{1}H_2$ or $C^{3}H_2$), 2.33 (2 H, t, $^{3}J_{H\text{-}H}$ = 7.4, $C^{1}H_2$ or $C^{3}H_2$), 2.43-3.02 (8 H, m), 3.04 (3 H, s, $C^{11}H_3$), 3.12-3.29 (8 H, m), 3.39-4.31 (15 H, m), 4.50 (2 H, s, $C^{4}H_2$), 7.55 (2 H, d, $^{3}J_{H\text{-}H}$ = 8.8, $C^{6}H$), 8.51 (2 H, d, $^{3}J_{H\text{-}H}$ = 8.4 $C^{7}H$).

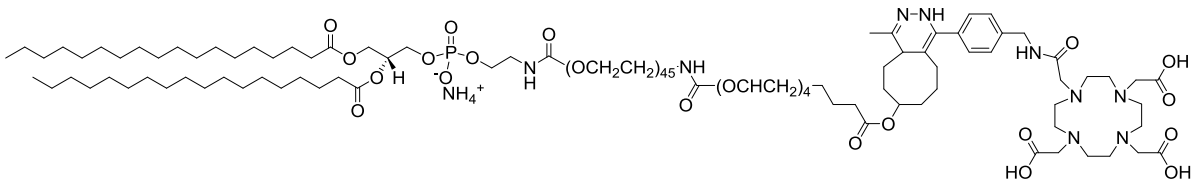
^{13}C NMR (125 MHz, CD_3OD) 21.1 ($C^{11}H_3$), 23.2 (C^2H_2), 28.5, 30.7, 36.2 (C^1H_2 or C^3H_2), 36.3 (C^1H_2 or C^3H_2), 40.0, 40.2, 43.8 (C^4H_2), 49.6, 51.1 (br), 54.3 (br), 54.5 (br), 56.2 (br), 57.5 (br), 129.1 (C^6H or C^7H), 129.3 (C^6H or C^7H), 132.4 (C^5), 145.2 (C^8), 165.2 (C^9), 168.8 (C^{10}), 175.5 (C=O), 175.5, 175.6, 175.7, 175.7.

MS (ES+) *m/z* calcd for $C_{36}H_{54}N_{11}O_{11}$ 816.4004 $[M+H]^+$, found 816.4010.

7.6.8 TCO-PEG$_4$ Reaction with 3.1 and 3.3

TCO-PEG$_4$ was added in 5 µL aliquots at a concentration of 8 M to the tetrazine solution at RT. Initial concentrations were 1.06 mM for **3.1** and 0.25 mM for **3.3**. All samples were in 400 µL of PBS at pH 7.6. Solutions were equilibrated for 1 min after addition prior to measurement.

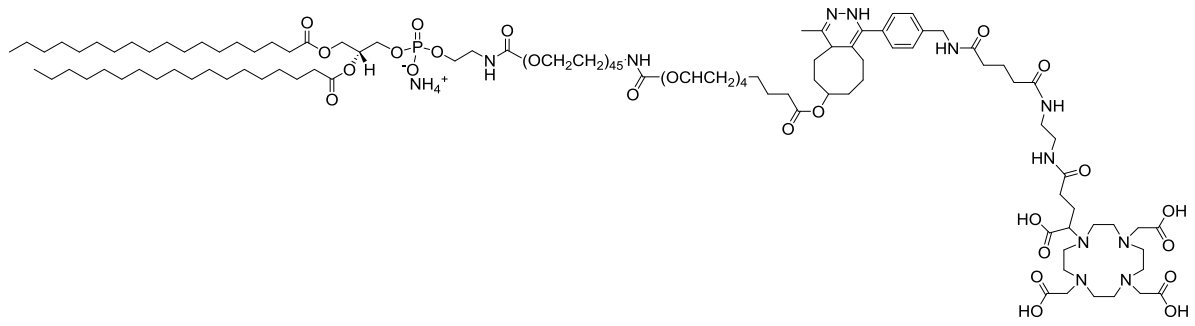
7.6.9 2.4 and 3.1 Reaction



3.1 (0.094 mg, 0.16 µmol) in PBS (400 µL) was added to 6 portions of **2.4** (6 x 0.26 mg, 0.48 µmol) at RT with the UV-vis. spectra recorded after each reaction. The lipids were also analysed by UPC^2(ES+) after each reaction.

MS UPC^2(ES+) *m/z* calcd. for $C_{180}H_{338}N_9O_{68}P$ 749.06 $[M-NH_4+6H]^{5+}$, found 748.53. t_R = 4.82 min.

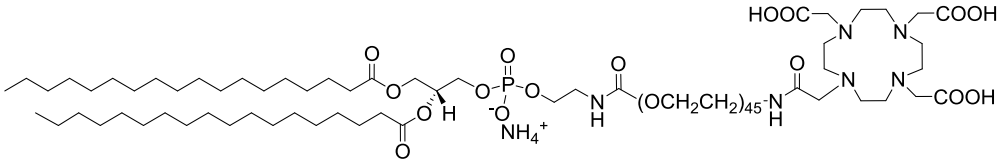
7.6.10 2.4 and 3.3 Reaction



3.3 (0.075 mg, 0.092 µmol) in PBS (400 µL) was added to 6 portions of **2.4** (6 x 0.26 mg, 0.48 µmol) at RT with the UV-vis. spectra recorded after each reaction. The lipids were also analysed by UPC^2(ES+) after each reaction.

MS UPC^2(ES+) *m/z* calcd. for $C_{192}H_{361}N_{12}O_{74}P$ 810.09 $[M\text{-}NH_4\text{+}6H]^{5+}$, found 809.93. t_R = 4.80 min.

7.6.11 DSPE-PEG$_{2000}$-DOTA – 3.5

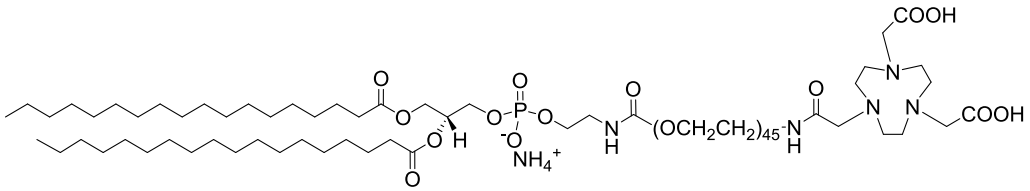


DOTA-NHS.HPF_6.TFA (10 mg, 13.1 µmol) and DSPE-PEG_{2000}-NH_2 (17.0 mg, 6.09 µmol) were dissolved in CH_3Cl (1 mL) and NEt_3 (6.4 µL, 0.046 mmol) added. The solution was stirred for 24 h at RT, following which the solvent was removed under reduced pressure and the residue dissolved in H_2O (5 mL). The crude product was purified by dialysis (Spectrum Labs float-a-lyzer 3.5-5 kD, G235053) over 24 h. The resulting solution was lyophilised, producing **3.5** (19.3 mg, 99 % yield) as a white solid.

MS UPC^2(ES+) *m/z* calcd. for $C_{148}H_{295}N_7O_{61}P$ 1059.33 $[M+3H]^{3+}$, found 1058.43. t_R = 4.51 min.

MS(MALDI) *m/z* calcd. for $C_{148}H_{290}N_6O_{61}P$ 3159.0 $[M\text{-}NH_4^+\text{+}2H]^+$, found 3162.4

7.6.12 DSPE-PEG$_{2000}$-NOTA – 3.6

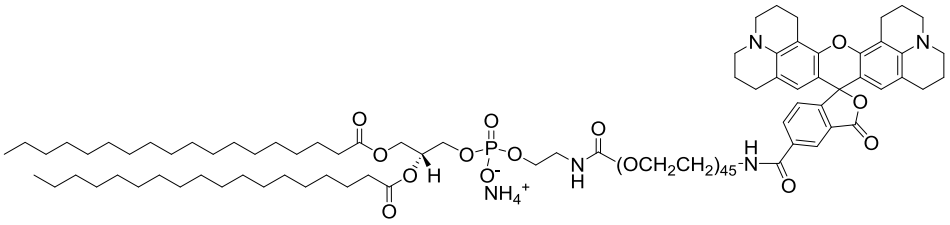


NOTA-NHS.HPF_6.TFA (8.4 mg, 12.8 µmol) and DSPE-PEG_{2000}-NH_2 (15.0 mg, 6.38 µmol) were dissolved in buffer (1.5 mL, carbonate buffer, pH 9.4) and the solution was stirred for 72 h at RT. The solution was analysed and further NOTA-NHS.HPF_6.TFA (4.2 mg, 6.4 µmol) was added. The solution was purified by dialysis (Spectrum Labs float-a-lyzer 3.5-5 kD, G235053) over 7 d. The resulting solution was lyophilised, producing **3.6** (16.1 mg, 82 % yield) as a white solid.

MS UPC^2(ES+) *m/z* calcd. for $C_{146}H_{296}N_7O_{61}P$ 788.75 $[M+4H+NH_4OAc]^{4+}$, found 789.81. t_R = 4.67 min.

7.7 Synthesis of Compounds in Chapter 4

7.7.1 DSPE-PEG$_{2000}$-ROX – 4.1



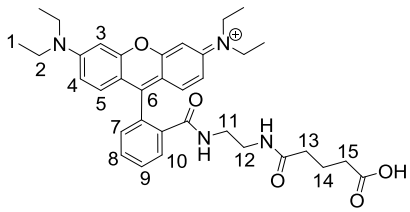
DSPE-PEG$_{2000}$-NH$_2$ (4.2 mg, 0.0015 mmol) was dissolved in $CHCl_3$ (2.5 mL) and Rhodamine-NHS (1.9 mg, 0.0030 mmol) added in DMF (76 µL). The solution was stirred for 24 h at RT, the solvent removed under reduced pressure and the residue dissolved in H_2O (5 mL). This was purified by dialysis (Spectum Labs float-a-lyzer 3.5-5 kD, G235053) over 48 h. The resulting solution was lyophilised, producing **4.1** (5.0 mg, 100 % yield) as a pink powder.

MS UPC^2(ES+) *m/z* calcd. for $C_{148}H_{295}N_7O_{61}P$ 846.51 $[M+4H+NH_4OAc]^{4+}$, found 847.71. t_R = 5.03 min.

MS(MALDI) *m/z* calcd. for $C_{165}H_{292}N_4O_{58}P$ 3289.0 $[M-NH_4^+ +2H]^+$, found 3291.2.

UV-vis. (0.1 M KCl, pH 7.18): λ_{max} = 580 nm.

7.7.2 Rh-COOH – 4.2b



4.2a (1.23 g, 2.53 mmol) and glutaric anhydride (1.44 g, 12.65 mmol) were dissolved in THF (50 mL) and heated to 70 ^oC for 4h, following which the temperature was reduced to 50 ^oC for 60 h. Once cooled, the solvent was removed under reduced pressure, dissolved in DCM (60 mL) and washed with water (3 x 60 mL). The organic fractions were combined, dried over $MgSO_4$ and the resulting pink solid purified by flash column chromatography (DCM/ MeOH 100:0 v/v to 95:5 v/v), producing **4.2b** (0.81 g, 54 % yield) as a pink solid. R_f = 0.20 (5 % MeOH/ DCM).

^{1}H NMR (400 MHz, $CDCl_3$) 1.11 (12 H, t, $^3J_{H\text{-}H}$ = 7.0, C^{1}H$_3$), 1.82-1.92 (2 H, m, C^{14}H$_2$), 2.15 (2 H, t, $^3J_{H\text{-}H}$ = 7.4, C^{13}H$_2$ or C^{15}H$_2$), 2.32 (2 H, t, $^3J_{H\text{-}H}$ = 7.0, C^{13}H$_2$ or C^{15}H$_2$), 2.98-3.04 (2 H, m, C^{11}H$_2$ or C^{12}H$_2$), 3.23-3.32 (10 H, m, C^{2}H$_2$ and C^{11}H$_2$ or C^{12}H$_2$), 6.21-6.27 (2 H, m, C^{4}H),

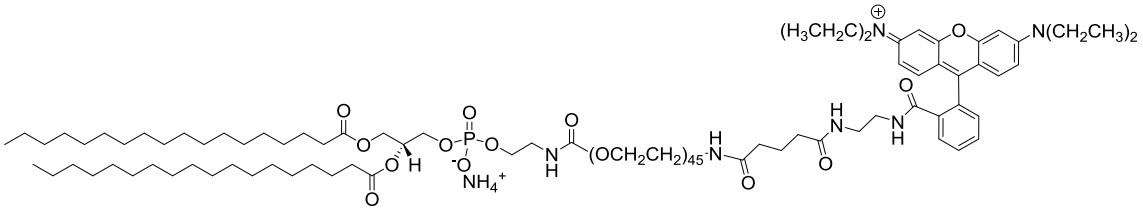
6.32-6.35 (2 H, m, C^3H), 6.36-6.40 (2 H, m, C^5H), 6.93 (1 H, s_{br}, OH or NH), 7.00-7.04 (1 H, m, C^7H), 7.36-7.42 (2 H, m, C^8H and C^9H), 7.84-7.90 (1 H, m, $C^{10}H$).

^{13}C NMR (100 MHz, $CDCl_3$) 12.6 (C^1H_3), 20.9 ($C^{14}H_2$), 33.5 ($C^{13}H_2$ or $C^{15}H_2$), 35.3 ($C^{13}H_2$ or $C^{15}H_2$), 40.2 ($C^{11}H_2$ or $C^{12}H_2$), 40.4 ($C^{11}H_2$ or $C^{12}H_2$), 44.5 (C^2H_2), 66.0 (C^6), 98.0 (C^3H), 104.6 (C^3H-$\underline{C}$-O), 108.5 (C^4H), 123.0 ($C^{10}H$), 124.0 (C^7H), 128.4 (C^5H or C^8H), 128.5 (C^5H or C^8H), 130.4 (C^7H-$\underline{C}$-C^6), 133.0 (C^9H), 149.0 (C^4H-$\underline{C}$-C^3H), 153.3 (C^5H-$\underline{C}$-C^6), 153.8 ($C^{10}H$-$\underline{C}$-C=O), 170.2 (Rh-C=O), 172.9 (C=O), 176.3 (C=O).

MS (ES+) *m/z* calcd. for $C_{35}H_{43}N_4O_5$ 599.3233 $[M+H]^+$, found 599.3251.

UV-vis. (PBS, pH 3.01): λ_{max} = 555 nm.

7.7.3 DSPE-PEG$_{2000}$-Rh – 4.2

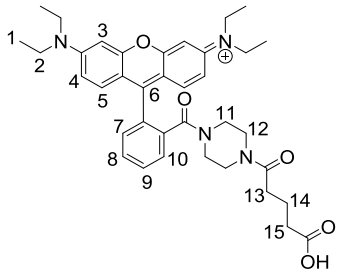


4.2b (3.15 mg, 5.25 x 10^{-3} mmol) and EDC.HCl (5.04 mg, 0.0263 mmol) were dissolved in $CHCl_3$ (1.2 mL) and stirred for 10 min. DSPE-PEG_{2000}-NH_2 (7.33 mg, 2.63 x 10^{-3} mmol) and NEt_3 (2.20 µL, 0.0158 mmol) were then added and the solution stirred for 72 h at RT. The solvent was removed under reduced pressure and the residue was purified by dialysis (Spectrum Labs float-a-lyzer 3.5-5 kS, G235053) over 24 h. The resulting solution was lyophilized, producing **4.2** (8.7 mg, 98 % yield) as an orange powder.

MS UPC^2(ES+) *m/z* calcd. for $C_{169}H_{317}N_8O_{60}P$ 862.54 $[M+3H+NH_4OAc]^{4+}$, found 863.38. t_R = 3.92 min.

UV−vis. (0.1 M KCl, pH 3.38): λ_{max} (nm) = 560 nm.

7.7.4 Rh+-COOH – 4.3c



4.3b (2.00 g, 3.91 mmol) and glutaric anhydride (2.23 g, 19.54 mmol) were dissolved in THF (40 mL) and the solution heated at reflux for 16 h. Once cooled, the solvent was removed under reduced pressure and the resulting pink solid purified by flash column chromatography (DCM/ MeOH 100:0 v/v to 80:20 v/v), producing **4.3c** (2.15 g, 88 % yield) as a pink solid. R_f = 0.13 (10 % MeOH/ DCM).

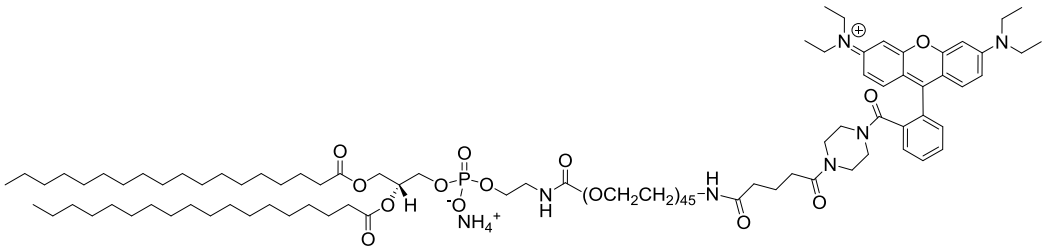
^{1}H NMR (400 MHz, CD_3OD) 1.31 (12 H, t, $^{3}J_{H\text{-}H}$ = 7.0, $C^{1}H_3$), 1.77-1.86 (2 H, m, $C^{14}H_2$), 2.25-2.35 (2 H, m, $C^{13}H_2$ or $C^{15}H_2$), 2.40 (2 H, t, $^{3}J_{H\text{-}H}$ = 7.4, $C^{13}H_2$ or $C^{15}H_2$), 3.36-3.49 (8 H, m, $C^{11}H_2$ and $C^{12}H_2$), 3.69 (8 H, q, , $^{3}J_{H\text{-}H}$ = 7.2), 6.99 (2 H, d, , $^{3}J_{H\text{-}H}$ = 2.4, $C^{3}H$), 7.08 (2 H, dd, , $^{3}J_{H\text{-}H}$ = 9.6, 2.4, $C^{4}H$), 7.28 (2 H, d, , $^{3}J_{H\text{-}H}$ = 9.6, $C^{5}H$), 7.51-7.55 (1 H, m, $C^{7}H$), 7.68-7.72 (1 H, m, $C^{10}H$), 7.74-7.80 (2 H, m, $C^{8}H$ and $C^{9}H$).

^{13}C NMR (100 MHz, CD_3OD) 12.8 ($C^{1}H_3$), 21.9 ($C^{14}H_2$), 33.1 ($C^{13}H_2$ or $C^{15}H_2$), 34.7 ($C^{13}H_2$ or $C^{15}H_2$), 42.2 ($C^{11}H_2$ or $C^{12}H_2$), 42,7 ($C^{11}H_2$ or $C^{12}H_2$), 43.1 ($C^{11}H_2$ or $C^{12}H_2$), 45.9 ($C^{11}H_2$ or $C^{12}H_2$), 46.9 ($C^{2}H_2$), 97.3 ($C^{3}H$), 114.9, 115.4 ($C^{4}H$), 128.9 ($C^{10}H$), 131.3 ($C^{7}H$, $C^{8}H$ or $C^{9}H$), 131.8 ($C^{7}H$, $C^{8}H$ or $C^{9}H$), 132.3, 133.2 ($C^{5}H$), 136.5 ($C^{7}H$-*C*-C^{6}), 157.0, 157.2 ($C^{3}H$-*C*-$C^{4}H$), 159.3, 163.1 (RhC=O), 169.6 (C=O), 173.7(C=O).

MS (ES+) *m/z* calcd. for $C_{37}H_{45}N_4O_5$ 625.3390 $[M+H]^+$, found 625.3404.

Excitation (PBS, pH 6.73): λ_{max} = 565 nm.

7.7.5 DSPE-PEG$_{2000}$-Rh+ - 4.3



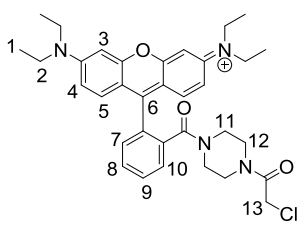
DSPE-PEG$_{2000}$-NH_2 (8.9 mg, 3.2 µmol) and **4.3c** (4.0 mg, 6.4 µmol) were dissolved in $CHCl_3$ (1 mL) following which EDC.HCl (6.1 mg, 31.8 µmol) and NEt_3 (2.7 µL, 19.2 µmol) were added. The solution was stirred for 16 h at RT, the solvent removed under reduced pressure and the residue was purified by dialysis (Spectrum Labs float-a-lyzer 3.5-5 kD, G235053) over 7 d. The resulting solution was lyophilized, producing **4.3** (10.3 mg, 94 % yield) as a pink powder.

MS UPC^2(ES+) *m/z* calcd. for $C_{171}H_{319}N_8O_{60}P$ 869.05 $[M+3H+NH_4OAc]^{4+}$, found 869.84. t_R = 4.89 min.

Excitation (PBS, pH 6.75): λ_{max} = 565 nm.

7.8 Synthesis of Compounds in Chapter 5

7.8.1 Rh+-Cl – 5.1a



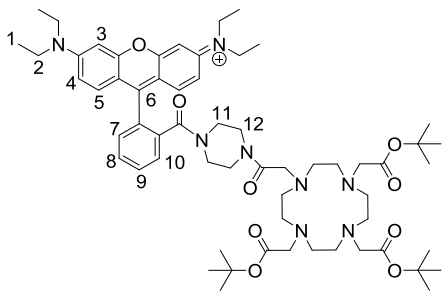
4.3b (1.53 g, 2.99 mmol) was dissolved in DCM (50 mL) and cooled to 0 ^{o}C in ice. NEt_3 (1.67 mL, 11.96 mmol) was added, followed by chloroacetyl chloride (261.8 µL, 3.29 mmol) and the solution was stirred for 3 h. H_2O (50 mL) was then added, the DCM layer separated and the water extracted with DCM (2 x 30 mL). The organic layers were combined, dried over $MgSO_4$, filtered and the solvent removed under reduced pressure. The crude pink solid was purified by flash column chromatography (DCM/ MeOH 100:0 v/v to 95:5 v/v), producing **5.1a** (1.00 g, 62 % yield) as a pink powder. R_f = 0.69 (DCM/ 10 % MeOH).

^{1}H NMR (400 MHz, $CDCl_3$) 1.26 (12 H, t, $^{3}J_{H\text{-}H}$ = 7.0, $C^{1}H_2$), 3.32-3.46 (8 H, m, $C^{11}H_2$ and $C^{12}H_2$), 3.50-3.65 (8 H, m, $C^{2}H_2$), 4.13 (2 H, s, $C^{13}H_2$), 6.67-6.72 (2 H, m, $C^{3}H$), 6.95-7.02 (2 H, m, $C^{4}H$), 7.17 (2 H, d, $^{3}J_{H\text{-}H}$ = 9.6, $C^{5}H$), 7.26-7.31 (1 H, m, $C^{7}H$), 7.46-7.52 (1 H, m, $C^{10}H$), 7.60-7.66 (2 H, m, $C^{8}H$ and $C^{9}H$).

^{13}C NMR (100 MHz, $CDCl_3$) 12.5 ($C^{1}H_3$), 41.2 ($C^{13}H_2$), 41.6 ($C^{11}H_2$ or $C^{12}H_2$), 46.0 ($C^{2}H_2$), 47.6 ($C^{11}H_2$ or $C^{12}H_2$), 96.1 ($C^{3}H$), 113.7, 114.4 ($C^{4}H$), 127.5 ($C^{10}H$), 130.1 (br, $C^{8}H$, $C^{9}H$ and $C^{7}H$), 130.2 (br, $C^{8}H$, $C^{9}H$ and $C^{7}H$), 131.0, 132.0 ($C^{5}H$), 135.0 (C^{7}-<u>C</u>-C^{6}), 155.7, 155.8, 157.7, 165.8 ($C^{13}H_2$-<u>C</u>=O), 167.7 (C=O).

MS(ES+) calc. for $C_{34}H_{40}ClN_4O_3$ 587.2789 $[M+H]^+$, found 587.2792.

7.8.2 ^{t}Bu-DO3A-Rh+ - 5.1b



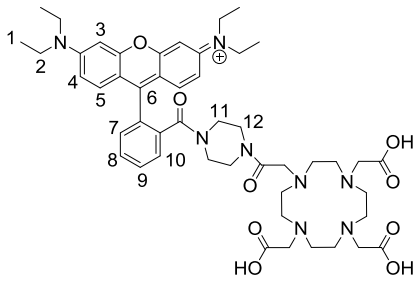
3.2 (0.14 g, 0.23 mmol) and Rh+-Cl (0.20 g, 0.34 mmol) were dissolved in CH_3CN (40 mL) and K_2CO_3 (0.127 g, 0.92 mmol) was added. The solution was heated to reflux for 48 h, cooled and filtered. The solvent was removed under reduced pressure and the crude pink solid purified by flash column chromatography (DCM/ MeOH 100:0 v/v to 95:5 v/v), producing **5.1b** (0.16 g, 66 % yield) as a pink solid. R_f = 0.73 (DCM/ 10 % MeOH).

^{1}H NMR (400 MHz, $CDCl_3$) 1.28 (12 H, t, $^{3}J_{H\text{-}H}$ = 7.0, $C^{1}H_3$), 1.40 (18 H, s, ^{t}Bu), 1.42 (9 H, s, ^{t}Bu), 1.70-2.68 (24 H, m), 3.23-3.40 (8 H, m, $C^{11}H_2$ and $C^{12}H_2$), 3.51-3.67 (8 H, m, $C^{2}H_2$), 6.73-6.77 (2 H, m, $C^{3}H$), 6.96-7.03 (2 H, m, $C^{4}H$), 7.15 (2 H, d, $^{3}J_{H\text{-}H}$ = 9.2, $C^{5}H$), 7.22-7.25 (1 H, m, $C^{7}H$), 7.42-7.46 (1 H, m, $C^{10}H$), 7.60-7.65 (2 H, m, $C^{8}H$ and $C^{9}H$).

^{13}C NMR (100 MHz, $CDCl_3$) 12.6 ($C^{1}H_3$), 27.9 (CH_3 ^{t}Bu), 41.1, 41.7, 44.4 (br, $C^{11}H_2$ and $C^{12}H_2$), 46.1 ($C^{2}H_2$), 47.6, 48.4 (br), 52.7 (br), 54.9, 55.7, 81.4 (4^{o} C ^{t}Bu), 81.8 (4^{o}C ^{t}Bu), 96.2 ($C^{3}H$), 113.8, 114.6 ($C^{4}H$), 127.4 ($C^{10}H$), 130.1 ($C^{7}H$, $C^{8}H$ or $C^{9}H$), 130.2 ($C^{7}H$, $C^{8}H$ or $C^{9}H$), 130.9 ($C^{7}H$, $C^{8}H$ or $C^{9}H$), 131.3, 132.0 ($C^{5}H$), 135.1 ($C^{7}H$-<u>C</u>-C^{6}), 155.4, 155.8, 157.8, 168.1 (Rh-C=O), 170.6 (C=O), 172.6 (C=O) 172.7 (C=O).

MS (ES+) *m/z* calcd. for $C_{60}H_{89}N_8O_9$ 1065.6753 $[M+H]^+$, found 1065.6842.

7.8.3 DO3A-Rh+ - 5.1



5.1b (101.6 mg, 95.3 µmol) was treated with TFA/CH_2Cl_2 (1/1 *v/v,* 4 mL) and stirred for 16 h at RT. The solvent was removed under reduced pressure and the residue purified by reverse phase flash column chromatography (H_2O/ MeOH/ TFA 95:5:0 v/v to 0:99.9:0.1 v/v), yielding **5.1** (63.5 mg, 74 % yield) as a pink solid.

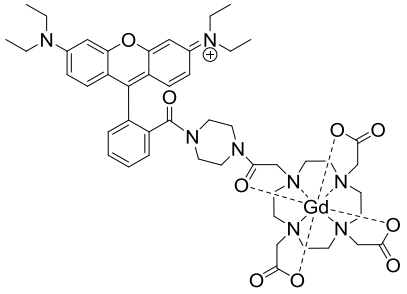
^{1}H NMR (400 MHz, CD_3OD) 1.30 (12 H, t, $^{3}J_{H\text{-}H}$ = 7.2, $C^{1}H_3$), 3.-04-3.14 (8 H, m, CH_2), 3.36-3.55 (10 H, m, CH_2), 3.64-3.73 (12 H, m, $C^{2}H_2$ and CH_2), 6.95 (2 H, d, $^{3}J_{H\text{-}H}$ = 2.4, $C^{3}H$), 7.05-7.11 (2 H, m, $C^{4}H$), 7.29 (2 H, d, $^{3}J_{H\text{-}H}$ = 9.6, $C^{5}H$), 7.48-7.49 (1 H, m, $C^{7}H$), 7.72-7.79 (3 H, m, $C^{8}H$, $C^{9}H$ and $C^{10}H$).

^{13}C NMR (100 MHz, CD_3OD) 12.9 ($C^{1}H_3$), 42.8 (br), 44.9, 45.4, 45.7, 46.9 ($C^{2}H_2$), 50.7 (br), 52.2 (br), 52.7 (br), 54.4 (br), 56.5, 57.1, 97.3 ($C^{3}H$), 114.8, 115.4 ($C^{4}H$), 129.0 ($C^{10}H$), 131.2 ($C^{8}H$ or $C^{9}H$), 131.3($C^{8}H$ or $C^{9}H$), 131.7 ($C^{7}H$), 132.1, 133.2 ($C^{5}H$), 136.6 ($C^{7}H$-<u>C</u>-C^{6}), 157.0, 157.2, 159.2, 169.5 (C=O), 170.0 (C=), 170.8 (C=O), 176.5 (C=O).

MS(ES+) calc. for $C_{48}H_{65}N_8O_9$ 897.4875 $[M+H]^+$, found 897.4906.

UV.vis (PBS, pH 6.99): λ_{max} = 565 nm.

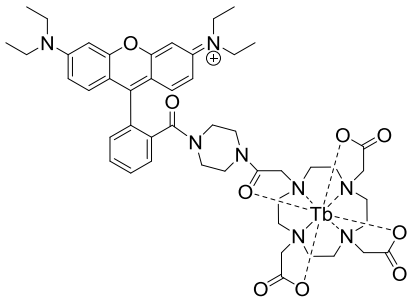
7.8.4 Gd-DO3A-Rh+ - 5.1-Gd



5.1 (33.8 mg, 38.0 μmol) and $GdCl_3.6H_2O$ (28.2 mg, 75.9 μmol) were dissolved in H_2O (10 mL) and the pH adjusted to 5.5 using 1 M NaOH. The solution was stirred for 16 h at RT, following which the solvent was removed under reduced pressure and the residue purified by reverse phase flash column chromatography (H_2O/ MeOH/ TFA 95:5:0 v/v to 0:99.9:0.1 v/v), yielding **5.1-Gd** (29.4 mg, 74 % yield) as a pink solid.

MS(ES+) calc. for $C_{48}H_{62}N_8O_9Gd$ 1052.3881 $[M+H]^+$, found 1052.3900.

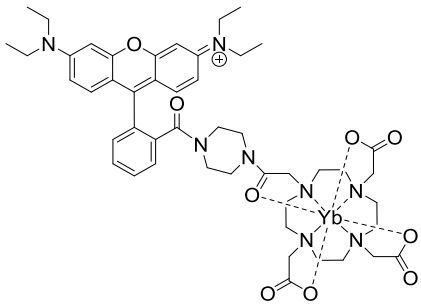
7.8.5 Tb-DO3A-Rh+ - 5.1-Tb



5.1 (5.3 mg, 5.0 μmol) and $TbCl_3.6H_2O$ (4.4 mg, 11.8 μmol) were dissolved in H_2O (2 mL) and the pH adjusted to 5.5 using 1 M NaOH. The solution was stirred for 16 h at RT, following which the solvent was removed under reduced pressure and the residue purified by LCMS, yielding **5.1-Tb** (6.1 mg, 65 % yield) as a pink solid.

MS(ES+) calc. for $C_{48}H_{62}N_8O_9Tb$ 1053.3893 $[M+H]^+$, found 1053.3883.

7.8.6 Yb-DO3A-Rh+ - 5.1-Yb



5.1 (6.6 mg, 7.3 μmol) and $YbCl_3.6H_2O$ (5.7 mg, 14.7 μmol) were dissolved in H_2O (2 mL) and the pH adjusted to 5.5 using 1 M NaOH. The solution was stirred for 16 h at RT, following which the solvent was removed under reduced pressure and the residue purified by reverse phase flash column chromatography (H_2O/ MeOH/ TFA 95:5:0 v/v to 0:99.9:0.1 v/v), yielding **5.1-Yb** (6.8 mg, 87 % yield) as a pink solid.

MS(ES+) calc. for $C_{48}H_{62}N_8O_9Yb$ 1068.4028 $[M+H]^+$, found 1068.4049.

7.9 Radiochemistry

$^{68}GaCl_3$ was produced from either an Eckert & Ziegler IGG100 $^{68}Ge/^{68}Ga$ generator or an iThemba 740 MBq $^{68}Ge/^{68}Ga$ generator using a fully-automated Modular-Lab system, elution details provided below. Cation exchange cartridges (Strata™-XC, 33µm, Strong Cation, 30 mg/mL, Phenomenex) were pre-activated using 1 mL 0.6 M HCl followed by washing with 10 mL H_2O. Cartridge purification was performed using a SepPac $^{t}C_{18}$ light cartridge which was pre-conditioned using EtOH (5 mL) and NaOAc buffer (5 mL 0.2 M pH 4). The sample was then loaded onto the cartridge, washed with NaOAc buffer (5 mL) and eluted in EtOH (0.5 mL).

HPLC was performed on an Agilent 1100 series HPLC system (Agilent Technologies, Stockport, UK) equipped with a UV (254 nm) detector and a LabLogic Flow-Count radio-detector. A flow rate of 1 mL/ min was used with one of the following three methods. Method 1: A Phenomenex Gemini C18 column (150 mm x 4.6 mm) was used with a gradient of 95-5 % A over 15 min, 5 % A for 5 min and 5-95 % A over 10 min. A = H_2O (0.1% TFA) B = CH_3CN (0.1% TFA). Method 2: A Phenomenex Gemini C18 column (150 mm x 4.6 mm) was used with a gradient of 95-5 % A over 15 min, 5 % A for 1 min, 5-95 % A over 1 min and 95 % A for 1 min. A = H_2O (0.1% TFA) B = CH_3CN (0.1% TFA). Method 3: A Phenomenex Gemini C18 column (150 mm x 4.6 mm) was used with a gradient of 95-35 % A over 10 min, 35-95 % A over 1 min and 95 % A for 1 min. A = H_2O (0.1% TFA) B = CH_3CN (0.1% TFA). Method 4: A Phenominex BioSep-SEC-s2000 column (300 x 7.80 mm) was used with 100 % A for 30 min. A = 0.02 M NaH_2PO_4. Laura 3 software (LabLogic, Sheffield, UK) was used to analyse HPLC chromatograms.

7.9.1 Eckert & Ziegler IGG100 $^{68}Ge/^{68}Ga$ Generator

7.9.1.1 HCl Elution

$^{68}GaCl_3$ was eluted from an Eckert & Ziegler IGG100 $^{68}Ge/^{68}Ga$ Generator in 2 mL of 0.1 M HCl and buffered prior to use.

7.9.1.2 NaCl Elution[16]

$^{68}GaCl_3$ was eluted from an Eckert & Ziegler IGG100 $^{68}Ge/^{68}Ga$ Generator in 10 mL of a 0.1 M HCl solution onto a pre-activated cation exchange cartridge (Strata™-XC, 33µm, Strong

Cation, 30 mg/mL, Phenomenex) and removed using 0.8 mL 50 % acidified saline (1:1 H_2O/ acidified saline).

7.9.2 iThemba 740 MBq $^{68}Ge/^{68}Ga$ Generator

7.9.2 1 HCl Elution

$^{68}GaCl_3$ was eluted from an iThemba 740 MBq $^{68}Ge/^{68}Ga$ Generator in 2.5 mL of 1 M HCl and the pH adjusted using 2 M NaOAc or appropriate buffer before use.

7.9.2.2 NaCl Elution[16]

$^{68}GaCl_3$ was eluted from an iThemba 740 MBq $^{68}Ge/^{68}Ga$ Generator in 10 mL of 0.6 M HCl and diluted into 80 mL of water. This was then trapped on a pre-activated cation exchange cartridge (Strata™-XC, 33µm, Strong Cation, 30 mg/mL, Phenomenex) and removed using 1 mL 50 % acidified saline (1:1 H_2O/ acidified saline).

7.9.3 DO3A-tetrazine – 3.1

The iThemba generator was used exclusively for this work, with elution using either the HCl or NaCl protocols above. The stated amount of **3.1** was dissolved in the relevant pH 0.2 M NaOAc buffer and the according volume of ^{68}Ga added. The solutions were heated to 90 ^oC for 10 min, followed by cooling. Purification was performed using a SepPac $^tC_{18}$ light cartridge, as explained above. HPLC analysis was performed using method 3. See **Table 3.6** for further details.

7.9.3.1 Reaction with TCO-Microbubbles

After purification, **3.1-Ga** was heated to dryness (15 min 90 ^oC), cooled and 0.1 mL of a microbubble solution containing 5 mol% **2.4** was added. This was incubated for 45 minutes at room temperature, following which it was analysed by SEC HPLC (method 4). The same solution was then heated to 90 ^oC for 45 min and again analysed by HPLC (method 4).

7.9.3.2 Reaction with DSPE-PEG_{2000}-TCO 2.4

After purification, **3.1-Ga** was added directly to **2.4** (0.136 mg). This was incubated for 45 minutes at room temperature, following which it was analysed by HPLC (method 4).

After purification, **3.1-Ga** was heated to dryness (15 min 90 ^oC), cooled and a solution of **2.4** in H_2O (0.25 mL, 1.66 mg/ mL) was added. This was incubated for 45 minutes at room

temperature, following which it was analysed by HPLC (method 4). The same solution was then heated to 90 ^{o}C for 45 min and again analysed by HPLC (method 4).

7.9.4 DOTAGA-tetrazine – 3.3

Activity was eluted using either the HCl or NaCl protocols above on either the an Eckert & Ziegler or iThemba generator. The stated amount of **3.3** was dissolved in the relevant pH 0.2 M NaOAc buffer and the according volume of ^{68}Ga added. The solutions were heated to 90 ^{o}C for 10 min, followed by cooling. Purification was performed using a SepPac $^{t}C_{18}$ light cartridge, as explained above. HPLC analysis was performed using method 3. See **Tables 3.2-3.5** for further details.

7.9.4.1 Reaction with TCO-Microbubbles

After purification, **3.3-Ga** was heated to dryness (15 min 90 ^{o}C), cooled and 0.1 mL of a microbubble solution containing 5 mol% **2.4** was added. This was incubated for 45 minutes at room temperature, following which it was analysed by SEC HPLC (method 4).

7.9.4.2 Reaction with DSPE-PEG$_{2000}$-TCO 2.4

After purification, **3.3-Ga** was heated to dryness (15 min 90 ^{o}C), cooled and a solution of **2.4** in H_2O (0.25 mL, 1.66 mg/ mL) was added. This was incubated for 45 minutes at room temperature, following which it was analysed by HPLC (method 4). The same solution was then heated to 90 ^{o}C for 45 min and again analysed by HPLC (method 4).

7.9.5 DSPE-DOTA – 3.5

General large scale reaction. For other reactions, modify volumes, quantities and centrifugation times appropriately (**Tables 3.7-3.11**)

The iThemba generator was used exclusively for this work, with elution using the NaCl protocol above. **3.5** was dissolved in pH 5 0.2 M NaOAc buffer (0.5 mL) and $^{68}GaCl_3$ (1 mL) added. The pH was measured and the solutions heated to 90 ^{o}C for 10 min, followed by cooling. Purification was performed by centrifugation. HPLC analysis was performed using SEC method 4.

0.5 mL filters: The reaction solution was split between four filters, the vial washed with PBS and placed in two further filters. These were centrifuged at 13,000 rpm for 15 min, followed by the addition of 400 μL PBS and a further 15 min centrifugation. For the removal of

activity, the filters were reversed and placed in new Eppendorf times. These were centrifuged at 2000 rpm for 2 min and the resulting solution used for further experiments.

15 mL filters: The reaction solution was placed in one filter and placed in the centrifuge balanced by another falcon tube. This was centrifuged at 5000 rpm for 15 min, followed by the addition of 1 mL PBS and a further 15 min centrifugation. Activity was removed directly from the filter.

Microbubble formation: The microbubble solution was premade with the desired lipids (minus **3.5**), propylene glycol and glycerol. 0.8 mL of the purified **3.5-Ga** solution was taken and added to this mixture, following which the vial was sealed, purged with perfluorobutane gas and shaken for 60 s as in the general microbubble procedure.

7.9.6 DSPE-NOTA – 3.6

General large scale reaction. For other reactions, modify volumes, quantities and centrifugation times appropriately (**Table 3.12**)

The iThemba generator was used exclusively for this work, with elution using the NaCl protocol above. **3.6** was dissolved in pH 5 0.2 M NaOAc buffer (0.225 mL) and $^{68}GaCl_3$ (0.15 mL) added. The pH was measured and the solutions heated to 90 ^{o}C for 10 min, followed by cooling. Purification was performed by centrifugation. HPLC analysis was performed using SEC method 4.

0.5 mL filters: The reaction solution was split between two filters. These were centrifuged at 13,000 rpm for 15 min, followed by the addition of 400 µL PBS and a further 15 min centrifugation.

15 mL filters: The reaction solution was placed in one filter and placed in the centrifuge balanced by another falcon tube. This was centrifuged at 5000 rpm for 15 min, followed by the addition of 1 mL PBS and a further 15 min centrifugation.

7.9.7 DO3A-Rh – 5.2

The iThemba generator was used exclusively for this work, with elution using the HCl protocol above. The 25 µ of **5.2** was dissolved in pH 4.5 0.2 M NaOAc buffer and 0.5 mL of ^{68}Ga (in 1 M HCl) added. The solutions were heated to 90 ^{o}C for 10 min, followed by cooling. Purification was performed using a SepPac $^{t}C_{18}$ light cartridge, as explained above. HPLC analysis was performed using method 3.

7.10 *In Vitro* Studies

These studies were performed by Marta Braga may be discussed in more detail in her thesis (not submitted).[17]

The MDA-MB-231.PE and M21 cell lines were plated in Opticell culture cassettes at a concentration of $2x10^6$ cells in 10 mL of media per Opticell. After incubation for 24 h, the desired microbubbles were formed (unmodified, 5 % TCO, 5 % TCO and 5 % RGD and 10 % RGD) and diluted in media to 1 x 10^7 MBs/ mL. The media was then removed and replaced with 10 mL of media containing MBs (total of 1 x 10^8 MBs added to each Opticell). The Opticell was flipped such that the cells were adhered to the top surface to ensure contact with the buoyant MBs and incubated at 37 ^oC for 15 min. The Opticell were then turned so that the cells were adhered to the bottom again and rested for 5 min. Images were taken by focussing on the upper membrane (free MBs) and the lower (calls and adhered MBs), with a minimum of 5 images of each taken.

7.10.1 Washing Studies

After the above images were taken, the Opticell were washed with PBS and 5 further images were taken.

7.10.2 Blocking Experiments

24 h post plating of cells, they were incubated with linear or cyclic RGD (1 mg in 10 mL media) for 15 min. The media was then removed and MBs added as described above. After the final images were taken, the Opticell were also washed with PBS and 5 further images taken.

7.11 *In Vivo* Studies

All animal procedures were performed in accordance with UK Home Office regulations and institutional guidelines. Prior to any experimental procedure, mice were anesthetised with oxygen (0.8 L/min) mixed with 2.0% vaporised isoflurane.

7.11.1 Ultrasound Imaging

This work was performed by Marta Braga and may be discussed in more detail in her thesis (not yet submitted).[17] Home office license number: 70/8651.

Female athymic nude mice were implanted with MDA-MB-231 tumours. Once tumours reached sufficient size, animals were sedated and ultrasound images obtained on a Verasonics Vantage 128 Elements machine (Kirkland, USA) using plane wave imaging with 15 compounded angles. Microbubbles were administered by tail vein injection, with two injections per animal. Image reconstruction was performed at 1000 Hz for 1 s of acquisition, whilst kinetic analysis used a frequency of 1 Hz over 300 s.

7.11.2 Ultrasound Delivery

This work was performed by Sophie Morse and may be discussed in more detail in her thesis.[18] Home office license number: 70/8585.

These experiments were performed on wild type C57b1/6 female mice using the experimental set up described in literature.[19] After sedation, the hair on the scalp was removed with an electric trimmer and depilatory cream, following which the location of the left hippocampus was identified. A solution containing SonoVue microbubbles and the desired contrast agent (**5.1-Gd** or **5.2**) were administered through tail vein injection and focussed ultrasound applied to the desired region.

Focused ultrasound pulses were generated using a 1 MHz single-element, spherical-segment focused ultrasound transducer (active diameter: 90 mm, geometric focus: 77 mm, H-198, Sonic Concepts, Bothell, USA). All experiments involved 125 ultrasound pulses emitted at 1 MHz centre frequency.

Short pulses: This used a PRP of 0.33 MPa and involved sonication burst lengths of 10 ms at a repetition frequency of 0.5 Hz. A pulse length of 0.005 ms and repetition frequency of 1250 Hz were used. Long pulses: This used a PRP of 0.49 MPa. A pulse length of 10 ms and repetition frequency of 0.5 Hz were used.

Following sonication, mice were transcardially perfused with 5 mL phosphate-buffered saline and 10 mL 4% paraformaldehyde (PFA) to first clear the bloodstream and then fix the tissue in situ. Brains were extracted from the skull and prepared for histological analysis. After 16 hours it was cryoprotected by submerging them into 15% sucrose for 6 hours and then 30% sucrose overnight. They were then embedded in an optimal cutting temperature (OCT) compound, frozen in a mould using cooled isopentane, and sectioned with a cryostat.

Delivery of the contrast agent was assessed using fluorescence microscopy images of brain sections, taken at 2000 ms exposure time. The rhodamine dye was excited at 550/25 nm and

emission was filtered at 605/70 nm. Three slices were selected from each brain, one dorsal, one central and one ventral. The relative dose and distribution was quantified by calculating the normalised optical density (NOD, the average increase in fluorescence in the targeted area normalised by the control).

7.12 References

1. B. Jagadish, G. L. Brickert-Albrecht, G. S. Nichol, E. A. Mash and N. Raghunand, *Tetrahedron Lett.*, 2011, **52**, 2058-2061.
2. F. Kielar, L. Tei, E. Terreno and M. Botta, *J. Am. Chem. Soc.*, 2010, **132**, 7836-7837.
3. P. Y. Cheong, Thesis, Novel Imaging Targets in Inflammation, Imperial College London, 2014.
4. K.-P. Eisenwiener, P. Powell and H. R. Mäcke, *Bioorg. Med. Chem. Lett.*, 2000, **10**, 2133-2135.
5. H. L. Evans, Q.-D. Nguyen, L. S. Carroll, M. Kaliszczak, F. J. Twyman, A. C. Spivey and E. O. Aboagye, *Chem. Commun.*, 2014, **50**, 9557-9560.
6. X. Zhang, Y. Shiraishi and T. Hirai, *Org. Lett.*, 2007, **9**, 5039-5042.
7. L. Bi, *Patent, WO2014063033 A3*, 2014.
8. C. Rivas, G. J. Stasiuk, J. Gallo, F. Minuzzi, G. A. Rutter and N. J. Long, *Inorg. Chem.*, 2013, **52**, 14284-14293.
9. G. R. Fulmer, A. J. M. Miller, N. H. Sherden, H. E. Gottlieb, A. Nudelman, B. M. Stoltz, J. E. Bercaw and K. I. Goldberg, *Organometallics*, 2010, **29**, 2176-2179.
10. D. M. Corsi, C. Platas-Iglesias, H. v. Bekkum and J. A. Peters, *Magn. Reson. Chem.*, 2001, **39**, 723-726.
11. C. A. Sennoga, V. Mahue, J. Loughran, J. Casey, J. M. Seddon, M. Tang and R. J. Eckersley, *Ultrasound Med. Biol.*, 2010, **36**, 2093-2096.
12. P. S. Sheeran, S. Luois, P. A. Dayton and T. O. Matsunaga, *Langmuir*, 2011, **27**, 10412-10420.
13. S. Li, S. Lin, Y. Cheng, T. O. Matsunaga, R. J. Eckersley and M.-X. Tang, *Ultrasound Med. Biol.*, 2015, **41**, 1422-1431.
14. C. Li, P. Winnard Jr and Z. M. Bhujwalla, *Tetrahedron Lett.*, 2009, **50**, 2929-2931.
15. H. L. Evans, L. Carroll, E. O. Aboagye and A. C. Spivey, *J. Labelled Compd. Radiopharm.*, 2014, **57**, 291-297.
16. D. Mueller, W. A. P. Breeman, I. Klette, M. Gottschaldt, A. Odparlik, M. Baehre, I. Tworowska and M. K. Schultz, *Nat. Protocols*, 2016, **11**, 1057-1066.
17. M. Braga, Thesis, Not Submitted, Imperial College London.
18. S. Morse, Thesis, Not Submitted, Imperial College London.
19. B. Baseri, J. J. Choi, Y.-S. Tung and E. E. Konofagou, *Ultrasound Med. Biol.*, 2010, **36**, 1445-1459.

Appendix

A.1 Microbubble Sizing

Errors propagated for size using: $\delta_{\bar{x}} = \frac{\sqrt{(\delta_1)^2+(\delta_2)^2+\ldots+(\delta_N)^2}}{N}$

Errors calculated for concentrations using: $\delta_{\bar{x}} = \frac{\sigma}{\sqrt{N}}$ where $\sigma = \sqrt{\frac{(x_1-\bar{x})^2+(x_2-\bar{x})^2+\ldots+(x_N-\bar{x})^2}{N}}$

Table A.1: Size and concentration information for unmodified microbubbles with a formulation containing DPPC, DPPA and DSPE-PEG_{2000}-NH_2 in the mol% ratio 82:8:10 respectively.

Phospholipid	**Unmodified**			
Iteration	**1**	**2**	**3**	**Average**
Size/ µm	2.10 ± 0.93	2.63 ± 1.36	2.53 ± 1.04	2.42 ± 0.65
Conc./ MB mL^{-1}	1.22 x 10^9	8.90 x 10^8	1.67 x 10^9	1.26 x 10^9 ± 1.85 x 10^8

Table A.2: Size and concentration information for microbubbles incorporating DSPE-PEG_{2000}-cRGDfK **2.1** in a formulation containing DPPC and DPPA in the mol% ratio 10:82:8 respectively.

Phospholipid	**2.1**			
Iteration	**1**	**2**	**3**	**Average**
Size/ µm	2.04 ±1.08	2.10 ± 0.83	1.73 ± 0.93	1.96 ± 0.55
Conc./ MB mL^{-1}	3.11 x 10^8	1.08 x 10^9	1.80 x 10^9	1.06 x 10^9 ± 2.51 x 10^8

Table A.3: Size and concentration information for microbubbles incorporating DSPE-PEG_{2000}-cRGDfK **2.1** and DSPE-PEG_{2000}-TCO **2.4** in a formulation containing DPPC and DPPA in the mol% ratio 5:5:82:8 respectively.

Phospholipid	**2.1/2.4**			
Iteration	**1**	**2**	**3**	**Average**
Size/ µm	1.73 ± 0.93	2.03 ± 0.85	1.83 ± 0.79	1.86 ± 0.50
Conc./ MB mL^{-1}	1.80 x 10^9	1.01 x 10^9	2.26 x 10^9	1.69 x 10^9 ± 2.98 x 10^8

Table A.4: Size and concentration information for microbubbles incorporating DSPE-PEG_{2000}-DOTA **3.5** in a formulation containing DPPC and DPPA in the mol% ratio 10:82:8 respectively.

Phospholipid	**3.5**			
Iteration	**1**	**2**	**3**	**Average**
Size/ µm	4.60 ± 1.74	4.85 ± 1.73	4.78 ± 1.77	4.74 ± 1.00
Conc./ MB mL^{-1}	8.45 x 10^8	5.47 x 10^8	4.33 x 10^8	6.08 x 10^8 ± 1.00 x 10^8

Table A.5: Size and concentration information for microbubbles incorporating DSPE-PEG_{2000}-NOTA **3.6** in a formulation containing DPPC and DPPA in the mol% ratio 10:82:8 respectively.

Phospholipid	**3.6**			
Iteration	**1**	**2**	**3**	**Average**
Size/ µm	4.05 ± 1.52	4.09 ± 1.55	4.20 ± 1.59	4.11 ± 0.89
Conc./ MB mL^{-1}	8.89 x 10^8	8.56 x 10^8	6.84 x 10^8	8.09 x 10^8 ± x 5.36 10^7

Table A.6: Size and concentration information for microbubbles incorporating DSPE-PEG_{2000}-DOTA **3.5** and DSPE-PEG_{2000}-cRGDfK **2.1** in a formulation containing DPPC and DPPA in the mol% ratio 5:5:82:8 respectively.

Phospholipid	**3.5/2.1**			
Iteration	**1**	**2**	**3**	**Average**
Size/ µm	4.53 ±1.73	4.97 ± 1.76	4.66 ± 1.70	4.72 ± 0.99
Conc./ MB mL^{-1}	5.10 x 10^8	4.39 x 10^8	5.45 x 10^8	4.98 x 10^8 ± 2.55 x 10^7

Table A.7: Size and concentration information for microbubbles incorporating DSPE-PEG_{2000}-NOTA **3.6** and DSPE-PEG_{2000}-cRGDfK **2.1** in a formulation containing DPPC and DPPA in the mol% ratio 5:5:82:8 respectively.

Phospholipid	**3.6/2.1**			
Iteration	**1**	**2**	**3**	**Average**
Size/ µm	4.36 ±1.70	4.40 ± 1.73	4.56 ± 1.78	4.44 ± 1.00
Conc./ MB mL^{-1}	8.04 x 10^8	4.03 x 10^8	4.33 x 10^8	4.47 x 10^8 ± 1.20 x 10^8

Table A.8: Size and concentration information for microbubbles incorporating phospholipid N-Rh-PE in a formulation containing DPPC, DPPA and DSPE-PEG_{2000}-NH_2 in the mol% ratio 1:82:8:9 respectively.

Phospholipid	**N-Rh-PE**
Iteration	**1**
Size/ µm	1.40 ± 1.24
Conc./ MB mL^{-1}	3.07 x 10^8

Table A.9: Size and concentration information for microbubbles incorporating DSPE-PEG_{2000}-ROX **4.1** in a formulation containing DPPC, DPPA and DSPE-PEG_{2000}-NH_2 in the mol% ratio 1:82:8:9 respectively.

Phospholipid	**4.1**			
Iteration	**1**	**2**	**3**	**Average**
Size/ µm	2.61 ±1.03	1.04 ± 0.37	2.74 ± 1.62	2.13 ± 0.65
Conc./ MB mL^{-1}	7.92 x 10^8	1.73 x 10^8	2.18 x 10^8	3.94 x 10^8 ± 1.63 x 10^8

Table A.10: Size and concentration information for unmodified microbubbles used to make nanodroplets in a formulation containing DPPC and DSPE-PEG_{2000}-OMe in the mol% ratio 90:10 respectively.

Phospholipid	**Unmodified ND**			
Iteration	**1**	**2**	**3**	**Average**
Size/ µm	4.73 ± 1.73	4.94 ± 1.72	4.60 ± 1.54	4.76 ± 0.96
Conc./ MB mL^{-1}	9.37 x 10^8	1.10 x 10^9	8.29 x 10^8	9.55 x 10^8 ± 6.43 x 10^7

Table A.11: Size and concentration information for microbubbles incorporating DSPE-PEG_{2000}-Rh **4.2** in a formulation containing DPPC and DSPE-PEG_{2000}-OMe in the mol% ratio 1:90:9 respectively.

Phospholipid	**4.2 (1 mol%)**			
Iteration	**1**	**2**	**3**	**Average**
Size/ µm	3.45 ± 1.40	3.78 ± 1.58	4.25 ± 1.54	3.83 ± 0.87
Conc./ MB mL^{-1}	6.69 x 10^8	1.03 x 10^9	6.55 x 10^8	7.84 x 10^8 ± 1.00 x 10^8

Table A.12: Size and concentration information for microbubbles incorporating DSPE-PEG_{2000}-Rh+ **4.3** in a formulation containing DPPC and DSPE-PEG_{2000}-OMe in the mol% ratio 1:90:9 respectively.

Phospholipid	**4.3 (1 mol%)**			
Iteration	**1**	**2**	**3**	**Average**
Size/ µm	3.77 ± 1.54	4.77 ± 1.67	3.68 ± 1.65	4.07 ± 0.93
Conc./ MB mL^{-1}	1.82 x 10^9	9.25 x 10^8	1.83 x 10^9	1.53 x 10^9 ± x 2.45 10^8

Table A.13: Size and concentration information for microbubbles incorporating DSPE-PEG_{2000}-Rh+ **4.3** in a formulation containing DPPC in the mol% ratio 4:96 respectively.

Phospholipid	**4.3 (4 mol%)**			
Iteration	**1**	**2**	**3**	**Average**
Size/ µm	4.11 ± 1.37	4.48 ± 1.64	4.04 ± 1.43	4.21 ± 1.52
Conc./ MB mL^{-1}	7.72 x 10^8	3.28 x 10^8	1.02x 10^9	7.07 x 10^8 ± 1.65 x 10^8

Table A.14: Size and concentration information for microbubbles incorporating DSPE-PEG_{2000}-Rh **4.2** in a formulation containing DPPC and DSPE-PEG_{2000}-OMe in the mol% ratio 1:90:9 respectively. pH modified to 3.5 before measurement.

Phospholipid	**4.2 (1 mol%, pH 3.5)**
Iteration	**1**
Size/ µm	2.14 ± 0.93
Conc./ MB mL^{-1}	1.26 x 10^9

A.2 NMR Spectra

A.2.1 DSPE-PEG$_{2000}$-Maleimide – 2.1a

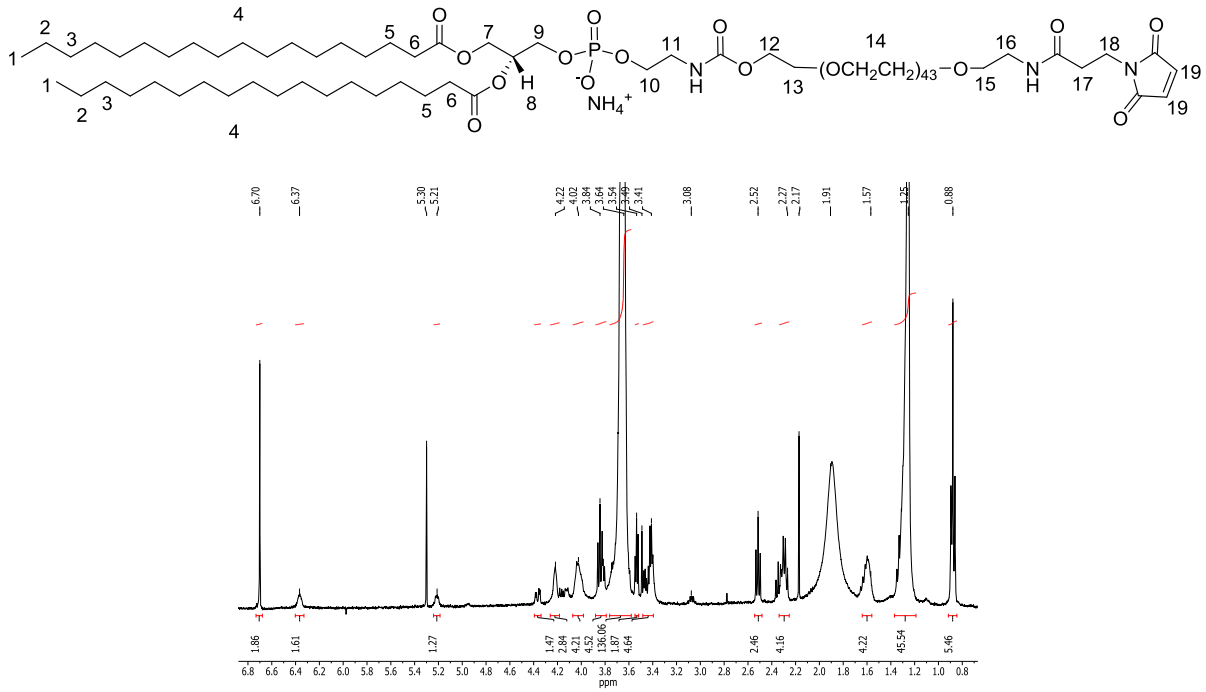


Figure A.1: Structure and ^{1}H NMR spectrum of DSPE-PEG$_{2000}$-maleimide **2.1a**. Solvent $CDCl_3$.

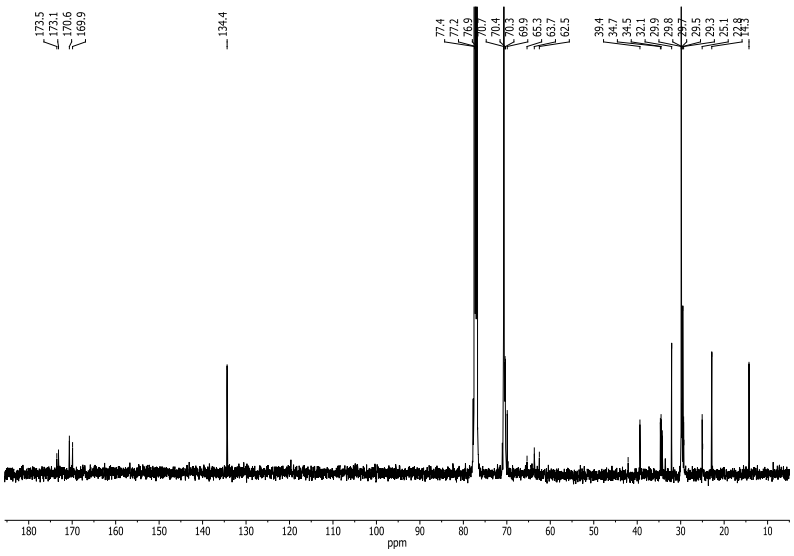


Figure A.2: ^{13}C NMR spectrum of DSPE-PEG$_{2000}$-maleimide **2.1a**. Solvent $CDCl_3$.

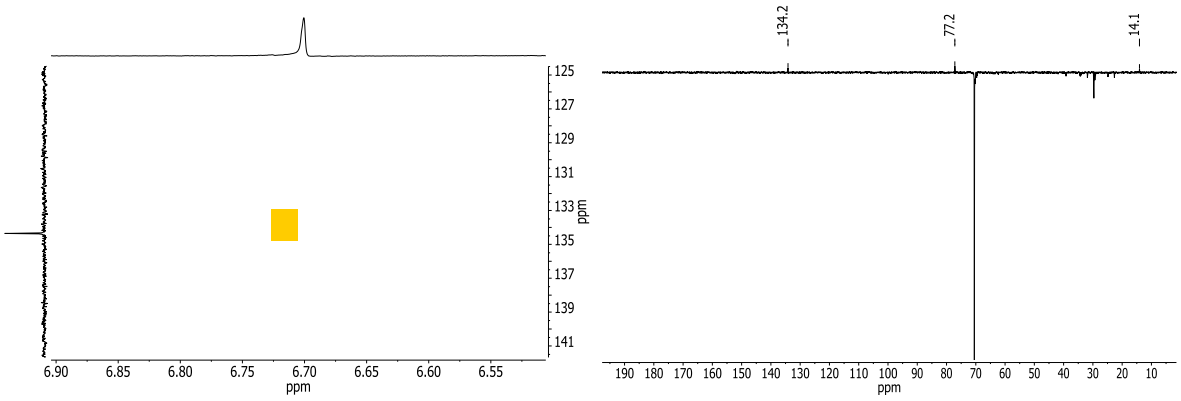


Figure A.3: Additional NMR spectra of DSPE-PEG$_{2000}$-maleimide **2.1a**. Left: HSQC showing the correlation between the maleimide proton peak at 6.70 ppm and the peak in the ^{13}C NMR at 134.4 ppm; Right: DEPT135 spectrum showing the peak at 134.4 ppm to be positive, corresponding to a CH or CH_3 proton. Solvent $CDCl_3$.

A.2.2 DSPE-PEG$_{2000}$-cRGDfK – 2.1

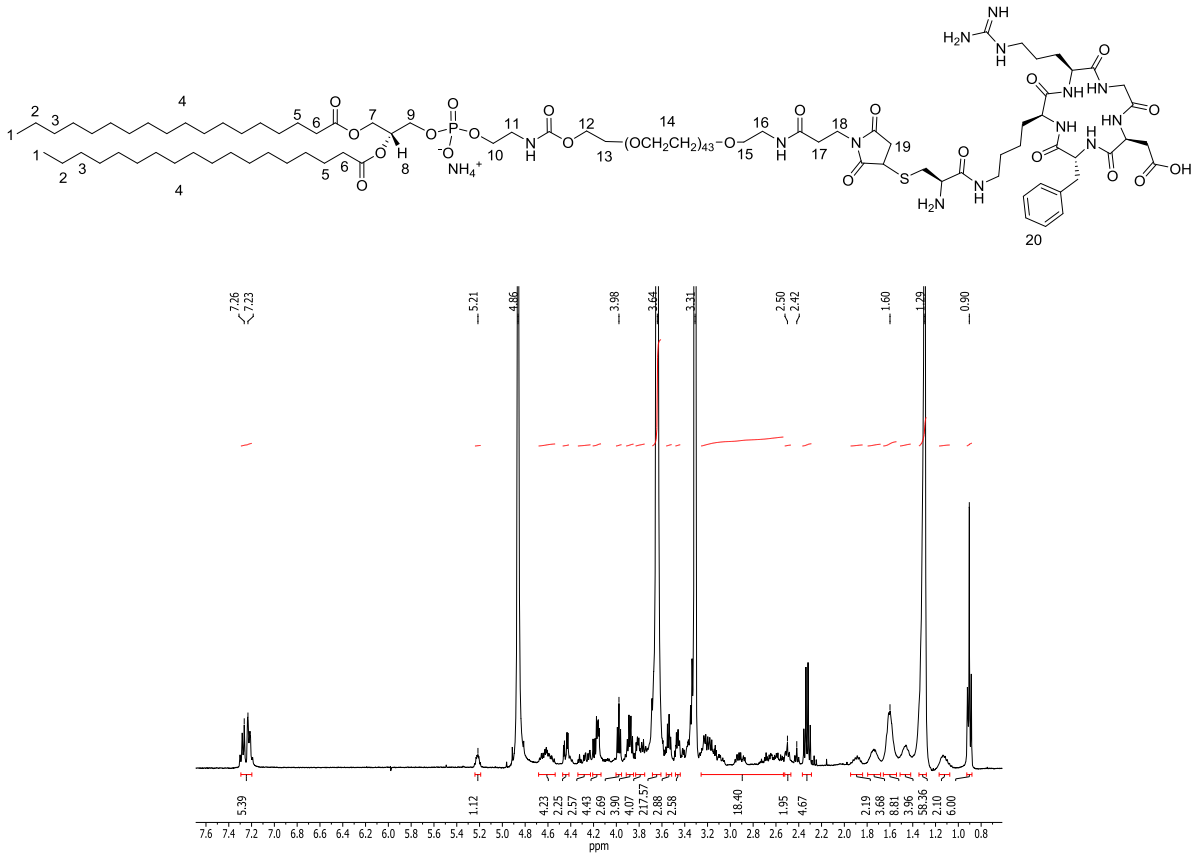


Figure A.4: Structure and ^{1}H NMR spectrum of DSPE-PEG$_{2000}$-cRGDfK **2.1**. Solvent CH_3OD.

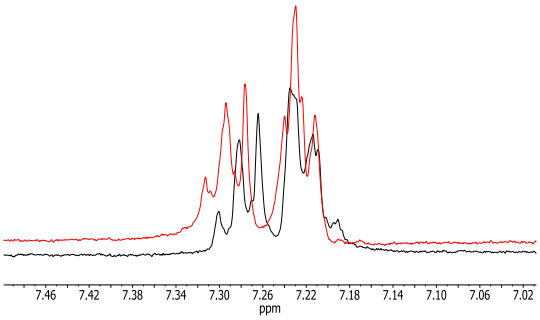


Figure A.5: Aromatic region of the ^{1}H NMR spectrum of DSPE-PEG$_{2000}$-cRGDfK **2.1** (black) and cRGDfK (red) showing overlay of the identifying peptide peak. Solvent CH_3OD.

A.2.3 DSPE-PEG$_{2000}$-TCO – 2.4

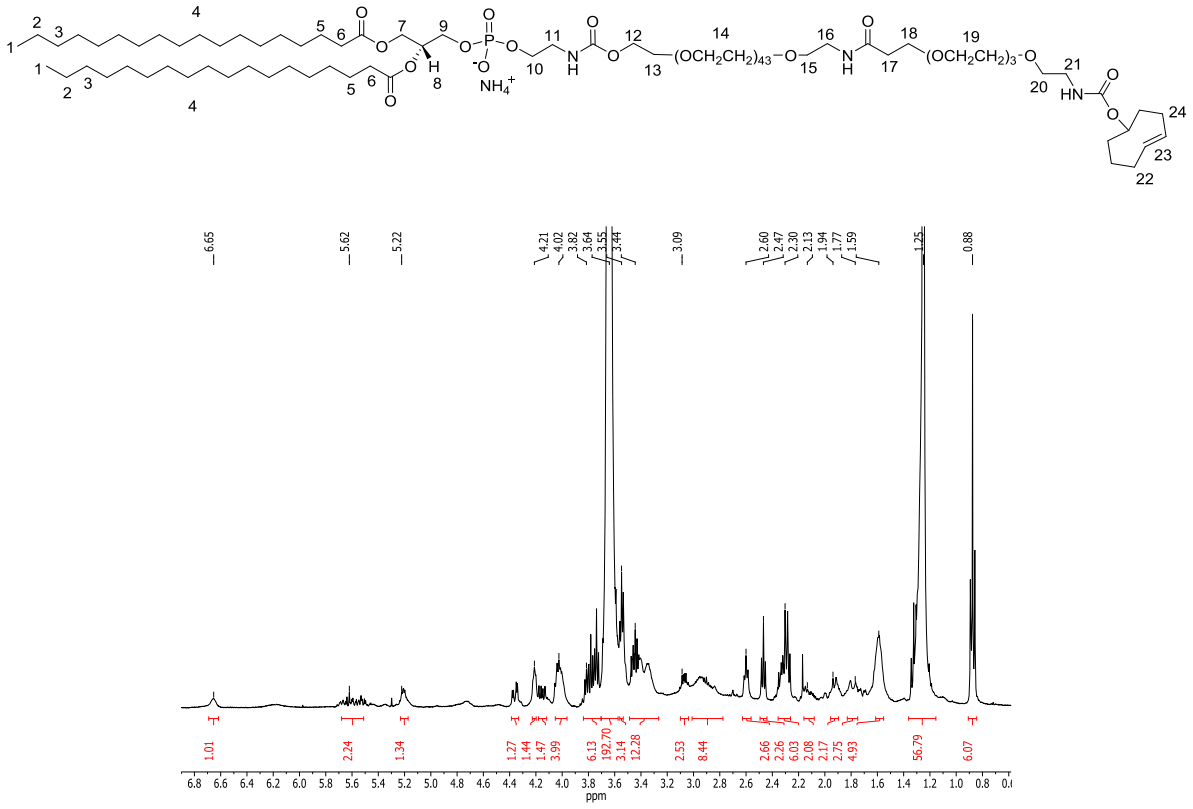


Figure A.6: Structure and ^{1}H NMR spectrum of DSPE-PEG$_{2000}$-TCO **2.4**. Solvent $CDCl_3$.

A.3 LCMS Spectra

A.3.1 DSPE-PEG$_{2000}$-cRGDfK – 2.1

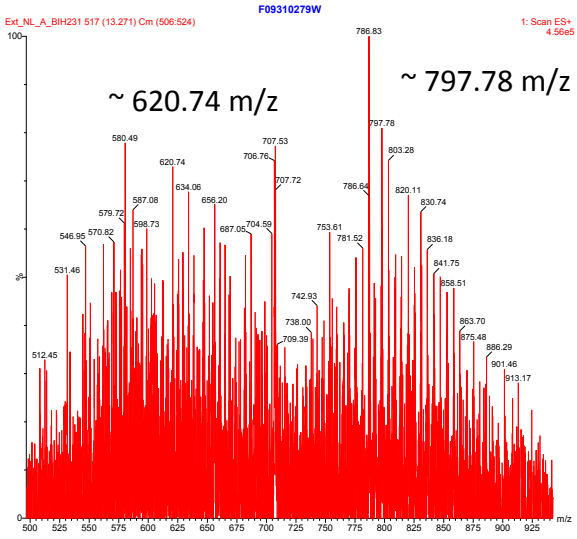


Figure A.7: MS(ES+) spectrum for the peak at 13.27 min (**Figure 2.7**) for compound DSPE-PEG$_{2000}$-cRGDfK **2.1**. Distribution around 797.78 m/z has a spacing ~5.5 m/z correlating to an 8+ charge state.

A.3.2 cRGDfK-C

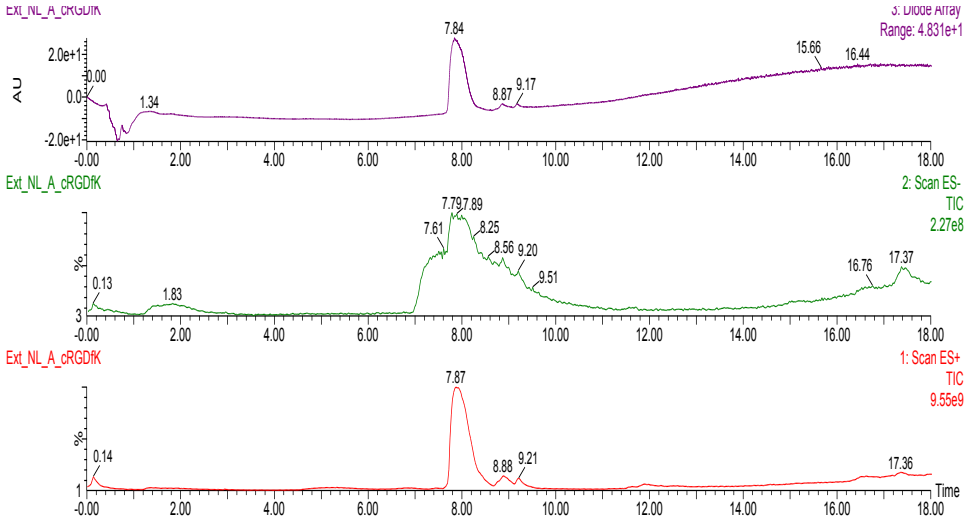


Figure A.8: LCMS chromatograms for cRGDfK-C. Descending: UV, MS(ES-) and MS(ES+).

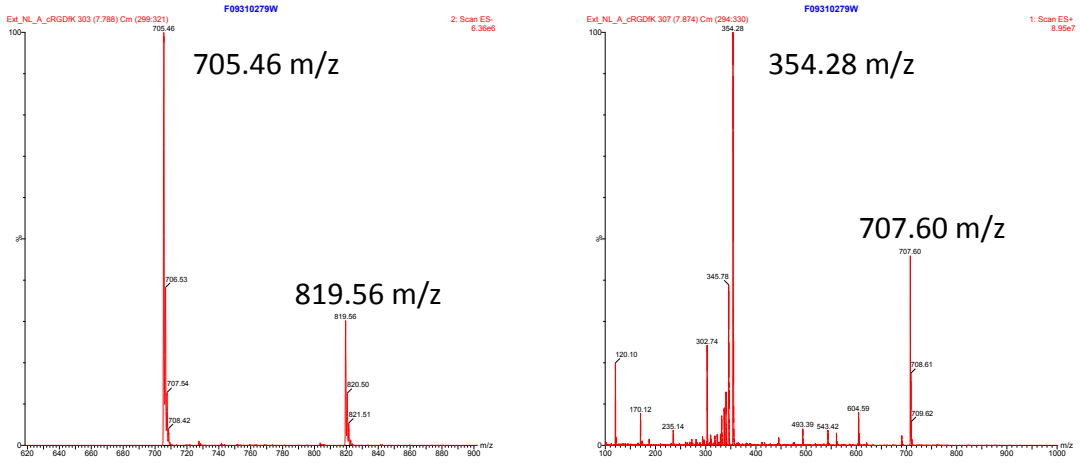


Figure A.9: MS(ES-) (left) and MS(ES+) (right) spectra of the peaks at 7.87 min in **Figure A.8** showing clearly the mass of cRGDfK-C.

A.4 MALDI Spectra

A.4.1 DSPE-PEG$_{2000}$-TCO – 2.4

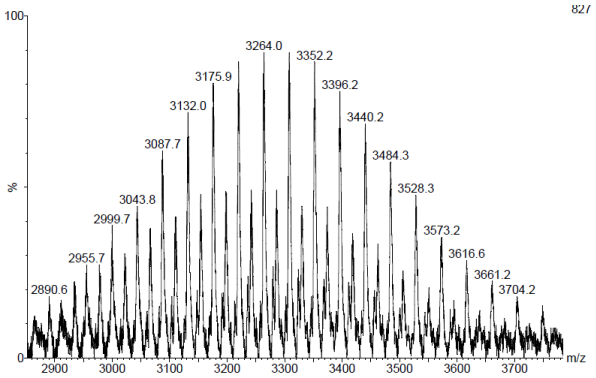


Figure A.10: MALDI spectrum in positive reflectron mode, matrix DHB, for DSPE-PEG$_{2000}$-TCO **2.4**.

A.4.2 DSPE-PEG$_{2000}$-DOTA – 3.5

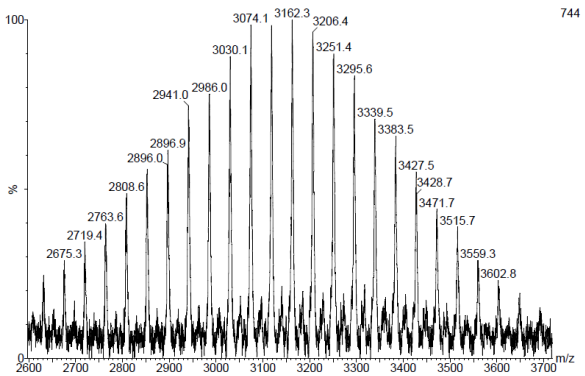


Figure A.11: MALDI spectrum in positive reflectron mode, matrix DHB, for DSPE-PEG$_{2000}$-DOTA **3.5**.

A.4.3 DSPE-PEG$_{2000}$-ROX – 4.1

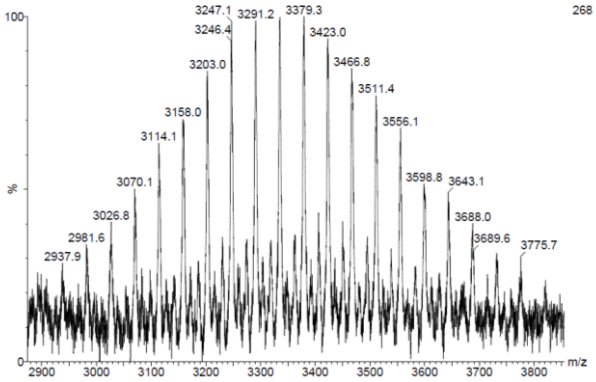


Figure A.12: MALDI spectrum in positive reflectron mode, matrix DHB, for DSPE-PEG$_{2000}$-ROX **4.1**.

A.5 UPC^2 Spectra

A.5.1 DSPE-PEG$_{2000}$-TCO – 2.4

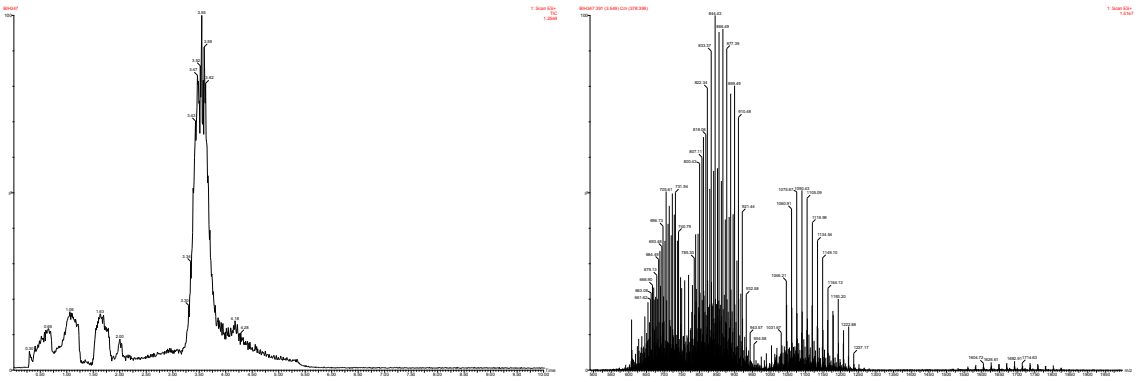


Figure A.13: UPC^2 MS(ES+) data obtained for DSPE-PEG$_{2000}$-TCO **2.4**. Left: UPC^2 chromatogram. Major peak t_R = 3.55 min. Right: MS(ES+) spectra integrated over this major peak. Peak distribution centered around 1090.43 m/z for a 3+ ion, 844.43 m/z for a 4 + ion and 705.61 for a 5+ ion.

A.5.2 Reaction between 3.1 and 2.4

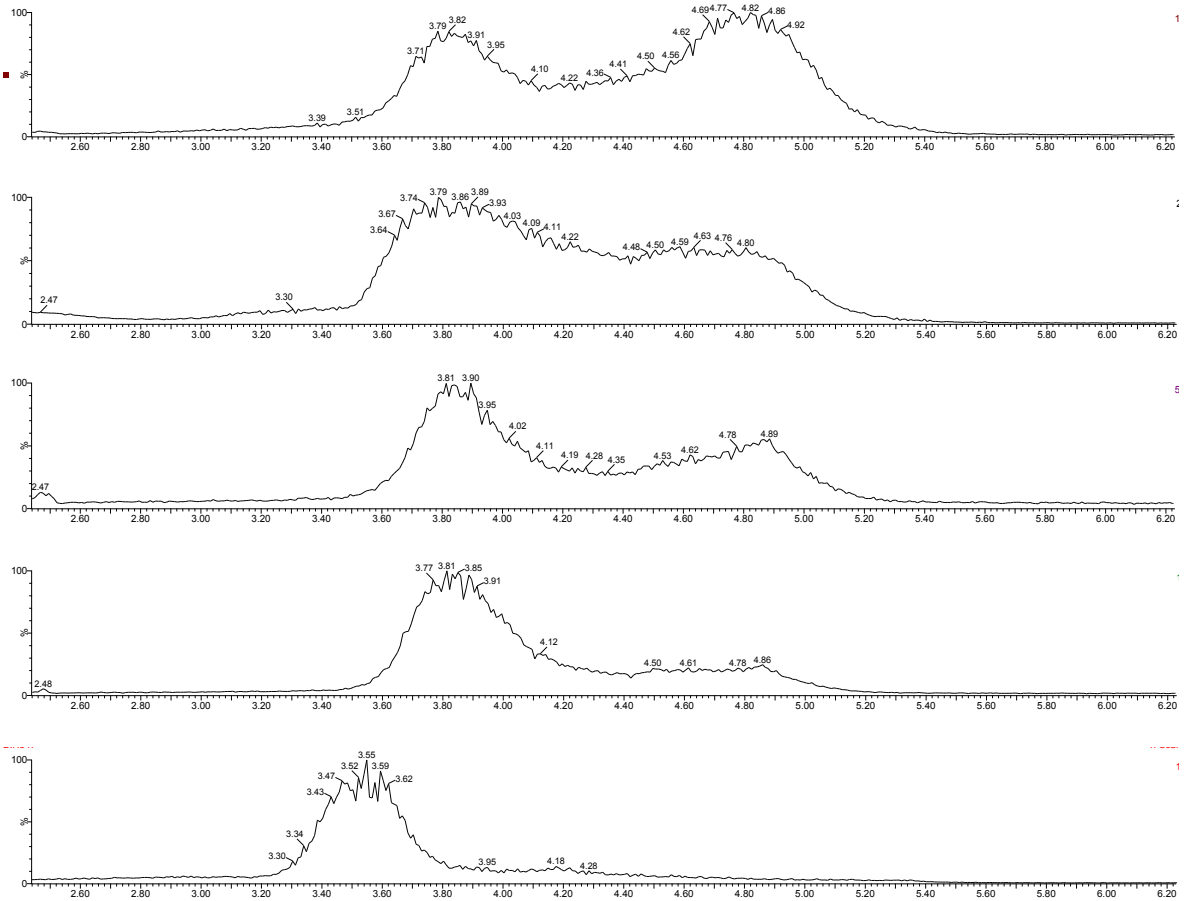


Figure A.14: UPC^2 MS(ES+) chromatograms upon reaction of DSPE-PEG$_{2000}$-TCO **2.4** with DOTA-tetrazine **3.1**. Bottom: unreacted **2.4**. Ascending: Addition of 0.44, 0.88, 1.3 and 2.6 equivalents of **2.4** to a solution of **3.1**. Retentaion times of the two peaks are ~3.80 min for the unreacted phospholipid (~3.55 min in the pure lipid) and ~4.80 min after reaction.

A.5.3 DSPE-PEG$_{2000}$-DOTA – 3.5

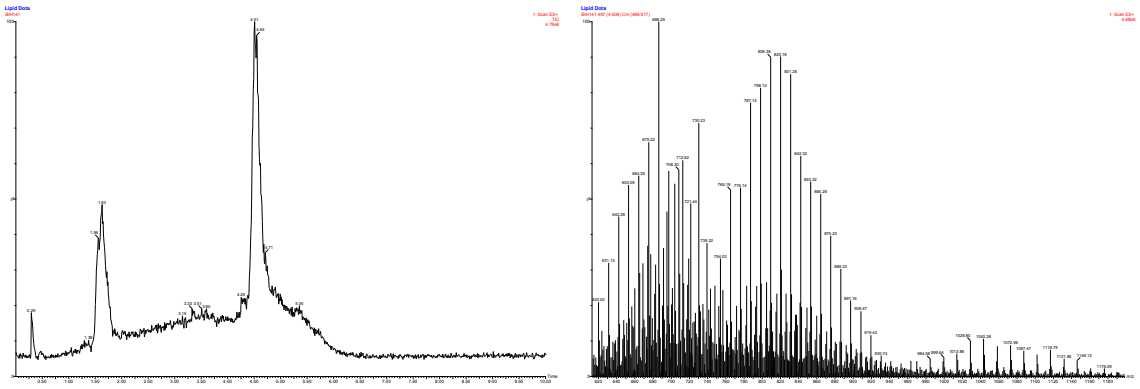


Figure A.15: UPC^2 MS(ES+) data obtained for DSPE-PEG$_{2000}$-DOTA **3.5**. Left: UPC^2 chromatogram. Major peak t_R = 4.51 min. Right: MS(ES+) spectra integrated over this major peak. Peak distribution centered around 1058.43 m/z for a 3+ ion and 820.16 m/z/ for a 4+ ion.

A.5.4 DSPE-PEG$_{2000}$-NOTA – 3.6

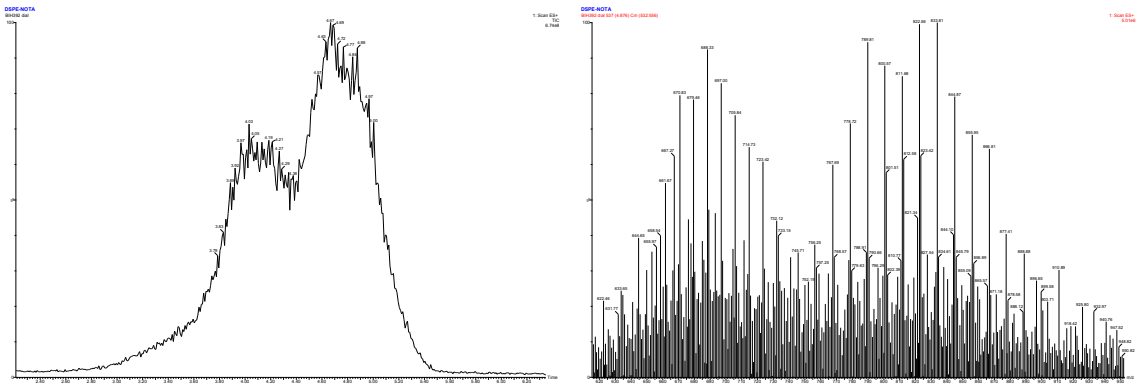


Figure A.16: UPC^2 MS(ES+) data obtained for DSPE-PEG$_{2000}$-NOTA **3.6**. Left: UPC^2 chromatogram. Major peak t_R = 4.67 min. Right: MS(ES+) spectra integrated over this major peak. Peak distribution centered around 822.56 m/z for a 4+ ion and 688.33 m/z for a 5 + ion.

A.5.5 DSPE-PEG$_{2000}$-ROX – 4.1

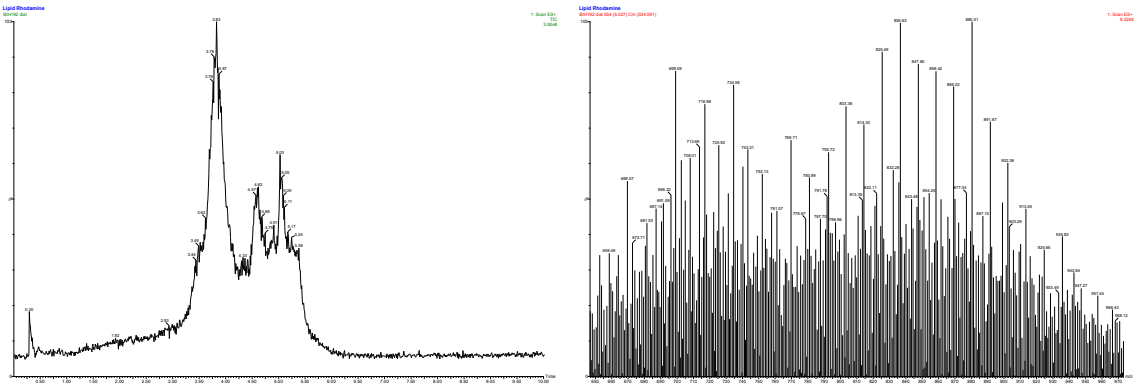


Figure A.17: UPC^2 MS(ES+) data obtained for DSPE-PEG$_{2000}$-ROX **4.1.** Left: UPC^2 chromatogram. Major peak t_R = 5.03 min. Right: MS(ES+) spectra integrated over this major peak. Peak distribution centered around 847.71 m/z for a 4+ ion.

A.5.6 DSPE-PEG$_{2000}$-Rh – 4.2

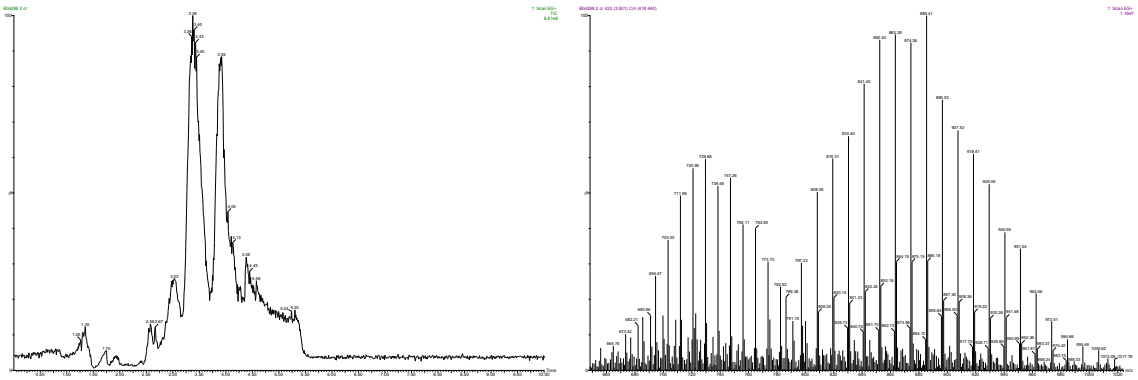


Figure A.18: UPC^2 MS(ES+) data obtained for DSPE-PEG$_{2000}$-Rh **4.2**:Left: UPC^2 chromatogram. Major peak t_R = 3.92 min. Right: MS(ES+) spectra integrated over this major peak. Peak distribution centered around 863.38 m/z for a 4+ ion and 729.66 for a 5+ ion.

A.5.7 DSPE-PEG$_{2000}$-Rh+ – 4.3

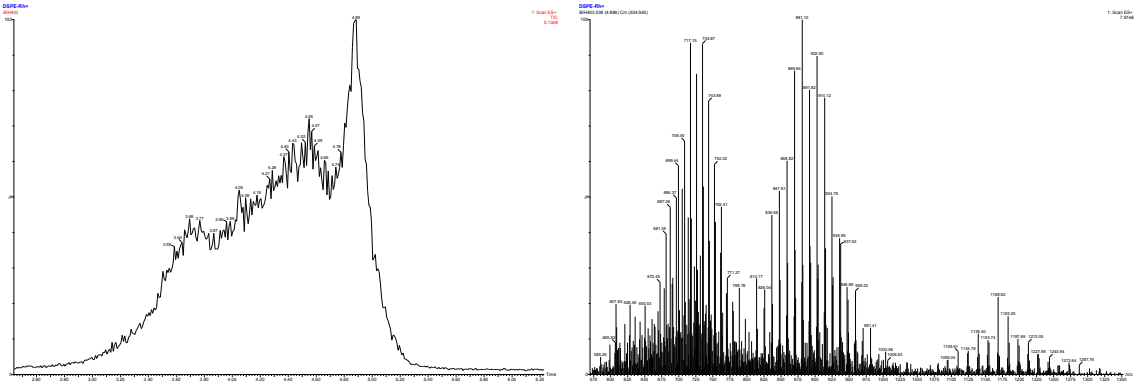
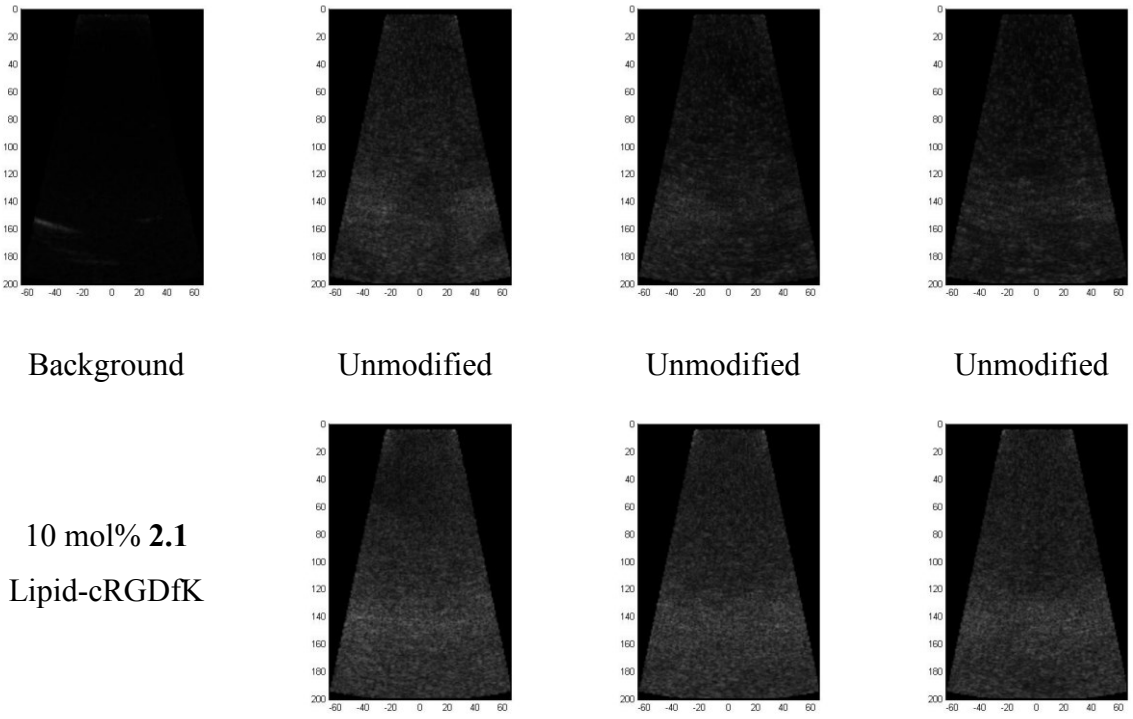
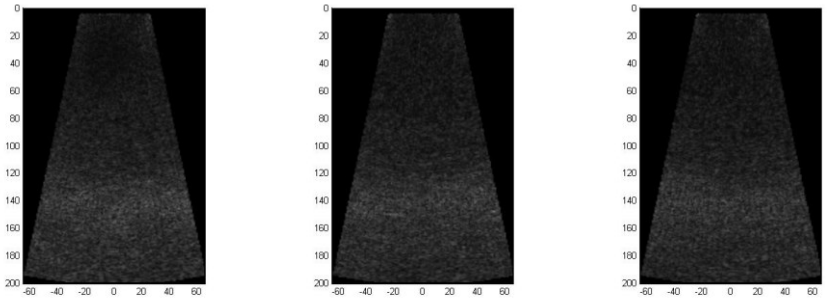


Figure A.19: UPC^2 MS(ES+) data obtained for DSPE-PEG$_{2000}$-Rh+ **4.3**:Left: UPC^2 chromatogram. Major peak t_R = 4.89 min. Right: MS(ES+) spectra integrated over this major peak. Peak distribution centered around 1183.30 m/z for a 3+ ion, 881.10 for a 4+ ion and 717.15 for a 5+ ion.

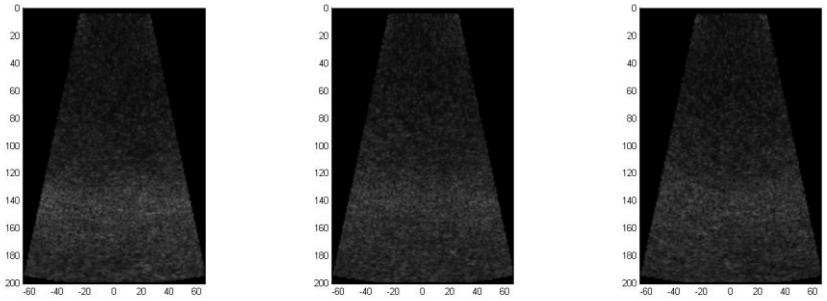
A.6 Acoustic Characterisation



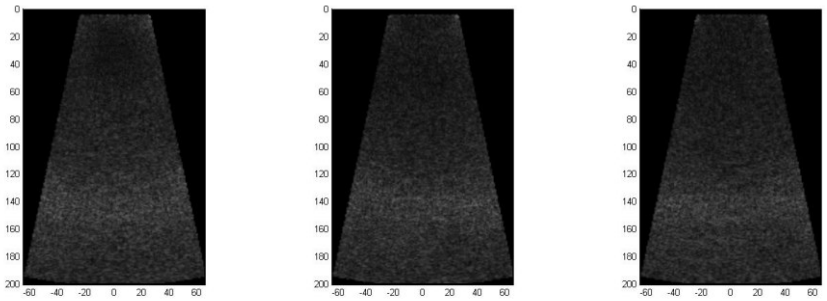
10 mol% **3.5**
Lipid-DOTA



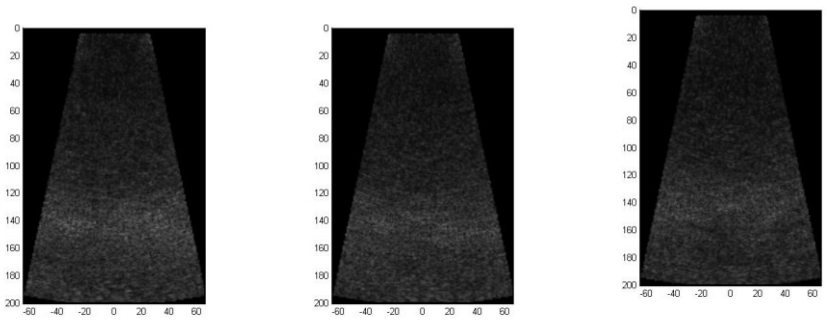
5 mol% **3.5**
Lipid-DOTA
5 mol% **2.1**
Lipid-cRGDfK



10 mol% **3.6**
Lipid-NOTA



5 mol% **3.6**
Lipid-NOTA
5 mol% **2.1**
Lipid-cRGDfK



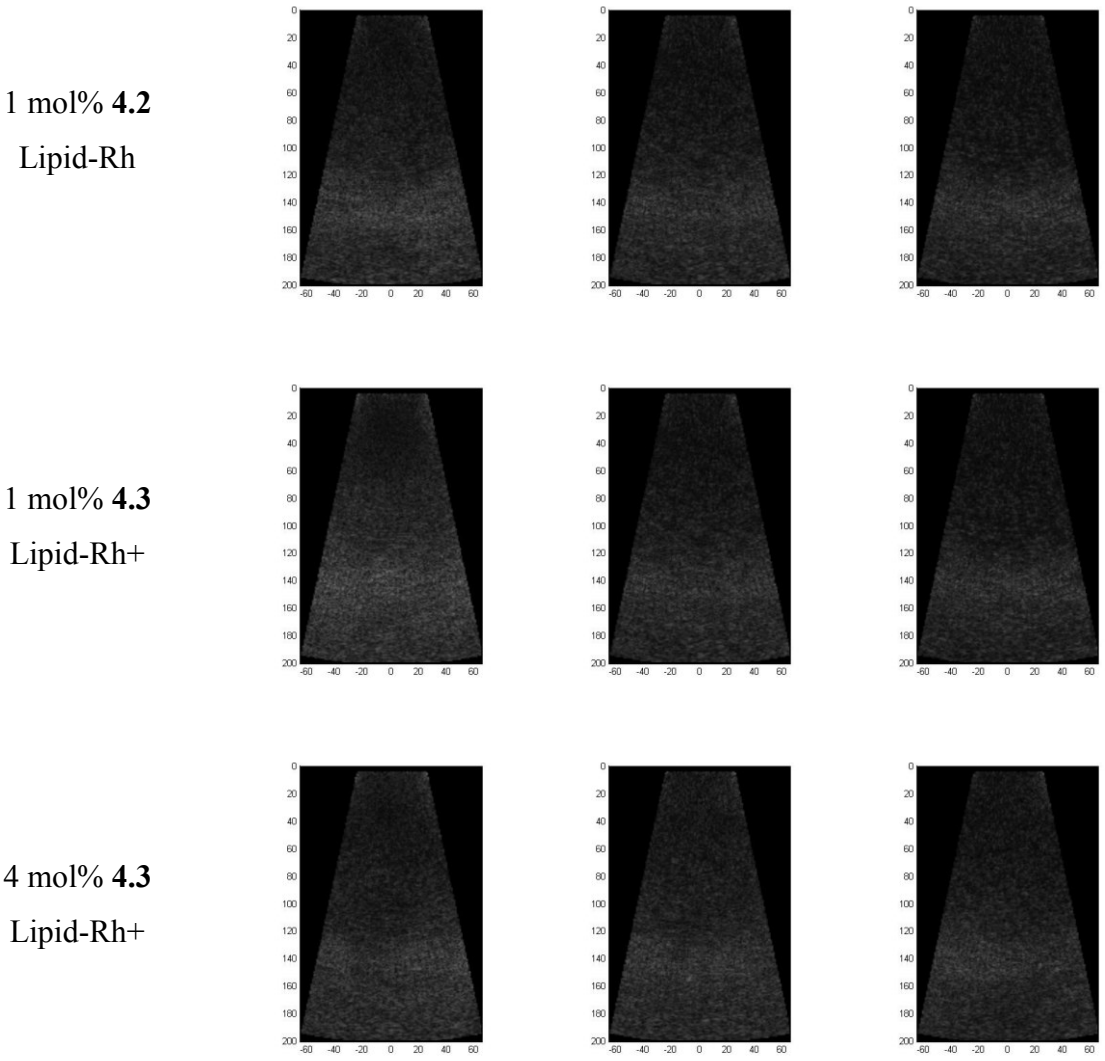


Figure A.20: Acoustic measurements of solutions containing various microbubble formulations. Measurements performed on a Verasonics ultrasound imaging system equipped with a P4-2v probe (2 MHz imaging frequency at a Mechanical Index of 0.08). 1.7 L H_2O was rested for 5 min following which 20 µL of the microbubble solution was added.

A.7 UV-Vis. Spectra

A.7.1 Tetrazine-COOH – 3.4

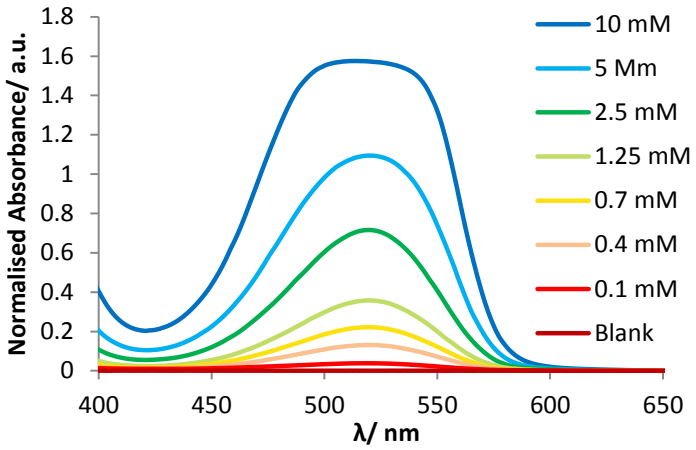


Figure A.21: UV-vis. absorbance of tetrazine at different concentrations using tetrazine-COOH **3.4**. λ_{max} = 520 nm.

A.7.2 Reaction between 3.1 and 2.4

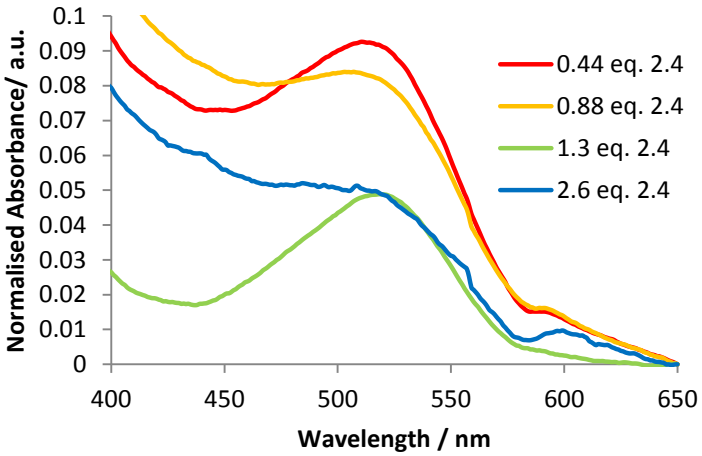


Figure A.22: UV-vis. tetrazine absorption spectra of DO3A-tetrazine **3.1** upon the addition of DSPE-PEG_{2000}-TCO **2.4**. All measurements were taken in PBS pH 7.6 by gradual addition to the dry phospholipid

A.8 Microscope Images

A.8.1 Microbubbles – 4 mol% 4.3

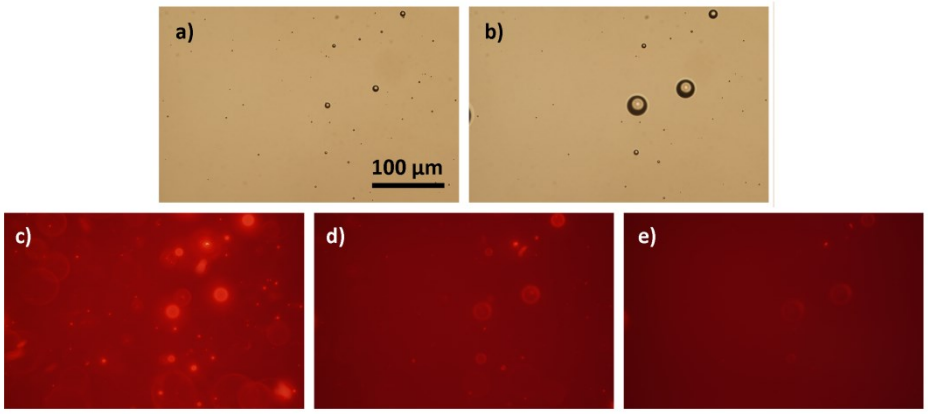


Figure A.23: Images of microbubbles containing 4 mol% **4.3** (40 x magnification). a) and b) show brightfield images before and after laser irradiation respectively. c), d) and e) are fluorescent images of the same field-of-view taken in immediate succession during irradiation. 100 times dilution with PBS.

A.8.2 Microbubbles – 1 mol% 4.2

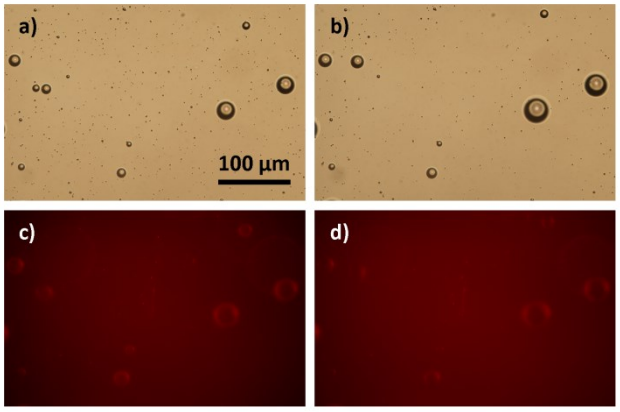


Figure A.24: Images of microbubbles containing 1 mol% **4.2** at pH 7.6 (40 x magnification). a) and b) show brightfield images before and after laser irradiation respectively. c) and d) are fluorescent images of the same field-of-view taken in immediate succession during irradiation. 100 times dilution with PBS.

A.8.3 Unmodified Nanodroplets

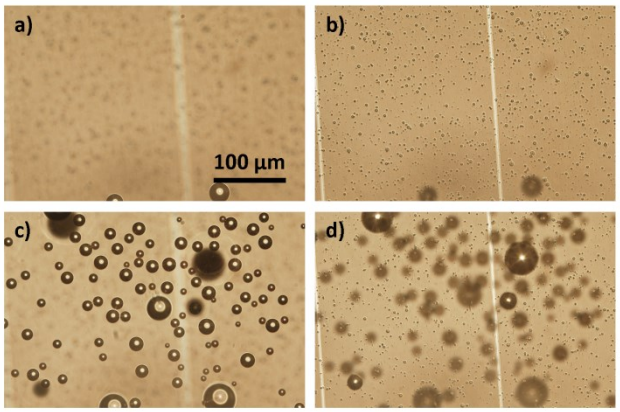


Figure A.25: Images of unmodified nanodroplets before (top) and after (bottom) fluorescence images were taken. a) Brightfield surface image (where microbubbles are expected); b) brightfield image focussed on the base (where nanodroplets are expected); c) brightfield surface image after irradiation; d) brightfield image focussed on the base after irradiation. Solution used at concentration synthesised.

A.8.4 Nanodroplet Laser Vaporisation Experiments

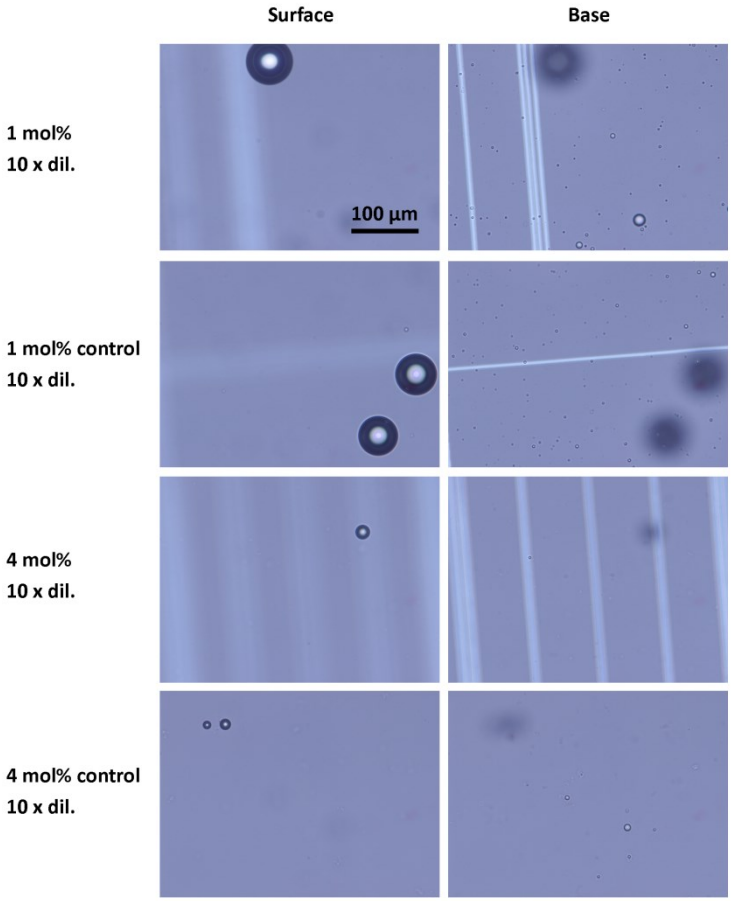


Figure A.26: Brightfield images taken of nanodroplet solutions containing **4.3** with and without laser irradiation. All experiments performed at 10 x dilution of nanodroplet solution. Images taken without further dilution. Left: Surface image where microbubbles are expected; Right: base images where nanodroplets are expected. Descending: 1 mol% nanodroplets after laser irradiation; control formulation of 1 mol% nanodroplets without laser irradiation; 4 mol% nanodroplets after laser irradiation; control formulation of 4 mol% nanodroplets without laser irradiation.

A.9 *In Vitro* Work

A.9.1 Microbubble Binding Experiments – 5 mol% 2.1 and 5 mol% 2.4

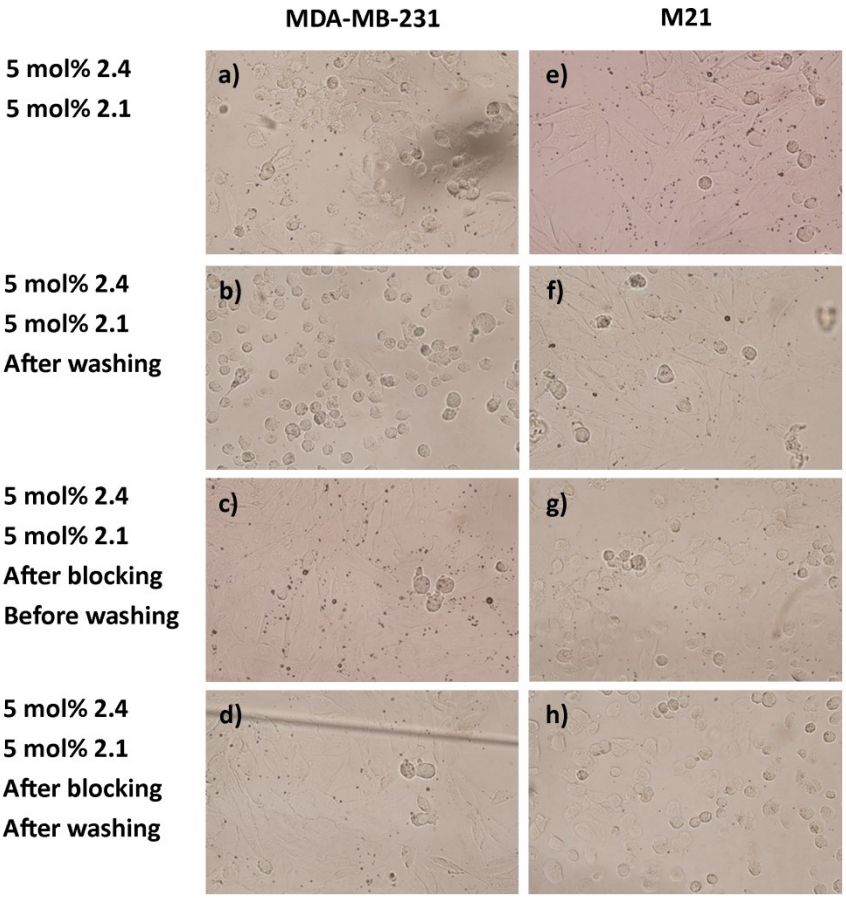


Figure A.27: *In vitro* work performed with microbubbles containing 5 mol% phospholipid **2.1** and 5 % phospholipid **2.4** on MDA-MB-231 (left) and M21 (right) cell lines using the incubation protocol described in Chapter 2. a) Microbubbles adhered to MDA-MD-231 cells on the lower membrane; b) microbubbles adhered to MDA-MD-231 cells on the lower membrane after washing; c) microbubbles adhered to MDA-MD-231 cells on the lower membrane after blocking using a linear RGD peptide; d) microbubbles adhered to MDA-MD-231 cells on the lower membrane after blocking using a linear RGD peptide and after being washed; e) microbubbles adhered to M21 cells on the lower membrane; f) microbubbles adhered to M21 cells on the lower membrane after washing; g) microbubbles adhered to M21 cells on the lower membrane after blocking using a linear RGD peptide; h) microbubbles adhered to M21 cells on the lower membrane after blocking using a linear RGD peptide and after being washed. These images show that washing reduces the number of microbubbles but that some are still retained, particularly in the M21 cell line. Blocking was only partially successful, with a greater effect in the M21 cell line. The same microbubble solution was used in all experiments with an initial concentration of 2.26 x 10^9 MB/ mL. Images obtained by Marta Braga.[1]

1. M. Braga, Thesis, Not Submitted, Imperial College London.